Qingkai Han
Jing Wei
Qingpeng Han
Hao Zhang

Dynamics and Vibration Analyses of Gearbox in Wind Turbine

Springer

Dynamics and Vibration Analyses of Gearbox in Wind Turbine

Qingkai Han · Jing Wei · Qingpeng Han
Hao Zhang

Dynamics and Vibration Analyses of Gearbox in Wind Turbine

Springer

Qingkai Han
Collaborative Innovation Center of Major Machine Manufacturing in Liaoning
Dalian University of Technology
Dalian
China

Jing Wei
The State Key Laboratory of Mechanical Transmissions
Chongqing University
Chongqing
China

Qingpeng Han
Shanghai University of Electric Power
Shanghai
China

Hao Zhang
Collaborative Innovation Center of Major Machine Manufacturing in Liaoning
Dalian University of Technology
Dalian
China

ISBN 978-981-10-2746-8 ISBN 978-981-10-2747-5 (eBook)
DOI 10.1007/978-981-10-2747-5

Library of Congress Control Number: 2016953209

Printed on acid-free paper

This Springer imprint is published by Springer Nature
The registered company is Springer Nature Singapore Pte Ltd.
The registered company address is: 152 Beach Road, #22-06/08 Gateway East, Singapore 189721, Singapore

Acknowledgments

This book is financially supported by Collaborative Innovation Center of Major Machine Manufacturing in Liaoning, National Basic Research Programs of China (Nos 2012CB026000-05, 2013CB035402-2), and Natural Science Foundations of China (Grant Nos 51175070, 11472068).

Contents

Abstract

Gearbox is the core part of a wind turbine which realizes the transmission and energy transfer from wind blades to electric generator. The dynamics and vibration properties of the gearbox especially of its geared rotor systems prominently determine the efficiency and operating quality, even the whole-life expectation and reliability of the machine set. In this book, the dynamic analyses and vibration behaviors are investigated for the gearboxes which are popularly used to modern wind turbines by using mechanics theories, finite element-based simulations, experimental measurements, and vibration signal processing techniques.

Firstly, the background and main ideas of the book are described. Secondly, the torsional dynamic model and vibration resonances are achieved based on the lumped mass model of the geared rotor system, which is composed of two stages of planetary gear trains and one parallel gear pair. Furthermore, the load sharing of the planetary gear train based on the given torsion model is presented with considering time-varying mesh stiffness, tooth backlash, fixing error, and manufacturing error of the gears and carrier. Also, the measured strains at the gear tooth roots are used to confirm that load-sharing analyses of the planetary gear train are acceptable. Based on the model, the vibrations of both the geared rotor systems and the gearbox housings are calculated under either the internal excitations coming from gear sets or external loads transferring from wind loads.

Next, the parameter optimization for planetary gear system is defined and processed based on the torsional dynamics of the geared rotor system of wind turbine. The fault-induced vibrations of the geared rotor system are simulated, which involves the popularly occurring fault of support misalignment of the rotor. The rotor-misaligned fault-induced vibrations are of importance in practical manufacturing error control and assembly processing optimization, even helpful in operating condition monitoring and fault diagnosis.

And then, the whole gearbox finite element model (WG-FEM) is built, and its natural frequencies and modes of the gearbox system (including shells and geared rotors) are calculated. Experimental measurements of vibrations on the wind turbine gearbox are performed on the test rig and on-site. The vibration signals of different testing points are analyzed in time and frequency domains to explore the underlying complicated behaviors. Some technologies of Hilbert–Huang transform-based analyses are also achieved in the vibration signal processing.

At last, the gear coupling frequencies and fault characteristic frequencies are obtained from the vibrations of the gearbox housing.

In summary, the technologies and results of this work provide some good references for dynamic design and vibration prediction and analysis for gearbox and its geared rotor system of wind turbine, even for many other machines.

Keywords Gearbox in wind turbine · Geared rotor system · Model of torsional dynamics · Parameter optimization · Load sharing of planetary gear train · Whole gearbox finite element model · Whole gearbox modes · Vibration signal processing · Vibration fault diagnosis

Chapter 1
Introduction

1.1 Requirement of Wind Turbine Gearbox

Wind energy is one of the most developed renewable energy prospects. The world's wind power industry developed rapidly in recent years, and the total wind power capacity reached 432 GW by the end of 2015. Chinese wind power capacity increases rapidly and becomes the largest one all over the world. By the end of 2015, the total installed capacity reached 145 GW, accounting for 33.6 % of the world's wind power capacity.

However, China's wind turbines are often operating in low efficiency, and the yearly average utilization time of a wind turbine set is only 1903 h, less than the expected 2500 h [1]. The main reasons are various premature failures and poor reliability of the wind turbines. Figure 1.1 shows the failure statistics of Chinese wind turbines from January 2011 to August 2011, in which 23,600 machine parts have been suffered from failures in operation and it happened more than 40,000 times [2]. It is also well known to be the similar situation in Europe and North America, including some famous companies [3]. Among these failures, massive problems belong to the core parts of the energy transmission chain, i.e., inside the gearboxes and the rotor systems.

The transmission chain of the wind turbine (here excluding the direct-drive wind turbine) contains the hub, the main shaft and its bearing, the gearbox, and the generator, as shown in Fig. 1.2. The gearbox is the major part to transfer energy and works under severe loading condition. The failures of the transmission chain of the wind turbine always cause a sudden shutdown. According to the statistics finished by wind energy companies, the mean time between failures (MTBF) of the gears and the bearings and other mechanical transmission parts in wind power equipment is as low as only hundreds of hours, and almost 20 % of the downtime is caused by the failures of the gearbox.

Due to the severe loading condition, such as strong wind, rain, dust, and together with the huge and changeable loads, the gearbox components of wind turbine often

Q. Han et al., *Dynamics and Vibration Analyses of Gearbox in Wind Turbine*,
DOI 10.1007/978-981-10-2747-5_1

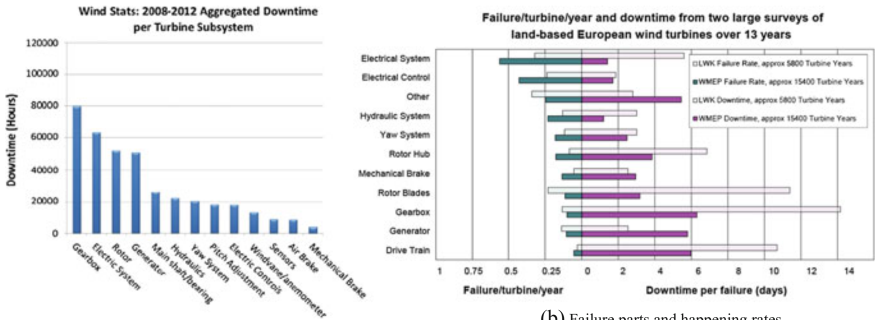

(a) Failure statistics of parts of wind turbine

(b) Failure parts and happening rates

Fig. 1.1 Failure statistics of wind turbines. **a** Failure statistics of parts of wind turbine. **b** Failure parts and happening rates

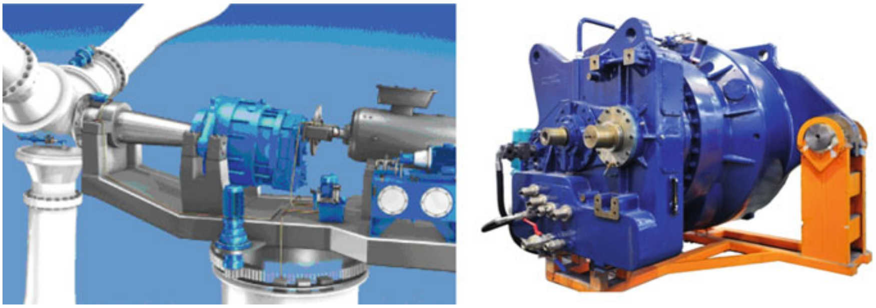

Fig. 1.2 Gearbox in a wind turbine

suffer from wear, pitting, crack, and other structural damages. Most structure faults stem from the bending and the torsion effects of the gear-rotor system in the gearbox, involving the coupling mechanism of them under the possible contact and shock loads because of the clearances between the gear sets and the bearings.

Recently, the gearbox failures and faults are in a more desperate situation in the wind energy industry, which brings high maintenance costs and frequent shutdowns. Many researchers and technicians are working hard to improve the reliability, especially focusing on its gearbox dynamics and vibration control technology.

1.2 Dynamics of Gearbox

Many researchers focus on the dynamics of the gear transmission system. Abboudi established the three-dimensional transient dynamic model for wind power transmission gearbox to show the dynamic return differences of planetary gears [4]. Bahk studied the effects of the uneven load distribution of the gearbox planetary and the planet wheel on the passing errors [5]. Helsen applied the flexible multibody simulation technology on the dynamic characteristics of wind turbine gearbox and analyzed the stresses of the gear under the meshing impact [6]. Zhang studied the dynamics of wind turbine gearbox by using Romax Designer software and obtained the effect of random fluctuations of the integrated system errors [7]. Chen established a torsional model of wind power planetary gear transmission system in which the gear meshing stiffness and transmission errors are regarded to be changeable timely [8]. Currently, many researches about the planetary gear system vibration analyses, dynamic models, and simulations are conducted [9, 10].

Due to the complex configurations of the planetary gear driven in wind turbine gearbox, it is not easy to detect the damages inside the gearbox. The fault information and its characteristic energy become very weak after passing the supports and the shells of the gearbox. Many researches have done lots of works in gearbox damage identification methods, but intensive researches are still needed to learn the damage principles under severe loading condition to find out effective damage prediction and identification technology.

1.3 Structure Description of Gearbox in Wind Turbine

There are many types of gearboxes used in wind turbine, such as cylindrical gearboxes, planetary growth boxes, and combined gearbox. Figure 1.3 shows a horizontal shaft wind turbine with a fixed parallel shaft gear and a planetary gear set.

The wind turbine gearbox is mainly composed of the housing shell, gear pairs, shafts, and bearings. They are described as follows.

(1) The housing shell of the gearbox should be sufficiently rigid to withstand the forces without deformation. The bearing support on the housing shell is also required to support the bearing rigidly and keep the shafts in good alignment situation. In order to prevent the gearbox vibrations transfer to the tower of the wind turbine, the gearbox is mounted on the elastic shock absorbers.

The static or dynamic stress distribution of the housing shell of wind turbine gearbox is often too complicated to calculate even by using finite element methods. Fracture mechanics and field measurement are also important for vibration damage analyses of the housing shells.

(2) The gears and the shafts are important in the transmission chain of wind turbine and require very strict material selection and structural design. They are not recommended to use prefabricated structures or welded assembly. The driving shaft and the driven shaft also need quenching and tempering to get high surface hardness and good ductile inside.
(3) The bearing life should not be less than 130,000 h in design opinion. The deformation of the shaft and the bearing in operating condition and the shaft misalignment will cause damages to both the gears and the bearings. The severe overload and improper lubrication can also lead to gear tooth and bearing fatigues on their contact surfaces.

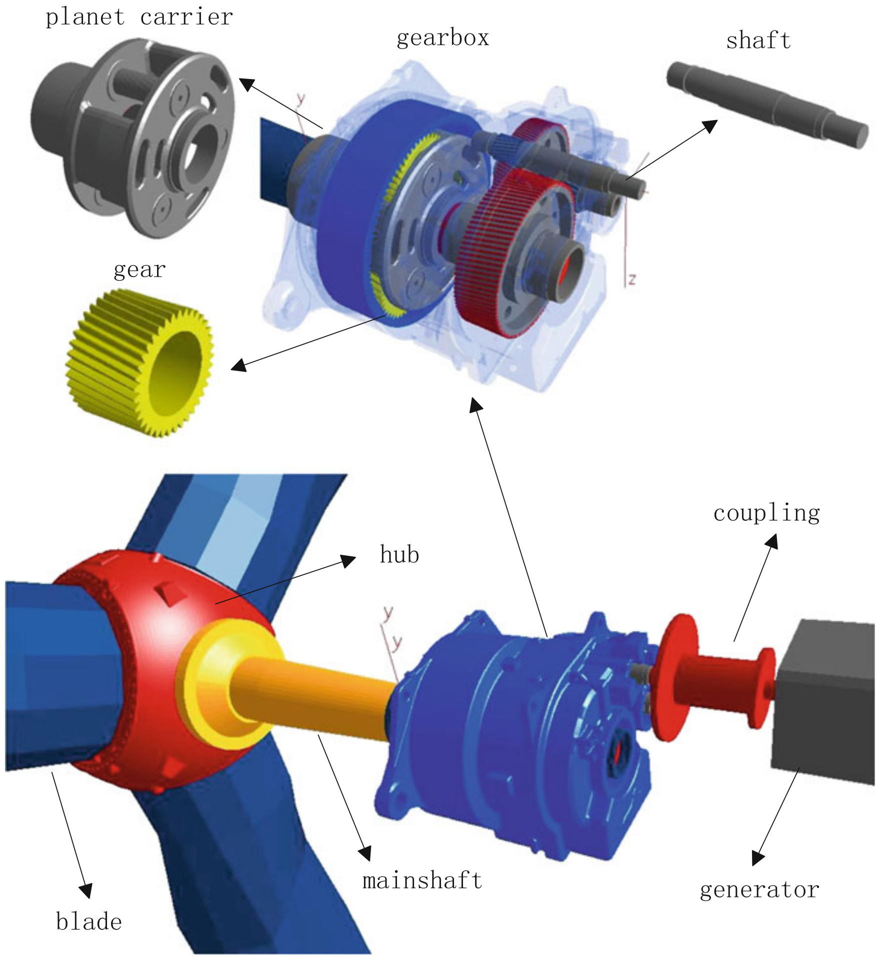

Fig. 1.3 Horizontal shaft wind turbine and its gearbox

1.4 Modeling Methods for Dynamic and Vibration Analyses

The multilevel modeling strategy can be adopted in modeling the wind turbine gearbox to analyze the system dynamics and its key parts. The different level models can be used to describe the whole machine modal matching, modal coupling among parts, vibration predictions of key positions, and so on. The whole machine model such as a WG-FEM can be built by using finite element method or by using simplified models of the sub-systems which is called as a hybrid model. An analysis method of the wind turbine gearboxes is shown in Fig. 1.4.

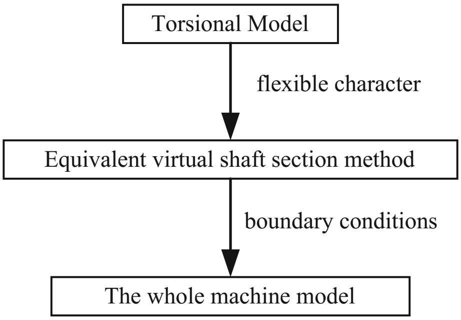

Fig. 1.4 Multilevel modeling strategy

Even in order to model the wind turbine transmission chain, the gearbox, hub, generator, etc. can be modeled and analyzed separately at first, and then, the whole model is built by coupling all these sub-systems or components.

1.5 Shaft Misalignment in Gearbox

Wind turbine generator system (WTGS) has a long transmission chain and a lot of components, which makes it hard to control the links causing misalignment. The main factors causing misalignment include machining error, installation error, deformation of components, changes in environment and working condition, and improper design.

High-precision component is the key factor of the shafts alignment. For example, there are strict requirements in machining accuracy, such as perpendicularity between the central axis of the bearing seat and the base, parallelism between the axes of gearbox input shaft and gearbox output shaft, and all of which should be strictly controlled in the process of the production and checkout. But in reality, it is hard to guarantee machining accuracy; for example, the relative altitude of several fixing positions in the base could not well meet high accuracy requirements through machining.

Alignment of shafts is always a difficult problem for a long transmission chain. However, the installation of WTGS is needed operated in the cabin, which is always tens of meters, even hundreds of meters high. What's more, the installation space is small, while the size and mass of components are relatively big, which might easily bring large misalignment in the installation. For this reason, manufacturers always assemble the transmission system in the ground and adjust the shafts again on the top of tower after hoisting.

The deformation of components mainly occurs in the rubber supporters of cabin base, gear case, and electric generator. Cabin base usually uses welding, casting, or molding, and the aging treatments should also be conducted in most cases. Even so, the resident stress is difficult to completely eliminate due to the large size. Moreover, the environment temperature changes rapidly in wind field, and the nonuniform deformation occurs in the cabin base during the process of WTGS operating, which can also lead to shafting misalignment.

Shafting misalignment is a typical failure mode of WTGS. Misalignment will increase the load on bearing and gearbox, causing vibrations of components or overall machine, and increase the dynamic load on bearing and gearbox. According to the basic fatigue life formula from ISO281-1990, when dynamic load is increased by 5 %, fatigue life will decrease by 15 %. Thus, shafting misalignment issue should be highly valued.

1.6 Measurement and Analysis of Gearbox Vibration

In the prototype test, the manufacturers of wind power machines will carry out different tests for different purposes before installation. As an example, Danish company Vestas set up a wind turbine test platform that can be used for V164-8.0 MW wind turbine testing. However, the wind turbine test platforms are hard to simulate the real load conditions. The internal information of a gearbox is also difficult to be measured such as the gear tooth contact stress distributions. In China, Shanghai Electric, Dongfang Electric, Guodian United Power, and other companies built many MW-class wind turbine test platforms to finish the machine performance testing. Throughout, the vibration measurement and fatigue life test are not conducted, even though these data are so important for the design and the maintenance of the gearbox.

Researchers have already studied the dynamics and vibration problems of the gear transmission from the aspects of the vibration characteristics, incentive mechanism, forced vibration, dynamic loading, and fatigue life and made a lot of achievements. Many test standards on the whole transmission chain and assessments, such as IEC61400, are made early and widely used. But the wind turbine failures resulted from gearboxes inevitably show that there are many underlying problems need to be solved in designing, manufacturing, and testing, such as the nonlinear dynamic behaviors of both whole machine and part structures when considering the varying mesh stiffness, damping, support stiffness, manufacturing errors, installation errors, and bearing stiffness.

1.7 Works in This Book

In this work, the dynamics analysis, vibration characteristics, response predictions, and test measurements of the wind turbine gearbox are introduced, which is one type of large wind turbine gearbox composed of two stages of planetary gear train and one parallel gear pair. Firstly, the torsional vibration resonances are obtained based on the lumped mass model of torsional dynamics of the gear-rotor system, where the time-varying mesh stiffness and tooth backlash are considered. Based on the model, parameter optimization and load factors of the gear-rotor system are achieved. Moreover, the equivalent virtual shaft section method of the geared rotor system is proposed,while the vibrations of the gear-rotor system involving the popularly occurring fault of unbalance and support misalignment are also simulated based on this model. And then, the whole gearbox finite element model (WG-FEM) is built, and the natural characteristics (natural frequencies and mode shapes) of the whole gearbox are calculated. Finally, Numbers of bench and field test of vibration data and time-frequency domain analysis results are introduced. The measured vibration signals are analyzed thoroughly in time domain and frequency domain by using modern time–frequency-domain analysis methods.

References

1. http://tj.cec.org.cn/tongji/niandushuji/2012-01-13/78769.html.
2. China State Electricity Regulatory Commission, Wind power safety supervision report, 2012.
3. Caithness Windfarm Information Forum 2012, http://www.caithnesswindfarms.co.uk.
4. Abboudi K, Walha L, Driss Y, et al. Dynamic behavior of a two-stage gear train used in a fixed-speed wind turbine. Mech Mach Theory. 2011;46(12):1888–900.
5. Bahk CJ, Parker RG. Analytical solution for the nonlinear dynamics of planetary gears. J Comput Nonlinear Dyn. 2011;6(2):267–74.
6. Helsen J, Vanhollebeke F, Marrant B, et al. Multibody modelling of varying complexity for modal behaviour analysis of wind turbine gearboxes. Renewable Energy. 2011;36(11): 3098–113.
7. Zhang Y. Simulation analysis of dynamics of gearbox used in a large-scale wind power system. PhD dissertation of Huabei University of Electric Power, 2009 (in Chinese).
8. Chen HT, Qin DT, Wu XL, et al. Dynamic characteristics of planetary gear transmission system of wind turbine with random manufacturing error. J Mech Eng. 2012;48(12):77–83.
9. Helsen J, Vanhollebeke F, Coninck FD, et al. Insights in wind turbine drive train dynamics gathered by validating advanced models on a newly developed 13.2 MW dynamically controlled test-rig. Mechatronics. 2011;21(4):737–52.
10. Toft HS, Branner K, Berring P, et al. Defect distribution and reliability assessment of wind turbine blades. Eng Struct. 2011;33(1):171–80.

Chapter 2
Torsional Dynamics of Gear-Rotor System in Wind Turbine Gearbox

A torsional dynamics modeling for planetary gear transmission system in wind turbine is established after comprehensively considering these nonlinear factors associated with time-varying mesh stiffness, dynamic transmission error, gear mesh impact, and input-varying load. Load factors of planetary gear transmission system are induced from the coupled nonlinear dynamics modeling. Then, the load-sharing performance is studied and the load balance method suited for this model which is validated by the test is obtained from the perspective of load-sharing structure. These results provide fundamental basis for multistage planetary gear transmission system design.

2.1 Lumped Mass Model for Torsional Dynamics

2.1.1 Mechanical Schematic

A two-stage planetary transmission gearbox system in the wind turbine is shown in Fig. 2.1, and its dynamic model is shown in Fig. 2.2. The equivalent dynamics model based on the lumped-parameters and Lagrange general function is shown in Fig. 2.3 [1, 2]. The 1st stage has four planet gears, and the 2nd has three ones. Since the relative position between the axial and meshing line direction is simple (there is a helix angle between them and the planetary location has no effect on it), there is no axial diagram for illustration [3, 4].

Q. Han et al., *Dynamics and Vibration Analyses of Gearbox in Wind Turbine*,
DOI 10.1007/978-981-10-2747-5_2

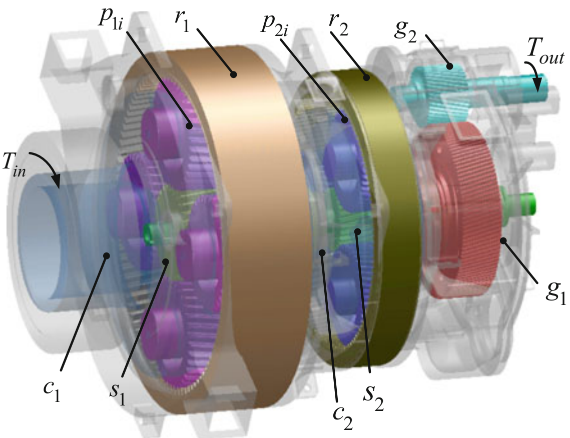

Fig. 2.1 A two-stage planetary gearbox used in wind turbine

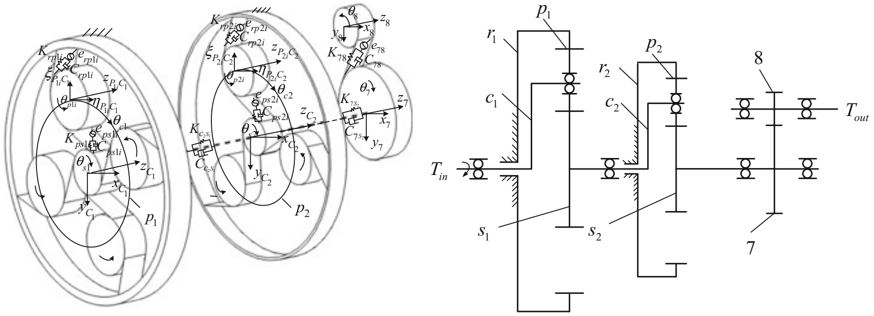

Fig. 2.2 Dynamic model for torsional dynamics

2.1.2 Definition of DOFs

The generalized coordinates of the planetary transmission in two stages are established in rotary coordinate systems which are rotating with each carrier, respectively. Because of the carriers in two stages rotating in plane, rotary coordinate system has no influence on DOF along z-axis. The definition of every variable and parameter of the planetary system is also shown in Fig. 2.3.

The displacement vector of the gear-rotor system of the two-stage planetary gearbox is defined as

$$\begin{aligned}\delta = (&u_{c1}, x_{c1}, y_{c1}, z_{c1}, u_{p1i}, \xi_{p1i}, \eta_{p1i}, z_{p1i}, u_{r1}, x_{r1}, y_{r1}, z_{r1}, u_{s1}, x_{s1}, y_{s1}, z_{s1}, u_{c2}, x_{c2}, y_{c2}, z_{c2},\\ &u_{p1i}, \ \xi_{p2i}, \eta_{p2i}, z_{p2i}, u_{r2}, x_{r2}, y_{r2}, z_{r2}, u_{s2}, x_{s2}, y_{s2}, z_{s2}, \theta_7, x_7, y_7, z_7, \theta_8, x_8, y_8, z_8)^T\end{aligned} \tag{2.1}$$

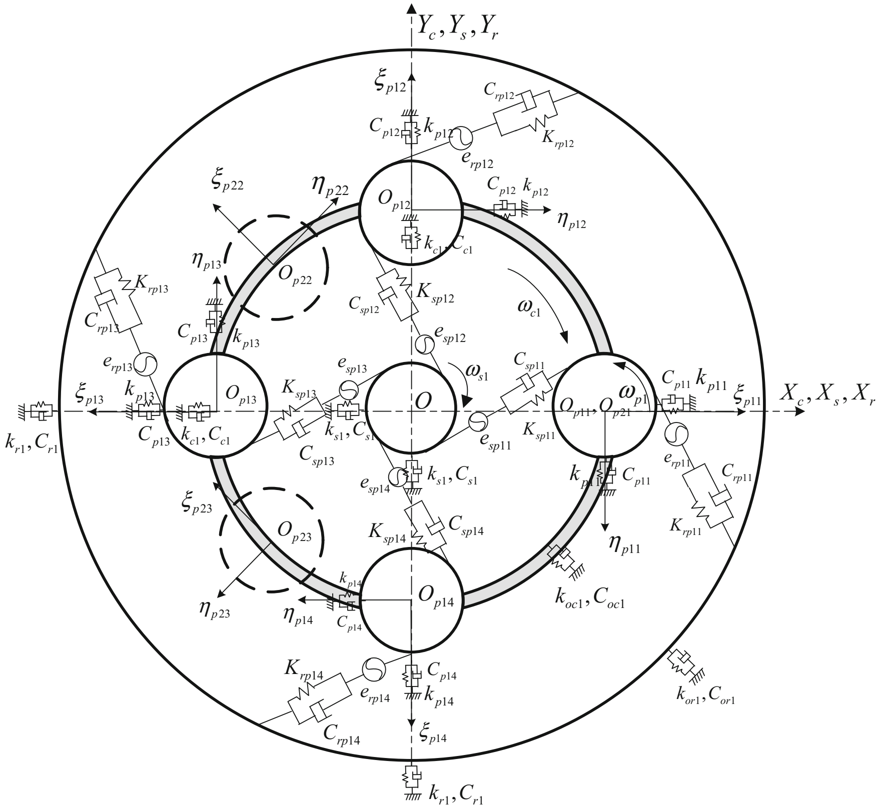

Fig. 2.3 Dynamics model of the planetary gear train

The vector is 60 degrees of freedom, in which x, y, z represents the deflection along the respective coordinate axes, u represents torsional deflection presented as $u = r_b\omega$, r_b represents base circle radius of gears or carriers, the subscripts of s, p, r, and c, respectively, represent sun gear, planet, ring gear, and carrier.

2.1.3 Mesh Stiffness Excitation

Considering the helical gear tooth meshing begins at one end and gradually extends to the entire tooth surface, time-varying mesh stiffness is proposed as the first-order harmonic instead of step waveforms to simulate helical gear mesh condition [5].

Supposing that the variation range of a meshing period is 2π and initial phase of Planet 1 is 0, the phase of Planet i should be $(Z_r, Z_s)\psi_i$. The inner and external time-varying mesh stiffness are presented in Eq. (2.2) [6].

$$\begin{aligned} k_{rp}(t) &= \bar{k}_{rp}[1 + S\sin(\omega_m t + Z_r\psi_i + \gamma_{sr})] \\ k_{sp}(t) &= \bar{k}_{sp}[1 + S\sin(\omega_m t + Z_s\psi_i)] \end{aligned} \tag{2.2}$$

$$\omega_{mi} = \frac{(\omega_{si} - \omega_{ci})Z_{si}\pi}{30} \tag{2.3}$$

In Eq. (2.2), $\bar{k}_{rp}, \bar{k}_{sp}$ are the average values of inner and external mesh stiffness. S is the amplitude ratio valuing 0.2. γ_{sr} is phase difference between inner mesh and external mesh in planetary transmission, which values 0 in case that planet teeth number is even and values π in case of odd. ω_{mi} is mesh frequency in the ith stage. The expression in case of fixed ring gear is Eq. (2.3). ω_{si} and ω_{ci} are rotational speeds of sun gear and carrier in the ith stage. Z_s and Z_r are the numbers of sun gear teeth and ring gear teeth. ψ_i is planetary phase represented as

$$\psi_i = 2\pi(i - 1)/N \tag{2.4}$$

where $N = 4$ for the 1st stage; $N = 3$ for the 2nd stage; $i = 1, \ldots N$.

2.1.4 Transmission Error Excitation

The component errors affecting load-sharing performance considered in this paper can be classified as tooth frequency error, shaft-frequency error, and constant error by frequencies which are shown in Table 2.1. θ_{ri} and θ_{si} are presented as Eq. (2.5). α_t is transverse pressure angle of the ring and sun.

$$\theta_{r,si} = \alpha_t \pm \psi_i \tag{2.5}$$

Equivalent accumulated errors are presented in Eqs. (2.6) and (2.7)

$$e_{spi} = e_{Es} + e_{As} + e_{sEpi} + e_{sApi} + e_{\mu sp} + e_{\varepsilon s} + e_{\varepsilon pi} \tag{2.6}$$

$$e_{rpi} = e_{Er} + e_{Ar} + e_{rEpi} + e_{rApi} + e_{\mu rp} + e_{\varepsilon r} + e_{\varepsilon pi} \tag{2.7}$$

where the errors are defined and listed in Table 2.1.

Table 2.1 Error definitions

Part name	Error name	Symbol	Equivalent error
Carrier	Eccentricity error	(E_c, β_c)	$e_{Ec} = -E_c\cos(y_i - b_c)$ (ξ_p-axis component) $e_{Ec} = -E_c\sin(b_c - y_i)$ (η_p-axis component)
	Planet shaft hole tangential error	(E_τ)	$e_{Et} = -E_t$
Sun	Manufacturing error	(E_s, β_s)	$e_{Es} = E_s \sin[\theta_{si} + \beta_s - \omega_s t]$
	Fixing error	(A_s, γ_s)	$e_{As} = A_s \sin(\theta_{si} + \gamma_s)$
	Tooth profile error of external mesh	(μ_{sp})	$e_{\mu sp} = \mu_{sp} \sin(\omega_m t + Z_s \psi_i)$
	Thickness deviation	(ε_s)	$e_{\varepsilon s} = -\varepsilon_s$
Planet	Manufacturing error	(E_{pi}, β_{pi})	$e_{sEpi} = -E_{pi} \sin[\beta_{pi} + \alpha_{sp} + \omega_p t]$ (external mesh) $e_{rEpi} = -E_{pi} \sin[\beta_{pi} - \alpha_{rp} + \omega_p t]$ (inner mesh)
	Fixing error	(A_{pi}, γ_{pi})	$e_{sApi} = -A_{pi} \sin(\gamma_{pi} + \alpha_{sp})$ (external mesh) $e_{rApi} = -A_{pi} \sin(\gamma_{pi} - \alpha_{rp})$ (inner mesh)
	Thickness deviation	(ε_{pi})	$e_{\varepsilon pi} = -\varepsilon_{pi}$
Ring	Manufacturing error	(E_r, β_r)	$e_{Er} = -E_r \sin(\theta_{ri} - \beta_r)$
	Fixing error	(A_r, γ_r)	$e_{Ar} = -A_r \sin(\theta_{ri} - \beta_r)$
	Tooth profile error of inner mesh	(ε_r)	$e_{\mu rp} = \mu_{rp} \sin(\omega_m t + Z_r \psi_i + \gamma_{sp})$
	Thickness deviation	(ε_r)	$e_{\varepsilon r} = -\varepsilon_r$

2.1.5 Mesh Damping in the Planetary Train

The damping coefficient of the gear tooth mesh is as follows [7]

$$c_{rp,sp} = 2\xi_g \sqrt{\frac{\bar{k}_{rp,sp} m_1 m_2}{m_1 + m_2}} \tag{2.8}$$

where ξ_g is damping ratio of tooth mesh, which is between 0.03 and 0.17. $\bar{k}_{rp,sp}$ is the average values of mesh stiffness. m_1 and m_2 represent the mass of driving and driven gears, respectively.

2.1.6 Governing Equations

Due to the use of helical gears in the transmission system, torsional deflection, radial deflection, and axial deflection of each gear should be taken into account in the model. Considering the influence of torsional deflection, radial deflection, and axial deflection of planet carrier, it totally has 60 degrees of freedom. The dynamics equations of the system are as follows.

Dynamic equations in the 1st stage are represented in Eqs. (2.9)–(2.12).

$$\begin{cases} (I_{c1}/r_{c1}^2)\ddot{u}_{c1} + C_{oc1}\dot{u}_{c1} + k_{oc1}u_{c1} + \sum\limits_{i=1}^{4}(k_{p1}\delta_{c\eta 1i} + C_{p1}\dot{\delta}_{c\eta 1i}) = T_{c1}/r_{c1} \\ m_{c1}(\ddot{x}_{c1} - 2\omega_{c1}\dot{y}_{c1} - \omega_{c1}^2 x_{c1}) + C_{c1}(\dot{x}_{c1} - \omega_{c1}y_{c1}) + k_{c1}x_{c1} \\ -k_{p1}\sum\limits_{i=1}^{4}(\delta_{c\xi 1i}\cos\psi_{1i} + \delta_{c\eta 1i}\sin\psi_{1i})] \\ -C_{p1}\sum\limits_{i=1}^{4}(\dot{\delta}_{c\xi 1i}\cos\psi_{1i} + \dot{\delta}_{c\eta 1i}\sin\psi_{1i}) = 0 \\ m_{c1}(\ddot{y}_{c1} + 2\omega_{c1}\dot{x}_{c1} - \omega_{c1}^2 y_{c1}) + C_{c1}(\dot{y}_{c1} + \omega_{c1}x_{c1}) + k_{c1}y_{c1} \\ -k_{p1}\sum\limits_{i=1}^{4}(\delta_{c\xi 1i}\sin\psi_{1i} + \delta_{c\eta 1i}\cos\psi_{1i}) \\ -C_{p1}\sum\limits_{i=1}^{4}(\dot{\delta}_{c\xi 1i}\sin\psi_{1i} + \dot{\delta}_{c\eta 1i}\cos\psi_{1i}) = 0 \\ m_{c1}\ddot{z}_{c1} + C_{c1}\dot{z}_{c1} + k_{c1}z_{c1} - k_{p1}\sum\limits_{i=1}^{4}\delta_{c\zeta 1i} - C_{p1}\sum\limits_{i=1}^{4}\dot{\delta}_{c\zeta 1i} = 0 \end{cases} \tag{2.9}$$

$$\begin{cases} (I_{p1}/r_{bp1}^2)\ddot{u}_{p1i} - [k_{rp1i}(t)f(\delta_{rp1i}, b_{r1}) + C_{rp1i}\dot{\delta}_{rp1i}]\cos\beta_{b1} \\ +[k_{sp1i}(t)f(\delta_{sp1i}, b_{s1}) + C_{sp1i}\dot{\delta}_{sp1i}]\cos\beta_{b1} = 0 \\ m_{p1}(\ddot{\xi}_{p1i} - 2\omega_{c1}\dot{\eta}_{p1i} - \omega_{c1}^2\xi_{p1i}) + C_{p1}(\dot{\delta}_{c\xi 1i} - \omega_{c1}\delta_{c\xi 1i}) + k_{p1}\delta_{c\xi 1i} \\ +[k_{rp1i}(t)f(\delta_{rp1i}, b_{r1}) + C_{rp1i}\dot{\delta}_{rp1i}]\sin\alpha_{t1}\cos\beta_{b1} - [k_{sp1i}(t)f(\delta_{sp1i}, b_{s1}) \\ +C_{sp1i}\dot{\delta}_{sp1i}]\sin\alpha_{t1}\cos\beta_{b1} = 0 \\ m_{p1}(\ddot{\eta}_{p1i} + 2\omega_{c1}\dot{\xi}_{p1i} - \omega_{c1}^2\eta_{p1i}) + C_{p1}(\dot{\delta}_{c\eta 1i} + \omega_{c1}\delta_{c\xi 1i}) + k_{p1}\delta_{c\eta 1i} \\ -[k_{rp1i}(t)f(\delta_{rp1i}, b_{r1}) + C_{rp1i}\dot{\delta}_{rp1i}]\cos\alpha_{t1}\cos\beta_{b1} - [k_{sp1i}(t)f(\delta_{sp1i}, b_{s1}) \\ +C_{sp1i}\dot{\delta}_{sp1i}]\cos\alpha_{t1}\cos\beta_{b1} = 0 \\ m_{p1}\ddot{\zeta}_{p1i} + C_{p1}\dot{\delta}_{c\zeta 1i} + k_{p1}\delta_{c\zeta 1i} + [k_{rp1i}(t)f(\delta_{rp1i}, b_{r1}) + C_{rp1i}\dot{\delta}_{rp1i}]\sin\beta_{b1} \\ -[k_{sp1i}(t)f(\delta_{sp1i}, b_{s1}) + C_{sp1i}\dot{\delta}_{sp1i}]\sin\beta_{b1} = 0 \end{cases} \tag{2.10}$$

$$\left\{\begin{array}{l}
(I_{r1}/r_{br1}^{2})\ddot{u}_{r1}+C_{or1}\dot{u}_{r1}+k_{or1}u_{r1}\\
\quad+\sum_{i=1}^{4}\left[k_{rp1i}(t)f(\delta_{rp1i},b_{r1})+C_{rp1i}\dot{\delta}_{rp1i}\right]\cos\beta_{b1}=0\\
m_{r1}(\ddot{x}_{r1}-2\omega_{c1}\dot{y}_{r1}-\omega_{c1}^{2}x_{r1})+C_{r1}(\dot{x}_{r1}-\omega_{c1}y_{r1})+k_{r1}x_{r1}\\
-\sum_{i=1}^{4}\left[k_{rp1i}(t)f(\delta_{rp1i},b_{r1})+C_{rp1i}\dot{\delta}_{rp1i}\right]\sin\theta_{r1i}\cos\beta_{b1}=0\\
m_{r1}(\ddot{y}_{r1}+2\omega_{c1}\dot{x}_{r1}-\omega_{c1}^{2}y_{r1})+C_{r1}(\dot{y}_{r1}+\omega_{c1}x_{r1})+k_{r1}y_{r1}\\
\quad+\sum_{i=1}^{4}\left[k_{rp1i}(t)f(\delta_{rp1i},b_{r1})+C_{rp1i}\dot{\delta}_{rp1i}\right]\cos\theta_{r1i}\cos\beta_{b1}=0\\
m_{r1}\ddot{z}_{r1}+C_{r1}\dot{z}_{r1}+k_{r1}z_{r1}\\
-\sum_{i=1}^{4}\left[k_{rp1i}(t)f(\delta_{rp1i},b_{r1})+C_{rp1i}\dot{\delta}_{rp1i}\right]\sin\beta_{b1}=0
\end{array}\right. \tag{2.11}$$

$$\left\{\begin{array}{l}
(I_{s1}/r_{bs1}^{2})\ddot{u}_{s1}+C_{os1}\dot{u}_{s1}+k_{osc}(u_{s1}-\frac{r_{bs1}}{r_{c2}}u_{c2})\\
-\sum_{i=1}^{4}\left[k_{sp1i}(t)f(\delta_{sp1i},b_{s1})+C_{sp1i}\dot{\delta}_{sp1i}\right]\cos\beta_{b1}=0\\
m_{s1}(\ddot{x}_{s1}-2\omega_{c1}\dot{y}_{s1}-\omega_{c1}^{2}x_{s1})+C_{s1}(\dot{x}_{s1}-\omega_{c1}y_{s1})+k_{s1}x_{s1}\\
\quad+\sum_{i=1}^{4}\left[k_{sp1i}(t)f(\delta_{sp1i},b_{s1})+C_{sp1i}\dot{\delta}_{sp1i}\right]\sin\theta_{s1i}\cos\beta_{b1}=0\\
m_{s1}(\ddot{y}_{s1}+2\omega_{c1}\dot{x}_{s1}-\omega_{c1}^{2}y_{s1})+C_{s1}(\dot{y}_{s1}+\omega_{c1}x_{s1})+k_{s1}y_{s1}\\
\quad+\sum_{i=1}^{4}\left[k_{sp1i}(t)f(\delta_{sp1i},b_{s1})+C_{sp1i}\dot{\delta}_{sp1i}\right]\cos\theta_{s1i}\cos\beta_{b1}=0\\
m_{s1}\ddot{z}_{s1}+C_{s1}\dot{z}_{s1}+k_{s1}z_{s1}+\sum_{i=1}^{4}\left(k_{sp1i}(t)f(\delta_{sp1i},b_{s1})+C_{sp1i}\dot{\delta}_{sp1i}\right)\sin\beta_{b1}=0
\end{array}\right. \tag{2.12}$$

Dynamic equations in the 2nd stage are represented in Eqs. (2.13)–(2.16).

$$\left\{\begin{array}{l}
(I_{c2}/r_{c2}^{2})\ddot{u}_{c2}+C_{oc2}\dot{u}_{c2}+k_{osc}(u_{c2}-\frac{r_{c2}}{r_{bs2}}u_{s1})+\sum_{i=1}^{3}(k_{p2}\delta_{c\eta 2i}+C_{p2}\dot{\delta}_{c\eta 2i})=0\\
m_{c2}(\ddot{x}_{c2}-2\omega_{c2}\dot{y}_{c2}-\omega_{c2}^{2}x_{c2})+C_{c2}(\dot{x}_{c2}-\omega_{c2}y_{c2})+k_{c2}x_{c2}\\
-k_{p2}\sum_{i=1}^{3}(\delta_{c\xi 2i}\cos\psi_{2i}+\delta_{c\eta 2i}\sin\psi_{2i})]\\
-C_{p2}\sum_{i=1}^{3}(\dot{\delta}_{c\xi 2i}\cos\psi_{2i}+\dot{\delta}_{c\eta 2i}\sin\psi_{2i})=0\\
m_{c2}(\ddot{y}_{c2}+2\omega_{c2}\dot{x}_{c2}-\omega_{c2}^{2}y_{c2})+C_{c2}(\dot{y}_{c2}+\omega_{c2}x_{c2})+k_{c2}y_{c2}\\
-k_{p2}\sum_{i=1}^{3}(\delta_{c\xi 2i}\sin\psi_{2i}+\delta_{c\eta 2i}\cos\psi_{2i})\\
-C_{p2}\sum_{i=1}^{3}(\dot{\delta}_{c\xi 2i}\sin\psi_{2i}+\dot{\delta}_{c\eta 2i}\cos\psi_{2i})=0\\
m_{c2}\ddot{z}_{c2}+C_{c2}\dot{z}_{c2}+k_{c2}z_{c2}-k_{p2}\sum_{i=1}^{3}\delta_{c\zeta 2i}-C_{p2}\sum_{i=1}^{3}\dot{\delta}_{c\zeta 2i}=0
\end{array}\right. \tag{2.13}$$

$$\begin{cases}
(I_{p2}/r_{bp2}^2)\ddot{u}_{p2i} - [k_{rp2i}(t)f(\delta_{rp2i}, b_{r2}) + C_{rp2i}\dot{\delta}_{rp2i}]\cos\beta_{b2} \\
+ [k_{sp2i}(t)f(\delta_{sp2i}, b_{s2}) + C_{sp2i}\dot{\delta}_{sp2i}]\cos\beta_{b2} = 0 \\
m_{p2}(\ddot{\xi}_{p2i} - 2\omega_{c2}\dot{\eta}_{p2i} - \omega_{c2}^2\xi_{p2i}) + C_{p2}(\dot{\delta}_{c\xi 2i} - \omega_{c2}\delta_{c\xi 2i}) + k_{p2}\delta_{c\xi 2i} \\
+ [k_{rp2i}(t)f(\delta_{rp2i}, b_{r2}) + C_{rp2i}\dot{\delta}_{rp2i}]\sin\alpha_{t2}\cos\beta_{b2} - [k_{sp2i}(t)f(\delta_{sp2i}, b_{s2}) \\
+ C_{sp2i}\dot{\delta}_{sp2i}]\sin\alpha_{t2}\cos\beta_{b2} = 0 \\
m_{p2}(\ddot{\eta}_{p2i} + 2\omega_{c2}\dot{\xi}_{p2i} - \omega_{c2}^2\eta_{p2i}) + C_{p2}(\dot{\delta}_{c\eta 2i} + \omega_{c2}\delta_{c\xi 2i}) + k_{p2}\delta_{c\eta 2i} \\
-[k_{rp2i}(t)f(\delta_{rp2i}, b_{r2}) + C_{rp2i}\dot{\delta}_{rp2i}]\cos\alpha_{t2}\cos\beta_{b2} - [k_{sp2i}(t)f(\delta_{sp2i}, b_{s2}) \\
+ C_{sp2i}\dot{\delta}_{sp2i}]\cos\alpha_{t2}\cos\beta_{b2} = 0 \\
m_{p2}\ddot{\zeta}_{p2i} + C_{p2}\dot{\delta}_{c\zeta 2i} + k_{p2}\delta_{c\zeta 2i} + [k_{rp2i}(t)f(\delta_{rp2i}, b_{r2}) + C_{rp2i}\dot{\delta}_{rp2i}]\sin\beta_{b2} \\
-[k_{sp2i}(t)f(\delta_{sp2i}, b_{s2}) + C_{sp2i}\dot{\delta}_{sp2i}]\sin\beta_{b2} = 0
\end{cases} \tag{2.14}$$

$$\begin{cases}
(I_{r2}/r_{br2}^2)\ddot{u}_{r2} + C_{or2}\dot{u}_{r2} + k_{or2}u_{r2} \\
+ \sum\limits_{i=1}^{3}[k_{rp2i}(t)f(\delta_{rp2i}, b_{r2}) + C_{rp2i}\dot{\delta}_{rp2i}]\cos\beta_{b2} = 0 \\
m_{r2}(\ddot{x}_{r2} - 2\omega_{c2}\dot{y}_{r2} - \omega_{c2}^2 x_{r2}) + C_{r2}(\dot{x}_{r2} - \omega_{c2}y_{r2}) + k_{r2}x_{r2} \\
- \sum\limits_{i=1}^{3}[k_{rp2i}(t)f(\delta_{rp2i}, b_{r2}) + C_{rp2i}\dot{\delta}_{rp2i}]\sin\theta_{r2i}\cos\beta_{b2} = 0 \\
m_{r2}(\ddot{y}_{r2} + 2\omega_{c2}\dot{x}_{r2} - \omega_{c2}^2 y_{r2}) + C_{r2}(\dot{y}_{r2} + \omega_{c2}x_{r2}) + k_{r2}y_{r2} \\
+ \sum\limits_{i=1}^{3}[k_{rp2i}(t)f(\delta_{rp2i}, b_{r2}) + C_{rp2i}\dot{\delta}_{rp2i}]\cos\theta_{r2i}\cos\beta_{b2} = 0 \\
m_{r2}\ddot{z}_{r2} + C_{r2}\dot{z}_{r2} + k_{r2}z_{r2} \\
- \sum\limits_{i=1}^{3}[k_{rp2i}(t)f(\delta_{rp2i}, b_{r2}) + C_{rp2i}\dot{\delta}_{rp2i}]\sin\beta_{b2} = 0
\end{cases} \tag{2.15}$$

$$\begin{cases}
(I_{s2}/r_{bs2}^2)\ddot{u}_{s2} - \sum\limits_{i=1}^{3}[k_{sp2i}(t)f(\delta_{sp2i}, b_{s2}) + C_{sp2i}\dot{\delta}_{sp2i}]\cos\beta_{b2} \\
+ C_{7s_2}\left(\dot{\theta}_{s2} - \frac{r_{s2}}{r_7}\dot{\theta}_7\right) + K_{7s_2}\left(\theta_{s2} - \frac{r_{s2}}{r_7}\theta_7\right) = 0 \\
m_{s2}(\ddot{x}_{s2} - 2\omega_{c2}\dot{y}_{s2} - \omega_{c2}^2 x_{s2}) + C_{s2}(\dot{x}_{s2} - \omega_{c2}y_{s2}) + k_{s2}x_{s2} \\
+ \sum\limits_{i=1}^{3}[k_{sp2i}(t)f(\delta_{sp2i}, b_{s2}) + C_{sp2i}\dot{\delta}_{sp2i}]\sin\theta_{s2i}\cos\beta_{b2} = 0 \\
m_{s2}(\ddot{y}_{s2} + 2\omega_{c2}\dot{x}_{s2} - \omega_{c2}^2 y_{s2}) + C_{s2}(\dot{y}_{s2} + \omega_{c2}x_{s2}) + k_{s2}y_{s2} \\
+ \sum\limits_{i=1}^{3}[k_{sp2i}(t)f(\delta_{sp2i}, b_{s2}) + C_{sp2i}\dot{\delta}_{sp2i}]\cos\theta_{s2i}\cos\beta_{b2} = 0 \\
m_{s2}\ddot{z}_{s2} + C_{s2}\dot{z}_{s2} + k_{s2}z_{s2} + \sum\limits_{i=1}^{3}(k_{sp2i}(t)f(\delta_{sp2i}, b_{s2}) + C_{sp2i}\dot{\delta}_{sp2i})\sin\beta_{b2} = 0
\end{cases} \tag{2.16}$$

Dynamics equations of the high-speed stage are shown as follows.

$$\left\{\begin{array}{l}(I_7/r_7^2)\ddot{\theta}_7+(C_{78}\dot{x}_{78}+k_{78}x_{78})r_{b7}\cos\beta_{b3}+C_{7s_2}\left(\dot{\theta}_7-\frac{r_7}{r_{s2}}\dot{\theta}_{s2}\right)+k_{7s_2}\left(\theta_7-\frac{r_7}{r_{s2}}\theta_{s2}\right)=0\\ m_7\ddot{x}_7+(C_{78}\dot{x}_{78}+k_{78}x_{78})\cos\beta_{b3}\sin\alpha_{t78}+C_{7x}\dot{x}_7+k_{7x}x_7=0\\ m_7\ddot{y}_7+(C_{78}\dot{x}_{78}+k_{78}x_{78})\cos\beta_{b3}\cos\alpha_{t78}+C_{7y}\dot{y}_7+k_{7y}y_7=0\\ m_7\ddot{z}_7+(C_{78}\dot{x}_{78}+k_{78}x_{78})\sin\beta_{b3}+C_{7x}\dot{z}_7+k_{7z}z_7=0\end{array}\right. \tag{2.17}$$

$$\left\{\begin{array}{l}(I_8/r_8^2)\ddot{\theta}_8-(C_{78}\dot{x}_{78}+k_{78}x_{78})r_{b8}\cos\beta_{b78}=-T_{out}/r_8\\ m_8\ddot{x}_8-(C_{78}\dot{x}_{78}+k_{78}x_{78})\cos\beta_{b78}\sin\alpha_{t78}+c_{8x}\dot{x}_8+k_{8x}x_8=0\\ m_8\ddot{y}_8-(C_{78}\dot{x}_{78}+k_{78}x_{78})\cos\beta_{b78}\cos\alpha_{t78}+c_{8y}\dot{y}_8+k_{8y}y_8=0\\ m_8\ddot{z}_8-(C_{78}\dot{x}_{78}+k_{78}x_{78})\sin\beta_{b78}+c_{8z}\dot{z}_8+k_{8z}z_8=0\end{array}\right. \tag{2.18}$$

In Eqs. (2.9)–(2.18), $\delta_{c\xi ij}, \delta_{c\eta ij}, \delta_{c\zeta ij}$ are relative displacements between carrier and planet gear along ξ, η, ζ axis, respectively, in rotational coordinate system which is presented in Eq. (2.19).

$$\left\{\begin{array}{l}\delta_{c\xi ij}=\xi_{pij}-x_{ci}\cos\psi_{ij}-y_{ci}\sin\psi_{ij}\\ \delta_{c\eta ij}=\eta_{pij}+x_{ci}\sin\psi_{ij}-y_{ci}\cos\psi_{ij}+u_{ci}\\ \delta_{c\zeta ij}=\zeta_{pij}-z_{ci}\end{array}\right. \tag{2.19}$$

where δ_{rpij} is relative displacement along the meshing line between ring gear and planet which is presented in Eq. (2.20).

$$\delta_{rpij}=(u_{ri}-u_{pij}-x_{ri}\sin\theta_{rij}+y_{ri}\cos\theta_{rij}+\xi_{pij}\sin\alpha_{ti}-\eta_{pij}\cos\alpha_{ti})\cos\beta_{bi}+(\zeta_{pij}-z_{ri})\sin\beta_{bi}+e_{rpij}(t) \tag{2.20}$$

where δ_{spij} is relative displacement along the meshing line between sun gear and planet which is presented in Eq. (2.21).

$$\delta_{spij}=(-u_{si}+u_{pij}+x_{si}\sin\theta_{sij}+y_{si}\cos\theta_{sij}-\xi_{pij}\sin\alpha_{ti}-\eta_{pij}\cos\alpha_{ti})\cos\beta_{bi}+(z_{si}-\zeta_{pij})\sin\beta_{bi}+e_{spij}(t) \tag{2.21}$$

The subscript i is the stage number and j is the planet number. Their relationship is presented in Eq. (2.22)

$$i=\left\{\begin{array}{ll}1, & j=1,\ldots 4\\ 2, & j=1,\ldots 3\end{array}\right. \tag{2.22}$$

The total relative displacement along the meshing line of high-speed stage is

$$x_{78}=[(r_{b7}\theta_7-r_{b8}\theta_8)+(y_7-y_8)\cos\alpha_{t78}+(x_7-x_8)\sin\alpha_{t78}]\cos\beta_{b78}-e_{78} \tag{2.23}$$

where r_{b7}, r_{b8}, α_{t78}, β_{b78}, and e_{78}, respectively, represent the base circle radius of wheel, the base circle radius of pinion, the working transverse pressure angle, the base helix angle, and the dynamic transmission error of high-speed stage.

The other terms are described as follows.

I_{c1}, I_{r1}, I_{p1}, I_{s1} are rotational inertia of carrier, ring gear, planets, and sun gear in the 1st stage.
I_{c2}, I_{r2}, I_{p2}, I_{s2} are rotational inertia of carrier, ring gear, planets, and sun gear in the 2nd stage.
m_{c1}, m_{r1}, m_{p1}, m_{s1} are mass of carrier, ring gear, planets, and sun gear in the 1st stage.
m_{c2}, m_{r2}, m_{p2}, m_{s2} are mass of carrier, ring gear, planets, and sun gear in the 2nd stage.
k_{oc1}, k_{or1} are torsional stiffness of carrier and ring gear in the 1st stage.
k_{oc2}, k_{or2} are torsional stiffness of carrier and ring gear in the 2nd stage.
k_{osc} is coupled torsional stiffness of the shaft connecting two stages in series.
k_{c1}, k_{r1}, k_{p1}, k_{s1} are supporting stiffness of carrier, ring gear, planets, and sun gear in the 1st stage.
k_{c2}, k_{r2}, k_{p2}, k_{s2} are supporting stiffness of carrier, ring gear, planets, and sun gear in the 2nd stage.
k_{rp1i} is mesh stiffness between ring gear and the ith planet gear in the 1st stage.
k_{sp1i} is mesh stiffness between sun gear and the ith planet gear in the 1st stage.
k_{rp2i} is mesh stiffness between ring gear and the ith planet gear in the 2nd stage.
k_{sp2i} is mesh stiffness between sun gear and the ith planet gear in the 2nd stage.
C_{rp1i} is mesh damping between ring gear and the ith planet gear in the 1st stage.
C_{sp1i} is mesh damping between sun gear and the ith planet gear in the 1st stage.
C_{rp2i} is mesh damping between ring gear and the ith planet gear in the 2nd stage.
C_{sp2i} is mesh damping between sun gear and the ith planet gear in the 2nd stage.
C_{c1}, C_{r1}, C_{p1}, C_{s1} are supporting damping of carrier, ring gear, planets, and sun gear in the 1st stage.
C_{c2}, C_{r2}, C_{p2}, C_{s2} are supporting damping of carrier, ring gear, planets, and sun gear in the 2nd stage.
β_{b1}, β_{b2} are base helix angles of two stages.
α_{t1}, α_{t2} are the working transverse pressure angle of two stages.
θ_{s1i}, θ_{r1i} are, respectively, the external and inner mesh phase angles in the 1st stage.
θ_{s2i}, θ_{r2i} are, respectively, the external and inner mesh phase angles in the 2nd stage.
k_{7s2} is the torsional stiffness between the 2nd-stage sun gear and high-speed stage wheel.
C_{7s2} is the torsional damping between the 2nd-stage sun gear and high-speed stage wheel.
k_{7x}, k_{7y}, k_{7z} are the supporting stiffness of wheel in x, y, z directions, respectively.
k_{8x}, k_{8y}, k_{8z} are the supporting stiffness of pinion in x, y, z directions, respectively.
C_{7x}, C_{7y}, C_{7z} are the supporting damping of wheel in x, y, z directions, respectively.
C_{8x}, C_{8y}, C_{8z} are the supporting damping of pinion in x, y, z directions, respectively.

Assembling the equations in matrix form, the global equation of motion of the planetary gearing system is written as

$$\boldsymbol{M}\ddot{\boldsymbol{x}} + \boldsymbol{C}\underline{\boldsymbol{x}} + \boldsymbol{K}\boldsymbol{x} = \boldsymbol{F} \tag{2.24}$$

where $\boldsymbol{M}$, $\boldsymbol{C}$, $\boldsymbol{K}$, and $\boldsymbol{F}$, respectively, represent mass matrix, damping matrix, stiffness matrix, and exciting force vector. $x, \dot{x}, \ddot{x}$ are the vectors of vibration displacement.

2.2 Torsional Dynamics of the Gearbox

The parameters of the above planetary system in this book are listed in Table 2.2.

According to Eqs. (2.9)–(2.18), the obtained nature frequencies and mode shapes of the system are shown in Table 2.3.

The modal energy distribution in each node of the system is obtained as shown in Table 2.4. Nodes 1–7 denote the planet carrier, 4 planet gears, annular gear, and sun gear in the first stage separately. Nodes 8–13 denote the planet carrier, 3 planet gears, annular gear, and sun gear in the second stage separately. Nodes 14 and 15 are output parallel gears.

2.3 Load Factors of Gear-Rotor System in Gearbox

2.3.1 Analysis of System Excitation and Damping

The equation of the two-parameter Weibull distribution is used to describe the wind speed [8, 9]:

$$f_v(v) = \left(\frac{k}{c}\right)\left(\frac{v}{c}\right)^{k-1} e^{-\left(\frac{v}{c}\right)^k}, \quad 0 < v < \infty \tag{2.25}$$

Table 2.2 The parameters of the planetary gear system

	z	m_n(mm)	β (°)	α (°)	B (mm)	m (kg)
Sun gear	29 (1st) 28 (2nd)	18 (1st) 12 (2nd)	20 (1st) 20 (2nd)	7.17 (1st) 8.67 (2nd)	470(1st) 260(2nd)	713 (1st) 139 (2nd)
Ring gear	99 (1st) 122 (2nd)					555 (1st) 265 (2nd)
Planet gear	35 (1st) 47 (2nd)					4419 (1st) 1537 (2nd)

Table 2.3 Nature frequencies and mode shapes of the planetary system

Order	Frequency (Hz)	Mode shape descriptions
1	27.8	Vibration of the output parallel gear
2	67.3	Vibration of the planet gear in the 1st stage
3	114.1	Vibration of the planet gear in the 2nd stage
4	134.2	Vibration of the annular gear in the 1st stage
5	144.7	Vibrations of the sun gear in the 2nd stage and the gear in the high-speed stage
6	189.0	Vibration of the planet carrier in the 1st stage
7	194.0	Vibration of the sun gear in the 1st stage and the planet carrier in the 2nd stage
8	194.3	Vibration of the annular gear in the 2nd sage
9	235.2	Vibration of the planet carrier in the 1st and 2nd stages
10	253.9	Vibration of the planet carrier in the 2nd stage
11	309.1	Vibration of the planet carrier in the 1st stage
12	332.4	Vibration of the planet carrier in the 1st stage

where v, k, and c represent the wind speed, the shape parameter, and the scale parameter separately, and the unit is m/s.

The mathematic expectation and variance of the wind speed can be determined based on Eq. (2.25). The expectation of the wind speed can be expressed as

$$E(v) = \bar{v} = \int_0^{+\infty} v \cdot f_v(v)\mathrm{d}v = c \cdot \Gamma\left(1 + \frac{1}{k}\right) \tag{2.26}$$

The expression of the variance of wind speed is

$$D(v) = \int_0^{+\infty} [v - E(v)]^2 f_v(v)\mathrm{d}v = c^2 \cdot \left\{\Gamma\left(1 + \frac{2}{k}\right) - \left[\Gamma\left(1 + \frac{1}{k}\right)\right]^2\right\} \tag{2.27}$$

where $\Gamma(x)$ is gamma function in Eqs. (2.26) and (2.27).

The parameters of wind turbine and wind speed are listed in Table 2.5.

According to Eqs. (2.26) and (2.27), the two parameters are determined, k is 5.5 and c is 11.9089. The time-domain model of the random wind based on the two-parameter Weibull distribution function is shown in Fig. 2.4 in 100 s.

Kinetic energy generated by the blade which is driven by natural wind per unit time is numerically equal to the output power of the blade, namely the input power of wind turbine gearbox. The relation between the input torque and the input

Table 2.4 The modal energy distributions of the planetary system of the first 12 orders

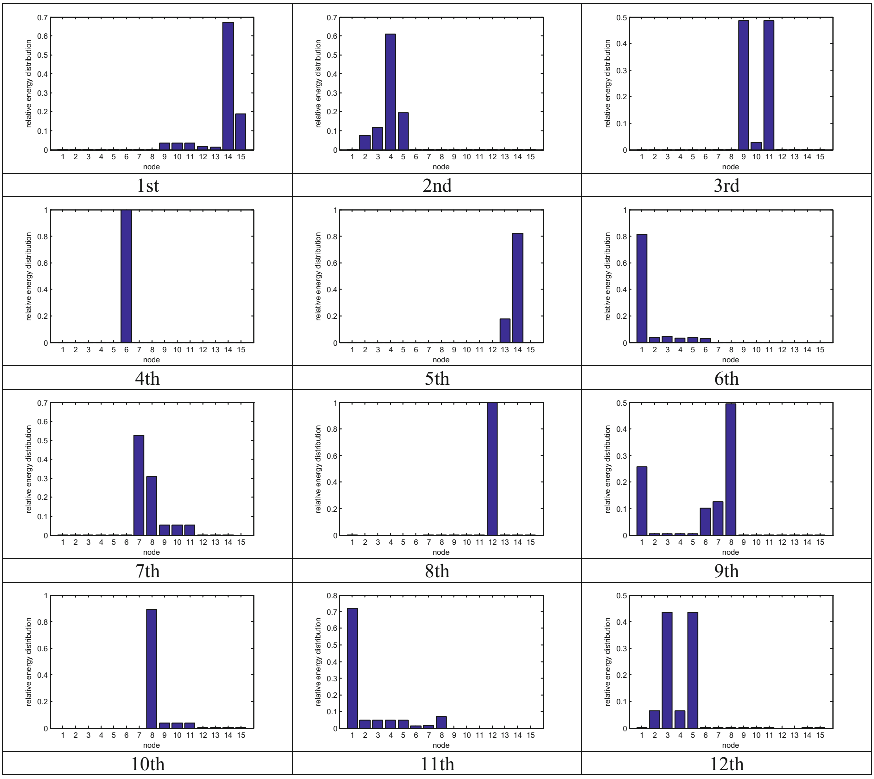

1st 2nd 3rd

4th 5th 6th

7th 8th 9th

10th 11th 12th

Table 2.5 Parameter values of the wind speeds

Parameters	Value
Rated design power P (kW)	3300
Rated working speed n_e (r/min)	13
Rated torque T_e (kNm)	2424.052
Rated wind speed V_e (m/s)	13.5
Radius of blade R (m)	52
Density of wind ρ (kg/m^3)	1.225
Average wind speed v_m (m/s)	11
Standard deviation σ_m (m/s)	2.27
Cut in speed $V_{\text{cut in}}$ (m/s)	3.5
Cut off speed $V_{\text{cut off}}$ (m/s)	25
Blade top speed ratio λ	9
Power coefficient C_p (λ)	0.485

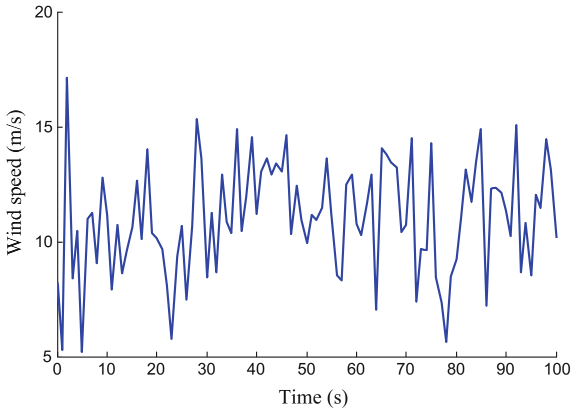

Fig. 2.4 Simulation of the random wind speeds

working speed of variable pitch can be obtained by the wind energy and blade top speed ratio. They are

$$T_{in} = \begin{cases} 0 & v < V_{\text{cut in}} \\ \frac{T_e}{V_e^2} \cdot v^2 & V_{\text{cut in}} \leq v \leq V_e \\ T_e & V_e \leq v \leq V_{\text{cut off}} \\ 0 & v > V_{\text{cut off}} \end{cases} \tag{2.28}$$

$$n_{in} = \begin{cases} 0 & v < V_{\text{cut in}} \\ \frac{n_e}{V_e} \cdot v & V_{\text{cut in}} \leq v \leq V_e \\ n_e & V_e \leq v \leq V_{\text{cut off}} \\ 0 & v > V_{\text{cut off}} \end{cases} \tag{2.29}$$

According to Eqs. (2.28) and (2.29), the simulated input working speeds are shown in Fig. 2.5.

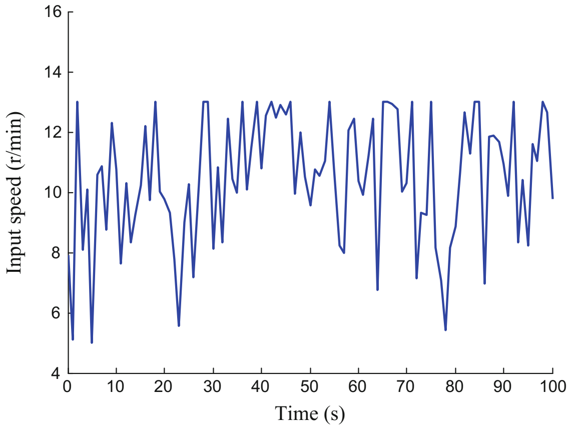

Fig. 2.5 Simulation of the input working speeds

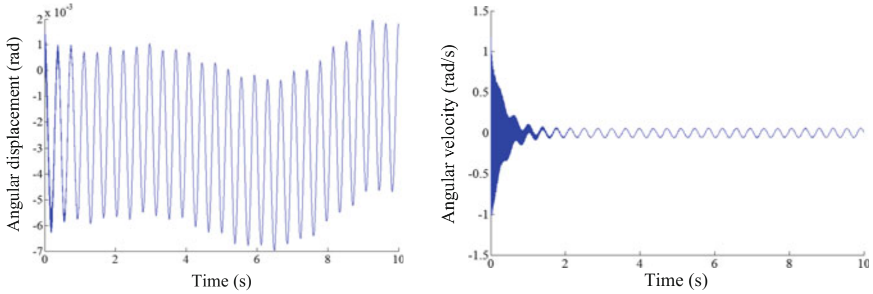

(a) Torsional displacement of planetary gear

(b) Torsional velocity of planetary gear

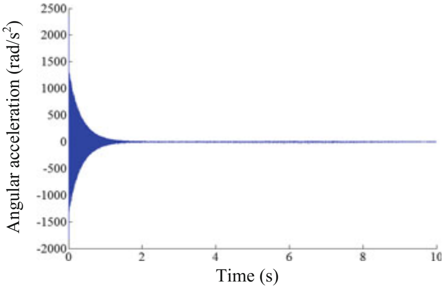

(c) Torsional acceleration of planetary gear

Fig. 2.6 Time-domain results of the planetary gear in the first-stage components. **a** Torsional displacement of planetary gear. **b** Torsional velocity of planetary gear. **c** Torsional acceleration of planetary gear

For the time-varying input load, the torsional displacement, velocity and acceleration of the sun gear and the planetary gear in the first-stage components are shown in Figs. 2.6 and 2.7, respectively. And the frequency spectrum results of torsional velocity and acceleration of planetary gear are shown in Figs. 2.8 and 2.9, respectively.

As shown in Figs. 2.6 and 2.7, the vibration displacement, velocity, and acceleration of the sun gear and planetary gear in the first-stage components along the torsional direction have same changing trends with the external load excitation. It mainly affects low-frequency vibration by the external load excitation while it affects the high-frequency vibration by the internal load excitation. If the input load is not stable, it will lead to relatively complex changing of the transverse vibration, and it has a very little influence on the vibration amplitude affected by the variable external load (Figs. 2.8 and 2.9).

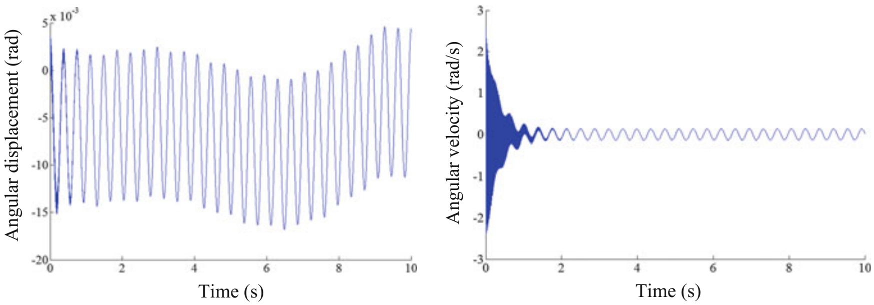

(a) Torsional displacement of sun gear

(b) Torsional velocity of sun gear

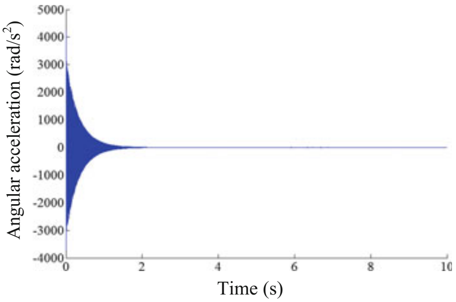

(c) Torsional acceleration of sun gear

Fig. 2.7 Time-domain results of the sun gear in the first-stage components. **a** Torsional displacement of sun gear. **b** Torsional velocity of sun gear. **c** Torsional acceleration of sun gear

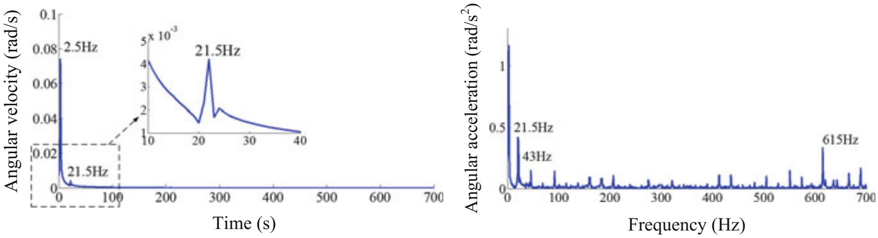

(a) Torsional velocity of planetary gear

(b) Acceleration of planetary gear

Fig. 2.8 Frequency spectrum results of torsional velocity and acceleration of planetary gear. **a** Torsional velocity of planetary gear. **b** Acceleration of planetary gear

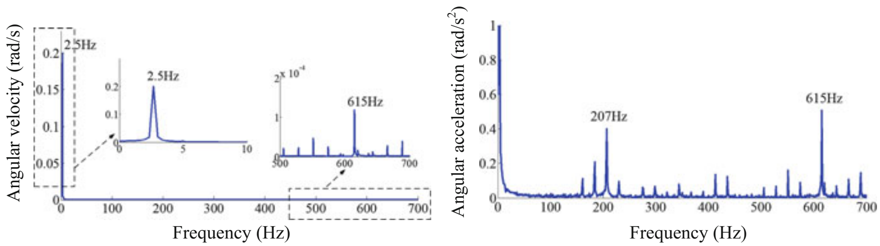

(a) Torsional velocity of sun gear (b) Acceleration of sun gear

Fig. 2.9 Frequency spectrum results of torsional velocity and acceleration of sun gear. **a** Torsional velocity of sun gear. **b** Acceleration of sun gear

2.3.2 Load Factors of Gear-Rotor System

The dynamics Eq. (2.24) can be expressed as

$$\boldsymbol{M}\ddot{\boldsymbol{x}} + C\dot{x} + [\boldsymbol{K_m} + \boldsymbol{\Delta K}(\mathrm{t})] \times [\boldsymbol{x} + \boldsymbol{x_s} - \boldsymbol{e}(\mathrm{t})] = \boldsymbol{F_s} + \boldsymbol{\Delta F}(\mathrm{t}) \tag{2.30}$$

where x_s, x, F_s, K_m, $\Delta K(t)$, and $\Delta F(t)$ represent the static relative displacement vector, the dynamic relative displacement vector, the static load, the average stiffness, the variable stiffness, and the variable part of external excitation separately.

Ignoring the smaller values, the expanded expression of Eq. (2.30) is rewritten as

$$\boldsymbol{M}\ddot{\boldsymbol{x}} + C\dot{x} + K_m\boldsymbol{x} = \boldsymbol{\Delta K}(\mathrm{t})\boldsymbol{e}(\mathrm{t}) + \boldsymbol{\Delta F}(\mathrm{t}) \tag{2.31}$$

where $\Delta K(\mathrm{t})e(\mathrm{t})$ is the additional dynamic load caused by internal excitation and $\Delta F(t)$ is the additional dynamic load caused by external excitation. The ratio of the sum of the additional internal (external) dynamic load is the tangential load application factor (dynamic load factor).

(a) The application factor

K_A is defined as the application factor of the external factors of the gear meshing to the additional dynamic load. For the wind turbine transmission system, the additional external dynamic load is mainly caused by the variation of the wind load. The common method to obtain the factor relies on the look-up table method; dynamic analysis results are used to obtain more accurate result here. K_A is expressed as

$$\boldsymbol{K_A} = (\boldsymbol{F_\tau} + \boldsymbol{F_{ex}})/\boldsymbol{F_\tau} \tag{2.32}$$

where F_τ and $F_{ex}(F_{ex} = k_m x_i)$ represent the tangential load of the gear set and the additional external dynamic load, respectively.

(b) The dynamic load factor

K_V is defined as the dynamic factor considering the influence of the manufacture accuracy and the working speed to the additional dynamic load. It is the important measurement of the dynamic characteristics of the system, which shows the condition of maximum load in the moving process. In traditional design, dynamic load factor is determined by existing chart according to accuracy of gear and working speed. The expression of dynamic load factor which is obtained from comprehensive dynamic analysis is

$$\boldsymbol{K_V} = (\boldsymbol{F_\tau} + \boldsymbol{F_{in}})/\boldsymbol{F_\tau} \tag{2.33}$$

In Eq. (2.33), F_{in} is additional internal dynamic load.

According to ISO 81400-4-2005: Wind turbines-Part 4 Design and Specification of Gearboxes, the life expectancy is 20 years under the circumstance of meeting design reliability requirement of 0.99. The application factor and the dynamic load factor are shown in Figs. 2.10, 2.11, 2.12, 2.13, 2.14, 2.15, 2.16, 2.17, 2.18, and 2.19 under the circumstance when system reliability requirement is 0.99.

The variation ranges of K_A and K_V of each gear pair, as shown in Figs. 2.18 and 2.19, have no obvious difference between the 1st and 2nd stages. K_A of the 1st-stage sun–planet and ring–planet gear pair is 1.10. K_A of the 2nd-stage sun–planet gear pair is 1.10. K_A of the 2nd-stage ring–planet gear pair is 1.12. K_A of the high-speed stage is 1.27, which is significantly increased. K_V of the 1st-stage sun–planet and

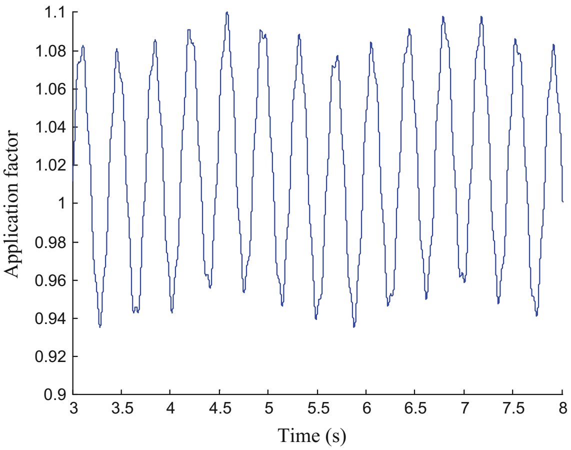

Fig. 2.10 K_A of the 1st-stage sun–planet gear pair

Fig. 2.11 K_V of the 1st-stage sun–planet gear pair

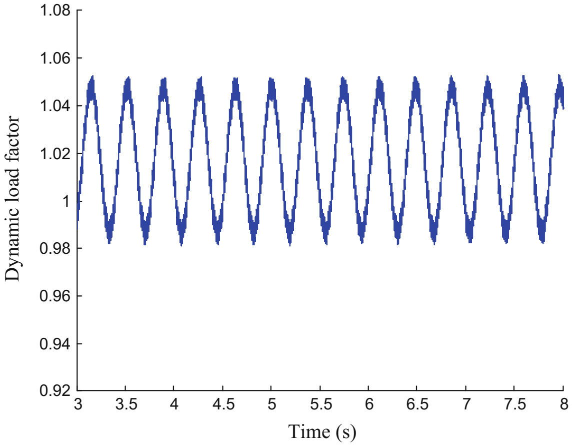

Fig. 2.12 K_A of the 1st-stage ring–planet gear pair

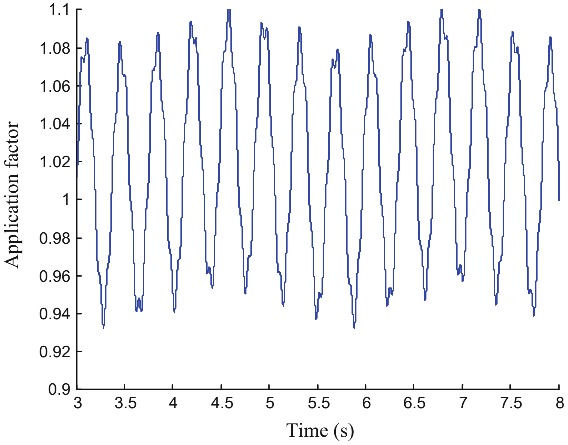

Fig. 2.13 K_V of the 1st-stage ring–planet gear pair

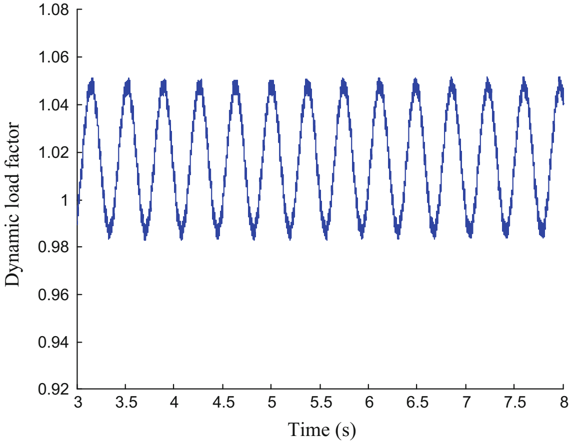

Fig. 2.14 K_A of the 2nd-stage sun–planet gear pair

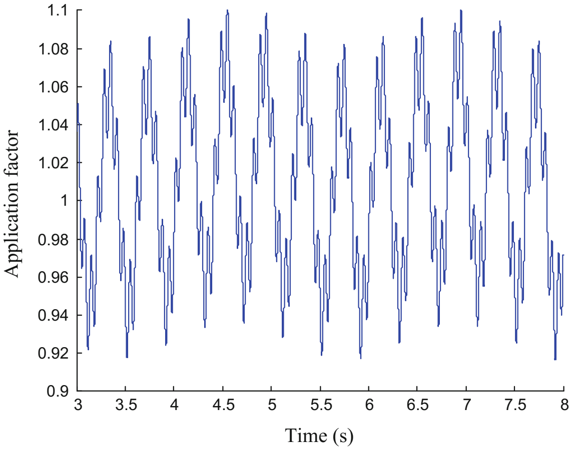

Fig. 2.15 K_V of the 2nd-stage sun–planet gear pair

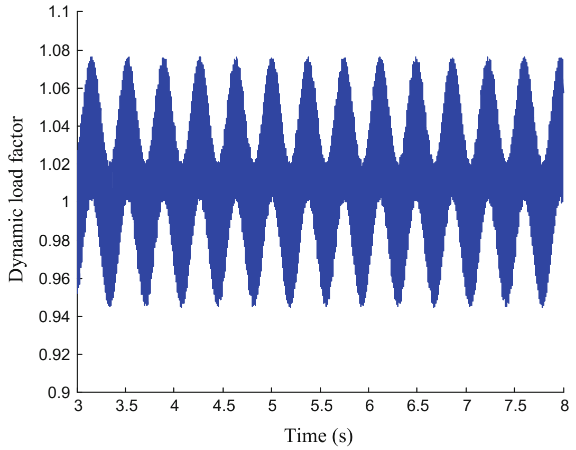

Fig. 2.16 K_A of the 2nd-stage ring–planet gear pair

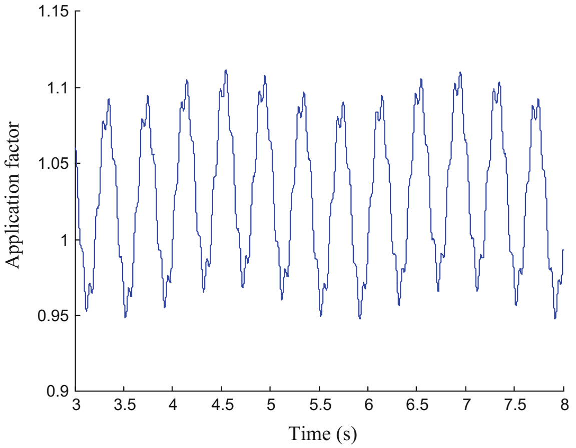

Fig. 2.17 K_V of the 2nd-stage ring–planet gear pair

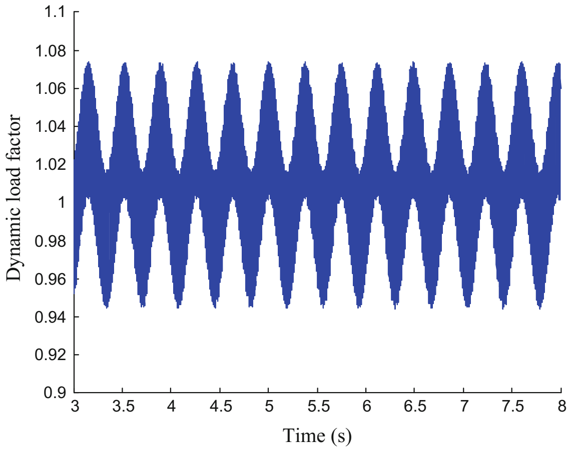

Fig. 2.18 K_A of high-speed stage

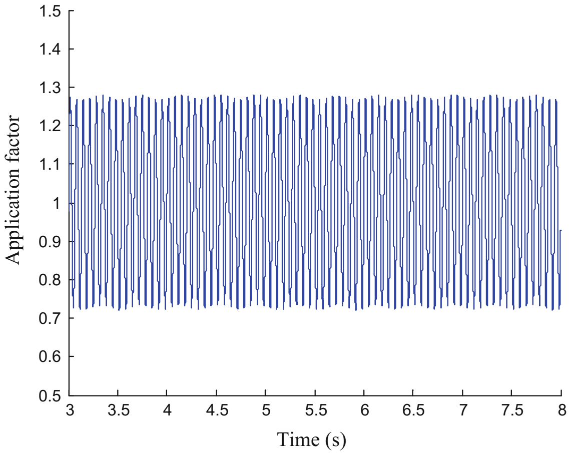

Fig. 2.19 K_V of high-speed stage

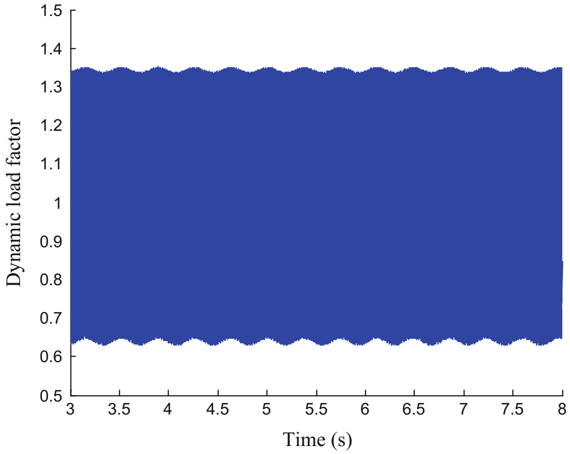

ring–planet gear pair is 1.05. K_V of the 2nd-stage sun–planet and ring–planet gear pair is 1.08 and 1.07, respectively. K_V of high-speed stage is 1.36, which is significantly increased similarly.

The computation program of K_A is attached in the Appendix A. The computation program of dynamic load factor K_V is similar to that of K_A, and it is ignored here.

2.4 Load-Sharing Coefficients Based on Torsional Dynamics

Load balance of a planetary gear train mainly refers to the engaging forces between each planet gear in planetary gear train. The basic floating components, such as the sun gear, the annular gear, or the planet carrier, are frequently used to realize better load balance among the planet gears. The floating component can move in the radial direction without radial support, which can make sure each planet gear shares the load equably under the unbalanced force. Load balance structure can decrease the load-sharing coefficient of the planetary gear transmission, reduce the noise, and improve the stability and the reliability of the system.

The supporting stiffness, mesh stiffness, and torsional stiffness of each gear in the system are calculated according to ANSI/AGMA ISO 1328-1 standard. The values are shown in Table 2.6.

The inner mesh force F_{rpij} and the external mesh force F_{spij} can be calculated by classical Runge–Kutta method according to Eqs. (2.9)–(2.18). Subsequently, planet load-sharing coefficient (PLSC) is defined as

$$b_{rpij} = NF_{rpij} / \sum_{j=1}^{N} \left(F_{rpij}\right), b_{spij} = NF_{spij} / \sum_{j=1}^{N} \left(F_{spij}\right) \tag{2.34}$$

The maximum of each PLSC in the same stage is defined as the system load-sharing coefficient (SLSC) as

$$B_{ri} = \frac{N \times \max(F_{rij})}{\sum_{j=1}^{N} F_{rij}}, B_{si} = \frac{N \times \max(F_{sij})}{\sum_{j=1}^{N} F_{sij}} \tag{2.35}$$

where b_{rpij} is the inner meshing PLSC of the jth planet in the ith stage, b_{spij} is the external meshing PLSC of the jth planet in the ith stage, B_{ri} is the inner meshing

Table 2.6 Stiffness values in the torsional model ($\times 10^9$N/m)

Stage	k_s	k_r	k_p	k_{oc}	k_{or}	$\bar{k}_{sp}$	$\bar{k}_{rp}$
1st	1.02	1.88	18.6	0.8	438.7	9.30	8.93
2nd	0.60	1.08	10.30	1.5	514.2	5.51	5.12

SLSC in the *i*th stage, B_{si} is the external meshing SLSC in the *i*th stage. N is the number of the planets in each stage.

2.4.1 Calculation of Load-Sharing Coefficients

The numerical solution for dynamical equations is obtained by the fourth-order Runge–Kutta method. Subsequently, the PLSC curve of each planet with rotation angle of the carrier in the 1th (θ_{c1}) is obtained according to Eq. (2.23) shown in Figs. 2.20 and 2.21. The SLSC curve of each stage is obtained according to Eq. (2.24) shown in Fig. 2.22. Finally, the maximum of SLSC for each planet gear is obtained, max (S_{r1}) = 1.066, max (S_{s1}) = 1.062, max (S_{r2}) = 1.130, max (S_{s2}) = 1.107, and is defined as the load-sharing coefficient.

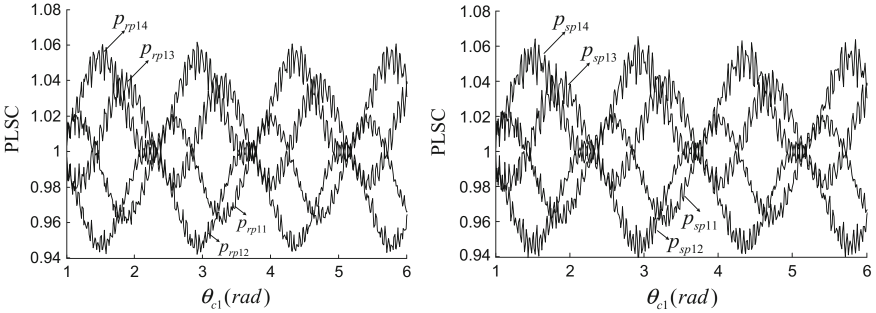

(a) PLSC of internal meshing (b) PLSC of external meshing

Fig. 2.20 PLSC in the 1st-stage planetary transmission. **a** PLSC of internal meshing. **b** PLSC of external meshing

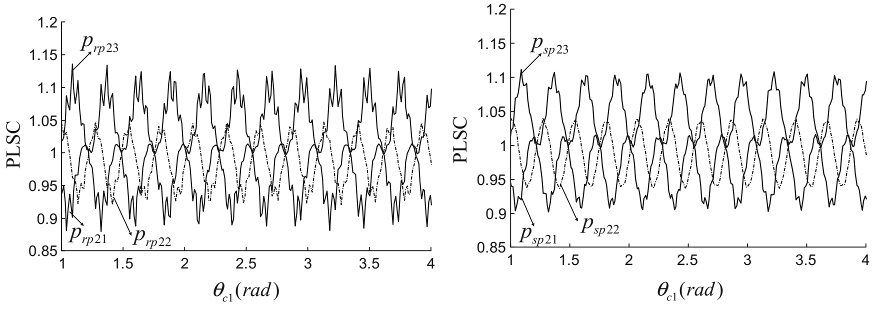

(a) PLSC of internal meshing (b) PLSC of external meshing

Fig. 2.21 PLSC in the 2nd-stage planetary transmission. **a** PLSC of internal meshing. **b** PLSC of external meshing

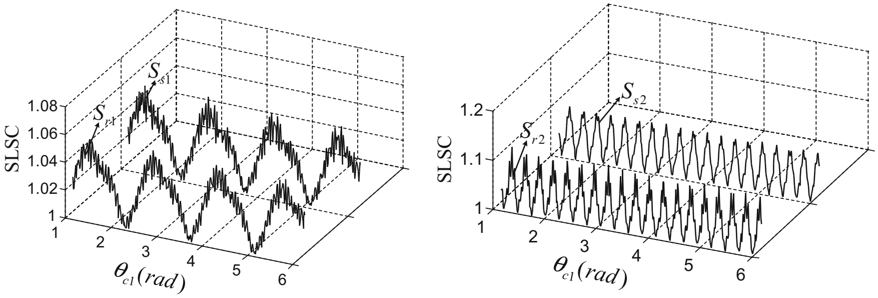

(a) SLSC in the 1st stage (b) SLSC in the 2nd stage

Fig. 2.22 SLSC of planetary transmission. **a** SLSC in the 1st stage. **b** SLSC in the 2nd stage

2.4.2 *Load-Sharing Structure Design*

Load-sharing performance of the planetary transmission can be improved by adopting appropriate load-sharing structure in practice. Two types of load-sharing structures are discussed according to the characteristics of the planetary model in this chapter.

(1) The elastic support of the planet gear

Elastic support of the planet gear is an effective load-sharing method and is becoming the future development direction of the load-sharing mechanism for the planetary transmission of the high-power wind turbine gearbox. The planets and the carrier in the same stage are connected by flexible pin to make the planets elastic float. SLSC is obtained by decreasing the planetary supporting stiffness to simulate the effect of the flexible pin. Since the SLSC variation between the external and internal meshing is mainly consistent shown in Fig. 2.22, the following calculation takes the external meshing for instance. S_{si} is reduced from 1.07 to 1.02 in the 1st stage and from 1.15 to 1.01 in the 2nd stage with the elastic supporting planets in Fig. 2.23. It indicates that the elastic supporting planets can improve load-sharing performance especially in the 2nd stage.

Each planet floating displacement range is represented by the shadow in Fig. 2.24. The value is a = 17 μm, b = 7.5 μm, c = 7 μm, d = 3 μm, e = 10 μm, and f = 57 μm. All displacements are within the limit of maximum deflection according to HG/T 4082-2009, and the dynamic stability of the system is not disturbed.

(2) The center part floating with clearance

Floating center part (sun gear, ring gear or carrier) of the planetary system can also make the load of the planets more uniform by allowing radial and torsional deflection of float parts. Double (single)-tooth gear coupling is used as the floating component to achieve clearance float. The supporting forces of center part P_x and P_y

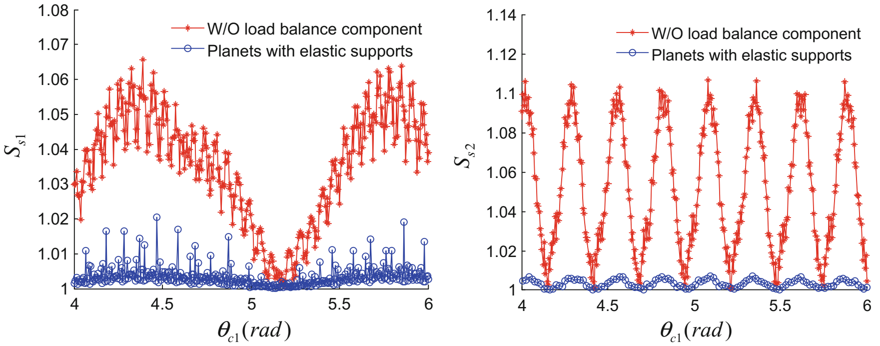

(a) SLSC in the 1st stage (b) SLSC in the 2nd stage

Fig. 2.23 SLSC of planets elastic support structure. **a** SLSC in the 1st stage. **b** SLSC in the 2nd stage

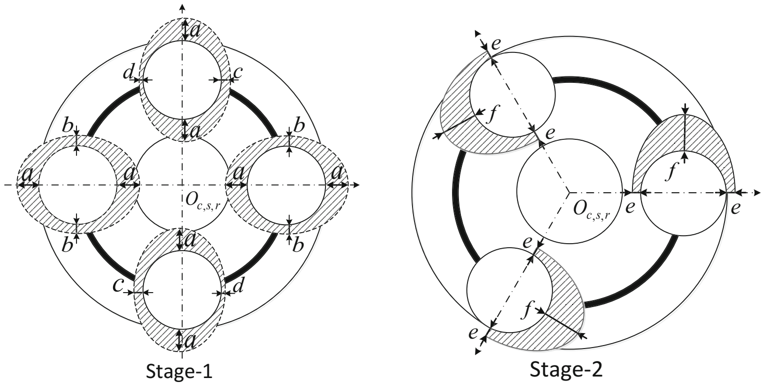

(a) Floating range in 1st stage (b) Floating range in 2nd stage

Fig. 2.24 Floating range of planets. **a** Floating range in 1st stage. **b** Floating range in 2nd stage

are presented in Eqs. (2.36)–(2.37) after considering supporting clearance nonlinearity. P_x and P_y are taken into dynamical equations and S_{si} is obtained.

$$P_x = \begin{cases} k_{si,ri,ci}(x_{si,ri,ci} - r_{si,ri,ci}), & |x_{si,ri,ci}| \geq r_{si,ri,ci} \\ 0, & |x_{si,ri,ci}| < r_{si,ri,ci} \end{cases} \tag{2.36}$$

$$P_y = \begin{cases} k_{si,ri,ci}(y_{si,ri,ci} - r_{si,ri,ci}), & |y_{si,ri,ci}| \geq r_{si,ri,ci} \\ 0, & |y_{si,ri,ci}| < r_{si,ri,ci} \end{cases} \tag{2.37}$$

where P_x and P_y are the supporting forces of center part in X_c- and Y_c-directions, respectively. r_{si}, r_{ri}, and r_{ci} are maximum permissible offset of center part presented in Eq. (2.38)–(2.39) [10].

$$\begin{cases} r_{s1,r1} = E_{s1} + 4\sqrt{2}E_{p1}\cos\alpha_{t1} + E_{r1} + 4E_{c1}\cos\alpha_{t1} + 2E_{\tau 1}\cos\alpha_{t1} \\ r_{c1} = \frac{E_{s1}+E_{r1}}{2\cos\alpha_{t1}} + 2E_{p1} + E_{c1} + E_{\tau 1} \\ (N = 4) \end{cases} \tag{2.38}$$

$$\begin{cases} r_{s2,r2} = E_{s2} + \frac{8}{3}E_{p2}\cos\alpha_{t2} + E_{r2} + 2E_{c2}\cos\alpha_{t2} + \frac{4}{3}E_{\tau 2}\cos\alpha_{t2} \\ r_{c2} = \frac{E_{s2}+E_{r2}}{2\cos\alpha_{t2}} + \frac{4}{3}E_{p2} + E_{c2} + E_{\tau 2} \\ (N = 3) \end{cases} \tag{2.39}$$

S_{si} of different floating parts are compared in Fig. 2.25 and is reduced obviously by floating any center part for both two stages. In particular, the S_{s1} is reduced from 1.068 to 1.002 and S_{s2} from 1.107 to 1.003 under sun gear floating. SLSC of the sun gear floating is minimum due to its little inertia and flexible movement. Floating center part of one stage has no influence on SLSC of the other stage.

SLSC can be reduced more in coupled floating mode, such as the sun gear of the 1st stage and the carrier of the 2nd stage floating together, compared with only one center part floating, as shown in Fig. 2.26. The value of SLSC with different load-sharing structure is listed in Table 2.7, where W/O represents system without load-sharing structure. It can be found that coupled floating mode, with a long spindle connecting sun gear of the 1st stage and carrier of the 2nd stage, can achieving a better load-sharing performance and is more suitable than any other structure for the two-stage planetary transmission.

Each center floating part displacement range is represented by the shadow in Fig. 2.27. The floating value is $g = 20$ μm, $h = 70$ μm, $i = 6$ μm, $j = 3$ μm, $k = 1$ μm, $l = 4$ μm, $m = 8$ μm, $n = 73$ μm, $o = 7$ μm, $p = 3$ μm, and $q = 2$ μm. All displacements are within the limit of maximum deflection according to HG/T 4082-2009, and dynamic stability of the system is not disturbed.

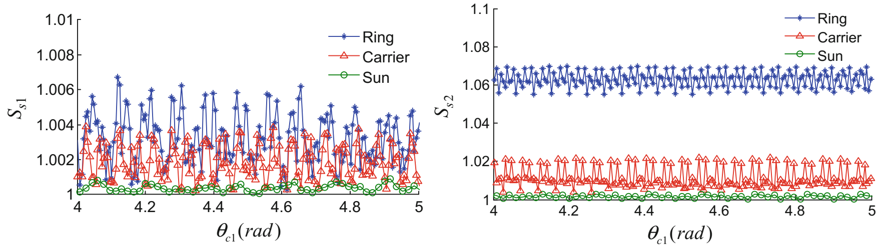

(a) SLSC in the 1st stage (b) SLSC in the 2nd stage

Fig. 2.25 SLSC of center part floating structure. **a** SLSC in the 1st stage. **b** SLSC in the 2nd stage

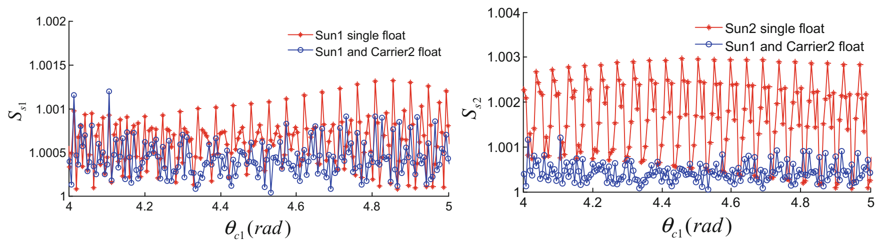

(a) SLSC in the 1st stage (b) SLSC in the 2nd stage

Fig. 2.26 SLSC of coupled float structure. **a** SLSC in the 1st stage. **b** SLSC in the 2nd stage

Table 2.7 SLSC of different load-sharing structure

		S_{s1}	S_{s2}
W/O		1.0681	1.1071
Planets elastic support		1.0231	1.0133
Center part floating	Ring	1.0073	1.0720
	Carrier	1.0043	1.0221
	Sun	1.0015	1.0030
	Coupled float	1.0012	1.0018

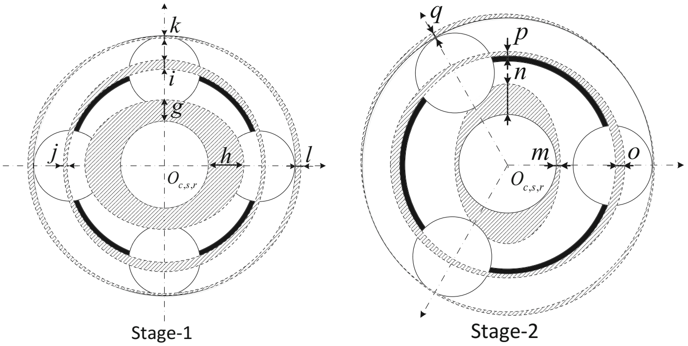

(a) Floating range in 1st stage (b) Floating range in 2nd stage

Fig. 2.27 Floating range of center floating parts. **a** Floating range in 1st stage. **b** Floating range in 2nd stage

2.4.3 Load-Sharing Performance Effected by the Errors

Since the component errors are major factors to make the planetary load distribution uneven, it is important to decrease the effect of the component errors on the load-sharing performance. The errors considered in this chapter are shown in

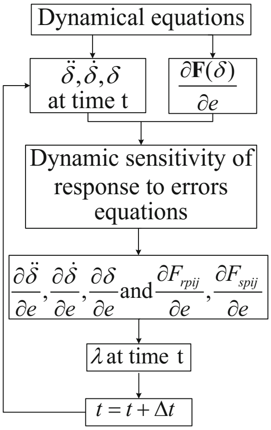

Fig. 2.28 Calculating flowchart of λ

nomenclature. λ is the dynamical sensitivity of PLSC to the errors, bigger λ means larger influence of the error on load-sharing performance. Direct derivative method is applied to obtain λ in this chapter. The calculating flowchart of λ is shown in Fig. 2.28. Equations (2.9)–(2.16) are organized into a matrix form with ignoring its tooth backlash nonlinearity and represented as follows

$$\boldsymbol{M}\ddot{\delta}+\boldsymbol{C}\dot{\delta}+\boldsymbol{K}\delta=\boldsymbol{F}(\delta) \tag{2.40}$$

Taking partial derivative of both sides with the errors, Eq. (2.28) is rewritten as

$$\boldsymbol{M}\frac{\partial\ddot{\delta}}{\partial e}+\boldsymbol{C}\frac{\partial\dot{\delta}}{\partial e}+\boldsymbol{K}\frac{\partial\delta}{\partial e}=\frac{\partial\boldsymbol{F}(\delta)}{\partial e}-\left(\frac{\partial\boldsymbol{M}}{\partial e}\ddot{\delta}+\frac{\partial\boldsymbol{C}}{\partial e}\dot{\delta}+\frac{\partial\boldsymbol{K}}{\partial e}\delta\right) \tag{2.41}$$

Since $\frac{\partial\boldsymbol{M}}{\partial e}\ddot{\delta}+\frac{\partial\boldsymbol{C}}{\partial e}\dot{\delta}+\frac{\partial\boldsymbol{K}}{\partial e}\delta=0$, Eq. (2.29) can be simplified as follows:

$$\mathbf{M}\left(\frac{\partial\delta}{\partial e}\right)''+\mathbf{C}\left(\frac{\partial\delta}{\partial e}\right)'+\mathbf{K}\left(\frac{\partial\delta}{\partial e}\right)=\tilde{\mathbf{F}}\left(\frac{\partial\delta}{\partial e}\right) \tag{2.42}$$

Partial derivative of dynamic response on the error is obtained by classical Runge–Kutta method, and the sensitivity of SLSC to the errors can be obtained in Eq. (2.43).

$$\lambda=\frac{\partial p_{rpij,spij}}{\partial e}=N\frac{F'_{rpij,spij}\left(\sum_{i=1}^{N}F_{rpij,spij}\right)+F_{rpij,spij}\left(\sum_{i=1}^{N}F'_{rpij,spij}\right)}{\left(\sum_{i=1}^{N}F_{rpij,spij}\right)^{2}} \tag{2.43}$$

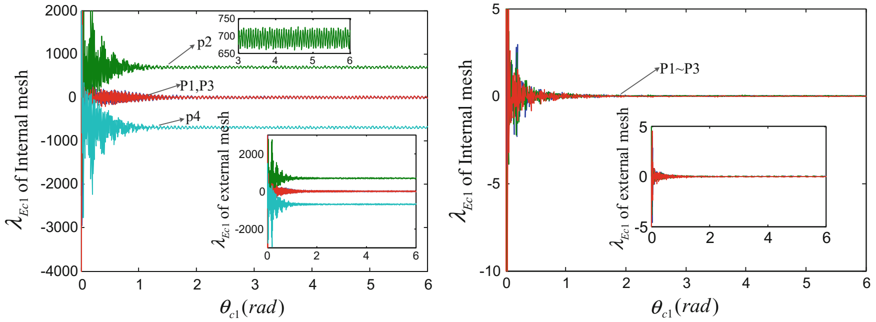

(a) Sensitivity of PLSC to E_{c1} in the 1st stage (b) Sensitivity of PLSC to E_{c1} in the 2nd stage

Fig. 2.29 Influence of E_{c1} on PLSC. **a** Sensitivity of PLSC to E_{c1} in the 1st stage. **b** Sensitivity of PLSC to E_{c1} in the 2nd stage

In Eq. (2.43), $F'_{rpij,spij}$ is partial derivative of the internal or external meshing force on error with its expression is

$$F'_{rpij,spij} = \frac{\partial F_{rpij,spij}}{\partial e} = F\left(\frac{\partial \delta}{\partial e}, \frac{\partial \dot{\delta}}{\partial e}\right)_{rpij,spij} \tag{2.44}$$

Taking E_{c1} for instance, dynamic sensitivity of PLSC to E_{c1} (λ_{Ec1}) is obtained without load-sharing structure in Fig. 2.29. λ_{Ec1} fluctuates within a certain range after the system maintains a stable state. Figure 2.29a shows that λ_{Ec1} of P_{12} is the largest of the four planets and λ_{Ec1} of P_{14} is opposite to P_{12} due to the symmetrical location of planets. λ_{Ec1} in the 2nd stage is close to 0 in Fig. 2.29b. It indicates that E_{c1} only affects PLSC in the same stage and has no influence on the other, with the same regularity as the other type of errors. The following research takes external meshing of P_{12} in the 1st stage for instance.

Dynamic sensitivity of PLSC to each type of error without load-sharing structure is given in Fig. 2.30. It shows that $E_{\tau 12}$ and E_{p12} have tremendous influence on PLSC compared with other type of errors in Fig. 2.30, which adequate attention should be paid on planetary transmission design. Sensitivity to $\varepsilon_{r1,s1,p12}$ is almost zero shown in Fig. 2.30e which can be ignored in planetary load-sharing research.

Figure 2.31 lists the root mean square (RMS) of sensitivities by each type of load-sharing structure this paper discussed above. It shows that when a component of planetary transmission is used as the load-sharing structure, the sensitivity to the relevant error is reduced. So it is concluded that adopting load-sharing structure not only can improve load-sharing performance but also can reduce the requirement of component precision for planetary transmission.

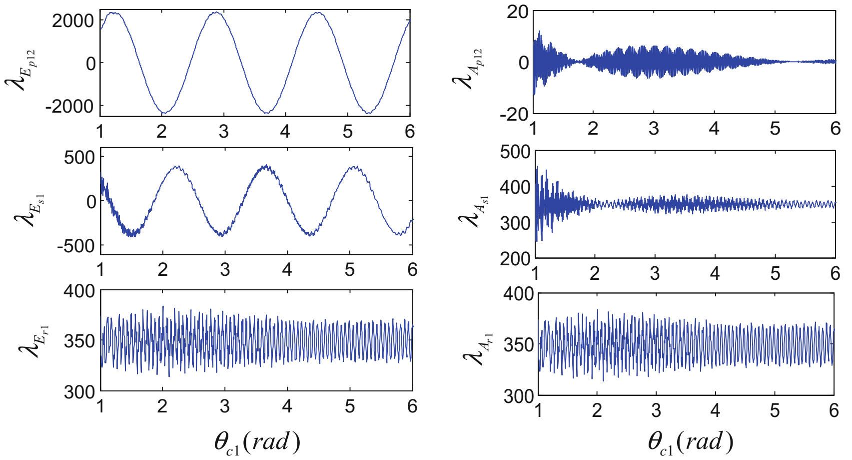

(a) Sensitivity to manufacturing errors (b) Sensitivity to fixing errors

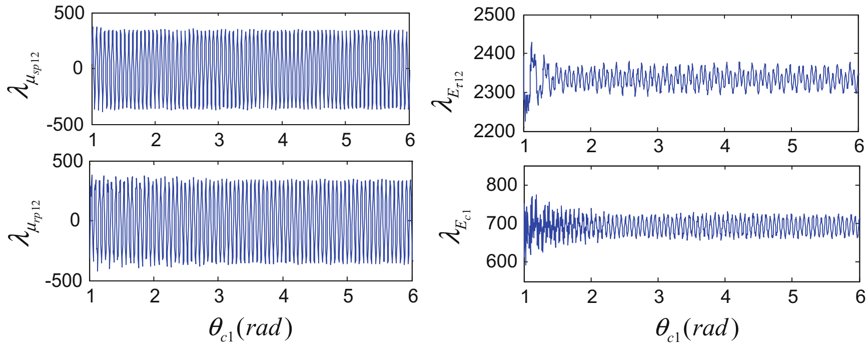

(c) Sensitivity to tooth profile error (d) Sensitivity to errors of carrier 1

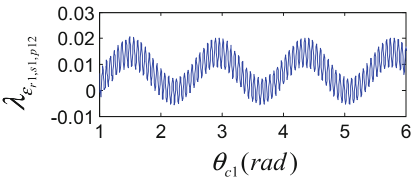

(e) Sensitivity to tooth thickness deviation

Fig. 2.30 Dynamic sensitivity of PLSC to errors. **a** Sensitivity to manufacturing errors. **b** Sensitivity to fixing errors. **c** Sensitivity to tooth profile error. **d** Sensitivity to errors of carrier 1. **e** Sensitivity to tooth thickness deviation

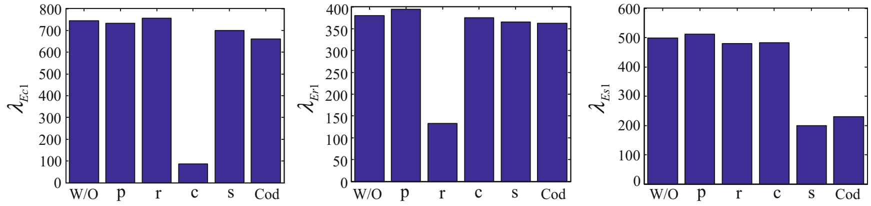

(a) Sensitivity to Ec1 (b) Sensitivity to Er1 (c) Sensitivity to Es1

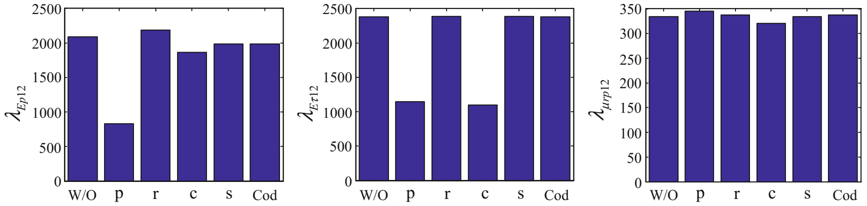

(d) Sensitivity to E_{p12} (e) Sensitivity to $E_{\tau12}$ (f) Sensitivity to $E_{\mu12}$

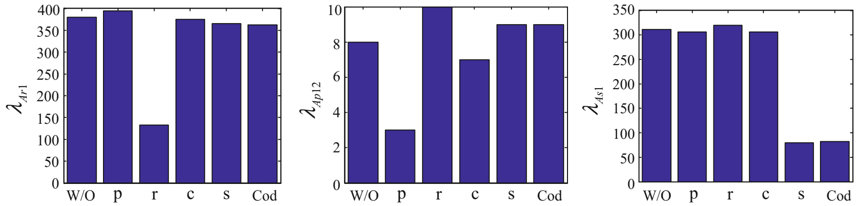

(g) Sensitivity to A_{r1} (h) Sensitivity to A_{p12} (i) Sensitivity to A_{s1}

W/O: without load sharing structure; p: planet elastic support; r: ring float;
c: carrier float; s: sun float; Cod: coupled float

Fig. 2.31 RMS of sensitivity to errors with different load-sharing structure. **a** Sensitivity to E_{c1}. **b** Sensitivity to E_{r1}. **c** Sensitivity to E_{s1}. **d** Sensitivity to E_{p12}. **e** Sensitivity to $E_{\tau12}$. **f** Sensitivity to $E_{\mu12}$. **g** Sensitivity to A_{r1}. **h** Sensitivity to A_{p12}. **i** Sensitivity to A_{s1}. *W/O* without load sharing structure; *p* planet elastic support; *r* ring float; *c* carrier float; *s* sun float; *Cod* coupled float

2.5 Experimental Test of Load Balances in Gearbox

Taking a planetary gearbox with single stage as an example, load-sharing experiment is carried out by using two load-sharing structures, W/O load balance structure, and floating sun gear with single-tooth coupling. Test bench layout is shown in Fig. 2.32. Electronic measure method was adopted in the experiment to acquire planetary gear load, testing points were arranged in the ring gear, as shown in Fig. 2.33.

The gearbox was loaded by 0, 50, and 100 % of the rated load with the motor speed 13 r/min, and the planetary strains were measured, as shown in Figs. 2.34 and 2.35.

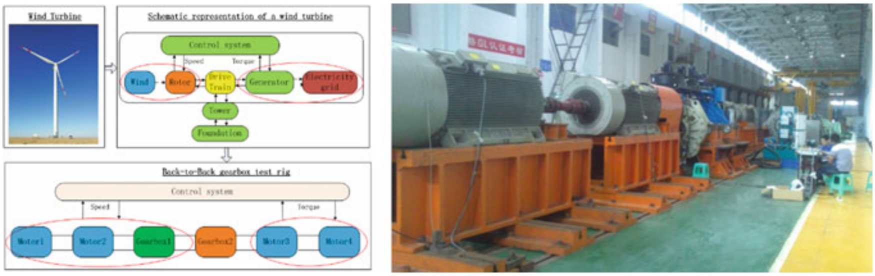

Fig. 2.32 Test bench of the load-sharing experiment

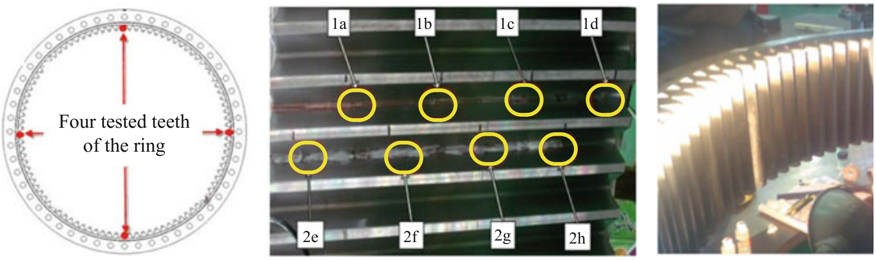

Fig. 2.33 Testing points arrangement

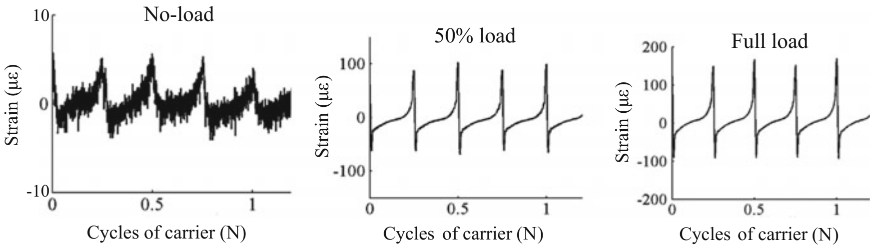

(a) inner meshing strain by no load

(b) inner meshing strain by 50% load

(c) inner meshing strain by 100% load

Fig. 2.34 Planetary strain W/O balance mechanism. **a** inner meshing strain by no load. **b** Inner meshing strain by 50 % load. **c** Inner meshing strain by 100 % load

The inner meshing strain is increased with the increasing of the load. The results of the experiment indicate that load fluctuation of the gear teeth is significantly reduced by floating sun gear and PLSC decreased correspondingly. It is concluded that the calculation results are agreed well with experiment. Due to the influence of the actual working conditions on the sharing load performance, such as manufacturing and installation errors, there is a little difference between the experimental and theoretical value, but same regularity they presented is consistent.

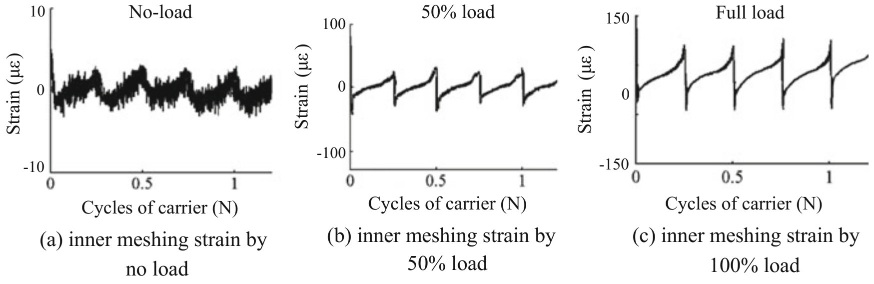

(a) inner meshing strain by no load

(b) inner meshing strain by 50% load

(c) inner meshing strain by 100% load

Fig. 2.35 Planetary strain with sun gear floating. **a** Inner meshing strain by no load. **b** Inner meshing strain by 50 % load. **c** Inner meshing strain by 100 % load

Table 2.8 SLSC of experiment results vs numerical calculations

		Exp. value	Cal. value	Error %
W/O load balance mechanism	50 % load	1.174	1.042	12.7
	100 % load	1.141	1.065	7.1
Sun gear float	50 % load	1.1061	1.001	10.5
	100 % load	1.087	1.002	8.5

Table 2.8 lists the comparative results of SLSC by experiment vs numerical calculation in the case of 50 and 100 % load, respectively.

References

1. Velex P, Ajmi M. Dynamic tooth loads and quasi-static transmission errors in helical gears—approximate dynamic factor formulae. Mech Mach Theory. 2007;42(11):1512–26.
2. Hedlund J, Lehtovaara A. A parameterized numerical model for the evaluation of gear mesh stiffness variation of a helical gear pair. In: ARCHIVE Proceedings of the Institution of Mechanical Engineers: Part C Journal of Mechanical Engineering Science 1989–1996 (vols. 203–210), 2008, 222(222):1321–1327.
3. Qin D, Wang J, Lim TC, et al. Flexible multibody dynamic modeling of a horizontal wind turbine drive train system. J Mech Des 2009; 131(11).
4. Helsen J, Vanhollebeke F, Marrant B, et al. Multibody modelling of varying complexity for modal behaviour analysis of wind turbine gearboxes. Renew Energy. 2011;36(11):3098–113.
5. Li R. Gear system dynamics-vibration, impact, noise. Beijing, China: Science Press; 1997.
6. Wei J, Lv C, Sun W, et al. A study on optimum design method of gear transmission system for wind turbine. Int J Precis Eng Manuf. 2013;14(5):767–78.
7. Kahraman A. Load sharing characteristics of planetary transmissions. Mech Mach Theory. 1994;29(8):1151–65.
8. Gualtieri G, Secci S. Methods to extrapolate wind resource to the turbine hub height based on power law: A 1-h wind speed vs. Weibull distribution extrapolation comparison. Renew Energy. 2012;43:183–200.

9. Chellali F, Khellaf A, Belouchrani A, et al. A comparison between wind speed distributions derived from the maximum entropy principle and Weibull distribution. Case of study; six regions of Algeria. Renew Sustain Energy Rev. 2012;16(1):379–85.
10. Cheng D. Mechanical design handbook-mechanical transmission. Beijing, China: Chemical Industry Press; 2010.

Chapter 3
Parameter Optimization for Planetary Gear System Based on Torsional Dynamics

As the key component of wind turbine, the weight of the gear transmission system becomes larger and larger with the increasing power of wind turbine [1]. The planetary gear system needs less weight and higher reliability to reduce cost and work healthily. Here, we take the minimal volume of the transmission system as the optimization objective and the reliability as the constraint. Based on the dynamic characteristics of wind turbine gearbox transmission system, a coupled nonlinear dynamic model of the transmission system is established considering the nonlinear factors associated with time-varying mesh stiffness, dynamic transmission error, gear mesh impact, and input varying load. In the dynamic model, the translational and rotational degrees of freedom of the gears are considered, and the major nonlinear factors are included. The application factor and the dynamic load factor of each gear pair are obtained by solving the dynamic model. The method to obtain the load factors in this chapter is more scientific and suitable than that by traditional look-up table method. Based on these load factors, an optimization design approach for the gear transmission system in wind turbine is presented.

3.1 Design Variables and Objective Function

The number of teeth (z_{sj}), the normal modulus (m_{nj}), the face width (b_j), the helix angle (β_j), the profile modify coefficient (x_{nsj}), and the working transverse pressure angle (α_{sjpj}) of sun gear are defined as design variables. The vector of design variable is expressed as

$$X = [X_1, X_2, X_3, X_4, X_5, X_6]^{\mathrm{T}} = [z_{z_j}, m_{n_j}, b_j, x_{ns_j}, \alpha_{s_jp_j}]^{\mathrm{T}} \tag{3.1}$$

Q. Han et al., *Dynamics and Vibration Analyses of Gearbox in Wind Turbine*,
DOI 10.1007/978-981-10-2747-5_3

The objective function for minimal volume is written as

$$\min(f_j) = \min(\pi b_j (d_{as_j}^2 + N \cdot d_{ap_j}^2 + d_{fr_j}^2 - d_{ar_j}^2)/4) \tag{3.2}$$

where d_{asj}, d_{apj}, d_{arj}, d_{frj}, and N represent the tip diameter of the sun gear, the planet gear, the ring gear, the root diameter of the ring gear, and the number of planet gears separately.

3.2 The Constraint Function

(1) Gear teeth matching

Transmission ratio

$$i = 1 + z_{r_j}/z_{s_j} \tag{3.3}$$

Concentricity

$$A_{sp_j} = A_{rp_j} \tag{3.4}$$

Assembling

$$(z_{s_j} + z_{r_j})/N = \text{Integer} \tag{3.5}$$

Adjacency

To avoid crash, the space between two adjacent planet gears should be greater than half of the modulus.

$$d_{ap_j} + 0.5 m_{t_j} - (z_{s_j} + z_{p_j}) m_{t_j} \sin(\pi/N) \le 0 \tag{3.6}$$

In Eqs. (3.3)–(3.6), z_{rj}, z_{pj}, m_{tj}, As_{pj}, and Ar_{pj}, respectively, represent teeth number of ring gear, teeth number of planet gear, transverse module, the actual center distance of sun–planet gear pair, and ring–planet gear pair.

(2) Contact ratio

$$1.2 \le \varepsilon_a \le 2.2 \tag{3.7}$$

$$1 - \varepsilon_\beta \le 0 \tag{3.8}$$

(3) Number of teeth

$$17 \le z_{s_j} \le 45 \tag{3.9}$$

(4) Modulus

$$6 \le m_{n_j} \le 20 \tag{3.10}$$

(5) Helix angle

$$6^\circ \le \beta_j \le 20^\circ \tag{3.11}$$

(6) Working transverse pressure angle

$$20^\circ \le \alpha_{s_j p_j} \le 23^\circ \tag{3.12}$$

(7) Profile modify coefficients

$$-0.5 \le x_{ns_j} \le 1.2 \tag{3.13}$$

$$0.5 \le x_{ns_j} + x_{np_j} \le 0.8 \tag{3.14}$$

$$-0.5 \le x_{nr_j} - x_{np_j} \le 0.4 \tag{3.15}$$

(8) Tooth thickness at the tip cylinder

$$0.4m_{t_j} - S_a \le 0 \tag{3.16}$$

(9) Width–radius ratio

$$0.125 \le b_j / d_{r_j} \le 0.30 \tag{3.17}$$

In Eqs. (3.7)–(3.17), ε_α, ε_β, x_{npj}, x_{nrj}, S_a, d_{rj}, represent the transverse contact ratio, the overlap ratio, the planet modify coefficient, the ring modify coefficient, the tooth thickness at the tip cylinder, and the pitch diameter of the ring gear separately.

(10) Avoiding fillet interference

Avoiding fillet interference between the root of the sun gear and the tip of the planet gear

$$-\tan\alpha_{ts_jp_j} - \frac{z_{p_j}}{z_{s_j}}\left(\tan\alpha_{atp_j} - \tan\alpha_{ts_jp_j}{}'\right) + \tan\alpha_{ts_jp_j}{}' + \frac{4\left(h_{an}^{*} - x_{ns_j}\right)\cos\beta_j}{z_{s_j}\sin 2\alpha_{ts_jp_j}} \geq 0 \tag{3.18}$$

Avoiding fillet interference between the tip of the sun gear and the root of the planet gear

$$-\tan\alpha_{ts_jp_j} - \frac{z_{s_j}}{z_{p_j}}\left(\tan\alpha_{ats_j} - \tan\alpha_{ts_jp_j}{}'\right) + \tan\alpha_{ts_jp_j}{}' + \frac{4\left(h_{an}^{*} - x_{np_j}\right)\cos\beta_j}{z_{p_j}\sin 2\alpha_{ts_jp_j}} \geq 0 \tag{3.19}$$

In above equations, h_{an}^{*}, α_{atpj}, α_{atsj}, α_{tsjpj}, $\alpha_{tsjpj'}$ represent the addendum coefficient, the working transverse pressure angle at the tip diameter of the planet gear and the sun gear, the transverse pressure angle and the working transverse pressure angle of the sun–planet gear pair.

(11) Avoiding profile overlap interference of ring gear

$$z_{r_j}(\mathrm{inv}\alpha_{atr_j} + \delta_{r_j}) - z_{p_j}(\mathrm{inv}\alpha_{ap_j} + \delta_{p_j}) - (z_{r_j} - z_{p_j})\mathrm{inv}\alpha'_{tr_jp_j} \leq 0 \tag{3.20}$$

where, $\delta_{p_j} = \arccos\frac{r_{ar_j}^2 - r_{ap_j}^2 - a_{r_jp_j}^2}{2r_{ap_j}a_{r_jp_j}}$, $\delta_{r_j} = \arccos\frac{r_{ar_j}^2 - r_{ap_j}^2 + a_{r_jp_j}^2}{2r_{ap_j}a_{r_jp_j}}$, and α_{trjpj} is the transverse pressure angle of the ring–planet gear pair.

(12) Equal strength principle

The relationship between the contact strength and the bending strength can be reflected by *m*/*a*, inappropriate ratio may cause excessive contact strength, bearing capacity per volume, and bending strength, which can result in large modulus and have influence on the stability, the contact ratio, and the economic benefit. Generally, the proper range of *m*/*a* is from 0.028 to 0.045.

$$\frac{m}{a} = \frac{2u}{(u \pm 1)^2}\left[\frac{Z_{\sigma\max}^2\sigma_{H\lim}^2}{Z_{\sigma}^2K_HS_{H\lim}^2}\right]\left[\frac{Y_{\sigma}K_FS_{F\min}}{\sigma_{F\lim}Y_{\sigma\lim}}\right] \tag{3.21}$$

$$0.028 \leq m/a \leq 0.045 \tag{3.22}$$

where, $Z_{\sigma\min} = Z_{NT}Z_LZ_VZ_RZ_WZ_X$, $Z_{\sigma} = Z_HZ_EZ_{\varepsilon}Z_{\beta}$, $K_H = K_{H\beta}K_{H\alpha}$, $K_F = K_{F\beta}K_{F\alpha}$, $Y_{\sigma\lim} = Y_{ST}Y_{NT}Y_{\delta\mathrm{relT}}Y_{R\mathrm{relT}}Y_X$, $Y_{\sigma} = Y_{F\alpha}Y_{S\alpha}Y_{\varepsilon}Y_{\beta}$. Z_{NT}, Z_L, Z_V, Z_R, Z_W, Z_X, Z_H, Z_E, Z_{ε},

Z_β, $K_{H\beta}$, $K_{F\beta}$, $K_{H\alpha}$, $K_{F\alpha}$, Y_{ST}, Y_{NT}, $Y_{\delta\mathrm{rel}T}$, $Y_{R\mathrm{rel}T}$, Y_X, $Y_{F\alpha}$, $Y_{S\alpha}$, Y_ε, Y_β, u, $\sigma_{H\mathrm{lim}}$, $\sigma_{F\mathrm{lim}}$ represent the finite life factor, the lubrication factor, the speed factor, the roughness factor, the material mating factor, the size coefficient, the zone factor, the elasticity coefficient, the contact ratio factor, the helix angle factor, the face coefficient (flank), the face coefficient (tooth root), the transverse coefficient (flank), the transverse coefficient (tooth root), the stress correction factor, the finite life factor (tooth root), the support factor, the surface factor, the size coefficient (tooth root), the tooth form factor, the stress correction factor for single tooth meshing, the contact ratio factor (tooth root), the helix angle factor (tooth root) and transmission ratio, the fatigue strength for Hertzian pressure, and the fatigue strength for tooth root stress.

(13) Reliability

Supposing the tooth surface contact stress, the contact fatigue strength, the bending stress, and the bending fatigue strength follow lognormal distribution, and the expressions of the reliability constraint are expressed as [2]

$$\frac{\ln \sigma'_{H\,\mathrm{lim}} - \ln \sigma'_H}{\sqrt{C^2_{\sigma'_{H\,\mathrm{lim}}} + C^2_{\sigma'_H}}} \geq z_R \tag{3.23}$$

$$\frac{\ln \sigma'_{F\,\mathrm{lim}} - \ln \sigma'_F}{\sqrt{C^2_{\sigma'_{F\,\mathrm{lim}}} + C^2_{\sigma'_F}}} \geq z_R \tag{3.24}$$

where $z_R, \sigma'_{H\,\mathrm{lim}}, \sigma'_{F\,\mathrm{lim}}, \sigma'_H, \sigma'_F, C_{\sigma'_{H\mathrm{lim}}}, C_{\sigma'_{F\mathrm{lim}}}, C_{\sigma'_H}, C_{\sigma'_F}$ represent the association coefficient, the average value of contact fatigue strength and the bending fatigue strength, the average value of contact stress and the bending stress, and the coefficient of the variation of each corresponding variable.

3.3 Parameter Optimization for High-Speed Transmission System with Parallel Axes

The normal modulus m_{n78}, the number of teeth z_7, the helix angle β_{78}, the profile modify coefficient x_{n7}, the face width b_{78}, the working transverse pressure angle α_{78} of the wheel are design variables. The vector of the design variables is defined as

$$X' = [X'_1, X'_2, X'_3, X'_4, X'_5, X'_6]^{\mathrm{T}} = [m_{n78}, z_7, \beta_{78}, x_{n7}, \alpha_{78}, b_{78}]^{\mathrm{T}} \tag{3.25}$$

The objective function of the minimal volume is expressed as

$$\min(f') = \min(\pi b_{78}(d^2_{a7} + d^2_{a8})/4) \tag{3.26}$$

where, d_{a7}, d_{a8} represent the tip diameter of the wheel and the pinion of the high-speed stage, respectively.

Similar to the planetary gear stage, the constraints of the high-speed stage contain the transmission ratio, the contact ratio, the number of teeth, the modulus, the helix angle, the equal strength principle, the reliability, etc.

3.4 Distribution of Reliability

Equal distribution method is used to distribute reliability of each unit. Only the reliability constraint of the gear is considered and is expressed as follows [3]:

$$R_i = [R_s]^{\frac{1}{n_s}} \tag{3.27}$$

where R_i, R_s, n_s represent the reliability index of each unit, the reliability index of the system, and the number of reliability constraints of the gear.

3.5 Example and Analysis

In the example, the parameters of the system are shown in Table 3.2 and the total ratio of transmission system is 69.21. Under the circumstance of reliability requirement of 0.99, 0.999, and 0.9999, optimization design is carried out based on the above approach. The optimized parameters K_A and K_V could be obtained from above analysis. The original and optimized parameters are shown below.

(1) Optimization results

On the basis of the load conditions and the optimization model, sequential quadratic programming algorithm is employed to carry out the optimization [4]. The results are shown in Tables 3.1, 3.2, and 3.3, and the number of teeth, the modulus, and the width of the gear are rounded.

(2) Application factor and dynamic load factor

K_A of each gear pair before and after optimization is shown in Table 3.4, and the reliability requirement is 0.99, 0.999, and 0.9999 in the optimization.

As shown in Table 3.4, K_A of transmission system changes little before and after optimization, which can be concluded that K_A does not change with the improvement of reliability. The reason is that the improvement of reliability could not change the additional external dynamic load, which is associated with the external excitation. K_A of high-speed stage is relatively large before and after optimization, which can be concluded that the influence of external excitation on the additional dynamic load of high-speed stage is greater.

Table 3.1 Original and optimized parameters of the 1st stage

Parameter	$R_n = 0.99$	$R_n = 0.999$	$R_n = 0.9999$	Original
Teeth number of sun	40	42	44	29
Teeth number of planet	47	51	53	35
Teeth number of ring	136	142	152	99
Normal modulus	11	11	11	18
Face width	470	485	530	470
Helix angle	9.959	9.484	9.072	7.167
Working pressure angle	21.582	21.491	21.413	21.800
Sun modify coefficient	1.097	1.098	1.098	0.222
Planet modify coefficient	−0.700	−0.697	−0.701	0.152
Ring modify coefficient	−0.293	−0.305	−0.296	0.543

Table 3.2 Original and optimized parameters of the 2nd stage

Parameter	$R_n = 0.99$	$R_n = 0.999$	$R_n = 0.9999$	Original
Teeth number of sun	34	36	38	28
Teeth number of planet	57	61	63	47
Teeth number of ring	149	156	166	122
Normal modulus	8	8	8	12
Face width	200	205	215	260
Helix angle	10.168	9.653	9.210	8.667
Working pressure angle	21.443	21.359	21.289	21.780
Sun modify coefficient	1.072	1.072	1.073	0.284
Planet modify coefficient	−0.707	−0.704	−0.707	0.131
Ring modify coefficient	−0.338	−0.344	−0.335	0.547

Table 3.3 Original and optimized parameters of high-speed stage

Parameter	$R_n = 0.99$	$R_n = 0.999$	$R_n = 0.9999$	Original
Teeth number of pinion	27	28	29	41
Teeth number of wheel	79	82	86	120
Normal modulus	8.500	8.500	8.500	8
Face width	310	295	345	240
Helix angle	4.794	7.220	4.355	12.500
Working pressure angle	18.076	18.266	18.246	21.649
Pinion modify coefficient	−0.600	−0.603	−0.605	0.327
Wheel modify coefficient	−0.005	0	0.004	0.363

K_V of each gear pair before and after optimization is shown in Table 3.5, and the reliability requirement is 0.99, 0.999, and 0.9999 in the optimization.

As shown in Table 3.5, under the circumstance of each reliability requirement, K_V of the 1st stage is minimal and high-speed stage is maximal in accordance with

Table 3.4 Original and optimized K_A of the gear pair

Stage	Gear pair	Original	$R_n = 0.99$	$R_n = 0.999$	$R_n = 0.9999$
The 1st stage	Sun–planet	1.10	1.13	1.10	1.11
	Ring–planet	1.10	1.16	1.11	1.13
The 2nd stage	Sun–planet	1.10	1.13	1.10	1.13
	Ring–planet	1.12	1.11	1.10	1.11
High-speed stage	Wheel-pinion	1.27	1.25	1.25	1.26

Table 3.5 Original and optimized K_V of the gear pair

Stage	Gear pair	Original	$R_n = 0.99$	$R_n = 0.999$	$R_n = 0.9999$
The 1st stage	Sun–planet	1.05	1.06	1.05	1.07
	Ring–planet	1.05	1.06	1.04	1.06
The 2nd stage	Sun–planet	1.08	1.08	1.11	1.10
	Ring–planet	1.07	1.07	1.09	1.10
High-speed stage	Wheel-pinion	1.36	1.09	1.10	1.12

that K_V increases with speed. K_V of the 1st and 2nd stage change little, which increase slightly with improvement of reliability requirement. Under the circumstance of different reliability requirement 0.99, 0.999, and 0.9999, K_V increases slightly, and the amplitude is small. After optimization, K_V of high-speed stage decreases significantly owing to big change of the teeth number, the modulus, the helix angle, etc.

The volume of gear pairs of the transmission system with different reliability requirement is shown in Fig. 3.1. It is obtained that the volume of the gear system is decreased after optimization but increased with the improvement of the reliability requirement, namely higher reliability requirement needs the gear to bear larger contact and bending fatigue loads.

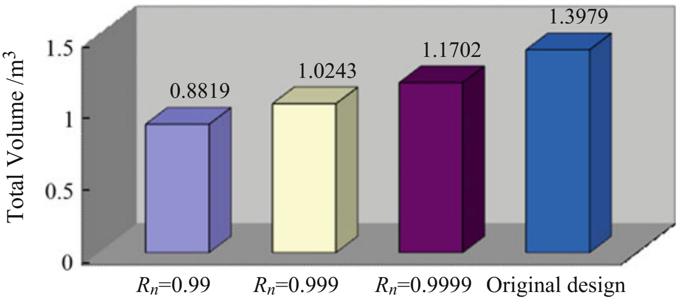

Fig. 3.1 Optimization results

References

1. Lin CH, Tsao TP. Depressing the torque vibrations of turbine blades using virtual inertia. Electr Power Syst Res. 2002;61(1):23–32.
2. Huang HZ. The reliability theory and application on mechanical transmission. Beijing: Science & Technology Press; 1995.
3. Mohan M, Gandhi OP, Agrawal VP, et al. Real-time reliability index of a steam power plant: a systems approach. Proc Inst Mech Eng Part A J Power Energy. 2008;222(4):355–69.
4. He HB, Li HY, Lyu SK, et al. Optimal design of a tilling machine reduction gearbox using Matlab. Int J Precis Eng Manufact. 2009;10(2):63–6.

Chapter 4

Influence of Unbalance and Misalignment on Load-Sharing Coefficient of Gear-Rotor System Based on Torsional Dynamics

The equivalent virtual shaft section method is proposed in this chapter based on linear mesh stiffness hypothesis, in which the rotating components are introduced as beam elements with the same mass and stiffness characteristics, and the effects of shaft stiffness and supporting stiffness of the gearbox are also taken into account. Then, the influence of unbalance and misalignment on the load-sharing coefficient is analyzed.

4.1 Modeling Method for Dynamic Analysis of Gear-Rotor System

The method of FEA (finite element analysis) can be used for rotor-gear system coupled from gears; all parts of system are split to different elements for modeling and theoretical analysis.

The various elements used in system modeling are described as follows.

4.1.1 Shaft Element

The rotating shaft of the rotor system can be modeled by the two node space rotating beam element shown in Fig. 4.1. The i and j are defined as the two end nodes of the beam element; each shaft element has 12 degrees of freedom and is expressed as follows [1]:

$$\boldsymbol{u}_{ij} = [x_i \quad y_i \quad z_i \quad \theta_{xi} \quad \theta_{yi} \quad \theta_{zi} \quad x_j \quad y_j \quad z_j \quad \theta_{xj} \quad \theta_{yj} \quad \theta_{zj}]^{\mathrm{T}} \tag{4.1}$$

Q. Han et al., *Dynamics and Vibration Analyses of Gearbox in Wind Turbine*,
DOI 10.1007/978-981-10-2747-5_4

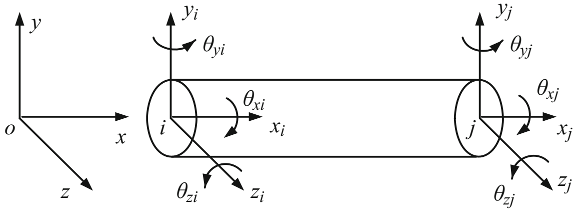

Fig. 4.1 Timoshenko beam element

Equation of motion of shaft element is written as

$$\mathbf{M}_s \ddot{u}_{ij} + (\mathbf{C}_s + \Omega \boldsymbol{G}_s)\dot{\mathbf{u}}_{ij} + \mathbf{K}_s \mathbf{u}_{ij} = \boldsymbol{F}_s \tag{4.2}$$

where $\boldsymbol{\Omega}$ is the rotational speed of shaft element, $\boldsymbol{F}_s$ is external load applied to shaft element, $\boldsymbol{M}_s$ is mass matrix, $\boldsymbol{C}_s$ is damping matrix, $\boldsymbol{G}_s$ is gyro force matrix, and $\boldsymbol{K}_s$ is the stiffness matrix of shaft element [2, 3].

Damping matrix $\boldsymbol{C}_{\mathrm{s}}$ can be expressed as the form of Rayleigh damping, which is defined as follows [4]:

$$\boldsymbol{C}_s = \alpha \cdot \mathbf{M}_b + \beta \cdot \mathbf{K}_b \tag{4.3}$$

where α and β denote the scale factors.

4.1.2 Lumped Mass Element

For the gears with large size, ignoring its deformation effect, it can be regarded as lumped mass with rotational effect. The degree of freedom of lumped mass element is 6, as shown in Fig. 4.2. The displacement vector can be expressed as

$$\boldsymbol{u}_i = [x_i \ y_i \ z_i \ \ \theta_{xi} \ \theta_{yi} \ \theta_{zi}]^{\mathrm{T}} \tag{4.4}$$

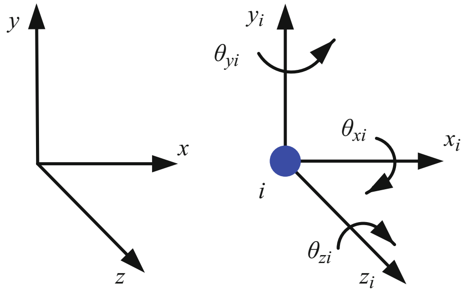

Fig. 4.2 Lumped mass element

Supposing that the mass of lumped mass element is m and diameter rotational inertia and polar rotational inertia through axis are J_d and J_p, the vibration differential equation of lumping mass element is expressed as follows:

$$\boldsymbol{M}_d \ddot{u} + \Omega \boldsymbol{G}_d \dot{\boldsymbol{u}} = \boldsymbol{F}_d \tag{4.5}$$

where Ω represents the rotational speed, $\boldsymbol{F}_d$ represents the generalized force vector, and $\boldsymbol{M}_d$ and $\boldsymbol{G}_{d,}$ respectively, are the mass matrix and gyro force matrix of element and are expressed as follows:

$$\boldsymbol{M}_d = \begin{bmatrix} m & 0 & 0 & 0 & 0 & 0 \\ 0 & m & 0 & 0 & 0 & 0 \\ 0 & 0 & m & 0 & 0 & 0 \\ 0 & 0 & 0 & J_p & 0 & 0 \\ 0 & 0 & 0 & 0 & J_d & 0 \\ 0 & 0 & 0 & 0 & 0 & J_d \end{bmatrix}, \quad \boldsymbol{G}_d = \begin{bmatrix} 0 & 0 & 0 & 0 & 0 & 0 \\ 0 & 0 & 0 & 0 & 0 & 0 \\ 0 & 0 & 0 & 0 & 0 & 0 \\ 0 & 0 & 0 & 0 & 0 & 0 \\ 0 & 0 & 0 & 0 & 0 & -J_p \\ 0 & 0 & 0 & 0 & J_p & 0 \end{bmatrix}$$

4.1.3 Bearing Element

In finite element model, the bearing can be treated as spring element with stiffness and damping, which is applied at rotor supporting point. For the general bearing, supposing that the point of coupling between one end of bearing and rotor is i and the other end of bearing is regarded as the full constraint, the coupling force model is shown in Fig. 4.3.

The degree of freedom of bearing element is 6, which is the displacement and rotation along the x, y, z directions; the displacement vector can be expressed as

$$\boldsymbol{u}_i = [x_i \, y_i \, z_i \, \theta_{xi} \, \theta_{yi} \, \theta_{zi}]^{\mathrm{T}} \tag{4.6}$$

Thus, the governing equations of the bearing can be written as

$$\mathbf{C}_b \dot{\mathbf{u}} + \mathbf{K}_b \mathbf{u} = \boldsymbol{F}_b \tag{4.7}$$

Fig. 4.3 Bearing element

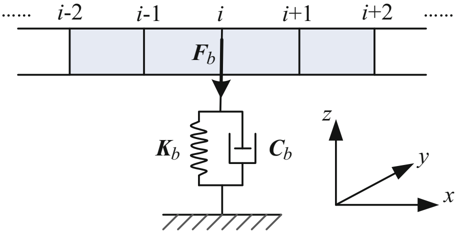

where $\boldsymbol{F}_b$ represents the generalized force vector and $\boldsymbol{C}_b$ and $\boldsymbol{K}_{b,}$ respectively, represent the damping matrix and stiffness matrix of bearing after the linearization of bearing force. Ignoring the effect of stiffness generated by the bearing on the shaft neck turning, stiffness of system can be expressed as

$$\boldsymbol{C}_b = \begin{bmatrix} c_{xx} & 0 & 0 & 0 & 0 & 0 \\ 0 & c_{yy} & c_{yz} & 0 & 0 & 0 \\ 0 & c_{zy} & c_{zz} & 0 & 0 & 0 \\ 0 & 0 & 0 & 0 & 0 & 0 \\ 0 & 0 & 0 & 0 & 0 & 0 \\ 0 & 0 & 0 & 0 & 0 & 0 \end{bmatrix}, \quad \boldsymbol{K}_b = \begin{bmatrix} k_{xx} & 0 & 0 & 0 & 0 & 0 \\ 0 & k_{yy} & k_{yz} & 0 & 0 & 0 \\ 0 & k_{zy} & k_{zz} & 0 & 0 & 0 \\ 0 & 0 & 0 & 0 & 0 & 0 \\ 0 & 0 & 0 & 0 & 0 & 0 \\ 0 & 0 & 0 & 0 & 0 & 0 \end{bmatrix}$$

4.1.4 Gear Meshing Element

(1) Helical cylindrical gear meshing element

Figure 4.4 shows the dynamic model of helical gear, i and j are a pair of helical gears meshing with each other, its transverse pressure angle is $\alpha_{ij,}$ and helix angle is β_{ij} (definition: gear i is right hand if $\beta_{ij} > 0$, and gear i is left hand if $\beta_{ij} < 0$), where gear i is driving gear, the driving torque is $T_{i,}$ and j is driven gear; on the meshing surface, k_{ij} is meshing stiffness and c_{ij} is meshing damping; the direction angle of the gear ϕ_{ij} is the angle between the centerline of gear and the x-axis; ψ_{ij} is the direction angle from y-axis to meshing surface, and it is expressed as

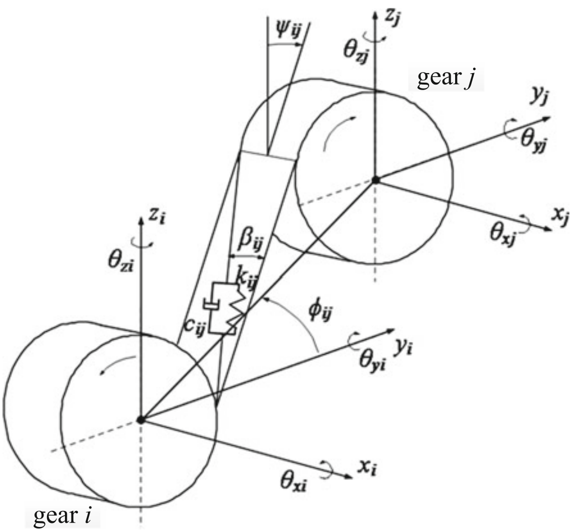

Fig. 4.4 The dynamic model of a helical gear pair

$$\psi_{ij} = \begin{cases} \alpha_{ij} - \phi_{ij} & \text{the torque on driving is counter - clockwise direction} \\ -\alpha_{ij} - \phi_{ij} & \text{the torque on driving is clockwise direction} \end{cases} \tag{4.8}$$

The degree of freedom of this gear pair is 12. Each gear has three translational degrees of freedom x, y, and z and three rotational degrees of freedom θ_x, θ_y, and θ_z, and degree of freedom is expressed as follows:

$$\mathbf{X}_{ij} = [x_i, y_i, z_i, \theta_{xi}, \theta_{yi}, \theta_{zi}, x_j, y_j, z_j, \theta_{xj}, \theta_{yj}, \theta_{zj}]^{\mathrm{T}} \tag{4.9}$$

The motion equation of gear pair ij is expressed as follows:

$$\begin{aligned} m_i\ddot{x}_i - [c_{ij}\dot{p}_{ij}(t) + k_{ij}p_{ij}(t)]\sin\beta_{ij} &= 0 \\ m_i\ddot{y}_i + [c_{ij}\dot{p}_{ij}(t) + k_{ij}p_{ij}(t)]\cos\beta_{ij}\sin\psi_{ij} &= 0 \\ m_i\ddot{z}_i + [c_{ij}\dot{p}_{ij}(t) + k_{ij}p_{ij}(t)]\cos\beta_{ij}\cos\psi_{ij} &= 0 \\ I_{pi}\ddot{\theta}_{xi} + r_i[c_{ij}\dot{p}_{ij}(t) + k_{ij}p_{ij}(t)]\cos\beta_{ij} &= T_i \\ I_{di}\ddot{\theta}_{yi} + r_i[c_{ij}\dot{p}_{ij}(t) + k_{ij}p_{ij}(t)]\sin\beta_{ij}\sin\psi_{ij} &= 0 \\ I_{di}\ddot{\theta}_{zi} + r_i[c_{ij}\dot{p}_{ij}(t) + k_{ij}p_{ij}(t)]\sin\beta_{ij}\cos\psi_{ij} &= 0 \\ m_j\ddot{x}_j + [c_{ij}\dot{p}_{ij}(t) + k_{ij}p_{ij}(t)]\sin\beta_{ij} &= 0 \\ m_j\ddot{y}_j - [c_{ij}\dot{p}_{ij}(t) + k_{ij}p_{ij}(t)]\cos\beta_{ij}\sin\psi_{ij} &= 0 \\ m_j\ddot{z}_j - [c_{ij}\dot{p}_{ij}(t) + k_{ij}p_{ij}(t)]\cos\beta_{ij}\cos\psi_{ij} &= 0 \\ I_{pj}\ddot{\theta}_{xj} - r_j[c_{ij}\dot{p}_{ij}(t) + k_{ij}p_{ij}(t)]\cos\beta_{ij} &= -T_j \\ I_{dj}\ddot{\theta}_{yj} - r_j[c_{ij}\dot{p}_{ij}(t) + k_{ij}p_{ij}(t)]\sin\beta_{ij}\sin\psi_{ij} &= 0 \\ I_{dj}\ddot{\theta}_{zj} - r_j[c_{ij}\dot{p}_{ij}(t) + k_{ij}p_{ij}(t)]\sin\beta_{ij}\cos\psi_{ij} &= 0 \end{aligned} \tag{4.10}$$

where $p_{ij}(t)$ represents the displacement deformation of gear teeth along the meshing line, mainly consists of four parts, namely deformation caused by gear on the torsion p_{ijr}, deformation caused by transverse vibration p_{ijl}, deformation caused by axial vibration $p_{ija,}$ and deformation caused by the swing around diameter p_{ijt}, and it is expressed as follows:

$$p_{ij}(t) = p_{ijr} + p_{ijl} + p_{ija} + p_{ijt} \tag{4.11}$$

where the deformation of gear teeth along the direction of the meshing line caused by axial vibration can be expressed as follows:

$$p_{ija} = (-x_i + x_j)\sin\beta_{ij} \tag{4.12}$$

The deformation along the direction of the meshing line caused by transverse vibration can be expressed as follows:

$$p_{ijl} = [(y_i - y_j) sin\psi_{ij} + (z_i - z_j)\cos\psi_{ij}]\cos\beta_{ij} \tag{4.13}$$

The deformation of gear teeth along the direction of the meshing line caused by torsional vibration around rotating shaft can be expressed as follows:

$$p_{ijr} = \cos\beta_{ij}(r_i\theta_{xi} - r_j\theta_{xj}) \tag{4.14}$$

The deformation of gear teeth along the direction of the meshing line caused by the swing around diameter can be expressed as follows:

$$p_{ijt} = ((r_i\theta_{yi} + r_j\theta_{yj})\sin\psi_{ij} + (r_i\theta_{zi} + r_j\theta_{zj})\cos\psi_{ij})\sin\beta_{ij} \tag{4.15}$$

where r_i and $r_{j,}$ respectively, represent base circle radius of gear i and gear j.

For the gear meshing element, Eq. (4.10) can be organized as a matrix as follows:

$$\boldsymbol{M}_{ij}\ddot{u} + \mathbf{C}_{ij}\dot{\mathbf{u}} + \mathbf{K}_{ij}\mathbf{u} = \boldsymbol{F} \tag{4.16}$$

where $\boldsymbol{F}$ represents generalized force vector of gear element, $\boldsymbol{u}$ represents displacement vector of gear pair, and $\boldsymbol{M}_{ij}$, $\boldsymbol{C}_{ij}$, and $\boldsymbol{K}_{ij,}$ respectively, represent mass matrix, damping matrix, and meshing stiffness matrix of gear element and are expressed as follows:

$$\mathbf{u} = [u_i, v_i, w_i, \theta_{xi}, \theta_{yi}, \theta_{zi}, u_j, v_j, w_j, \theta_{xj}, \theta_{yj}, \theta_{zj}]^{\mathrm{T}} \tag{4.17}$$

$$\mathbf{M}_{ij} = \begin{pmatrix}
m_i &&&&&&&&&&& \\
& m_i &&&&&&&&&& \\
&& m_i &&&&&&&&& \\
&&& J_i &&&&&&&& \\
&&&& I_i &&&&&&& \\
&&&&& I_i &&&&&& \\
&&&&&& m_j &&&&& \\
&&&&&&& m_j &&&& \\
&&&&&&&& m_j &&& \\
&&&&&&&&& J_j && \\
&&&&&&&&&& I_j & \\
&&&&&&&&&&& I_j
\end{pmatrix}$$

$$\mathbf{C}_{ij} = c_{ij} \cdot \mathbf{a}_{ij}^{\mathrm{T}} \cdot \mathbf{a}_{ij} = \begin{pmatrix} c_{1,1} & \cdots & c_{1,12} \\ \vdots & \ddots & \vdots \\ c_{12,1} & \cdots & c_{12,12} \end{pmatrix},$$

$$\mathbf{K}_{ij} = k_{ij} \cdot \mathbf{a}_{ij}^{\mathrm{T}} \cdot \mathbf{a}_{ij} = \begin{pmatrix} k_{1,1} & \cdots & k_{1,12} \\ \vdots & \ddots & \vdots \\ k_{12,1} & \cdots & k_{12,12} \end{pmatrix},$$

where

$$\begin{aligned}\mathbf{a}_{ij} = [&-\sin\beta_{ij} \quad \sin\psi_{ij}\cos\beta_{ij} \quad \cos\psi_{ij}\cos\beta_{ij} \quad \mathrm{sgn}r_i\cos\beta_{ij} \quad \mathrm{sgn}r_i\sin\psi_{ij}\sin\beta_{ij} \quad \mathrm{sgn}r_i\cos\psi_{ij}\sin\beta_{ij} \\ &\sin\beta_{ij} \quad -\sin\psi_{ij}\cos\beta_{ij} \quad -\cos\psi_{ij}\cos\beta_{ij} \quad \mathrm{sgn}r_j\cos\beta_{ij} \quad \mathrm{sgn}r_j\sin\psi_{ij}\sin\beta_{ij} \quad \mathrm{sgn}r_j\cos\psi_{ij}\sin\beta_{ij}]\end{aligned}$$

Meshing stiffness k_{ij} is comprehensive effect of meshing gear teeth in the whole meshing zone. In the linear analysis, the average meshing stiffness can be used as its value. The expression of average meshing stiffness for spur gear and helical gear with helix angle $\beta \leq 30°$ is given in the reference.

$$k_{\mathrm{ij}} = c_{\gamma}B \tag{4.18}$$

where B represents gear thickness and c_{γ} represent average meshing stiffness of gear along the direction of tooth width on unit length. The unit is N mm^{-1} μm^{-1}. It is expressed as follows:

$$c_{\gamma} = (0.75\varepsilon_a + 0.25)c' \tag{4.19}$$

where ε_a is transverse contact ratio, and c' is stiffness of single tooth and is expressed as follows:

$$c' = c'_{\mathrm{th}}C_M C_R C_B \cos\beta \tag{4.20}$$

where c'_{th} is theoretical value of stiffness of single tooth, $c'_{\mathrm{th}} = 1/q'$. For external meshing gear, the equivalent tooth number of pinion and big gear is known as z_{n1} and z_{n2}, modification coefficients are known as x_1 and x_2, and q' can be expressed as

$$\begin{aligned}q' =&0.04723 + \frac{0.15551}{z_{n1}} + \frac{0.25791}{z_{n2}} - 0.00635x_1 - 0.11654\frac{x_1}{z_{n1}} \\ &- 0.00193x_2 - 0.24188\frac{x_2}{z_{n2}} + 0.00529x_1^2 + 0.00182x_2^2\end{aligned} \tag{4.21}$$

where C_M is theoretical correction coefficient, and the general value is $C_M = 0.8$.

C_R is gear billets structure coefficient; for solid gear, the value is $C_R = 1$.

C_B is basic tooth profile coefficient, $C_B = [1 + 0.5(1.2 - h_{fp}/m_n)][1 - 0.02(20° - \alpha_n)]$; for the standard gear that basic tooth profile meets $\alpha = 20°$, $h_{fp} = 1.2m_n$, the value of C_B is 1.

Fig. 4.5 The dynamic diagram of gear coupling

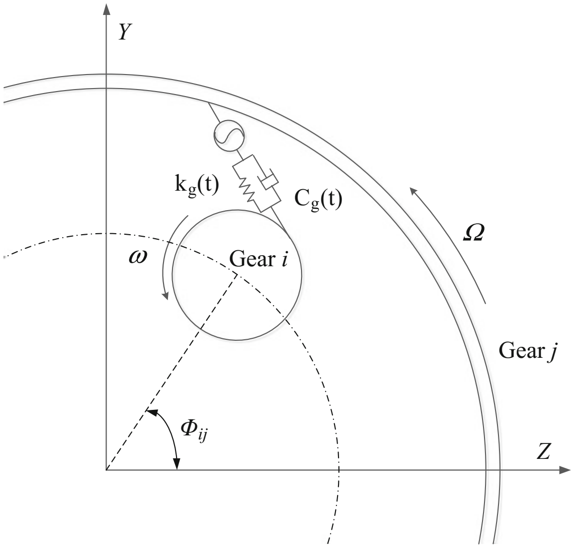

(2) Internal mesh spur gear mesh element

The dynamic effect of gear mesh can be approximately equivalent to spring damping element. The big gear and the drive pinion are coupled through the gear mesh stiffness; schematic diagram of coupling dynamics is shown in Fig. 4.5.

Comprehensive mesh stiffness of gear teeth k_g is comprehensive effect of the gear teeth involved in meshing in the whole meshing zone, mainly related to the elastic deformation of the single tooth, comprehensive elastic deformation of single gear pair(comprehensive stiffness), and gear contact ratio. In the research of gear deformation, the most widely used is the Ishikawa formula.

$$k_g = \frac{F_{\text{mesh}}}{\delta_{Br} + \delta_{Bt} + \delta_s + \delta_G} \tag{4.22}$$

where δ_{Br} is bending deformation of rectangular section, δ_{Bt} is bending deformation of trapezoid section, δ_s is deformation caused by shearing, and δ_G is deformation caused by elastic tilt on the root of gear tooth.

Supposing the nodes of mesh gear pair are i and j, i is on pinion, comprehensive mesh stiffness of gear pair on the mesh area is kg, and the direction angle of the gear ϕ_{ij} is the angle between the centerline of gear and the y-axis; ψ_{ij} is the angle from z-axis to mesh surface, and it is defined as follows:

$$\psi_{ij} = \begin{cases} \alpha_{ij} - \phi_{ij} & \text{the torque on driving is counter - clockwise direction} \\ -\alpha_{ij} - \phi_{ij} & \text{the torque on driving is clockwise direction} \end{cases} \tag{4.23}$$

where α_{ij} is transverse pressure angle of gear pair.

Symbolic function sgn is defined as

$$\mathrm{sgn} = \begin{cases} 1 & \text{the driving gear is counter - clockwise direction} \\ -1 & \text{the driving gear is clockwise direction} \end{cases} \tag{4.24}$$

One gear pair has 12 degrees of freedom. Each gear has three translational degrees of freedom including x-axis direction as well as transverse of the y and z directions and three rotational degrees of freedom θ_x, θ_y, and θ_z. For gear pair i and j, motion equation without damping can be expressed as follows:

$$\begin{array}{lll} m_i\ddot{y}_i + k_{ij}p_{ij}(t)\sin\psi_{ij} = 0; & m_i\ddot{z}_i + k_{ij}p_{ij}(t)\cos\psi_{ij} = 0; & J_i\ddot{\theta}_{xi} + \mathrm{sgn}r_ik_{ij}p_{ij}(t) = T_i \\ m_j\ddot{y}_j - k_{ij}p_{ij}(t)\sin\psi_{ij} = 0; & m_j\ddot{z}_j - k_{ij}p_{ij}(t)\cos\psi_{ij} = 0; & J_j\ddot{\theta}_{xj} + \mathrm{sgn}r_jk_{ij}p_{ij}(t) = -T_j \end{array};$$

where $p_{ij}(t)$ represent relative position from normal direction of gear mesh to contact surface and expressed as

$$\begin{aligned} p_{ij}(t) = {} & \left(y_i\sin\psi_{ij} - y_j\sin\psi_{ij} + z_i\cos\psi_{ij} - z_j\cos\psi_{ij} + \mathrm{sgn}r_i\theta_{xi} + \mathrm{sgn}r_j\theta_{xj}\right) \\ & + \left(-x_i + x_j + \mathrm{sgn}r_i\theta_{yi}\sin\psi_{ij} + \mathrm{sgn}r_j\theta_{yj}\sin\psi_{ij} + \mathrm{sgn}r_i\theta_{zi}\cos\psi_{ij} + \mathrm{sgn}r_j\theta_{zj}\cos\psi_{ij}\right) \end{aligned}$$

Above equation can be organized as a matrix as follows:

$$\mathbf{K}_{ij}\mathbf{u} = \boldsymbol{F} \tag{4.25}$$

where $\boldsymbol{F}$ represents generalize force vector of gear element, $\boldsymbol{u}$ represents displacement vector of gear pair, and $\boldsymbol{K}_{ij}$ represent mesh stiffness matrix of gear element and are expressed as follows:

$$\mathbf{u} = [u_i, v_i, w_i, \theta_{xi}, \theta_{yi}, \theta_{zi}, u_j, v_j, w_j, \theta_{xj}, \theta_{yj}, \theta_{zj}]^{\mathrm{T}}$$

$$\mathbf{K}_{ij} = k_{ij}\cdot\mathbf{a}_{ij}^{\mathrm{T}}\cdot\mathbf{a}_{ij} = \begin{pmatrix} k_{1,1} & \cdots & k_{1,12} \\ \vdots & \ddots & \vdots \\ k_{12,1} & \cdots & k_{12,12} \end{pmatrix} \tag{4.26}$$

where

$$\mathbf{a}_{ij} = [\,0 \quad \sin\psi_{ij} \quad \cos\psi_{ij} \quad \mathrm{sgn}r_i \quad 0 \quad 0 \quad 0 \quad -\sin\psi_{ij} \quad -\cos\psi_{ij} \quad \mathrm{sgn}r_j \quad 0 \quad 0\,]$$

4.1.5 Basic Principles and Dynamics Model

Based on equivalent virtual shaft section method, hybrid model including various influence factors is built. Method of control variable analysis is used to study the sensitivity of system vibration to each influence factor and the influence of various factors on the system vibration. Research technical route is shown in Fig. 4.6.

A hierarchical model of gear mesh system is established. The multistage planetary gear pair is decomposed into multiple independent subsystems, and intermediate shaft connection element is used to couple boundary among the mechanical simplified model of various subsystems. Based on the mechanical simplified model, the lumped mass model of the whole gear system with less degree of freedom is established. Based on component composition, lumped mass model divides the system into a number of lumped mass which are connected by springs and dampers; the degree of freedom is determined by the complexity of the structure and the dynamics of the problem. By solving lumped mass model, transient response time series of the lumped mass points are obtained, and transient loads of every moment are obtained from the time series. Considering the coupling of the pinion and ring gear mesh among the component and using the three-dimensional finite element, the three-dimensional Timoshenko beam element, and the analytical model, the multibody model of the gear-rotor system is established. The transient load obtained from the calculation of lumped mass model is loaded into a multibody mixture model, and then, the nonlinear static analysis is carried out to obtain the instantaneous stress and deformation of the key parts, especially the joint parts under the condition of multicause excitation. Based on the boundary condition of the joint, the stiffness and damping of the joint parts under the multifactors are calculated

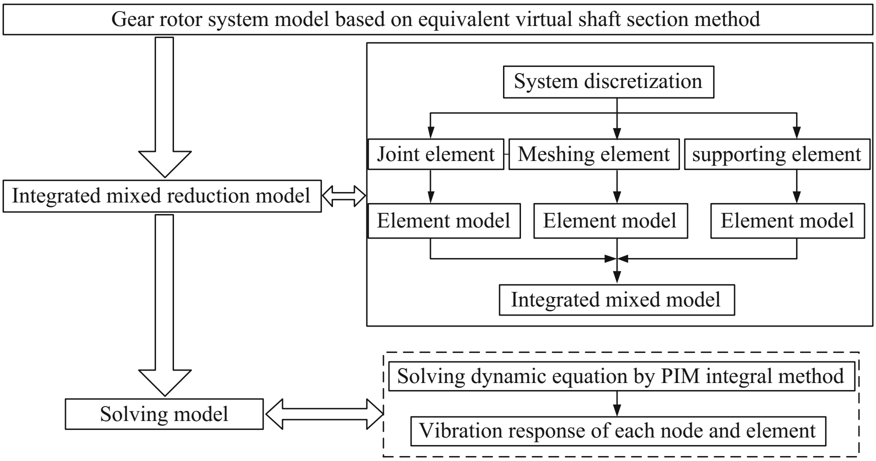

Fig. 4.6 Basic modeling idea

explicitly, and the coupling vibration characteristics of the composite structure are analyzed.

Aimed at a certain type of wind turbine gearbox system, its structure is similar to Fig. 3.2. The gears are spur gears, the mesh angle of gear pair is 20, and the main parameters are defined as in Tables 4.1 and 4.2.

Table 4.1 Main design parameters of planetary gear train

The first-stage planetary gear train		The second-stage planetary gear train	
Name	Parameter	Name	Parameter
Transmission ratio	3.9:1	Transmission ratio	3.52:1
Number of planetary gear	3	Number of planetary gear	4
The module of sun gear	5	The module of sun gear	4
The module of planetary gear	5	The module of planetary gear	4
The module of internal gear	5	The module of internal gear	4
Number of sun gear tooth	20	Number of sun gear tooth	25
Number of planetary gear tooth	19	Number of planetary gear tooth	19
Number of internal gear tooth	58	Number of internal gear tooth	63
Tooth width/mm	50	Tooth width/mm	50
The mass of sun gear/Kg	4.8	The mass of sun gear/Kg	3
The mass of planetary gear/Kg	2.8	The mass of planetary gear/Kg	2.7
The mass of internal gear/Kg	8	The mass of internal gear/Kg	8
The mass of planetary shelf/Kg	5	The mass of planetary shelf/Kg	5
Rotational inertia of sun gear/Kgm^2	0.09	Rotational inertia of sun gear/Kgm^2	0.04
Rotational inertia of planetary gear/Kgm^2	0.03	Rotational inertia of planetary gear/Kgm^2	0.03
Rotational inertia of internal gear/Kgm^2	0.2	Rotational inertia of internal gear/Kgm^2	0.2
Rotational inertia of planetary shelf/Kgm^2	0.08	Rotational inertia of planetary shelf/Kgm^2	0.08
Diameter rotational inertia of sun gear/Kgm^2	0.06	Diameter rotational inertia of sun gear/Kgm^2	0.025
Diameter rotational inertia of planetary gear/Kgm^2	0.02	Diameter rotational inertia of planetary gear/Kgm^2	0.02
Diameter rotational inertia of internal gear/Kgm^2	0.1	Diameter rotational inertia of internal gear/Kgm^2	0.1
Diameter rotational inertia of planetary shelf/Kgm^2	0.05	Diameter rotational inertia of planetary shelf/Kgm^2	0.05

Table 4.2 The main design parameters of spur gear pair

Design parameters	Gear 7	Gear 8
Module	4	
Tooth width/mm	40	
Number of gear tooth	68	17
Mass/Kg	5	2.7
Rotational inertia/Kgm^2	0.14	0.03
Diameter rotational inertia/Kgm^2	0.08	0.02

4.2 Load-Sharing Coefficient Analyses

4.2.1 Load-Sharing Coefficient of Planetary Gear Trains

Using the dynamic model established and considering the dynamic stiffness of gear meshing and the change of transmission error, load-sharing coefficient of planetary gear and sun gear in the two-stage planetary gear trains is obtained as shown in Fig. 4.7. Influenced by internal incentive of gear mesh, load-sharing coefficient of planetary gear is not a fixed value, but a value of periodic fluctuation.

4.2.2 Influence of Unbalance on Load-Sharing Coefficient

In the practical manufacturing, unbalance of rotor system is unable to eliminate, and its existence has significant influence on load-sharing coefficient of planet gear [5–8]. Using the data in Table 4.3, the influence of unbalance value on planet gear is analyzed, and the result is shown in Fig. 4.8.

As the result shows, unbalance value increases the amplitude of the average load coefficient of the planetary gear and makes the average load coefficient more complex; the waveform is coupled of multiharmonics. This result shows that the

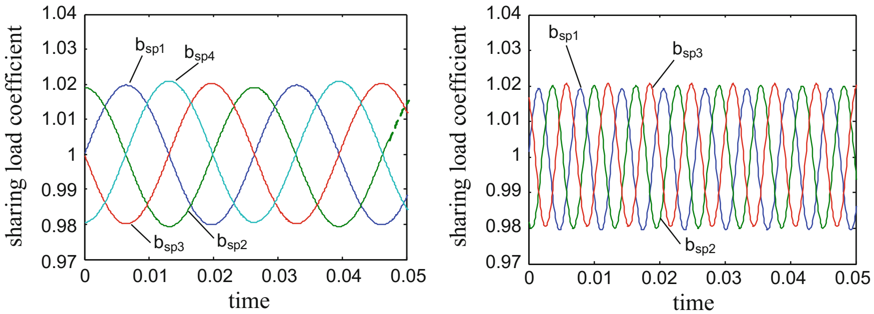

(a) The second stage planetary gear train (b) The first stage planetary gear train

Fig. 4.7 Sharing load coefficient of planetary gear train

Table 4.3 Unbalance value of gear system

Node position	Unbalance value (gmm)	Phase of unbalance value (rad)
1	1500	0
8	1000	0

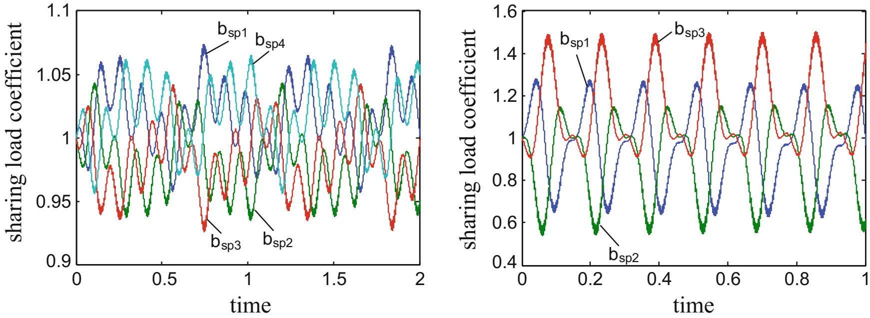

(a) The second stage planetary gear train (b) The first stage planetary gear train

Fig. 4.8 Sharing load coefficient of planetary gear train under the influence of unbalance

unbalance value of rotor system increases the uneven degree of load distribution and is bad for transmission performance of planetary gear transmission system.

4.2.3 Influence of Misalignment on Load-Sharing Coefficient

As shown in Fig. 4.9a, the misalignment angle at the coupling part of two planetary gear train is set as α. Let one shaft axis is projected to the yz plane, and the angle of axis of projection y-axis stands by angle β, as shown in Fig. 4.9b. Torque $\boldsymbol{T}$ can be decomposed into two components T_x and T_s, and can be expressed as follows [9, 10]:

$$T_x = T\cos\alpha, \quad T_s = T\sin\alpha \tag{4.27}$$

where T_x is the torque transmitted to the rotor, and T_s is the torque vertical to the rotor radial direction, which can cause the bending vibration of the rotor.

As shown in Fig. 4.9b, T_s also can be decomposed into two bending moments in y-axis and z-axis directions as follows:

$$T_y = T\sin\alpha\cos\beta, \quad T_z = T\sin\alpha\sin\beta \tag{4.28}$$

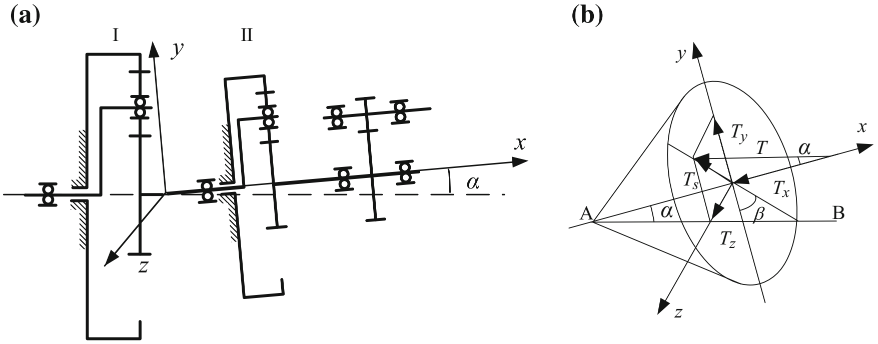

Fig. 4.9 Torque decomposition of misalignment rotor system

Then, T_x, T_y, and T_z can also be calculated from the Euler's equation of the motion

$$\begin{aligned} T_x &= I_x\dot{\omega}_x + \omega_y\omega_z\left(I_z - I_y\right) \\ T_y &= I_y\dot{\omega}_y + \omega_z\omega_y(I_x - I_z) \\ T_z &= I_z\dot{\omega}_z + \omega_x\omega_y\left(I_y - I_x\right) \end{aligned} \tag{4.29}$$

where ω_i is the rotor angular velocity, I_i is the rotational inertia of the rotor around i-axis, and $i = x, y, z$.

Because of the rotation of the rotor only around the x-axis, Eq. (4.29) can be simplified as

$$T\cos\alpha = I_R\varepsilon_R \tag{4.30}$$

where I_R is the polar moment of inertia of rotor, and ε_R is the angular acceleration of rotor.

For the rotor with angle α, the angular velocity meets the following relation.

$$\omega_R/\omega_M = C/(1 + D\cos 2\theta_M) \tag{4.31}$$

where $C = 4\cos\alpha/(3 + \cos 2\alpha)$, $D = (1 - \cos\alpha)/(3 + \cos 2\alpha)$.

Equation (40) can be expanded as follows:

$$\omega_R/\omega_M = A_0 - A_2\cos 2\theta_M + A_4\cos 4\theta_M - \cdots + (-1)^n A_{2n}\cos 2n\theta_M + \cdots \tag{4.32}$$

where ω_M is the input shaft angular velocity, θ_M is the input shaft angle, and ω_R is the output shaft angular velocity.

$$
\begin{aligned}
&A_0 = C\left(1 + D^2/2 + 3D^4/8 + 5D^6/16 + 35D^8/128 + \cdots\right) = 1 \\
&A = C\left(D + 3D^3/4 + 5D^5/8 + 35D^7/64 + \cdots\right) \\
&A_4 = C\left(D^2/2 + D^4/2 + 15D^6/32 + 7D^8/16 + \cdots\right) \\
&\cdots
\end{aligned}
$$

Equation (4.32) can be rewritten as

$$\varepsilon_R/\omega_M^2 = B_2 \sin 2\theta_M - B_4 \sin 4\theta_M + \cdots + (-1)^{n+1} B_{2n} \sin 2n\theta_M + \cdots \tag{4.33}$$

where n = 1, 2, 3..., $B_2 = 2A_2$, $B_4 = 4A_4$, $B_6 = 6A_6 \ldots$

Defining $\theta_M = \Omega t$, the transfer torque can be obtained From Eqs. (4.30) and (4.33)

$$T = \left(I_R \Omega^2 / \cos \alpha\right)\left(\sum_{n=1}^{\infty} (-1)^{n+1} B_{2n} \sin 2n\Omega t\right) \tag{4.34}$$

Equation (4.28) can be expressed as

$$T_y = \sum_{n=1}^{\infty} E_{2n} \sin 2n\Omega t, \quad T_z = \sum_{n=1}^{\infty} G_{2n} \sin 2n\Omega t \tag{4.35}$$

where $E_{2n} = (-1)^{n+1} I_R \Omega^2 B_{2n} \tan\alpha \cos\beta$, $G_{2n} = (-1)^{n+1} I_R \Omega^2 B_{2n} \tan\alpha \sin\beta$.

Therefore, the transfer misalignment force $\boldsymbol{F}_r$ is obtained as follows:

$$\mathbf{F}_r = \sum_{n=1}^{\infty} \mathbf{F}_{2n} \sin 2n\Omega t \tag{4.36}$$

where $F_{2n} = [0, \ldots, E_{2n}, G_{2n}]^{\mathrm{T}}$.

Selecting the misalignment angle 1°and 2.5°of two planetary gear trains, the influence of misalignment on average load coefficient of planetary gear train is analyzed, and the result is shown in Figs. 4.10 and 4.11.

As the result shows, in the same with unbalance value, misalignment also increases the amplitude of the average load coefficient of the planetary gear. With the increase in the misalignment angle, the amplitude variation increases with the geometric progression; meanwhile, compared with the second-stage planetary gear train, the influence of misalignment angle on average load coefficient of the first-stage planetary gear train is more sensitive.

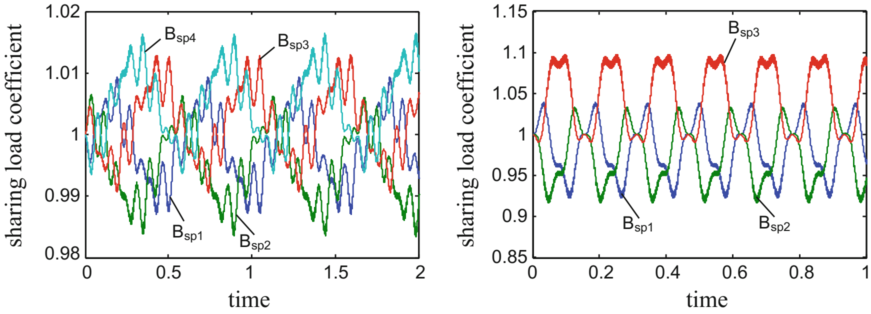

(a) The second stage planetary gear train (b) The first stage planetary gear train

Fig. 4.10 Sharing load coefficient of planetary gear train under the misalignment angle 1°

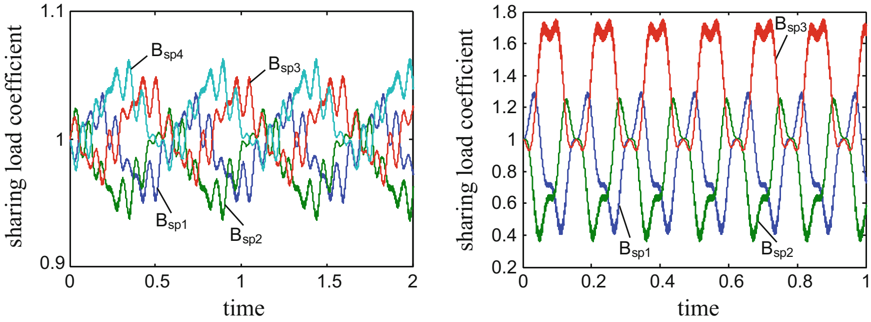

(a) The second stage planetary gear train (b) The first stage planetary gear train

Fig. 4.11 Sharing load coefficient of planetary gear train under the misalignment angle 2.5°

References

1. Kahrobaiyan MH, Asghari M, Ahmadian MT. A Timoshenko beam element based on the modified couple stress theory. Int J Mech Sci. 2014;79(2):75–83.
2. Ren Y, Zhang Y, Zhang X. Vibration and stability of internally damped rotating composite Timoshenko shaft. J VibroEng. 2015;17(8):4404–20.
3. Vosoughi AR. A developed hybrid method for crack identification of beams. Smart Struct Syst. 2015;16(3):401–14.
4. Izadparast AH, Niedzwecki JM. Comparison of moment-Based parameter estimation methods for Rayleigh-Stokes distribution of wave crests and troughs. Int J Offshore Polar Eng. 2013;22(3):200–8.
5. Kim JG, Lee GH, Park YJ, et al. Study of load distribution and sharing characteristics of planetary geartrain for wind turbines. Appl Mech Mater. 2011;86:674–9.
6. Singh A. Application of a system level model to study the planetary load sharing behavior. J Mech Des. 2005;127(3):469–76.
7. Singh A. Epicyclic load sharing map-development and validation. Mech Mach Theory. 2011;46(5):632–46.

8. Yu H, Eberhard P, Zhao Y, et al. Sharing behavior of load transmission on gear pair systems actuated by parallel arrangements of multiple pinions. Mech Mach Theory. 2013;65(65): 58–70.
9. Xu M, Marangoni RD. Vibration analysis of a motor-flexible coupling-rotor system subject to misalignment and unbalance, part I: theoretical model and analysis. J Sound Vib. 1994;176 (5):663–79.
10. Xu M, Marangoni RD. Vibration analysis of a motor-flexible coupling-rotor system subject to misalignment and unbalance, part II: experimental validation. J Sound Vib. 1994;176(5): 681–91.

Chapter 5

Modal Analyses Based on Whole Gearbox FE Model in Wind Turbine

Dynamic analysis result of the geared rotor system is always important in the wind turbine gearboxes' design stage, but there is sometimes great distinction between the calculation value and the real one because the wind turbine gearboxes is an integrated system, which is composed by many components besides the geared rotor. To improve the simulation precision, a reasonable modeling method of each component and connection method among components are needed. In this chapter, the whole gearbox finite element model is built and the natural characteristics (natural frequencies and mode shapes) of the whole gearbox are calculated.

5.1 FE Model of Transmission Chain System in Wind Turbine

According to the multilevel modeling strategy, the whole model for dynamic analysis of a wind turbine transmission chain can be expressed as shown in Fig. 5.1. It is a simplified model, which is used as a reference for coming modal analyses based on the whole gearbox finite element model (WG-FEM), where the other components besides the geared rotor and the contact mechanics model are considered [1, 2].

According to the whole model, the natural frequencies of the transmission chain system of wind turbine are listed in Table 5.1.

The modal energy distributions of the system are different on different modes. The modal energy distribution analysis can help to find out which part of the transmission chain system is sensible effectively. As shown in Fig. 5.2, the modal energy distributions of the 1st mode and 14th mode are quite different.

Q. Han et al., *Dynamics and Vibration Analyses of Gearbox in Wind Turbine*,
DOI 10.1007/978-981-10-2747-5_5

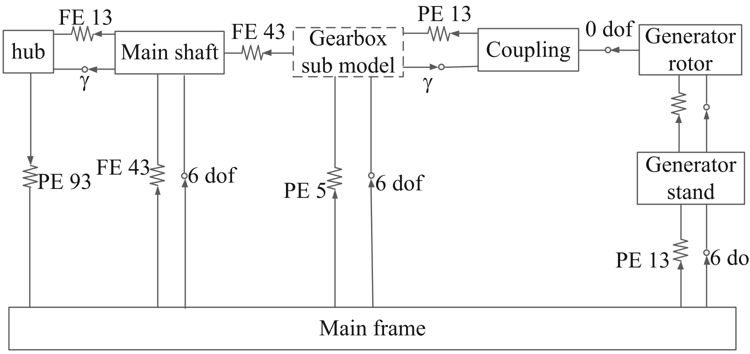

Fig. 5.1 Whole model of a transmission chain

Table 5.1 Nature frequencies of the wind turbine transmission chain

Order	1	2	3	4	5	6	7
Natural frequency/Hz	1.72	9.10	184.18	224.36	419.49	663.59	894.6
Order	8	9	10	11	12	13	14
Natural frequency/Hz	1028.3	1125.49	1318.12	1343.6	1401.97	1537.9	1621.71

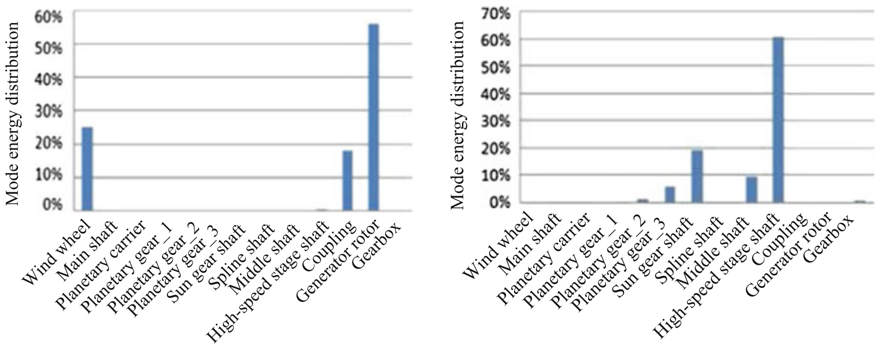

(a) The 1st mode (b) The 14th mode

Fig. 5.2 The modal energy distribution of the transmission chain based on whole model

5.2 Whole Gearbox FE Model (WG-FEM) of Wind Turbine

The wind turbine gearbox is modeled by using finite element method in which the rotor systems and substructures are all included. The bearings are equivalently modeled by linear spring elements in which extending lines go through the shaft cross sections and fix on both sides of the housing shells. The whole gearbox model

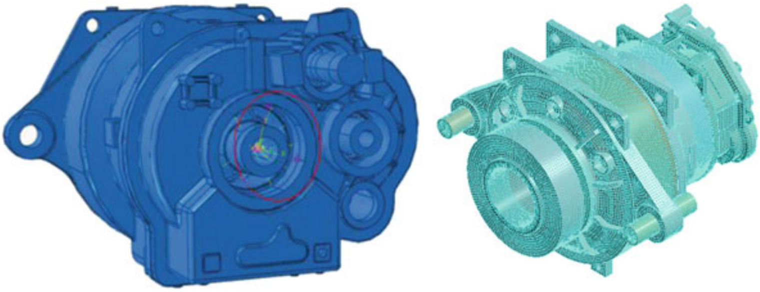

Fig. 5.3 Bearing element and WG-FEM of gearbox

Table 5.2 Bearing stiffnesses of the gearbox

Bearing position		Lateral stiffness (N/m)	Axial stiffness (N/m)
The 1st stage	Driving shaft	5.389×10^9	8.542×10^8
	Driven shaft	2.718×10^{10}	2.692×10^9
The 2nd stage	Driving shaft	6.101×10^9	1.396×10^9
	Driven shaft	6.382×10^9	1.904×10^9
High-speed stage	Driving shaft	3.960×10^9	0
	Driven shaft	3.973×10^9	0

is then achieved by coupling of the above sub-systems for dynamic analyses. The obtained WG-FEM is shown in Fig. 5.3. The stiffness values of the bearings are shown in Table 5.2.

5.3 Modal Analysis of the Gearbox

Based on the above WG-FEM, the modal analysis of the gearbox is achieved, and the obtained natural frequencies and mode shapes are shown in Table 5.3 and Fig. 5.4, where the first 20 modes are listed. It can be found that, different from the torsional dynamic model in previous section, more modes are obtained by using the WG-FEM, which is important for detecting substructure coupling of the gearbox.

Table 5.3 Natural frequencies based on WG-FEM of gearbox

Order	Natural frequency (Hz)	Mode shape description
1	25.5	The gearbox swings along the supporting shaft, the maximum deformation occurs at the long bushing at the output end
2	106.9	The gearbox swings from side to side, the maximum deformation occurs at the second stage planet frame
3	113	The long bushing deforms severely, the maximum deformation occurs at the middle of long bushing
4	115.9	The long bushing deforms severely, the maximum deformation occurs at the middle of long bushing
5	116.4	The gear-rotor system rotates, the maximum deformation occurs at the output gear
6	160.4	The gearbox swings up and down along the supporting shaft, the maximum deformation occurs at locking plate at the end of the input shaft
7	214.9	The gearbox swings from side to side, the maximum deformation occurs in the back cover
8	228.3	The output end deforms seriously, the maximum deformation occurs at the back cover of the box
9	241.5	The geared rotor system rotates, the maximum deformation occurs at tooth at the output end
10	266.4	The gearbox folds up and down, the maximum deformation occurs at the back cover of output end
11	304.3	The housing shell deforms locally, the maximum deformation occurs at the back cover
12	310.5	The output shaft deforms complexly, the maximum deformation occurs at the meshing place of the second stage sun wheel and the planet gear
13	312.1	The output shaft deforms complexly, the maximum deformation occurs at the meshing place of the first stage sun wheel and the planet gear
14	330.7	The output end deforms largely, the maximum deformation occurs at the back cover of the box
15	358.4	The output end deforms largely, the maximum deformation occurs at the back cover of the box
16	375.3	The geared rotor system deforms complexly, the maximum deformation occurs at the output end
17	382.7	The geared rotor system deforms complexly, the maximum deformation occurs at tooth of the high-speed stage
18	396.0	The output end deforms largely, the maximum deformation occurs at the back cover of the box
19	422.8	The output end deforms largely, the maximum deformation occurs at the back cover of the box
20	434.5	The geared rotor system rotates, the maximum deformation occurs at tooth at the output end

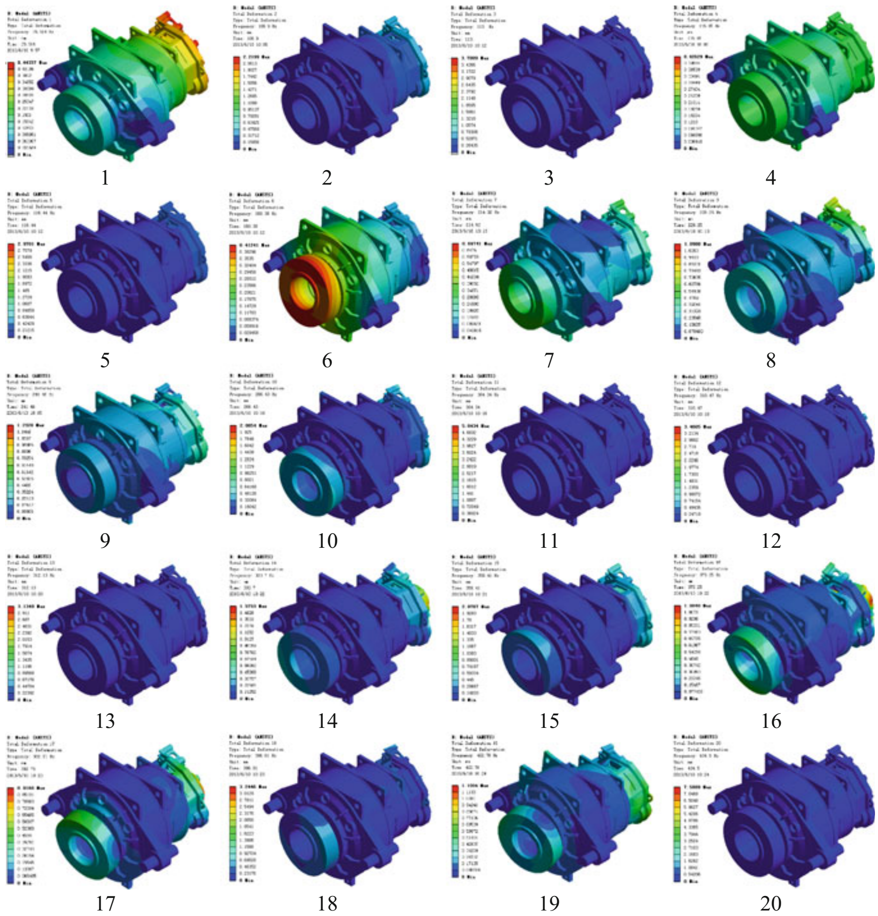

Fig. 5.4 The first 20 modes of the gearbox based on WG-FEM

References

1. Parker RG, Agashe V, Vijayakar SM. Dynamic response of a planetary gear system using a finite element/contact mechanics model. J Mech Des. 2000;122(3):304–10.
2. Thornton Earl A. The finite element method for engineers. USA: Wiley; 1982.

Chapter 6
Vibration Measurements of Wind Turbine Gearbox

Wind turbine manufacturers will conduct many product performance tests before on-site installation. Many wind turbine test platforms are built and used to support design in many companies all over the world, for example, the wind turbines test platform in Denmark Vestas Corporation, the wind turbine gearbox test platform in Hansen Corporation, and the 5 MW wind turbine transmission chain platform in Spain Center Corporation, which is equipped with a torque load simulator with five degrees of freedom. But these wind turbine test platforms are often lack of simulating the real working condition accurately, especially lack of measuring dynamic and fatigue data of structures inside the gearbox.

6.1 Bench Tests

In bench tests of wind turbine transmission chain, the dynamics and vibration characteristics, and the lifetime and reliability of the multistage planetary gear train are the most important tasks. At present, traditional transducers and sensors such as piezoelectric accelerators and strain gauges are used to measure signals of the gearbox. The transmission property, load characteristics, and vibration or noise of the gearbox are obtained by bench tests.

In order to predict the possible failures of gearbox, some tests with different faults are also carried out, such as the tooth crack and the tooth contact fatigue. The strain measurements of gear tooth surfaces and roots in rotating state are more important and challenging. The load and the mechanical properties in the process of continuous dynamic meshing, especially the tooth root bending stress testing, will be more valuable to grasp the dynamic deformation behavior and fatigue life of

Q. Han et al., *Dynamics and Vibration Analyses of Gearbox in Wind Turbine*,
DOI 10.1007/978-981-10-2747-5_6

Fig. 6.1 Bench test of a wind turbine gearbox

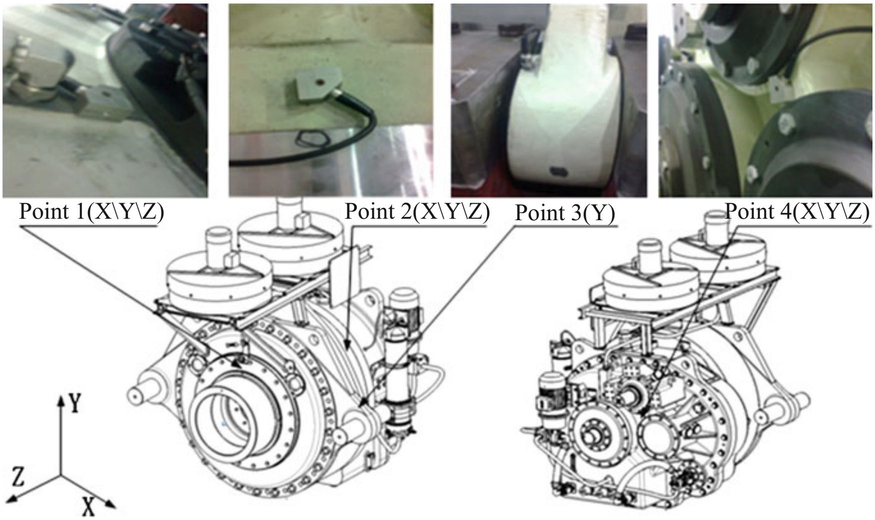

Fig. 6.2 Picking positions for vibration measurement on gearbox

gears. Recently, it was reported that the spiral gear tooth root bending stress had been measured by using the embedding strain gauges (the size is 0.38 mm). It is also known that the bending strains at gear tooth roots under static load are measured by using the embedding strain gauges with the help of wireless transducer. Here, the fiber Bragg strain sensors are used to measure the bending stresses of the tooth roots.

A bench test rig of wind turbine gearbox is shown in Fig. 6.1. The vibration measure positions are shown in Fig. 6.2.

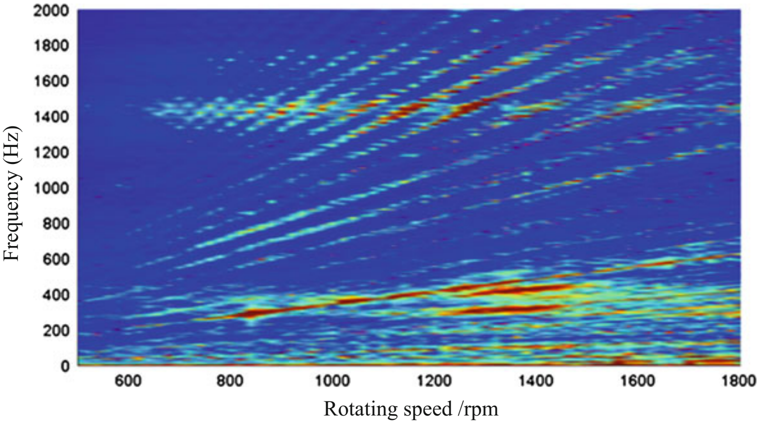

Fig. 6.3 3D spectra of vibrations at high-speed shaft

Table 6.1 Loading ratios in experiment

Speed (rpm)	Load (%)							
1000	0	20	40	60	80	–	–	–
1200	0	20	40	60	80	–	–	–
1300	0	20	40	60	80	100	–	–
1500	0	20	40	60	80	100	110	120
1600	0	20	40	60	80	100	110	120
1700	0	20	40	60	80	100	110	120
1790	0	20	40	60	80	100	110	120

The measured 3D spectra of the vibrations at the high-speed shaft are shown in Fig. 6.3. Given different loading ratios (listed in Table 6.1) and different rotating speeds, the measured vibration energy or severity values are plotted in Fig. 6.4.

It can be seen from the measured vibration signals at high-speed shaft that the vibration amplitudes are increased along the rotating speeds but not along the increment of the external loads. Only the vibration amplitudes increase slightly at the near 40 % rated load level.

6.2 Operating Modal Tests

In the modal analysis, it is needed to measure the data of reference points and response points of at the same time, and the testing points are selected as shown in Fig. 6.5, in which the numbers ‘1’–‘9’ indicate the points of putting accelerators, and the letter ‘F’ refers to the reference point. All the picking points are selected to ensure that interesting modes of the gearbox can be triggered. Before the modal test,

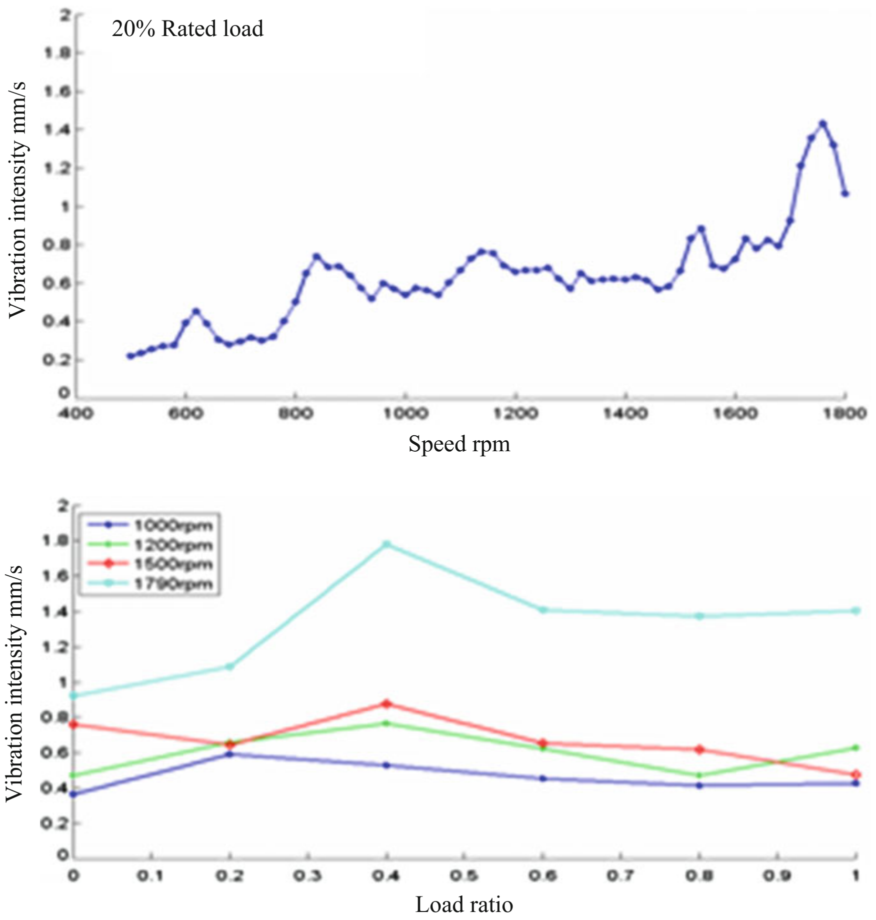

Fig. 6.4 Vibration energy

the structure analysis of gearbox is analyzed, and the natural frequencies and modes are calculated.

The acceleration responses of the 21 points in each condition are obtained; typical spectra are shown in Fig. 6.6.

From the spectra, it can be seen that the fundamental frequencies and their harmonics are obvious in many picking points. The signals are more complicated near the high-speed shaft. Besides, many vibrations are excited due to the housing shell coupling mechanism.

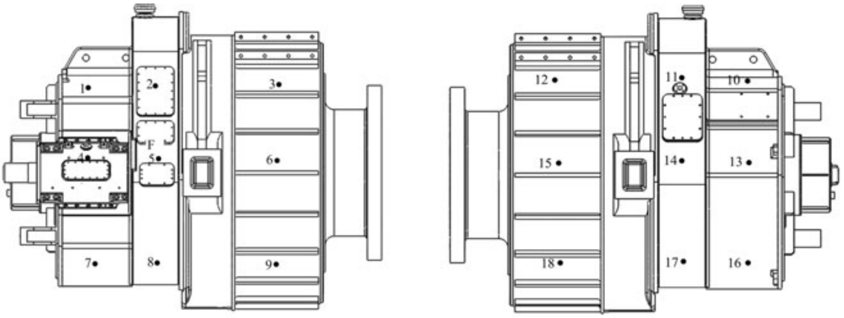

(a) The arrangement of testing points in frontage

(b) The arrangement of testing points in the reverse side

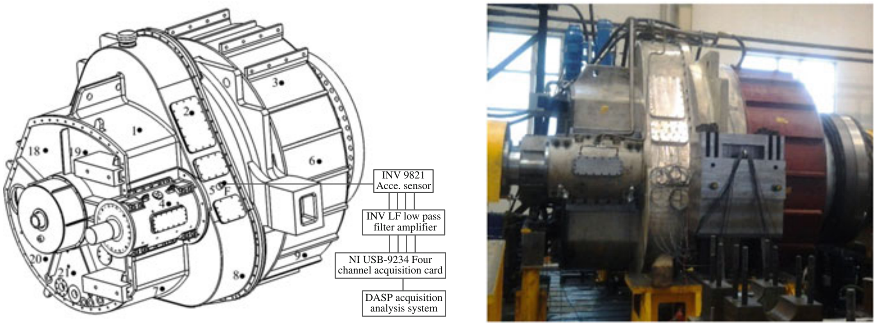

(c) The testing system

(d) Test site of 5MW wind turbine gearbox

Fig. 6.5 Arrangement of testing points in operating modal test. **a** The arrangement of testing points in frontage. **b** The arrangement of testing points in the reverse side. **c** The testing system. **d** Test site of 5 MW wind turbine gearbox

Using the least squares method in the complex frequency domain to perform modal analysis, the operation diagram of stable modal analysis is shown in Fig. 6.7. In Fig. 6.7, the letters ‘s’, ‘d’, ‘v’, ‘f’, and ‘o’ stand for the pole characteristics of different order calculation model correspondingly, where ‘s’ stands for the frequency, damping and modal are stable; ‘d’ stands for the frequency and damping are stable; ‘v’ stands for the frequency and vibration mode are stable; ‘f’ stands for the frequency is stable; ‘o’ stands for the ordinary poles. By selecting the pole ‘s’, much order modes are obtained.

The obtained natural frequencies under different load cases are listed in Table 6.2.

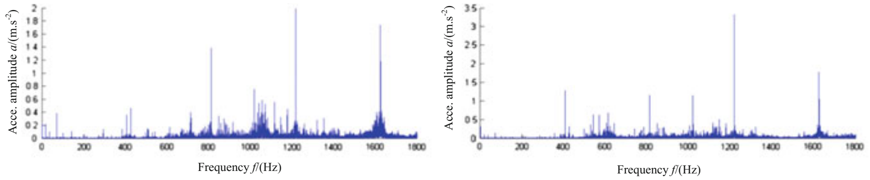

(a) Point 1

(b) Point2

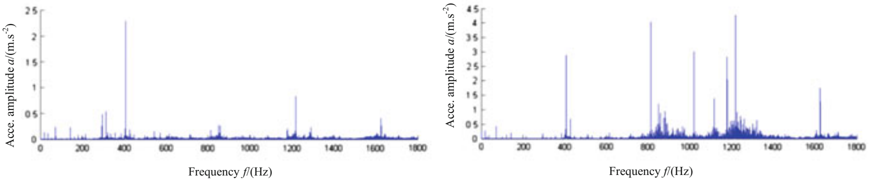

(c) Point 3

(d) Point4

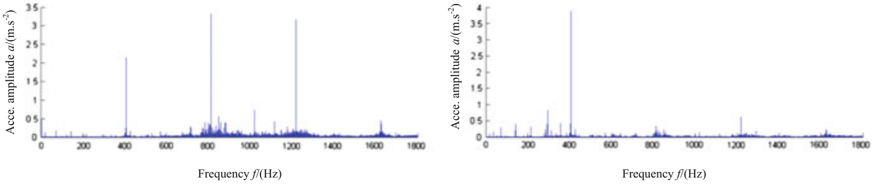

(e) Point 5

(f) Point6

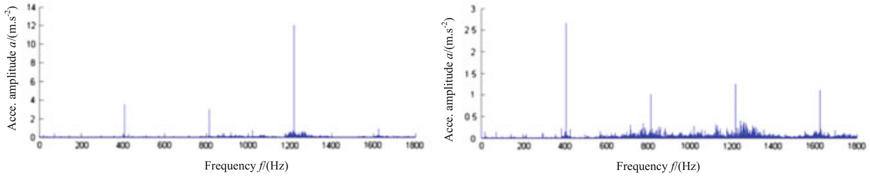

(g) Point 7

(h) Point8

Fig. 6.6 Acceleration spectra on the case of 100 % rated load. **a** Point 1. **b** Point 2. **c** Point 3. **d** Point 4. **e** Point 5. **f** Point 6. **g** Point 7. **h** Point 8

According to the identified results of natural frequencies as shown in Table 6.2, enough input load is needed to recognize more order natural frequency; namely, low-power input is not enough to trigger all natural frequencies. It is also found that the modal characteristics of the geared rotor system cannot easily be measured by testing on the housing shell.

Comparing the results of the finite element analysis with the test results of the whole gearbox, the mode frequencies results of the first 20 orders are shown in Table 6.3. The measured mode frequencies are lesser than the calculated results by using finite element method.

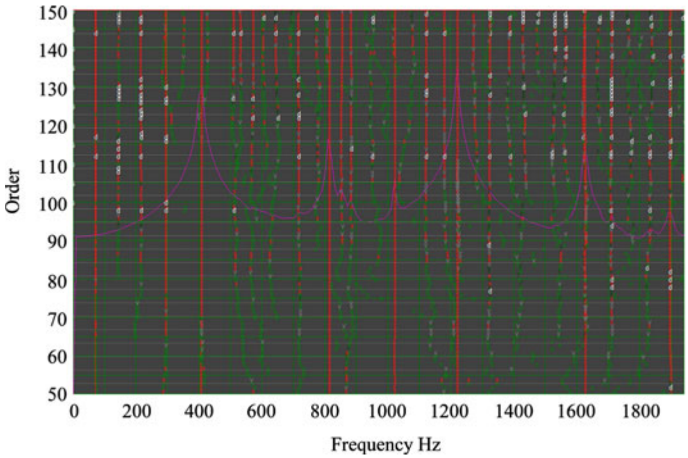

Fig. 6.7 Operation diagram of stable modal analysis

Table 6.2 Identified natural frequencies of the gearbox under different loads

Order	50 % load		75 % load		100 % load	
	Frequency (Hz)	Damping (%)	Frequency (Hz)	Damping (%)	Frequency (Hz)	Damping (%)
1	294.27	1.27	294.18	1.38	294.13	1.1
2	–	–	–	–	311.55	6.31
3	–	–	400.21	6.11	405.42	2.91
4	–	–	–	–	425.36	2.56
5	508.82	1.99	509.55	1.49	508.76	1.27
6	513.59	3.20	513.12	1.95	513.40	2.98
7	532.78	2.04	529.84	1.68	530.07	1.64
8	567.25	0.95	570.15	0.65	570.48	0.85
9	–	–	–	–	575.45	0.85
10	–	–	585.75	1.23	588.76	1.05
11	595.26	2.25	–	–	593.98	2.28
12	–	–	601.74	1.05	605.55	0.56

6.3 Vibrations of On-site Tests

The wind field tests on the 1.5 MW/2 MW wind power unit transmission chain are shown in Fig. 6.8. The testing points are shown in Fig. 6.9. The measured testing results of test point 5 are shown in Fig. 6.10.

Table 6.3 Comparison of modal frequency results with the measured and FEM

Order	FEM (Hz)	Test (Hz)	Errors (%)
1	220.550	–	–
2	227.657	–	–
3	268.695	–	–
4	302.756	294.127	2.93
5	320.590	–	–
6	340.622	311.553	9.33
7	438.303	405.418	8.11
8	446.255	425.358	4.91
9	471.031	–	–
10	493.814	508.758	2.94
11	517.864	513.404	0.87
12	547.183	530.070	3.22
13	565.099	570.484	0.94
14	580.953	575.451	0.96
15	587.886	588.762	0.15
16	591.478	–	–
17	596.098	593.982	0.36
18	600.371	–	–
19	630.985	–	–
20	656.754	605.552	8.45

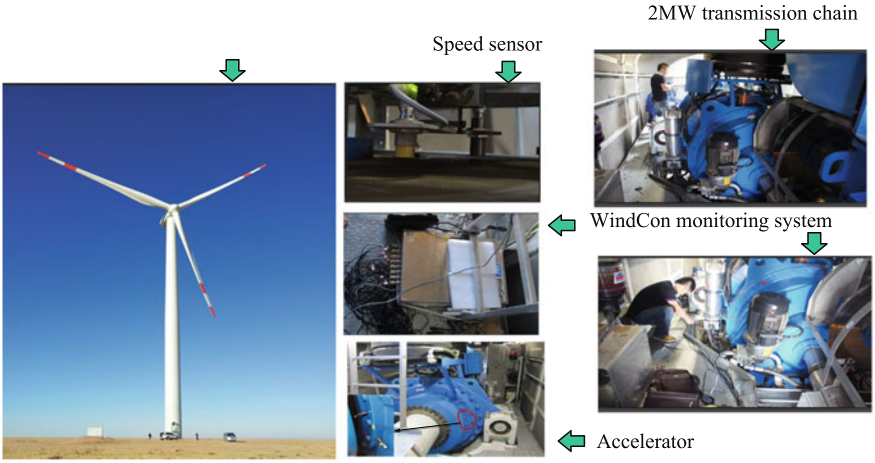

Fig. 6.8 Vibration test of the wind turbine transmission chain

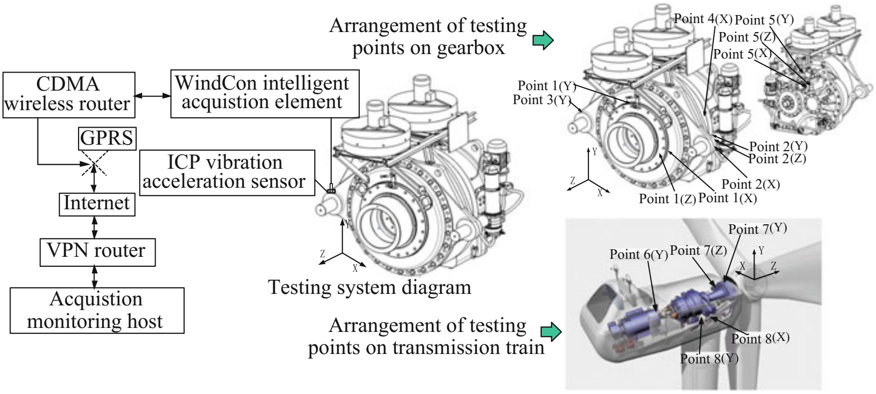

Fig. 6.9 Arrangement of testing points

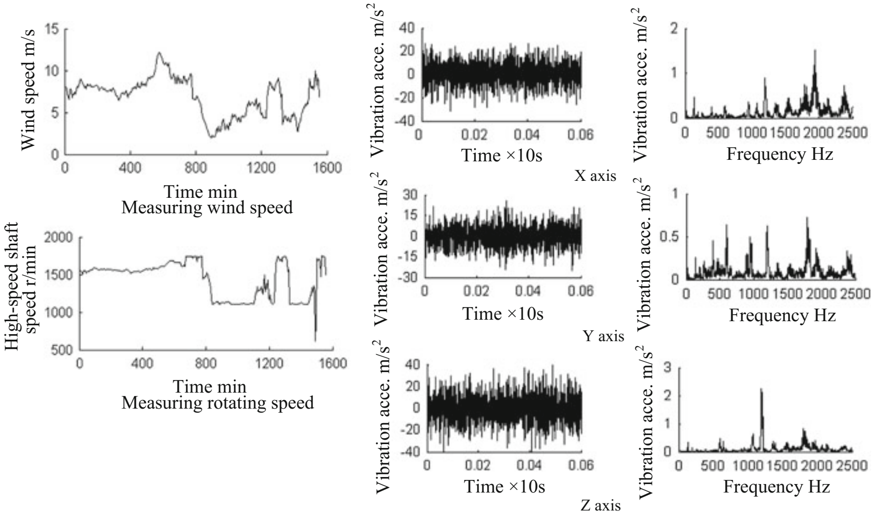

Vibration acceleration time domain curve and frequency spectrum at point 5

Fig. 6.10 Testing results at point 5

6.4 Fault Diagnoses for Wind Turbine Gearbox Based on Vibration Measurements

Vibration monitoring is one of the main technologies for condition monitoring and fault diagnosis of wind turbine [1, 2]. The typical vibration faults of the geared rotor systems and their main causes are listed in Table 6.4.

Based on the vibration test results of a wind turbine gearbox, the reason of the abnormal vibration is analyzed, considering the vibration data of gear case under

Table 6.4 Popular faults of gear system and their causes

Fault type	Causes	Time-domain features	Frequency-domain features
Uniform abrasion	Caused by the lubrication, material and other reasons or long-time high-work load	The backlash increases constantly, and the meshing waveform suffered some damage	Position of the meshing frequency and its harmonic components in the spectrum is the same, but their amplitude will change greatly. In particular, the harmonic amplitude will increase obviously. When the wear is intensified, it may produce the fractional harmonic $1/k(k = 2, 3, \cdots)$ of meshing frequency f_m
Eccentricity	Misalignment of the gear center and of rotating shaft center which is caused by processing	When a gear exists eccentric in the gear pair, the vibration waveform will produce amplitude vibration	The additional pulse amplitude which uses the rotation frequency of gear for the characteristics will increase, and the load fluctuation appears, which leads to the phenomenon of amplitude modulation. Frequency modulation for the time is gear-rotating frequency, lesser than the modulation meshing frequency
misalignment	Misalignment of gear and shaft caused by improper assembly of the gear and shaft	There is obvious phenomenon of amplitude modulation	It will produce side frequency clusters, with each order meshing frequency nf_m as its center, the rotation frequency of gear f_r as the interval, and the harmonic of f_r will also be reflected in the spectrum
Local anomaly	Broken teeth, tooth crack, partial tooth profile error, partial tooth wear, etc.	The time-domain vibration waveform is the shock pulse waveform which uses the rotation frequency of gear as the cycle	In the frequency domain, it will use instantaneous impact and rotation frequency as the main features
Pitch error	Each gear pitch is not equal and caused by tooth profile error	Effect of the change in gear rotation angle, resulting in AM and FM phenomenon	The frequency spectra of vibration signal contain the order meshing frequency nf_m, harmonics of rotation frequency nf_r, and the side frequency $nf_m \pm mf_r(n, m = 1, 2, \ldots)$, which uses rotation frequency of fault gear as spaced, etc.

(continued)

Table 6.4 (continued)

Fault type	Causes	Time-domain features	Frequency-domain features
Imbalance gear	Gear rotary center does not coincide with the center of mass	Vibration on unbalance force, in which amplitude modulation as based and frequency as a supplement	The meshing frequency f_m and its harmonics will produce side frequency cluster, in which frequency is $nf_m \pm mf_r(n, m = 1, 2, \ldots)$ on both sides. Under the unbalanced force, gear shaft rotation frequency and its harmonic energy will increase

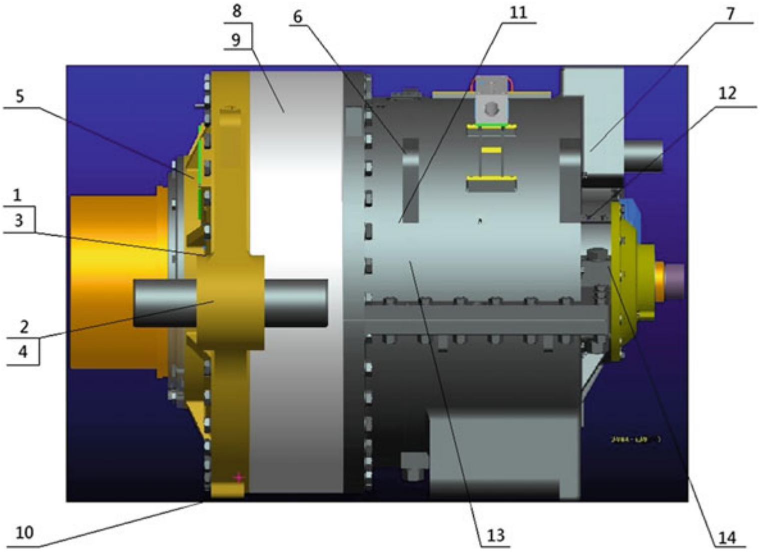

Fig. 6.11 Vibration monitoring points on a gearbox. *1* Vertical of the left flexible support, *2* horizontal of the left flexible support, *3* vertical of the right flexible support, *4* horizontal of the right flexible support, *5* vertical of the front bearing on input shaft, *6* horizontal of the front bearing of output shaft, *7* horizontal of the rear bearing of output shaft, *8* horizontal of the inner gear ring (*left*), *9* horizontal of the inner gear ring (*right*), *10* horizontal of the base horizontal, *11* vertical of the second-level active front bearing vertical, *12* vertical of the second-level active rear bearing, *13* vertical of the front bearing of intermediate shaft, *14* vertical of the rear bearing of intermediate shaft

the 100 % rated load can most effectively reflect the presence of faults in gearbox, as shown in Fig. 6.11. The vibration sensors are fixed as closely as possible to the measured objects and the rotating parts. The sampling frequency of vibration data is 10.24 kHz.

Table 6.5 Tooth number and the modulus of each gear

	Gear ring	Planet wheel	Sun wheel	Medium-speed shaft gear	Output gear shaft	Medium-speed gear shaft	Low-speed shaft gear
m	14	14	14	7	7	10	10
z	102	40	21	94	23	23	100

Table 6.6 Main existent frequencies of the gearbox (Hz)

High-speed shaft rotational frequency	Middle-speed shaft rotational frequency	Low-speed shaft rotational frequency	Planet carrier rotational frequency
30	7.343	1.69	0.2883
Gear meshing frequency of middle-to high-speed shaft	Gear meshing frequency of middle-to low-speed shaft	Meshing frequency of sun and planet gear	Meshing frequency of inner ring–planet gear
690.2	168.9	124.5	29.4

The input speed of the gearbox is 17.3 rpm and the output speed is 1800.55 rpm. The number of teeth and the modulus of each gear are shown in the Table 6.5.

The rotation and the revolution cycle frequency and the existent meshing frequency of each rotating parts are calculated and listed in Table 6.6.

Some of the measured vibrations (time-domain waveform and frequency-domain spectra) at the testing points in 100 % rated load are shown in Fig. 6.12.

Figure 6.12a is the signal of vibration at the testing point 2, which contains the frequency components of 30, 170, 690 Hz that reflect the gear meshing frequency, while 105 Hz was not obvious. But the 2× and 4× harmonics of 105 Hz, 2× and 3× harmonics of 170 Hz, 2× and 3× and 4× harmonics of 690 Hz are very obvious. In addition, it also contains other low-energy burr compositions.

Figure 6.12b is the signal of testing point 4, which contains the frequency components of 30, 170, 690 Hz that reflect the gear meshing frequency. In addition, the 2× and 3× harmonics of 170 Hz, the 2× and 3× and 4× harmonics of 690 Hz are also very obvious.

Figure 6.12c is the signal of testing point 6, which contains the frequency components of 170, 690 Hz that reflect the gear meshing frequency. In addition, the 2× and 3× harmonics of 170 Hz, the 2× and 3× and 4× and 5× and 6× harmonics of 690 Hz are all very obvious. And 1320 Hz is also more obvious.

From the vibration spectra of each testing point under different loads, some conclusions can be drawn as follows:

1. The gear pair meshing frequency between the medium- and the high-speed shafts is 690 Hz, and that of the medium-to low-speed shaft is 170 Hz. The inner gear ring–planetary gear meshing frequency is 30 Hz, and the low-speed shaft of the sun wheel–planetary wheel meshing frequency of 107 Hz. These four meshing frequencies are relatively not clear. It is because the first three of

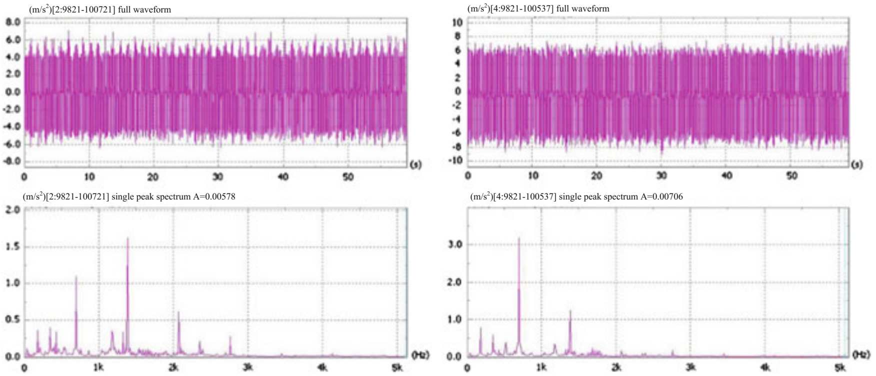

(a) Testing point 2 (b) Testing point 4

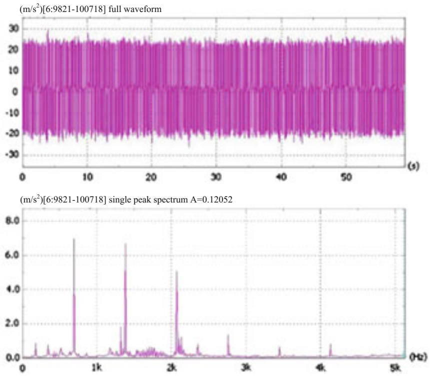

(c) Testing point 6

Fig. 6.12 Time-domain and the frequency-domain signals at different testing points on gearbox. **a** Testing point 2. **b** Testing point 4. **c** Testing point 6

the gear pair meshing energy are easily transferred to the housing shells, but the meshing of the sun wheel and a planetary wheel is difficult to transfer outward.

2. There are no fractional or sub-harmonics of each meshing frequency, and it indicates that there are no tooth-broken and other serious faults.
3. The energy of the fundamental frequency, two times, three times or even higher frequency of medium–high-speed shaft gear pair meshing frequency 690 Hz are all lager, which illustrates that the high-speed shaft alignment is not good enough. There may be two reasons: The shaft centering alignment accuracy of the high-speed shaft is not high. The centering alignment accuracy in the connections of motor and the high-speed shaft is not high. It is suggested that the centering positioning precision of high-speed shaft should be increased. No matter in experimental or working conditions, it should be ensured that the centering positioning accuracy requirements of the joint meet the requirements in the installation of the connecting piece of high-speed shaft and the outside.

Otherwise here is easy to produce the extra stress, which will greatly reduce the service life of the high-speed shaft.

4. The energy of the fundamental frequency, two times, three times or even higher frequency of the medium- to low-speed shaft gear pair meshing frequency 170 Hz are lager, which illustrates the high-speed shaft alignment is not good enough. There are two reasons: The shaft centering alignment accuracy of the middle-speed shaft is not high, and the additional stress caused by the non-centering of the high-speed shaft, which transfer the stress through the high-speed to middle-speed shaft gear pair.
5. There are many edge clusters of 30 and 60 Hz around the rotating frequency and its harmonics of the high-speed shaft (170, 690 Hz). The possible reasons are imbalance gear, tooth pitch error, and the misalignment of gears to its shaft.

References

1. He H, Meng Q, Zhao J, et al. Time-frequency (scale) analysis and diagnosis for nonstationary dynamic signal of machinery. Int J Plant Eng Manage. 1996;1(1):5–26.
2. Meltzer GS, Ivanov Y. Fault detection in gear drives with non-stationary rotational speed- Part I: the time-frequency approach. Mech Syst Signal Process. 2003;17(5):1033–47.

Chapter 7
Vibration Signal Analyses of Gearbox in Time-Domain, Frequency-Domain, and Time–Frequency Domain

The vibration signals of different testing points on the wind turbine gearbox are analyzed in time and frequency domains to explore the underlying dynamic behaviors of wind turbine gearbox applying light or severe loads. Some technologies of data processing including Hilbert–Huang transform (HHT) are achieved in this chapter.

7.1 Structure Description and Measuring Method

A 5.0-MW wind turbine gearbox is composed of one inner ring driving planetary gear train, one fixed axis gear train, and one stage of parallel shaft, as shown in Fig. 7.1. The technical parameters and the rated input powers of the wind turbine gearbox are listed in Table 7.1.

The speed ratio of the first transmission stage is 4.333; those of the second transmission stage and the parallel shaft are 3.609 and 6.550, respectively. Then, the total speed ratio is 102.426. The first stage of planetary gear train has three planet gears which are all circumferential distribution structure with load sharing as sun float gear train. The fixed shaft driving transmission is parallel gear train.

The gear meshing frequencies of the wind turbine gearbox and its shaft frequencies are shown in Table 7.2. As the wind turbine gearbox was driven by ring gear, the rated input speed is 11.9 rpm at rated power 5560 kW. The input shaft frequency is only 0.198 Hz (i.e., 11.9 r/min), and the meshing frequency of output stage is 406.293 Hz under the rated input speed. The range of working speed of this type of wind turbine gearbox is from 5 to 23 rpm. Therefore, the input shaft frequency is only 0.083 Hz if the input speed is 5 rpm, while the meshing frequency of output stage is 785.272 Hz if the input speed is 23 rpm. The frequency of each shaft and gear pair changes from 0.083 to 785.272 Hz under the normal operation condition.

Q. Han et al., *Dynamics and Vibration Analyses of Gearbox in Wind Turbine*,
DOI 10.1007/978-981-10-2747-5_7

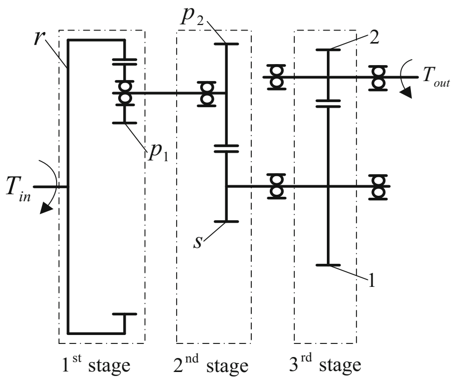

(a) Transmission principle

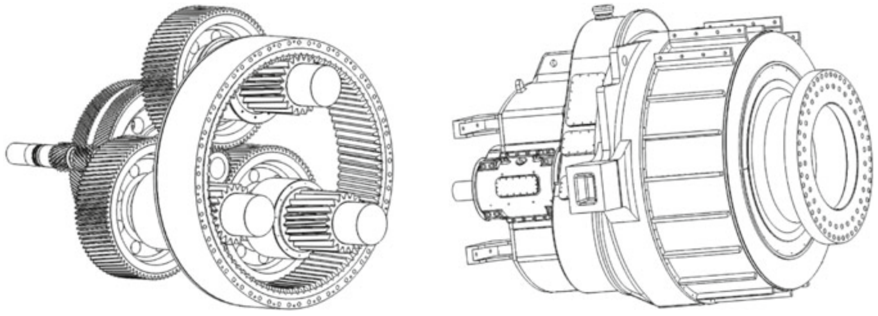

(b) Gear system

(c) whole model

Fig. 7.1 A wind turbine gearbox

Table 7.1 Basic parameters and rated input loads of a wind turbine gearbox

Rated input power	5730 kW
Rated input speed	11.9 r/min
Transmission configuration	NW planetary + one stage parallel shaft gear train
Total transmission ratio	102.426

Table 7.2 Frequency of each shaft and gear pair under rated input speed

Parameters	Frequency (Hz)
Meshing frequency of input stage	18.048
Meshing frequency of middle stage	71.334
Meshing frequency of output stage	406.293
Input shaft frequency	0.198
Planetary gear shaft frequency	0.859
Sun gear shaft frequency	3.1
Output shaft frequency	20.3

7.2 Vibration Measurements of Wind Turbine Gearbox

The on-site measurement of the 5.0-MW wind turbine gearbox is carried out. Vibration signals of the wind turbine gearbox are measured under different rated input loads of 50, 100, and 110 %.

The on-site test machine is shown in Fig. 7.2, and the testing points are shown in Fig. 7.3, in which the numbers ‘1’–‘9’ indicate the points of putting accelerators, and the letter ‘F’ refers to the reference point. The testing points of 1, 4, and 7 are located at the driving side; points of 3, 6, and 9 are located at the driven side. The sensors are fixed as closely as possible to the measured objects and the rotating parts.

7.3 Analysis of Vibration Signals of Gearbox Based on Time Domain

The measured vibration signals at the points of 1, 2, and 3 at cases of 50, 100, and 110 % rated load are shown in Figs. 7.4, 7.5, and 7.6. Point 1 is located at the low-speed shaft; point 2 is the reference testing point. Point 3 is located at the high-speed shaft.

Preliminary time history curves are illustrated with the measured vibration signals under different rated input loads, as shown Figs. 7.4, 7.5, and 7.6. From Figs. 7.4, 7.5, and 7.6, we can see the acceleration level is increasing as load increases. The vibration of input side shaft is much more severe than that of output side shaft.

Fig. 7.2 The on-site measurement of gearbox

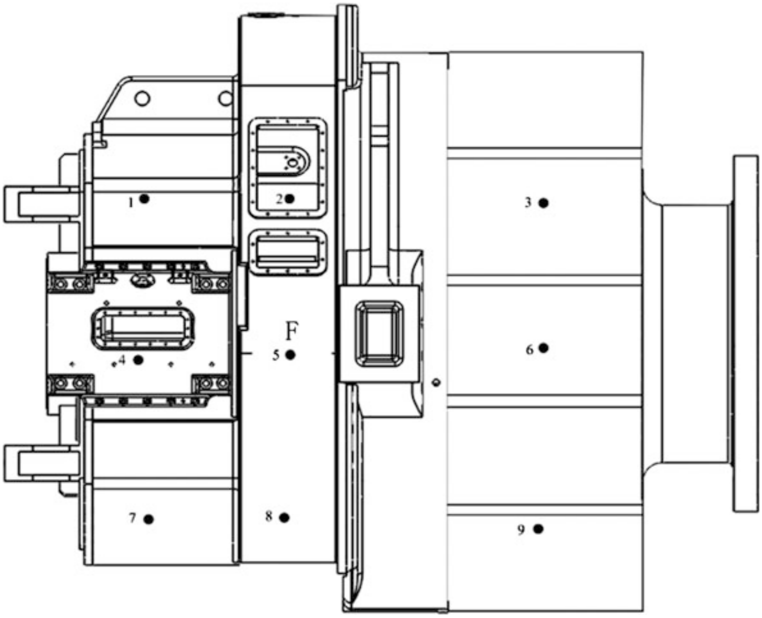

Fig. 7.3 The test points on the gearbox

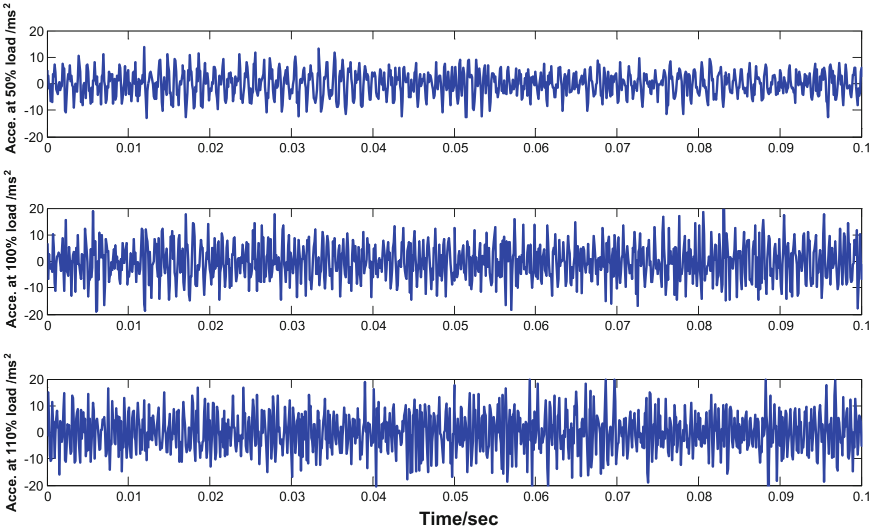

Fig. 7.4 The vibration signals of point 1 at cases of 50, 100, and 110 rated input load

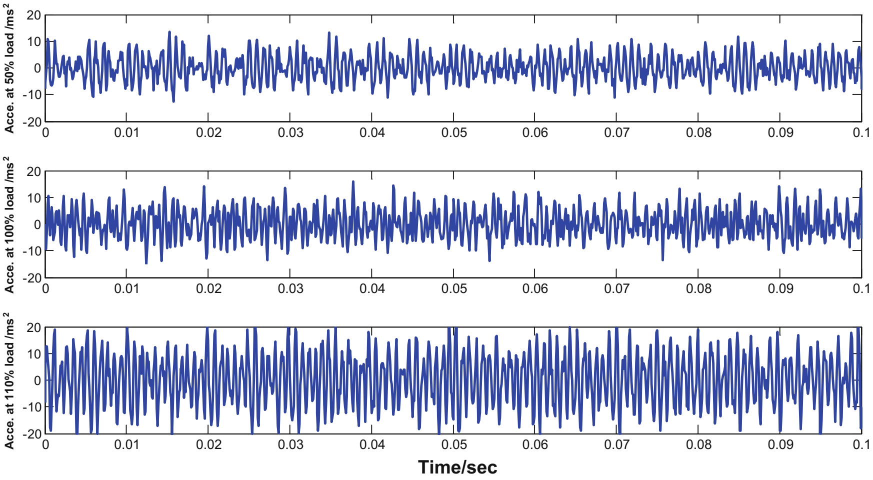

Fig. 7.5 The vibration signals of point 2 at cases of 50, 100, and 110 % rated input load

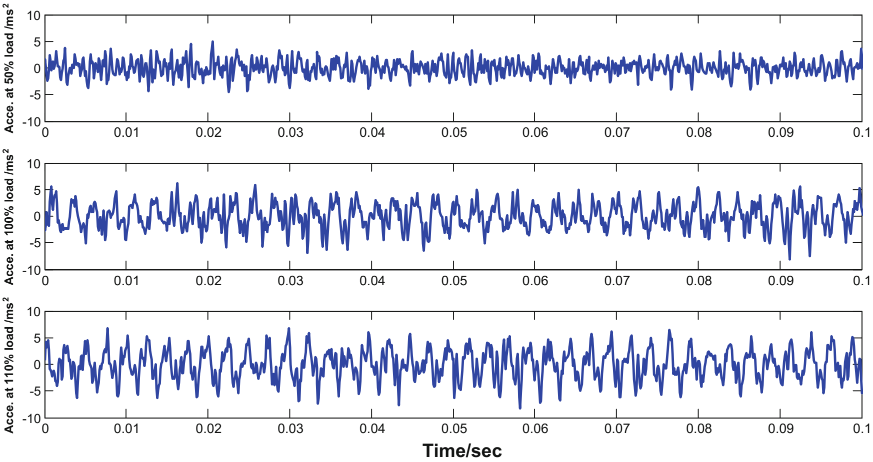

Fig. 7.6 The vibration signals of point 3 at cases of 50, 100, and 110 % rated input load

7.4 Cross-Correlation Function Estimates of Vibration Signals

The time-domain analysis is further carried out in order to explore the relationship between the different picking points at either input side or output side. In order to analysis the vibration signals in time domain, besides the amplitudes of vibrations, the correlation analyses including autocorrelation and cross-correlation are used to identify the relationship and similarity of vibration signals under different rated input loads of the wind turbine gearbox.

In MATLAB, C = XCORR(A, B), where A and B are length of M vectors (M > 1), returns the length 2*M − 1 cross-correlation sequence C. XCORR produces an estimate of the correlation between two random (jointly stationary) sequences:

$$C(m) = E[A(n+m) \times conj(B(n))] = E[A(n) \times conj(B(n-m))] \tag{7.1}$$

It is also the deterministic correlation between two deterministic signals. XCORR(A), when A is a vector, is the autocorrelation sequence.

Autocorrelation and cross-correlation function estimates of different vibration signals picked at driving side shaft of point 1, reference point 2, and driven side shaft of point 3 at the cases of 50, 100, and 110 % rated input load are shown, respectively, in Figs. 7.7, 7.8, and 7.9.

The values of autocorrelation and cross-correlation incline to zero as time delay increases. Periodic and regularity impulse does not exist. The vibration signals are the results of vibrating and impacting of the wind turbine system which has wide and uniform spectra. It is preliminarily adjudged that the vibration signals of the wind turbine gearbox are stationary. Through analyzing the autocorrelation and cross-correlation relationship of vibration signals of the wind turbine gearbox, it can also diagnose the gearbox healthy or not.

7.5 Spectra Analysis of Vibration Signals of the Wind Turbine Gearbox

The frequency-domain analysis techniques based on FFT are used to analyze the vibration signals of the wind turbine gearbox under different rated input loads.

In MATLAB, FFT(X) is the discrete Fourier transform (DFT) of vector X. For length N input vector x, the DFT is a length N vector X, with elements N

$$X(k) = \underset{n=1}{\overset{N}{\text{sum}}}\, x(n) * \exp(-j * 2 * \text{pi} * (k-1) * (n-1)/N), \quad 1 \le \text{k} \le \text{N}. \tag{7.2}$$

The inverse DFT (computed by IFFT) is given by

$$x(n) = (1/N)\ \underset{k=1}{\overset{N}{\text{sum}}} X(k) * \exp(j * 2 * \text{pi} * (k-1) * (n-1)/N), \quad 1 \le \text{n} \le \text{N}. \tag{7.3}$$

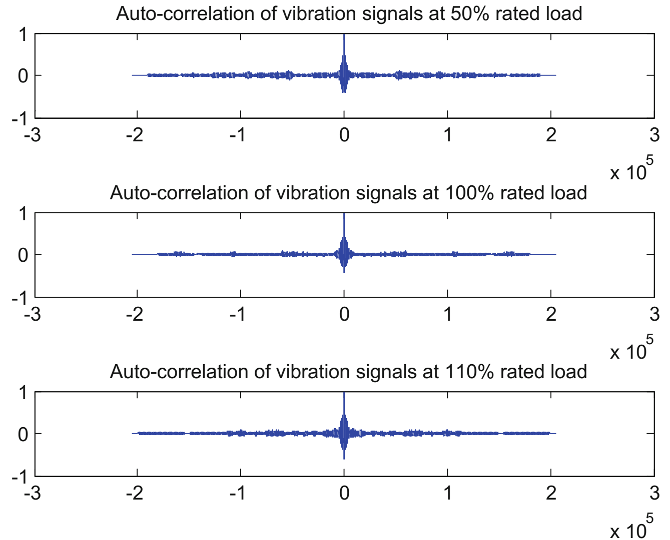

(a) auto-correlation

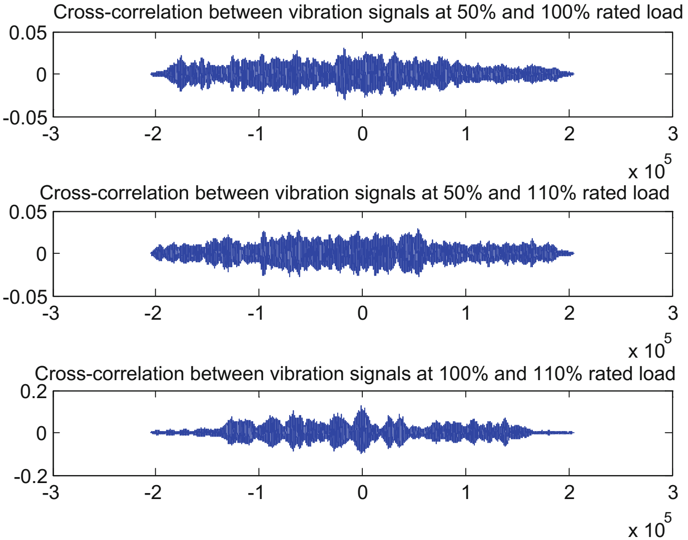

(b) cross-correlation

Fig. 7.7 Autocorrelation and cross-correlation of vibration signals of point 1 at cases of 50, 100, and 110 % rated input load. **a** Autocorrelation. **b** Cross-correlation

Frequency spectra of vibration signals picked at driving side shaft of point 1 and driven side shaft of point 3 and reference point 2 at cases of 50, 100, and 110 % rated input load are shown in Figs. 7.10, 7.11, and 7.12. The amplitude spectra

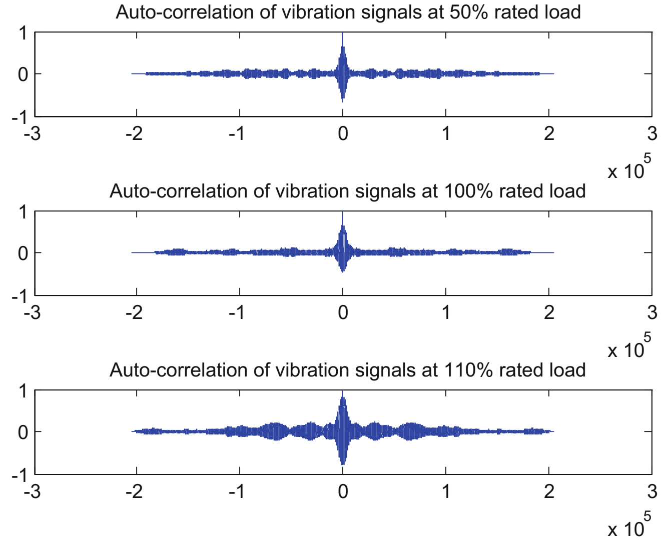

(a) auto-correlation

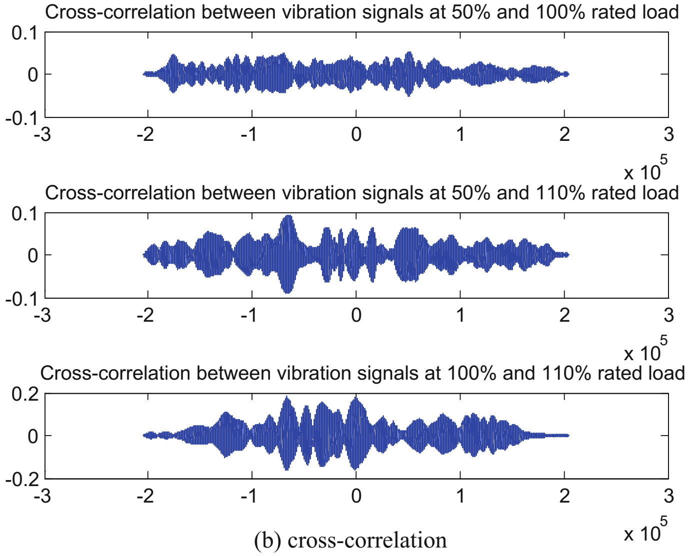

(b) cross-correlation

Fig. 7.8 Autocorrelation and cross-correlation of vibration signals of point 2 at cases of 50, 100, and 110 % rated input load. **a** Autocorrelation. **b** Cross-correlation

provide the running information of the gearbox under different input loads. As rated input load increases, the amplitude of line spectrum increases obviously. The frequency bands of the vibration signals of the gearbox under different rated input

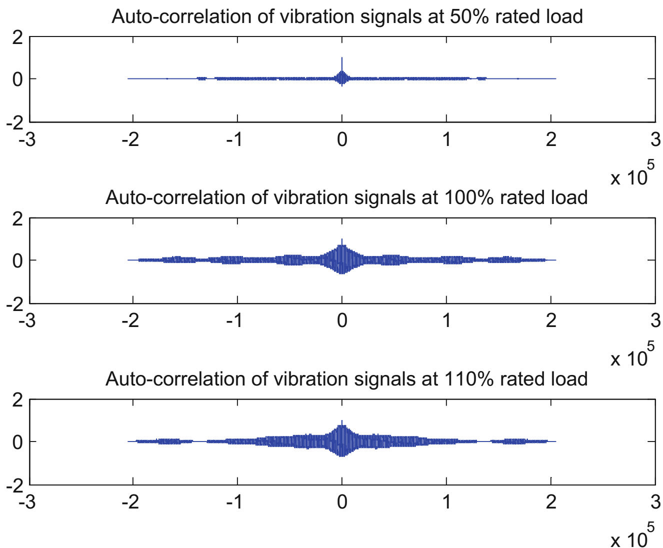

(a) auto-correlation

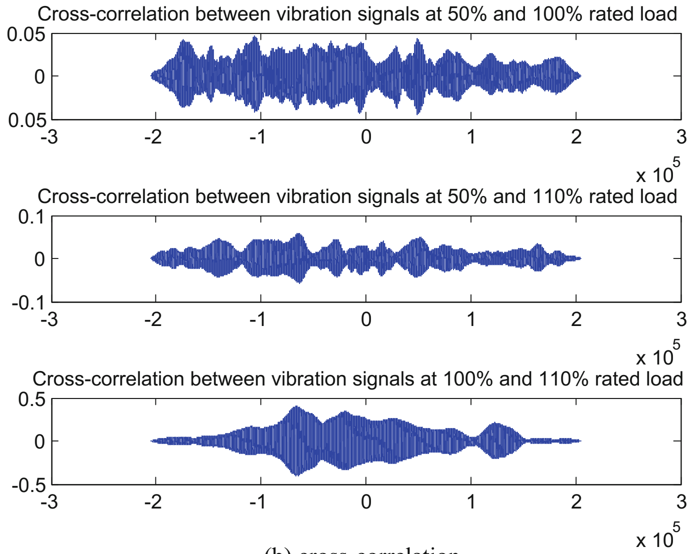

(b) cross-correlation

Fig. 7.9 Autocorrelation and cross-correlation of vibration signals of point 3 at cases of 50, 100, and 110 % rated input load. **a** Autocorrelation. **b** Cross-correlation

loads are certainly wide which means the vibrations excited by different components of the gear train are also obvious. The suitable frequency bands are useful for monitoring the gearbox operating conditions.

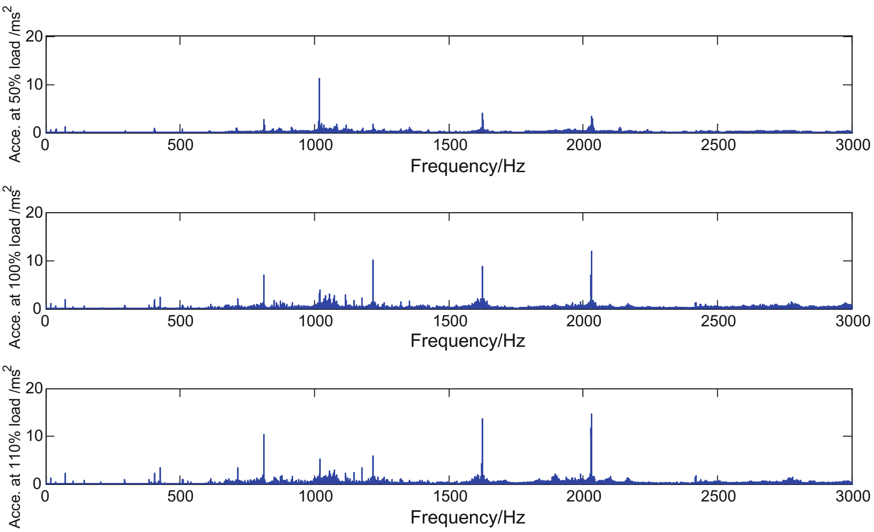

Fig. 7.10 The vibration signals of point 1 at cases of 50, 100, and 110 % rated input load

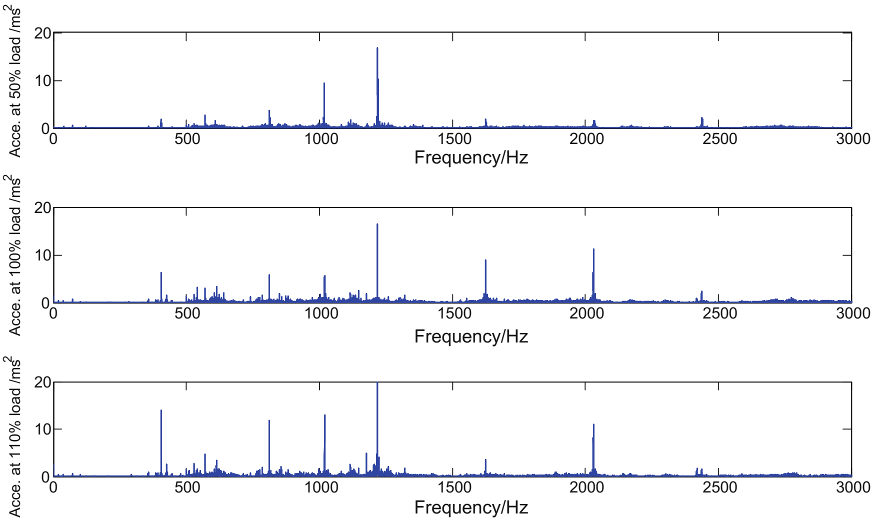

Fig. 7.11 The vibration signals of point 2 at cases of 50, 100, and 110 % rated input load

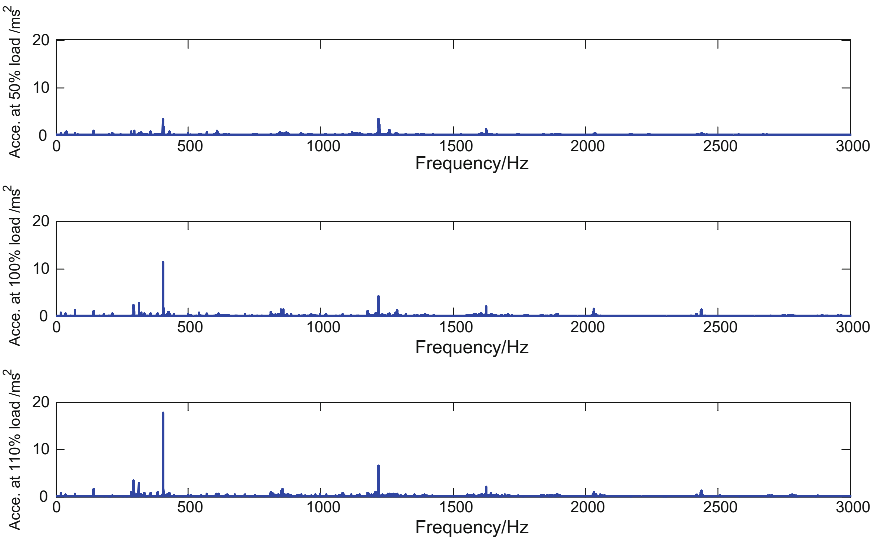

Fig. 7.12 The vibration signals of point 3 at cases of 50, 100, and 110 % rated input load

7.6 Phase Analysis of Vibration Signals of Wind Turbine Gearbox

It is known that the traditional FFT phase analysis of a signal has two disadvantages. The first is the great noise which makes the maxima detection and the peaks discrimination difficult. The second is that the shape of the phase is not fixed. Phase analysis based on analytic signal theory with Hilbert transform estimates of vibration signals of the wind turbine gearbox at cases of 50, 100, and 110 % rated input load is researched in this part.

7.6.1 Phase Analysis Based on Analytic Signal Theory with Hilbert Transform

In order to stabilize the phase shape, a solution to control the real and imaginary part values of the DFT spectrum must be found. Consequently, the real part must be null excepted at characteristic frequencies. The solution is to interpret the DFT modulus as the real part of a new signal called 'analytic signal.' Indeed, the modulus contains very weak values, and Dirac impulsions are studied often. So, the shape of the real part is well-known at each frequency point, and the signal-to-noise ratio (SNR) is increased.

The analytic signal is obtained by a HT of the line current spectrum modulus. Considering a signal $s(t)$, the analytic signal $\tilde{s}(t)$ can be expressed as

$$\tilde{s}(t) = s(t) + j\rho(t) \tag{7.4}$$

where

$$\rho(t) = H(s(t)) = s(t) * \frac{1}{\pi t} \tag{7.5}$$

The HT $\rho(t) = H(s(t))$ is defined as the convolution product of the signal $s(t)$ (which becomes the real part of $\tilde{s}(t)$) by a filter whose the impulse response is $h(t) = \frac{1}{\pi t}$. The analytic signal can be obtained by a HT of the spectrum modulus.

The Fourier transform of the signal $\rho(t)$, which represents the HT of the signal $s(t)$, is given by the following equation

$$\rho(t) \xrightarrow{\mathrm{FT}} -j\mathrm{sgn}(\omega)S(\omega) \tag{7.6}$$

where $S(\omega)$ is the Fourier transform of $s(t)$, and $\mathrm{sgn}(\omega) = \{1, 0, -1\}$ when $\omega > 0, = 0, < 0$.

Consequently, the analytic signal $\tilde{s}(t)$ can be obtained by using the Fourier transform with the expression

$$\tilde{s}(t) \xrightarrow{FT} S(\omega) + j[-j\mathrm{sgn}(\omega)]S(\omega) = [1 + \mathrm{sgn}(\omega)]S(\omega) \tag{7.7}$$

The Fourier image of the analytic signal is doubled at positive frequencies and canceled at negative frequencies with respect to $S(\omega)$. The advantage of this transformation is that the result remains in the same domain as the signal analyzed (time, e.g.).

A particularity here is that the HT is applied on the spectrum modulus of original time signal data, such as $|Y(\omega)|$ of $y(t)$. Hence, the analytic signal of this modulus provides

$$\tilde{Y}(\omega) = |Y(\omega)| + jY_{\mathrm{HT}}(\omega) \tag{7.8}$$

where $Y_{\mathrm{HT}}(\omega) = H(Y(\omega))$.

The analytic signal phase $\Psi_{HT}(\omega)$ can be calculated with the expression

$$\Psi_{\mathrm{HT}}(\omega) = \arctan\frac{\mathrm{Im}(\tilde{Y}(\omega))}{\mathrm{Re}(\tilde{Y}(\omega))} = \arctan\frac{Y_{\mathrm{HT}}(\omega)}{|Y(\omega)|} \tag{7.9}$$

The HT applied to the spectrum modulus of signal gives a phase restricted to the interval $[-\pi/2, \pi/2]$. Moreover, the knowledge of the imaginary part from HT allows predicting the exact form of the analytic signal phase. Besides, due to the noise reduction, phase jumps are more pronounced which permits easier nonlinearity factor detection.

7.6.2 Results of Phase Analysis of Vibration Signals of Wind Turbine Gearbox

Phase analysis of vibration signals picked at driving side shaft of point 1 and driven side shaft of point 3 and reference point of point 2 of the wind turbine gearbox at cases of 50, 100, and 110 % rated input load is shown in Figs. 7.13, 7.14, and 7.15.

It is clear that the phase spectra of vibration signals of the wind turbine gearbox under different rated input load are in the same phase pattern. They have small difference from each other.

7.7 Hilbert–Huang Transform Analysis of Vibration Signals of Wind Turbine Gearbox

In a nonstationary data, it is mostly difficult to make sure of the perfect periods of harmonic components. The time–frequency analysis method named HHT has merits such as uniform resolution at the low- and high-frequency parts, ability to deal with the signals of large size, and so on [1–3].

HHT estimates of vibration signals of the wind turbine gearbox at cases of 50, 100, and 110 % rated input load are researched in this part.

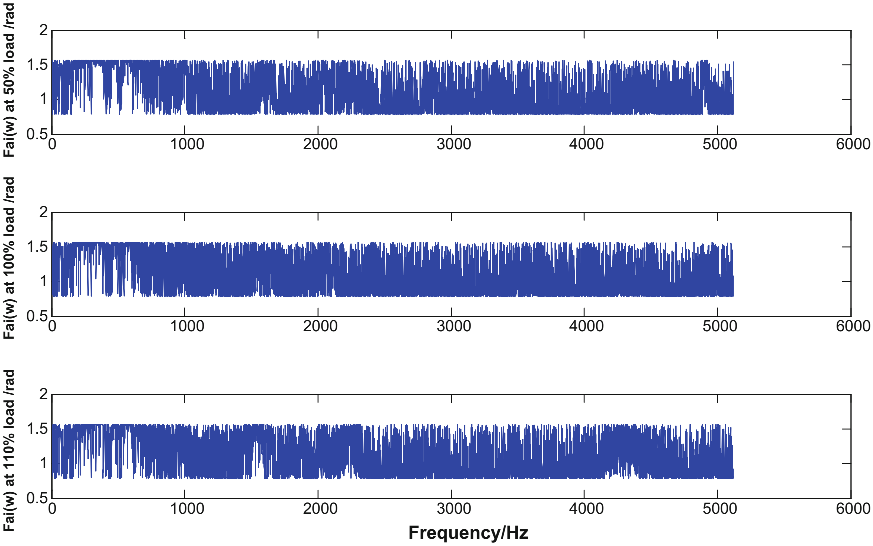

Fig. 7.13 Phase spectra of vibrations of point 1 with Hilbert transform at 50, 100, and 110 % rated input load

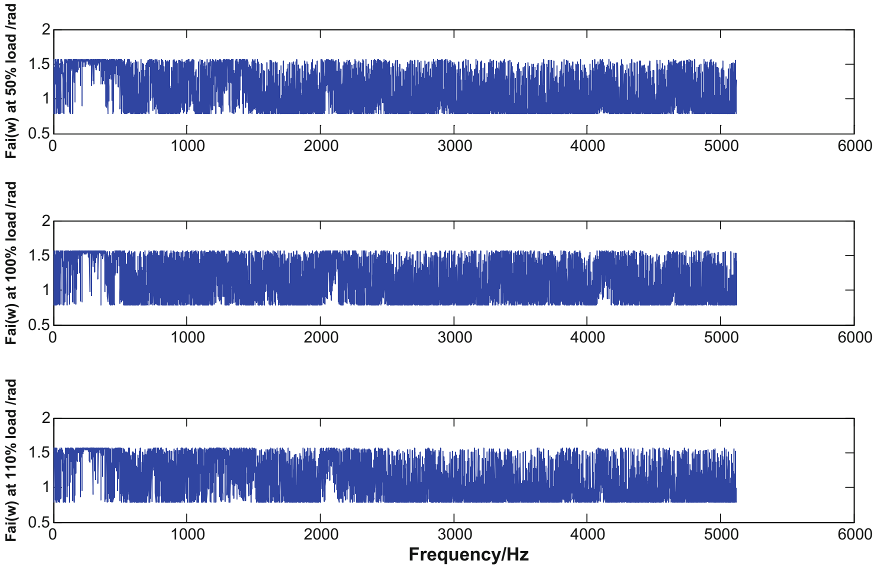

Fig. 7.14 Phase spectra of vibrations of point 2 with Hilbert transform at 50, 100, and 110 % rated input load

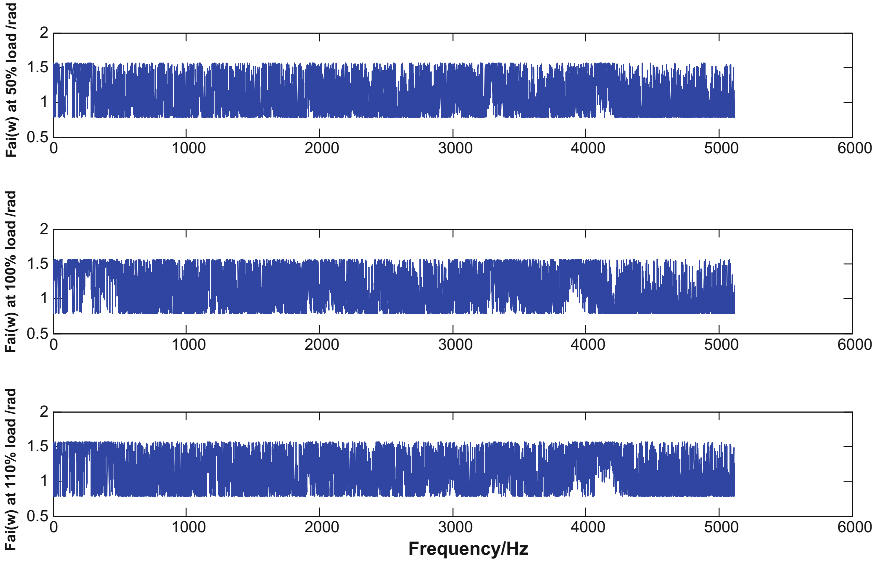

Fig. 7.15 Phase spectra of vibrations of point 3 with Hilbert transform at 50, 100, and 110 % rated input load

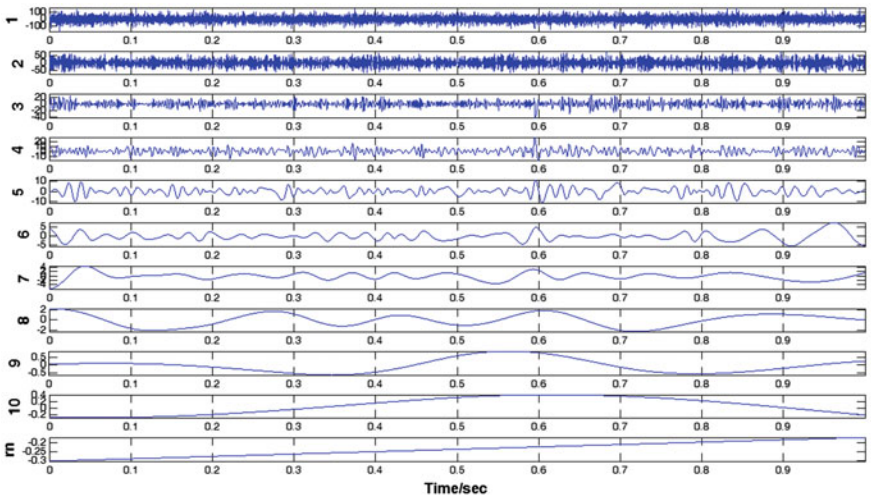

(a) IMFs and residue of point 1

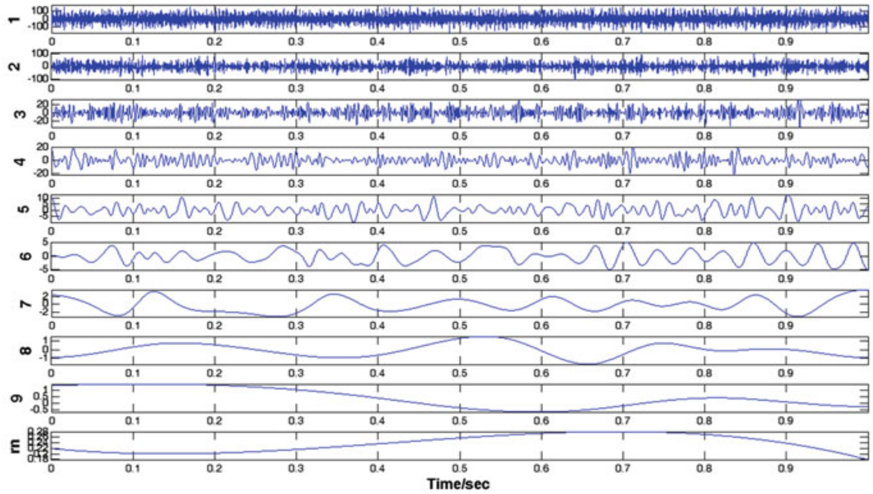

(b) IMFs and residue of point 2

Fig. 7.16 IMFs and residue of vibration signals of point 1, 2, and 3 at case of 50 % rated input load. **a** IMFs and residue of point 1. **b** IMFs and residue of point 2. **c** IMFs and residue of point 3

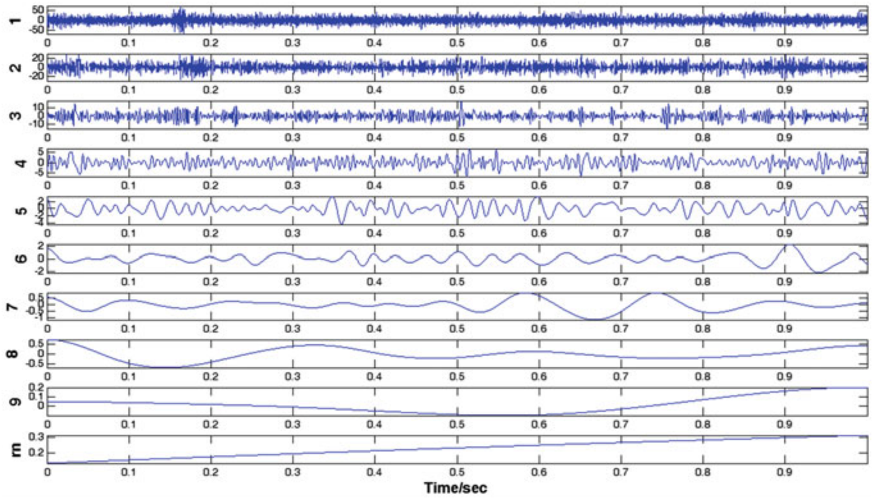

(c) IMFs and residue of point 3

Fig. 7.16 (continued)

7.7.1 Basic Principle of Hilbert–Huang Transform Technique

The technique works by performing a time adaptive decomposition operation named empirical mode decomposition (EMD) on the signal and decomposing it into a set of complete and almost orthogonal components named intrinsic mode function (IMF), which is almost mono-component [4].

Utilizing Hilbert transform on those obtained IMFs, we can get a full energy–frequency–time distribution of the signal, designated as the Hilbert–Huang spectrum. Every IMF component can be amplitude modulation and/or frequency modulation [5, 6]. So, it is powerful to extract the two kinds of modulations for a nonstationary or nonlinear data. In particular, it can separate the nonlinear component from background noise, and it is useful for nonlinear identification. The IMFs satisfy the following requirements: (1) The number of extrema and the number of zero crossings in the IMF must either be equal or different at most by one; and (2) at any point, the mean value of the envelopes defined by the local maxima and local minima must be zero.

Some recent works show that HHT is powerful in machine fault diagnosis. For example, the periodic rub-impact in a rotor system will induce the amplitude

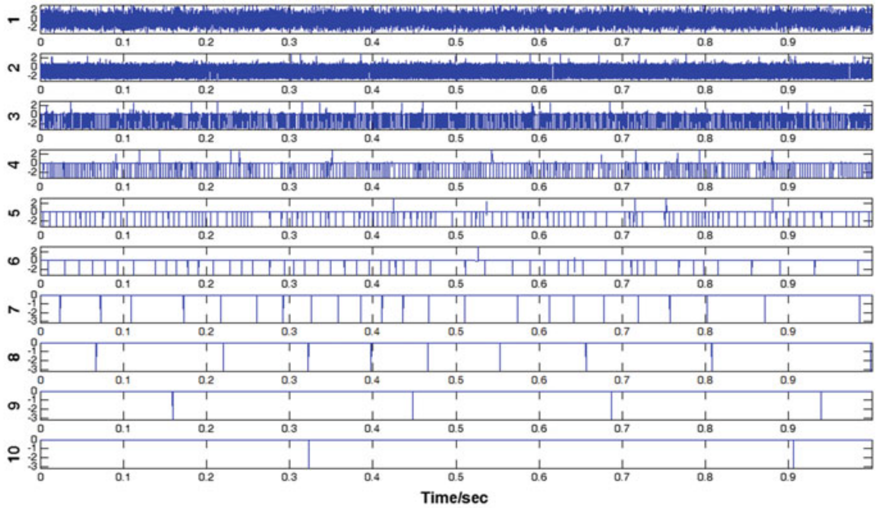

(a) Instantaneous frequencies of point 1

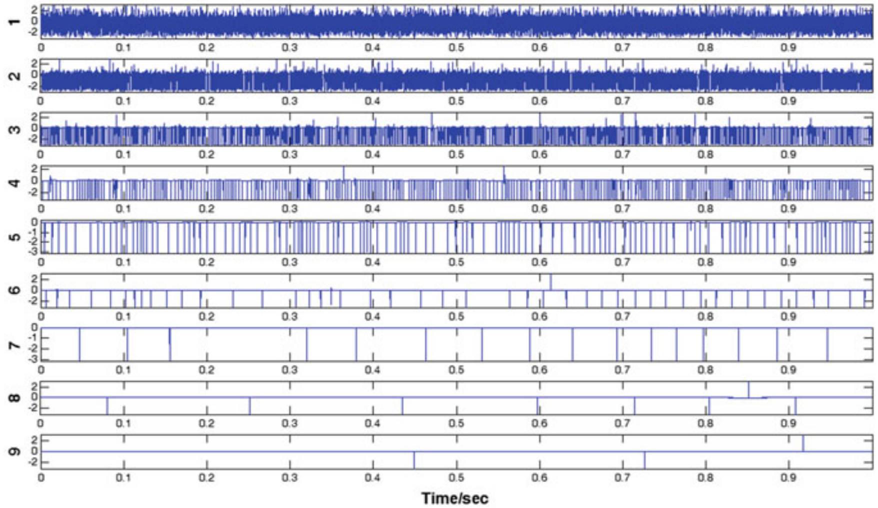

(b) Instantaneous frequencies of point 2

Fig. 7.17 Instantaneous frequencies of vibration signals of points 1, 2, and 3 at case of 50 % rated input load. **a** Instantaneous frequencies of point 1. **b** Instantaneous frequencies of point 2. **c** Instantaneous frequencies of point 3

modulated nonlinear signals. Besides the rub-impact components, there are strong components coming from rotating and other processes.

Here, we apply EMD and Hilbert envelope analysis to the nonstationary and nonlinear data. With EMD, signals are decomposed into a series of zero-mean

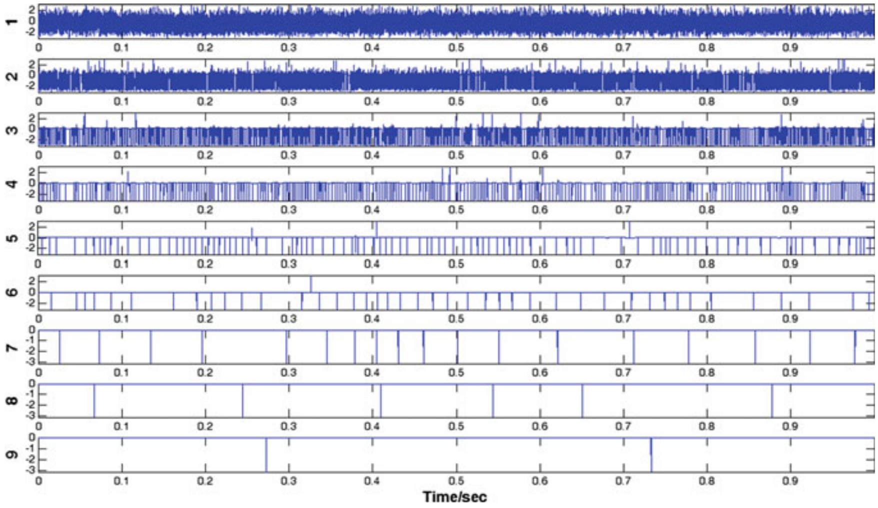

(c) Instantaneous frequencies of point 3

Fig. 7.17 (continued)

amplitude-modulation frequency-modulation (AM-FM) components, i.e., IMFs, which represent the characteristic timescale of the observation.

The process to find the IMFs of a signal x(t) comprises the following steps:

(1) Find the positions and amplitudes of all local maxima and minima in the input signal $x(t)$. Then, create an upper envelope by cubic spline interpolation of the local maxima and a lower envelope by cubic spline interpolation of the local minima. (The reason why the cubic spline is suitable for envelope function is given in known references.)
(2) Calculate the mean of the upper and lower envelopes; this is defined as $m_1(t)$.
(3) Subtract the envelope mean from the original input signal and give the sifting results $h_1(t)$

$$h_1(t) = x(t) - m_1(t) \tag{7.10}$$

(4) Check whether $h_1(t)$ meets the requirements to be an IMF. If $h_1(t)$ is an IMF, stop.
(5) Otherwise, treat $h_1(t)$ as the new signal data and iterate on $h_1(t)$ through the previous step (1)–(4). That is, to set

$$h_{11}(t) = x(t) - m_{11}(t) \tag{7.11}$$

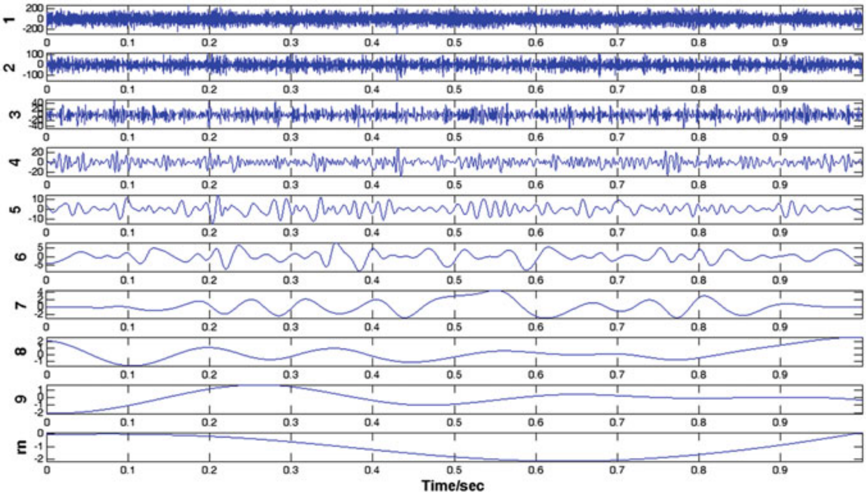

(a) IMFs and residue of point 1

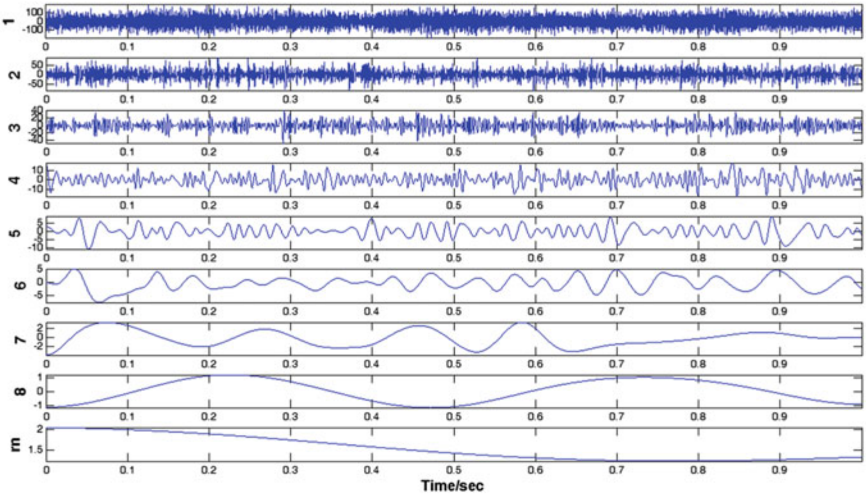

(b) IMFs and residue of point 2

Fig. 7.18 IMFs and residue of vibration signals of point 1, 2, and 3 at case of 100 % rated input load. **a** IMFs and residue of point 1. **b** IMFs and residue of point 2. **c** IMFs and residue of point 3

(6) Repeat this sifting procedure k times until $h_{1k}(t)$ is an IMF; this is designated as the first IMF. Note the first-order IMF is

$$c_1(t) = h_{1k}(t) \tag{7.12}$$

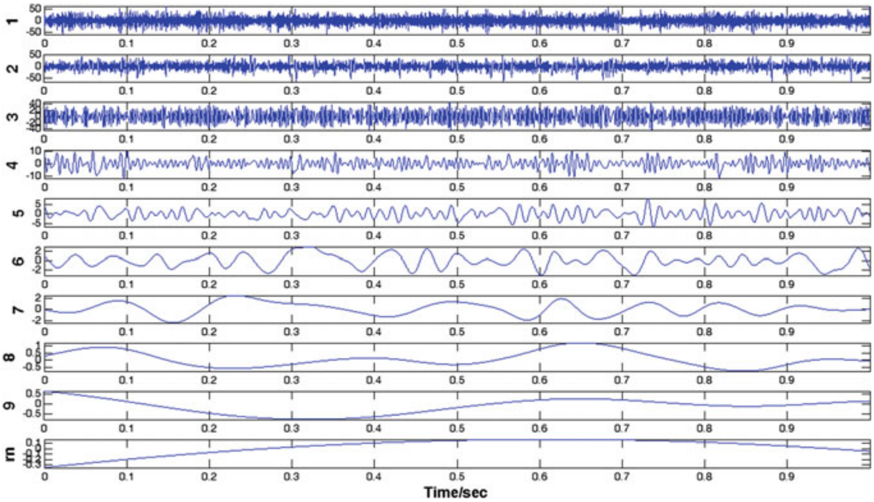

(c) IMFs and residue of point 3

Fig. 7.18 (continued)

Subtract $c_1(t)$ from the input signal, and define the remainder as the first residue $r_1(t)$ as follows:

$$r_1(t) = x(t) - c_1(t) \tag{7.13}$$

(7) Since the residue $r_1(t)$ still contains information related to longer period components, it is treated as a new data stream, and the above-described sifting process is repeated until reaching the last order IMF.

This procedure can be repeated j times to generate j residues, $r_j(t)$, resulting in

$$r_2(t) = r_1(t) - c_2(t), \ldots, r_n(t) = r_{n-1}(t) - c_n(t) \tag{7.14}$$

The sifting process is stopped when either of two criteria are met: (1) The component $c_n(t)$, or the residue $r_n(t)$, becomes so small as to be considered inconsequential, or (2) the residue, $r_n(t)$, becomes a monotonic function from which an IMF cannot be extracted. For example, the stopping condition for an IMF is

$$\sum_t \frac{[h_{k-1}(t) - h_k(t)]^2}{h_{k-1}^2(t)} < SD \tag{7.15}$$

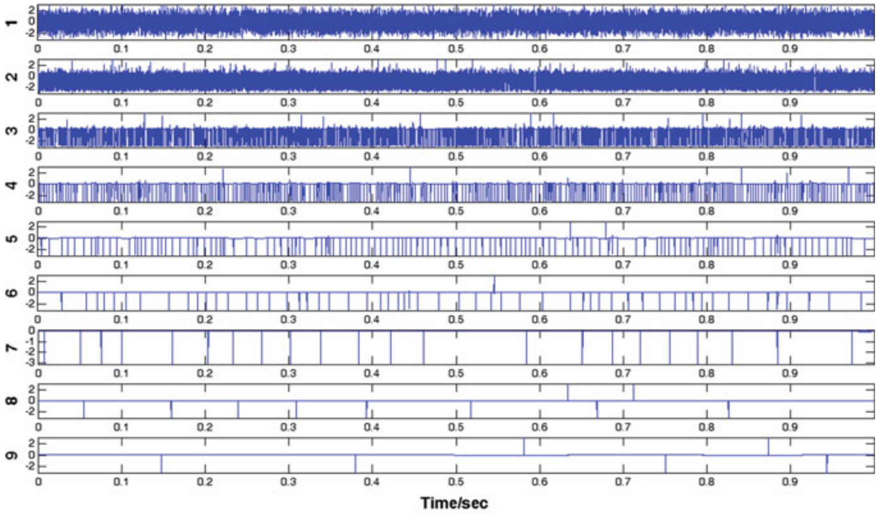

(a) Instantaneous frequencies of point 1

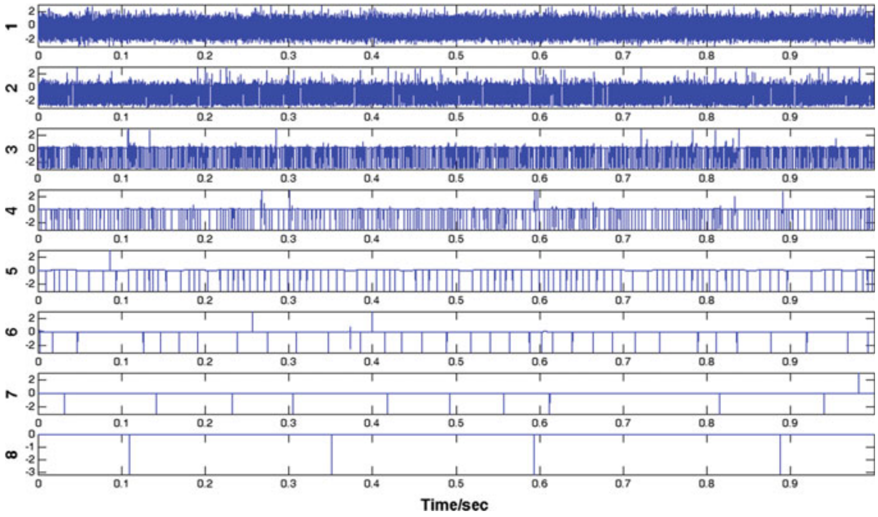

(b) Instantaneous frequencies of point 2

Fig. 7.19 Instantaneous frequencies of vibration signals of points 1, 2, and 3 at case of 100 % rated input load. **a** Instantaneous frequencies of point 1. **b** Instantaneous frequencies of point 2. **c** Instantaneous frequencies of point 3

where $h_k(t)$ is the sifting result in the kth iteration, and SD is typically set between 0.2 and 0.3. Besides, in order to achieve the last IMF, a simple way can be used, that is, the last order IMF will be obtained when the cubic spline fitting stops because the number of local maxima or minima of the residue is less than 2.

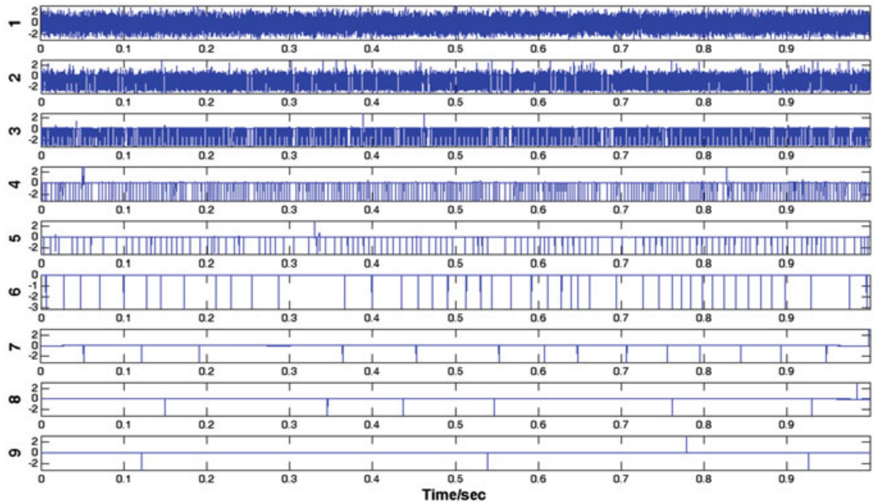

(c) Instantaneous frequencies of point 3

Fig. 7.19 (continued)

Finally, we obtain the decomposed components of the original signal by HHT as

$$x(t) = \sum_{j=1}^{n} c_j(t) + r_n(t) \tag{7.16}$$

In other words, the original signal can now be represented as the sum of a set of intrinsic mode functions plus a residue.

Now, applying the Hilbert transform to all IMFs, we get

$$H[c_j(t)] = \frac{1}{\pi} \int_{-\infty}^{\infty} \frac{c_j(\tau)}{t - \tau} \mathrm{d}\tau \tag{7.17}$$

After the Hilbert transform, $H\left[c_j(t)\right]$ and $c_j(t)$ together form a complex signal, $\left(a_j(t) = \sqrt{c_j^2(t) + (H[c_j(t)])^2}\right)$. So that, the phase function of every IMF is

$$\Phi_j(t) = \arctan \frac{H[c_j(t)]}{c_j(t)} \tag{7.18}$$

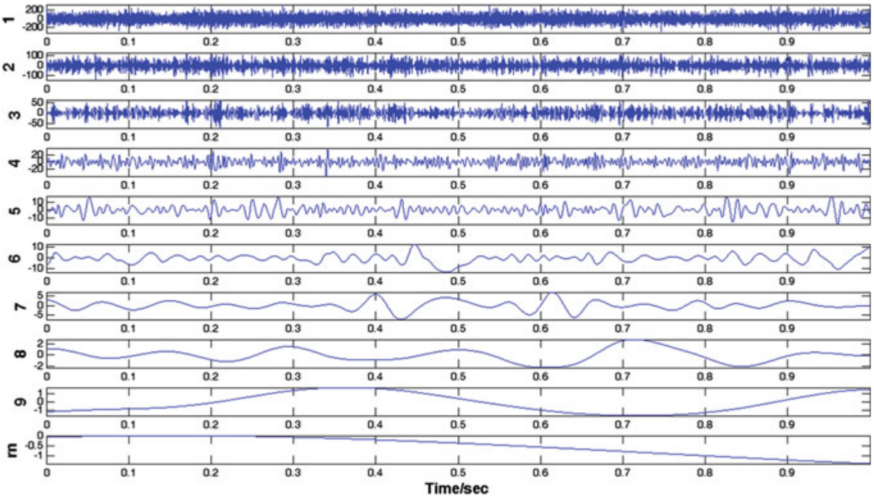

(a) IMFs and residue of point 1

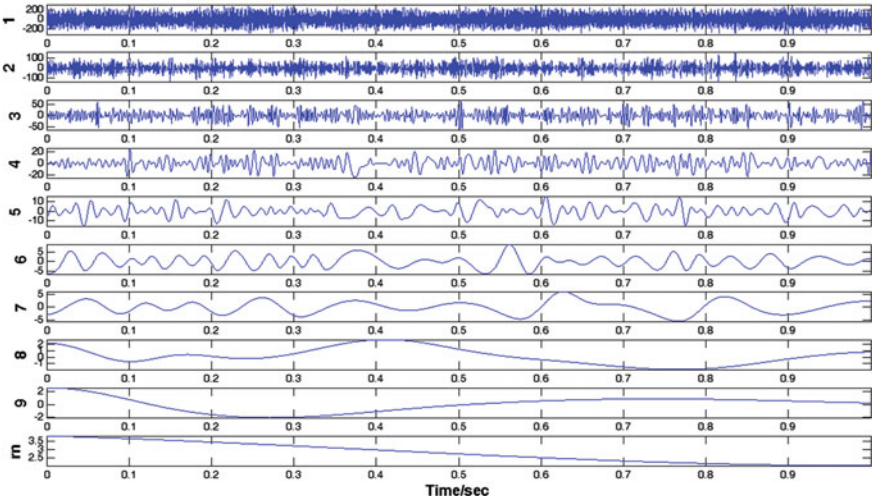

(b) IMFs and residue of point 2

Fig. 7.20 IMFs and residue of vibration signals of point 1, 2, and 3 at case of 110 % rated load. **a** IMFs and residue of point 1. **b** IMFs and residue of point 2. **c** IMFs and residue of point 3

The instantaneous frequency of the IMF is obtained by time differential operation as

$$\omega_j(t) = \frac{\mathrm{d}\Phi_j(t)}{\mathrm{d}t} \tag{7.19}$$

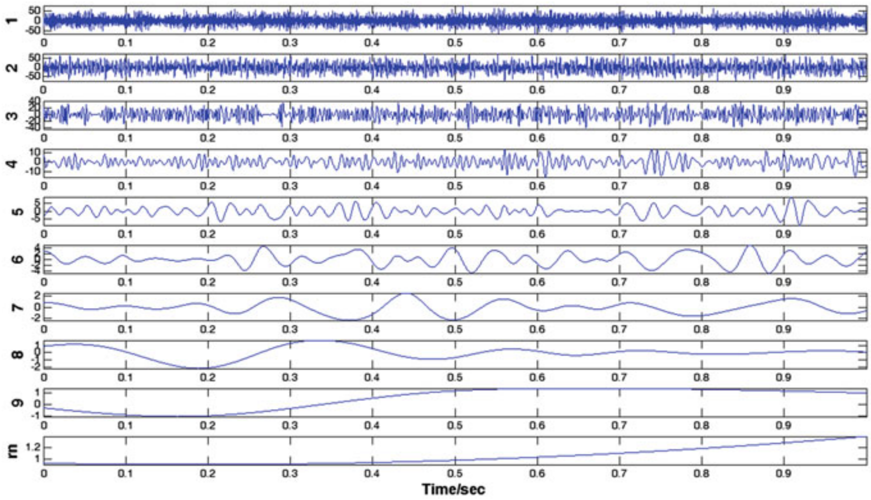

(c) IMFs and residue of point 3

Fig. 7.20 (continued)

7.7.2 *HHT Analysis of Vibrations of Wind Turbine Gearbox*

HHT analysis of vibration signals picked at driving side shaft of point 1 and driven side shaft of point 3 and reference point of point 2 of the wind turbine gearbox at cases of 50, 100, and 110 % rated input load is shown in Figs. 7.16, 7.17, 7.18, 7.19, 7.20 and 7.21.

It is clear that the HHT vibration signals of the wind turbine gearbox under different rated input loads can be used to distinguish each other. The vibration signals of the gearbox at case of 50 % rated input load are selected to introduce the difference between point 1 and point 2.

There are 10 IMFs of vibration signals of point 1 at case of 50 % rated input load, but 9 IMFs of point 2. The first IMF c_1 of point 1 appears as amplitude modulation; in contrast, c_1 of point 2 is quite different. The second- and third-order IMFs of point 1 and 2, c_2 and c_3, appear frequency modulation. The changing patterns of the instantaneous frequencies of point 1 and point 2 are also different. The vibration signal of points 1 and 2 could be regarded as a nonstationary data without strongly nonlinear.

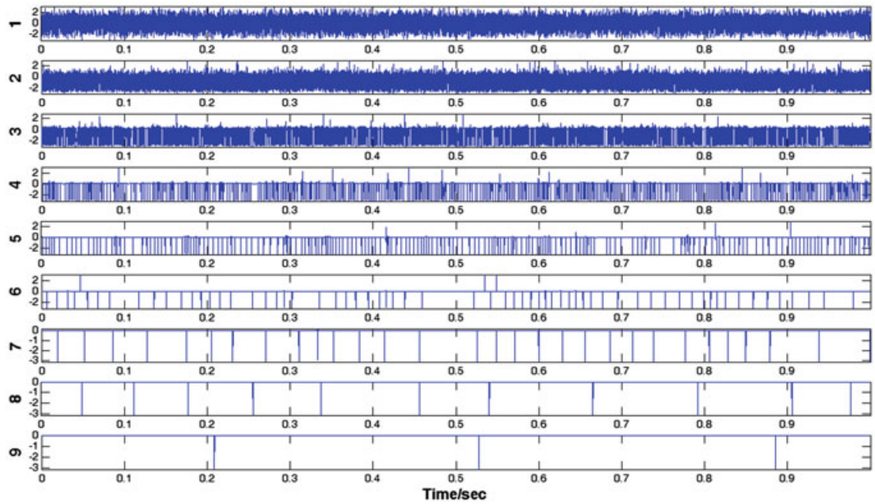

(a) Instantaneous frequencies of point 1

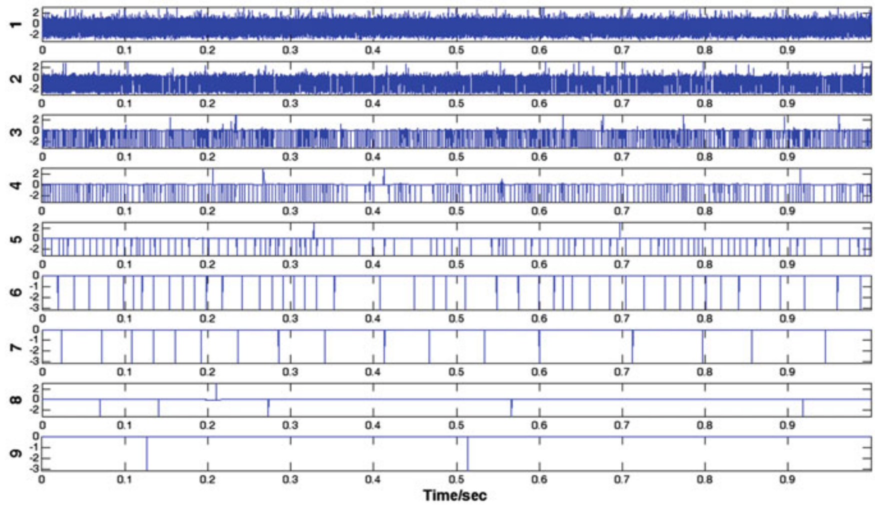

(b) Instantaneous frequencies of point 2

Fig. 7.21 Instantaneous frequencies of vibration signals of point 1, 2, and 3 at case of 100 % rated input load. **a** Instantaneous frequencies of point 1. **b** Instantaneous frequencies of point 2. **c** Instantaneous frequencies of point 3

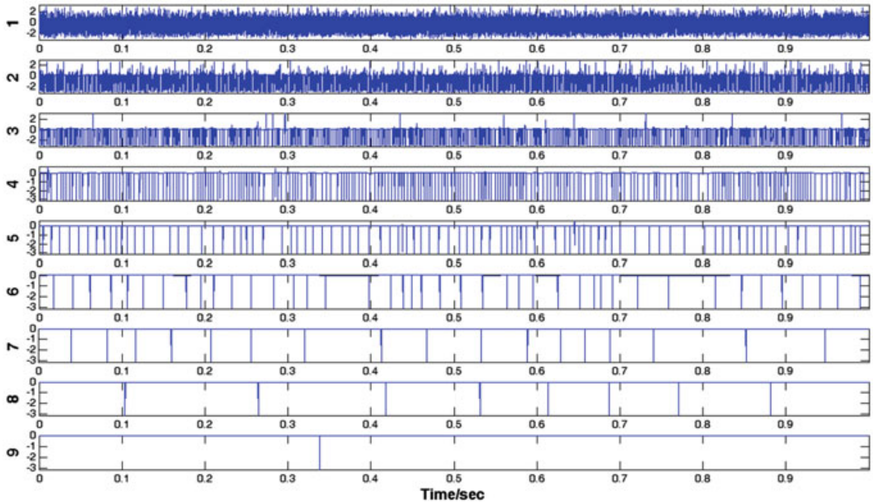

(c) Instantaneous frequencies of point 3

Fig. 7.21 (continued)

References

1. Sakawa Y, Matsuno F, Fukushima S. Modeling and feedback control of a flexible arm. J Robot Syst. 2007;2(4):453–72.
2. Bailey T, Ubbard JE. Distributed piezoelectric-polymer active vibration control of a cantilever beam. J Guid Control Dyn. 2015;8(5):605–11.
3. Guo XW. Research on filtering technology of accelerometer signal. Sci Tech Innovation Herald. 2008;22:4–5.
4. Huang NE, Shen Z, Long SR. A new view of nonlinear water waves: the Hilbert spectrum. Annu Rev Fluid Mech. 2003;31(1):417–57.
5. Cheng J, Yu D, Yu Y. The application of energy operator demodulation approach based on EMD in machinery fault diagnosis. Mech Syst Signal Process. 2007;21(2):668–77.
6. Peng ZK, Tse PW, Chu FL. A comparison study of improved Hilbert-Huang transform and wavelet transform: application to fault diagnosis for rolling bearing. Mech Syst Signal Process. 2005;19(5):974–88.

Chapter 8
Conclusions

This book discusses the dynamic analysis methods and test measurements of the wind turbine gearbox systemically.

Modal characteristics and mode energy distributions of a wind turbine gearbox composed of a two-stage planetary gears and a high-speed output shaft are obtained based on the lumped mass model according to torsionals of geared rotor system.

The load-sharing distributions of the gears within the wind turbine transmission chain are also compared considering different internal excitation and external load. The measured tooth strains under different load-sharing conditions show that the prediction based on the torsional model of the geared rotor system is acceptable.

The load-sharing distribution of the geared system under misalignment is obtained and compared with that of the normal condition. The coupling misalignment has a significant effort on PLSC of geared rotor system, so as to affect the reliability of the system greatly.

The modal characteristics of the gearbox are also analyzed based on the whole gearbox finite element model (WG-FEM) by using finite element method. The operating modal measurements are also obtained to check the calculated modes for the whole machine based on the WG-FEM.

The measured vibrations on bench test and on-site test show the modal characteristics, vibration responses, and vibrations induced by faults that are also valuable for wind turbine design.

Q. Han et al., *Dynamics and Vibration Analyses of Gearbox in Wind Turbine*,
DOI 10.1007/978-981-10-2747-5_8

Appendix A
Codes of Factor KA

A.1 Main_Program.m

```
clc;
clear;
% options=0.1;
% tspan=[0,5];
%define iteration scope
options = odeset;
options.RelTol=1e-6;
%define initial value
x0=[0;0;0;0;0;0;0;0;0;0;0;0;0;0;0;0;0;0;0;0;0;0;0;0;0;0;0;0;0;0;0;0;0;0;0;0;0;0;0;0;0;0;0;0;0;0;0;0;0;0;0;0;0;0;0;0;0;0;0
;0;0;0;0;0;0;0;0;0;0;0;0;0;0;0;0;0;0;0;0;0;0;0;0;0;0;0;0;0;0;0;0;0;0;0;0;0;0;0;0;0;0;0;0;0;0;0];
w=jili(13,44,151);
T=2*pi/w;
[t,x]=ode45(@mkcf,[0:T/500:300*T],x0,options);
%%%%%%%%%%%%%%%%%%%%%%%%%%%%%%%%%%%%%%%%%%%%%
midu=1.225;          %wind density      unit Kg/m3
R=52;                %radius of wind wheel      unit m
lamad=9;             %blade tip speed ratio
Cplamad=0.485;       % wind energy utilization coefficient
Ctlamad=Cplamad/lamad;      %torque coefficient
Vc=0.85;             % change coefficient
Vm=13;               % average wind speed
Va=Vm*Vc;            %wind velocity amplitude
Tinm=1/2*midu*pi*R^3*Ctlamad*Vm^2;
%input gear parameters:      born_internal gear       c_planet carrier       p_planet gear          s_sun gear
mn=12;                   %input stage module    mm
mn1=8;                   %middle stage module    mm
mn2=8;                   %output stage module    mm
bet=9.0724;              %input stage helix angle
bet1=9.20947;            %middle stage helix angle
bet2=4.35489;            %output stage helix angle
beta=bet*pi/180;         % input stage helix angle    radian
```

Q. Han et al., *Dynamics and Vibration Analyses of Gearbox in Wind Turbine*,
DOI 10.1007/978-981-10-2747-5

```
beta1=bet1*pi/180;        % middle stage helix angle    radian
beta2=bet2*pi/180;        % output stage helix angle    radian
zs=44;                    %the number of input stage sun gear
zs1=38;                   % the number of middle stage sun gear
zp=53;                    % the number of output stage planetary gear
zp1=64;                   % the number of middle stage planetary gear
zb=151;                   %the number of input stage internal gear
zb1=165;                  % the number of middle stage internal gear
z1=86;                    %the number of out stage large gear
z2=29;                    %the number of output stage pinion
nin=13;                   %the input speed of input stage planetary carrier    r/min
wc1=2*pi*nin/60;
p=Tinm*nin/9549;          %power    KW
deltaT=1/2*midu*pi*R^3*Ctlamad*Va^2*sin(wc1*t).*sin(wc1*t);      %alternating section of input torque
Tin=Tinm+deltaT;          %input torque
i1=1+zb/zs;               % transmission ratio of input stage
i2=1+zb1/zs1;             % transmission ratio of middle stage
i3=z1/z2;                 % transmission ratio of out stage
nout=nin*i1;              %the speed of middle stage planetary carrier(the speed of input stage sun gear)    r/min
wc2=2*pi*nout/60;
n1=nout*i2;               % the speed of out stage large gear( the speed of middle stage sun gear)      r/min
n2=n1*i3;                 %the speed of output pinion      r/min
wc3=2*pi*n2/60;
alfa=20;                     %pressure angle of input stage
alfa1=20;                    % pressure angle of middle stage
alfa2=20;                    % pressure angle of output stage
afaw=alfa*pi/180;            %out meshing normal pressure angle of input stage    radian
afan=alfa*pi/180;            %internal meshing normal pressure angle of input stage    radian
afaw1=alfa1*pi/180;          %out meshing normal pressure angle of middle stage    radian
afan1=alfa1*pi/180;          % internal meshing normal pressure angle of middle stage    radian
afaw2=alfa2*pi/180;          % out meshing normal pressure angle of output stage    radian
gw=0.532;                    %tooth width of input stage    m
gw1=0.213;                   % tooth width of middle stage    m
gw2=0.346;                   % tooth width of output stage    m
bs=gw;                       %tooth width of input stage sun gear    m
bs1=gw1;                  % tooth width of middle stage sun gear    m
bp=gw;                    %tooth width of input stage planetary gear    m
bp1=gw1;                  % tooth width of middle stage planetary gear    m
bb=gw;                    %tooth width of input stage internal gear    m
bb1=gw1;                  % tooth width of middle stage internal gear    m
b1=gw2;                   % tooth width of out stage large gear    m
b2=gw2;                   % tooth width of out stage pinion    m
```

```
xb=-0.298194;           %normal modification coefficient of input stage internal gear    mm
xb1=-0.337459;          % normal modification coefficient of middle stage internal gear    mm
xp=-0.698194;           % normal modification coefficient of input stage planetary gear
xp1=-0.705062;          % normal modification coefficient of middle stage planetary gear
xs=1.09819;             % normal modification coefficient of input stage sun gear
xs1=1.07267;            % normal modification coefficient of middle stage sun gear
x1=0;                   % normal modification coefficient of output stage large gear
x2=-0.605264;           % normal modification coefficient of output stage pinion
%%%%%%%%%%%%%%%%%%%%%%%%%%%%%%%%%%%%%%% Parameters
afat=atan(tan(afaw)/cos(beta));              % pressure angle at reference diameter of input stage    radian
betab=atan(tan(beta)*cos(afat));             % helix angle at base diameter of input stage    radian
afat1=atan(tan(afaw1)/cos(beta1));           % pressure angle at reference diameter of middle stage    radian
betab1=atan(tan(beta1)*cos(afat1));           % helix angle at base diameter of middle stage    radian
afat2=atan(tan(afaw2)/cos(beta2));           % pressure angle at reference diameter of output stage    radian
betab2=atan(tan(beta2)*cos(afat2));          % helix angle at base diameter of output stage    radian
rs=mn*zs/cos(beta)/2000;                     %reference radius of input stage sun gear    m
rs1=mn1*zs1/cos(beta1)/2000;                 % reference radius of middle stage sun gear    m
rbs=rs*cos(afat);                             %base radius of input stage sun gear    m
rbs1=rs1*cos(afat1);                          % base radius of middle stage sun gear    m
rp=mn*zp/cos(beta)/2000;                      % reference radius of input stage planetary gear    m
rp1=mn1*zp1/cos(beta1)/2000;                  % reference radius of middle stage planetary gear    m
rbp=rp*cos(afat);                              % base radius of input stage planetary gear    m
rbp1=rp1*cos(afat1);                         % base radius of middle stage planetary gear    m
rb=mn*zb/cos(beta)/2000;                      % reference radius of input stage inner gear rim    m
rb1=mn1*zb1/cos(beta1)/2000;                  % reference radius of middle stage inner gear rim    m
rbb=rb*cos(afat);                              % base radius of input stage inner gear rim    m
rbb1=rb1*cos(afat1);                           % base radius of middle stage inner gear rim    m
a1=mn*(zp+zs)/2000/cos(beta);          %centre distance of input stage external engagement before modification    m
a2=mn*(zb-zp)/2000/cos(beta);           % centre distance of input stage internal engagement before modification    m
a3=mn1*(zp1+zs1)/2000/cos(beta1); % centre distance of middle stage external engagement before modification    m
a4=mn1*(zb1-zp1)/2000/cos(beta1);    % centre distance of middle stage internal engagement before modification    m
a5=mn2*(z1+z2)/2000/cos(beta2);      % centre distance of output stage external engagement before modification    m
afatt1=21.4134*pi/180;        %transverse mesh angle of input stage external engagement    radian
afatt2=21.4134*pi/180;        % transverse mesh angle of input stage internal engagement    radian
afatt3=21.2891*pi/180;        % transverse mesh angle of middle stage external engagement    radian
afatt4=21.2891*pi/180;        % transverse mesh angle of middle stage internal engagement    radian
afatt5=18.2459*pi/180;        % transverse mesh angle of output stage external engagement    radian
aa=a1*cos(afat)/cos(afatt1);       %actual center distance of input stage    m
aa1=a3*cos(afat1)/cos(afatt3);    % actual center distance of middle stage    m
aa2=a5*cos(afat2)/cos(afatt5);    % actual center distance of output stage    m
rc=aa;                              %rotation radius of input stage planetary carrier    m
```

```
rc1=aa1;                    % rotation radius of middle stage planetary carrier    m
rbc=aa*cos(afat);           %equivalent base radius of input stage planetary carrier    m
rbc1=aa1*cos(afat1);        % equivalent base radius of middle stage planetary carrier    m
r1=mn2*z1/cos(beta2)/2000;   % equivalent base radius of output stage planetary carrier    m
r2=mn2*z2/cos(beta2)/2000;     %reference radius of output stage pinion    m
r1b=r1*cos(afat2);             % base radius of output stage large gear    m
r2b=r2*cos(afat2);             % base radius of output stage pinion    m
rD=1.0475;
rD1=0.85;
han=1.0;    %addeneum coefficient
ysp=(aa-a1)*1000/mn;        %center distance modification coefficient of input stage external engagement
ysp1=(aa1-a3)*1000/mn1;     % center distance modification coefficient of middle stage external engagement
yrp=(aa-a2)*1000/mn;        % center distance modification coefficient of input stage internal engagement
yrp1=(aa1-a4)*1000/mn1;     % center distance modification coefficient of middle stage internal engagement
yn12=(aa2-a5)*1000/mn2;     % center distance modification coefficient of output stage external engagement
xsp=xp+xs;           % total modification coefficient
xsp1=xp1+xs1;
xrp=xb-xp;
xrp1=xb1-xp1;
xn12=x1+x2;
deltaysp=xsp-ysp;       %addendum modification coefficient
deltaysp1=xsp1-ysp1;
deltayrp=xrp-yrp;
deltayrp1=xrp1-yrp1;
deltay12=xn12-yn12;
hap=(han+xp-deltaysp)*mn/1000;          % addendum
hap1=(han+xp1-deltaysp1)*mn1/1000;
has=(han+xs-deltaysp)*mn/1000;
has1=(han+xs1-deltaysp1)*mn1/1000;
hab=(han-xb+deltayrp)*mn/1000;
hab1=(han-xb1+deltayrp1)*mn1/1000;
ha1=(han+x1-deltay12)*mn2/1000;
ha2=(han+x2-deltay12)*mn2/1000;
dap=2*rp+2*hap;          %tip diameter of input stage planetary gear    m
dap1=2*rp1+2*hap1;       % tip diameter of middle stage planetary gear    m
das=2*rs+2*has;         % tip diameter of input stage sun gear    m
das1=2*rs1+2*has1;      % tip diameter of middle stage sun gear    m
dab=2*rb-2*hab;         % tip diameter of input stage inner gear rim    m
dab1=2*rb1-2*hab1;      % tip diameter of middle stage inner gear rim    m
d1a=2*r1+2*ha1;          % tip diameter of output stage large gear    m
d2a=2*r2+2*ha2;        % tip diameter of output stage pinion gear    m
```

```
afaatp=acos(rbp/dap*2);                  % pressure angle at tip circle of input stage planetary gear
afaatp1=acos(rbp1/dap1*2);               % pressure angle at tip circle of middle stage planetary gear
afaatb=acos(rbb/dab*2);                  % pressure angle at tip circle of input stage inner gear rim
afaatb1=acos(rbb1/dab1*2);               % pressure angle at tip circle of middle stage inner gear rim
afaats=acos(rbs/das*2);                  % pressure angle at tip circle of input stage sun gear
afaats1=acos(rbs1/das1*2);               % pressure angle at tip circle of middle stage sun gear
afaat1=acos(r1b/d1a*2);                   % pressure angle at tip circle of output stage large gear
afaat2=acos(r2b/d2a*2);                   % pressure angle at tip circle of output stage pinion
%%%%%%%%%%%%%%%%%%%%%%%%%%%%%%%%%%%%%%%%%mass matrix
% % 1:seeking the actual volume
vs=pi*rs*rs*bs;                 %the volume of input stage sun gear    m^3
vs1=pi*rs1*rs1*bs1;             % the volume of middle stage sun gear    m^3
vp=pi*rp*rp*bp;                 % the volume of input stage planetary gear    m^3
vp1=pi*rp1*rp1*bp1;             % the volume of middle stage planetary gear    m^3
vb=pi*(rD*rD-rb*rb)*bb;           % the volume of input stage inner gear rim    m^3
vb1=pi*(rD1*rD1-rb1*rb1)*bb1;     % the volume of middle stage inner gear rim    m^3
v1=pi*r1*r1*b1;                   % the volume of high speed stage large gear    m^3
v2=pi*r2*r2*b2;                   % the volume of high speed stage pinion    m^3
%2:seeking actual mass
no=7850;                    %density    unit: Kg/m^3
ms=vs*no;
ms1=vs1*no;
mp=vp*no;
mp1=vp1*no;
mb=vb*no;
mb1=vb1*no;
m1=v1*no;
m2=v2*no+180;
mc=4836+4*mp;
mc1=1915+3*mp1;
% 3: seeking rotating inertia
js=0.5*ms*rbs*rbs;              %rotating inertia at base circle of input stage sun gear    unit: Kg·m^2
js1=0.5*ms1*rbs1*rbs1;          % rotating inertia at base circle of middle stage sun gear    unit: Kg·m^2
jp=0.5*mp*rbp*rbp;              % rotating inertia at base circle of input stage planetary gear    unit: Kg·m^2
jp1=0.5*mp1*rbp1*rbp1;          % rotating inertia at base circle of middle stage planetary gear    unit: Kg·m^2
jc=0.5*mc*rbc^2;                % rotating inertia of input stage planetary carrier    unit: Kg·m^2
jc1=0.5*mc1*rbc1^2;             % rotating inertia of middle stage planetary carrier    unit: Kg·m^2
jj1=0.5*m1*r1b^2;               % rotating inertia of output stage large gear    unit: Kg·m^2
jj2=0.5*m2*r2b^2;               % rotating inertia of output stage pinion    unit: Kg·m^2
% 4:seeking equivalent tooth number
zsn=zs/(cos(beta)^3);                 % equivalent tooth number of input stage sun gear
```

```
zsn1=zs1/(cos(beta1)^3);                    % equivalent tooth number of middle stage sun gear
zpn=zp/(cos(beta)^3);                        % equivalent tooth number of input stage planetary gear
zpn1=zp1/(cos(beta1)^3);                    % equivalent tooth number of middle stage planetary gear
zbn=zb/(cos(beta)^3);                        % equivalent tooth number of input stage inner gear rim
zbn1=zb1/(cos(beta1)^3);                    % equivalent tooth number of middle stage inner gear rim
zbn1=zb1/(cos(beta1)^3);                    % equivalent tooth number of output stage large gear
zn2=z2/(cos(beta2)^3);                      % equivalent tooth number of output stage pinion
%transverse contact ratio of external engagement
epxla1=(zp*(tan(afaatp)-tan(afatt1))+zs*(tan(afaats)-tan(afatt1)))/2/pi;           %input stage
epxla3=(zp1*(tan(afaatp1)-tan(afatt3))+zs1*(tan(afaats1)-tan(afatt3)))/2/pi;     %middle stage
epxla5=(z1*(tan(afaat1)-tan(afatt5))+z2*(tan(afaat2)-tan(afatt5)))/2/pi;           %output stage
% transverse contact ratio of internal engagement
epxla2=(zp*(tan(afaatp)-tan(afatt2))+zb*(tan(afatt2)-tan(afaatb)))/2/pi;           % input stage
epxla4=(zp1*(tan(afaatp1)-tan(afatt4))+zb1*(tan(afatt4)-tan(afaatb1)))/2/pi;     % middle stage
% flexibility of external engagement single tooth along the direction of tooth width on unit length
q1=0.04723+0.15551/zsn+0.25791/zpn-0.00635*xs-0.11654*xs/zsn-0.00193*xp-0.24188*xp/zpn+0.00529*xs*xs+0.0
0182*xp*xp;       %unit：mm*um/n
q3=0.04723+0.15551/zsn1+0.25791/zpn1-0.00635*xs1-0.11654*xs1/zsn1-0.00193*xp1-0.24188*xp1/zpn1+0.00529*
xs1*xs1+0.00182*xp1*xp1;
q5=0.04723+0.15551/zn2+0.25791/zn1-0.00635*x2-0.11654*x2/zn2-0.00193*x1-0.24188*x1/zn1+0.00529*x2*x2+0
.00182*x1*x1;
% flexibility of internal engagement single tooth along the direction of tooth width on unit length
q2=0.04723+0.15551/zpn+0.25791/zbn-0.00635*xp-0.11654*xp/zpn+0.00193*xb+0.24188*xb/zbn+0.00529*xp*xp+
0.00182*xb*xb;          %unit：mm*um/n
q4=0.04723+0.15551/zpn1+0.25791/zbn1-0.00635*xp1-0.11654*xp1/zpn1+0.00193*xb1+0.24188*xb1/zbn1+0.0052
9*xp1*xp1+0.00182*xb1*xb1;
CB=(1+0.5*(1.2-1.4))*(1-0.02*((20-afan)*pi/180));
CM=0.8;
CR=1;
% meshing stiffness of external engagement single tooth along the direction of tooth width on unit length
kp1=CM*CR*CB*cos(beta)/q1;
kp3=CM*CR*CB*cos(beta1)/q3;
kp5=CM*CR*CB*cos(beta2)/q5;
% meshing stiffness of internal engagement single tooth along the direction of tooth width on unit length
kp2=CM*CR*CB*cos(beta)/q2;
kp4=CM*CR*CB*cos(beta1)/q4;
% meshing stiffness of external engagement single tooth along the direction of tooth width on whole length
tempKsp1=(0.75*epxla1+0.25)*kp1;
tempKsp3=(0.75*epxla3+0.25)*kp3;
tempKsp5=(0.75*epxla5+0.25)*kp5;
km1=tempKsp1*bp*1000000000;   %average stiffness, suitable for steel gear, meshing stiffness on whole gear tooth
```

```
width, and converted into N/m
km3=tempKsp3*bp1*1000000000;
km5=tempKsp5*b1*1000000000;
ksp=km1;
ksp1=km3;
k78=km5;
% meshing stiffness of internal engagement single tooth along the direction of tooth width on whole length
tempKsp2=(0.75*epxla2+0.25)*kp2;
tempKsp4=(0.75*epxla4+0.25)*kp4;
km2=tempKsp2*bp*1000000000;         %average stiffness, suitable for steel gear, meshing stiffness on whole gear
tooth width, and converted into N/m
km4=tempKsp4*bp1*1000000000;
knp=km2;
knp1=km4;
% determine the support stiffness of each shaft on each gear    unit:N/m
kp=5*km2;                     %support stiffness of planetary gear
kp1=5*km4;
ks=1.5*km1;                  % support stiffness of sun gear
ks1=1.5*km3;
k7=1.5*km5;                  % support stiffness of large gear 7
k8=1.5*km5;                  % support stiffness of large gear 8
kcp=1.5*km2;                 % support stiffness of planetary carrier
kcp1=1.5*km4;
%ratational stiffness of planetary carrier
E=2.06e11;       %elastic modulus    Pa
% ko=0.02725*bc*(rc*2)^2*E/2;      %ratational stiffness of planetary carrier
ko=xxjstiffness(2.06e11,0.3,4,825,587,515,100,18.5,0.003,510,1.061,1,1.2,11.256,63.8,26.327,131.7,50,1.3,1.35);   %t
orsional rigidity of first stage planetary carrier
ko1=xxjstiffness(2.06e11,0.3,3,640,240,420,80,18.5,0.003,300,1.045,1,1.2,7.52,83.38,37.04,127.68,60,0.89,1.3);      %
torsional rigidity of second stage planetary carrier
v=0.3;             %poisson's ratio
G=E/2/(1+v);    %shear elastic modulus
D1=0.308;       % transverse diameter of gear section
L1=0.532;       %length of gear section
D2=0.42;       % transverse diameter of shaft section
L2=0.22;       % length of shaft section
kk1=G*pi*D1^4/32/L1;          %stiffness of gear section
kk2=G*pi*D2^4/32/L2;          % stiffness of shaft section
kcs=1/(1/kk1+1/kk2+1/ko1);     %equivalent torsional stiffness of sun shaft
D3=0.24;         % transverse diameter of shaft section
L3=0.265;       % length of shaft section
```

```
D4=0.969;      % transverse diameter of gear section
L4=0.346;      % length of gear section
kk3=G*pi*D3^4/32/L3;     %stiffness of shaft section
kk4=G*pi*D4^4/32/L4;     % stiffness of gear section
kcs1=1/(1/kk3+1/kk4);      % equivalent torsional stiffness of middle stage sun shaft
%damping matrix
%damping of inner gear rim
Qg=0.1;
Cnp=2*Qg*sqrt(km2*mb*mp/(mp+mb));          %%meshing damping of inner gear rim and planetary gear
Cnp1=2*Qg*sqrt(km4*mb1*mp1/(mp1+mb1));
Csp=2*Qg*sqrt(km1*ms*mp/(mp+ms));          %% meshing damping of sun gear and planetary gear
Csp1=2*Qg*sqrt(km3*ms1*mp1/(mp1+ms1));
C78=2*Qg*sqrt(km5*m1*m2/(m1+m2));
%all of support damping is 0
Cs=0;%Csp;                       %support damping of sun gear
Cs1=0;
%CQs=0;                            %ratational damping of sun gear
%Cn=0;%=Cnp;                        % support damping of inner gear rim
%CQn=0;%=0.0001*Cnp ;      % rotational damping of inner gear rim
Cp=0;%=0.5*Cnp;                % support damping of planetary gear
Cp1=0;
%CQp=0;%=0.0001*Cnp ;        % rotational damping of planetary gear
Ccp=0;                              % support damping of planetary carrier
Ccp1=0;
C7=0;           % support damping of large gear 7
C8=0;             % support damping of pinion 8
Ccs=0;          % rotational damping of input stage sun shaft
Ccs1=0;   % rotational damping of middle stage sun shaft
Co=0;                 % rotational damping of planetary carrier
% Co1=0;

%degree of freedom of input stage planetary carrier (torsion x、y、z): x(1), x(2), x(3), x(4)derivative: x(53), x(54), x(55), x(56)
%degree of freedom of input stage planetary gear 1 (torsion x、y、z): x(5), x(6), x(7), x(8) derivative: x(57), x(58), x(59), x(60)
%degree of freedom of input stage planetary gear 2 (torsion、x、y、z): x(9), x(10), x(11), x(12) derivative: x(61), x(62), x(63), x(64)
% degree of freedom of input stage planetary gear 3 (torsion、x、y、z): x(13), x(14), x(15), x(16) derivative: x(65), x(66), x(67), x(68)
% degree of freedom of input stage planetary gear 4 (torsion、x、y、z): x(17), x(18), x(19), x(20) derivative: x(69), x(70), x(71), x(72)
```

```
% degree of freedom of input stage sun gear(torsion、x、y、z):x(21),x(22),x(23),x(24)
derivative:x(73),x(74),x(75),x(76)
% degree of freedom of middle stage sun gear( torsion、x、y、z): x(25), x(26), x(27), x(28) derivative: x(77), x(78),
x(79), x(80)
% degree of freedom of middle stage planetary gear 1( torsion、x、y、z): x(29), x(30), x(31), x(32) derivative:x(81),
x(82), x(83), x(84)
% degree of freedom of middle stage planetary gear 2( torsion、x、y、z): x(33), x(34), x(35), x(36) derivative: x(85),
x(86), x(87), x(88)
% degree of freedom of middle stage planetary gear 3( torsion、x、y、z): x(37), x(38), x(39), x(40) derivative: x(89),
x(90), x(91), x(92)
% degree of freedom of middle stage sun gear( torsion、x、y、z): x(41), x(42), x(43), x(44) derivative: x(93), x(94) ,
x(95), x(96)
% degree of freedom of output stage large gear( torsion、x、y、z): x(45), x(46), x(47), x(48) derivative: x(97), x(98),
x(99), x(100)
% degree of freedom of output stage pinion( torsion、x、y、z): x(49), x(50), x(51), x(52) derivative: x(101), x(102),
x(103), x(104)

% synthetic error
ea1=0;      % synthetic error of input stage external engagement
ea2=0;      % synthetic error of input stage internal engagement
ea3=0;      % synthetic error of middle stage external engagement
ea4=0;      % synthetic error of middle stage internal engagement
ea5=0;      % synthetic error of output stage external engagement
%displacement of input stage external engagement along meshing line
%relative displacement of equivalent torsional deformation along meshing line
xps1sita1=cos(betab)*(rbp*(x(:,5)+x(:,1))-rbs*(x(:,21)-x(:,1)));
xps1sita2=cos(betab)*(rbp*(x(:,9)+x(:,1))-rbs*(x(:,21)-x(:,1)));
xps1sita3=cos(betab)*(rbp*(x(:,13)+x(:,1))-rbs*(x(:,21)-x(:,1)));
xps1sita4=cos(betab)*(rbp*(x(:,17)+x(:,1))-rbs*(x(:,21)-x(:,1)));
% relative displacement derivative of equivalent torsional deformation along meshing line
Dxps1sita1=cos(betab)*(rbp*(x(:,57)+x(:,53))-rbs*(x(:,73)-x(:,53)));
Dxps1sita2=cos(betab)*(rbp*(x(:,61)+x(:,53))-rbs*(x(:,73)-x(:,53)));
Dxps1sita3=cos(betab)*(rbp*(x(:,65)+x(:,53))-rbs*(x(:,73)-x(:,53)));
Dxps1sita4=cos(betab)*(rbp*(x(:,69)+x(:,53))-rbs*(x(:,73)-x(:,53)));
% relative displacement of sun gear and planetary carrier equivalent radial deformation along meshing line
xps1sc1=cos(betab)*(sin(afat)*x(:,22)-cos(afat)*x(:,23)-sin(afat)*x(:,2)+cos(afat)*x(:,3));
xps1sc2=cos(betab)*(sin(afat-pi/2)*x(:,22)-cos(afat-pi/2)*x(:,23)-sin(afat-pi/2)*x(:,2)+cos(afat-pi/2)*x(:,3));
xps1sc3=cos(betab)*(sin(afat-pi)*x(:,22)-cos(afat-pi)*x(:,23)-sin(afat-pi)*x(:,2)+cos(afat-pi)*x(:,3));
xps1sc4=cos(betab)*(sin(afat-pi/2*3)*x(:,22)-cos(afat-pi/2*3)*x(:,23)-sin(afat-pi/2*3)*x(:,2)+cos(afat-pi/2*3)*x(:,3));
%
xps1sc4=cos(betab)*(sin(afat-pi/2*3+wc1*t).*x(:,22)-cos(afat-pi/2*3+wc1*t).*x(:,23)-sin(afat).*x(:,2)+cos(afat).*x(:,
```

```
3));
% relative displacement derivative of sun gear and planetary carrier equivalent radial deformation along meshing line
Dxps1sc1=cos(betab)*(sin(afat)*x(:,74)-cos(afat)*x(:,75)-sin(afat)*x(:,54)+cos(afat)*x(:,55));
Dxps1sc2=cos(betab)*(sin(afat-pi/2)*x(:,74)-cos(afat-pi/2)*x(:,75)-sin(afat-pi/2)*x(:,54)+cos(afat-pi/2)*x(:,55));
Dxps1sc3=cos(betab)*(sin(afat-pi)*x(:,74)-cos(afat-pi)*x(:,75)-sin(afat-pi)*x(:,54)+cos(afat-pi)*x(:,55));
Dxps1sc4=cos(betab)*(sin(afat-pi/2*3)*x(:,74)-cos(afat-pi/2*3)*x(:,75)-sin(afat-pi/2*3)*x(:,54)+cos(afat-pi/2*3)*x(:,
55));
%
Dxps1sc1=cos(betab)*(sin(afat+wc1*t).*(x(:,74))+wc1*cos(afat+wc1*t).*(x(:,22))-cos(afat+wc1*t).*(x(:,75))+wc1*s
in(afat+wc1*t).*(x(:,23))-sin(afat).*x(:,54)+cos(afat).*x(:,55));
%
Dxps1sc2=cos(betab)*(sin(afat-pi/2+wc1*t).*(x(:,74))+wc1*cos(afat-pi/2+wc1*t).*(x(:,22))-cos(afat-pi/2+wc1*t).*(x
(:,75))+wc1*sin(afat-pi/2+wc1*t).*(x(:,23))-sin(afat).*x(:,54)+cos(afat).*x(:,55));
%
Dxps1sc3=cos(betab)*(sin(afat-pi+wc1*t).*(x(:,74))+wc1*cos(afat-pi+wc1*t).*(x(:,22))-cos(afat-pi+wc1*t).*(x(:,75))
+wc1*sin(afat-pi+wc1*t).*(x(:,23))-sin(afat).*x(:,54)+cos(afat).*x(:,55));
%
Dxps1sc4=cos(betab)*(sin(afat-pi/2*3+wc1*t).*(x(:,74))+wc1*cos(afat-pi/2*3+wc1*t).*(x(:,22))-cos(afat-pi/2*3+wc
1*t).*(x(:,75))+wc1*sin(afat-pi/2*3+wc1*t).*(x(:,23))-sin(afat).*x(:,54)+cos(afat).*x(:,55));
% relative displacement of planetary gear equivalent radial deformation along meshing line
xps1p1=cos(betab)*(cos(afat)*x(:,7)-sin(afat)*x(:,6));
xps1p2=cos(betab)*(cos(afat)*x(:,11)-sin(afat)*x(:,10));
xps1p3=cos(betab)*(cos(afat)*x(:,15)-sin(afat)*x(:,14));
xps1p4=cos(betab)*(cos(afat)*x(:,19)-sin(afat)*x(:,18));
% relative displacement derivative of planetary gear equivalent radial deformation along meshing line
Dxps1p1=cos(betab)*(cos(afat)*x(:,59)-sin(afat)*x(:,58));
Dxps1p2=cos(betab)*(cos(afat)*x(:,63)-sin(afat)*x(:,62));
Dxps1p3=cos(betab)*(cos(afat)*x(:,67)-sin(afat)*x(:,66));
Dxps1p4=cos(betab)*(cos(afat)*x(:,71)-sin(afat)*x(:,70));
%external engagement synthetic error
eps1wc1=ea1*sin(pi*(nout-nin)*zs*t/30);
eps1wc2=ea1*sin(pi*(nout-nin)*zs*t/30);
eps1wc3=ea1*sin(pi*(nout-nin)*zs*t/30);
eps1wc4=ea1*sin(pi*(nout-nin)*zs*t/30);
%external engagement synthetic error derivative
Deps1wc1=ea1*pi*(nout-nin)*zs/30*cos(pi*(nout-nin)*zs*t/30);
Deps1wc2=ea1*pi*(nout-nin)*zs/30*cos(pi*(nout-nin)*zs*t/30);
Deps1wc3=ea1*pi*(nout-nin)*zs/30*cos(pi*(nout-nin)*zs*t/30);
Deps1wc4=ea1*pi*(nout-nin)*zs/30*cos(pi*(nout-nin)*zs*t/30);
%relative displacement of external engagement along the meshing line
xps1x1=xps1sita1+xps1sc1+xps1p1-eps1wc1;
```

```
xps1x2=xps1sita2+xps1sc2+xps1p2-eps1wc2;
xps1x3=xps1sita3+xps1sc3+xps1p3-eps1wc3;
xps1x4=xps1sita4+xps1sc4+xps1p4-eps1wc4;
%relative displacement derivative of external engagement along the meshing line
Dxps1x1=Dxps1sita1+Dxps1sc1+Dxps1p1-Deps1wc1;
Dxps1x2=Dxps1sita2+Dxps1sc2+Dxps1p2-Deps1wc2;
Dxps1x3=Dxps1sita3+Dxps1sc3+Dxps1p3-Deps1wc3;
Dxps1x4=Dxps1sita4+Dxps1sc4+Dxps1p4-Deps1wc4;
%external engagement elastic force
Fps1x1=ksp.*xps1x1;
Fps1x2=ksp.*xps1x2;
Fps1x3=ksp.*xps1x3;
Fps1x4=ksp.*xps1x4;
%external engagement damping force
Dps1x1=Csp.*Dxps1x1;
Dps1x2=Csp.*Dxps1x2;
Dps1x3=Csp.*Dxps1x3;
Dps1x4=Csp.*Dxps1x4;
%displacement of input stage internal engagement along meshing line
%relative displacement of equivalent torsional deformation along meshing line
xrp1sita1=cos(betab)*(rbb*x(:,1)-rbp*(x(:,5)+x(:,1)));
xrp1sita2=cos(betab)*(rbb*x(:,1)-rbp*(x(:,9)+x(:,1)));
xrp1sita3=cos(betab)*(rbb*x(:,1)-rbp*(x(:,13)+x(:,1)));
xrp1sita4=cos(betab)*(rbb*x(:,1)-rbp*(x(:,17)+x(:,1)));
%relative displacement derivative of equivalent torsional deformation along meshing line
Dxrp1sita1=cos(betab)*(rbb*x(:,53)-rbp*(x(:,57)+x(:,53)));
Dxrp1sita2=cos(betab)*(rbb*x(:,53)-rbp*(x(:,61)+x(:,53)));
Dxrp1sita3=cos(betab)*(rbb*x(:,53)-rbp*(x(:,65)+x(:,53)));
Dxrp1sita4=cos(betab)*(rbb*x(:,53)-rbp*(x(:,69)+x(:,53)));
%relative displacement of planetary gear and planetary carrier equivalent radial deformation along meshing line
xrp1pc1=cos(betab)*(sin(afat)*x(:,2)+cos(afat)*x(:,3)+sin(afat)*x(:,6)+cos(afat)*x(:,7));
xrp1pc2=cos(betab)*(sin(afat+pi/2)*x(:,2)+cos(afat+pi/2)*x(:,3)+sin(afat)*x(:,10)+cos(afat)*x(:,11));
xrp1pc3=cos(betab)*(sin(afat+pi)*x(:,2)+cos(afat+pi)*x(:,3)+sin(afat)*x(:,14)+cos(afat)*x(:,15));
xrp1pc4=cos(betab)*(sin(afat+pi/2*3)*x(:,2)+cos(afat+pi/2*3)*x(:,3)+sin(afat)*x(:,18)+cos(afat)*x(:,19));
%relative displacement derivative of planetary gear and planetary carrier equivalent radial deformation along meshing line
Dxrp1pc1=cos(betab)*(sin(afat)*x(:,54)+cos(afat)*x(:,55)+sin(afat)*x(:,58)+cos(afat)*x(:,59));
Dxrp1pc2=cos(betab)*(sin(afat+pi/2)*x(:,54)+cos(afat+pi/2)*x(:,55)+sin(afat)*x(:,62)+cos(afat)*x(:,63));
Dxrp1pc3=cos(betab)*(sin(afat+pi)*x(:,54)+cos(afat+pi)*x(:,55)+sin(afat)*x(:,66)+cos(afat)*x(:,67));
Dxrp1pc4=cos(betab)*(sin(afat+pi/2*3)*x(:,54)+cos(afat+pi/2*3)*x(:,55)+sin(afat)*x(:,70)+cos(afat)*x(:,71));
% internal engagement synthetic error
```

```
erp1wc1=ea2*sin(pi*(nout-nin)*zs*t/30);
erp1wc2=ea2*sin(pi*(nout-nin)*zs*t/30);
erp1wc3=ea2*sin(pi*(nout-nin)*zs*t/30);
erp1wc4=ea2*sin(pi*(nout-nin)*zs*t/30);
%internal engagement synthetic error derivative
Derp1wc1=ea2*pi*(nout-nin)*zs/30*cos(pi*(nout-nin)*zs*t/30);
Derp1wc2=ea2*pi*(nout-nin)*zs/30*cos(pi*(nout-nin)*zs*t/30);
Derp1wc3=ea2*pi*(nout-nin)*zs/30*cos(pi*(nout-nin)*zs*t/30);
Derp1wc4=ea2*pi*(nout-nin)*zs/30*cos(pi*(nout-nin)*zs*t/30);
%relative displacement of internal engagement along the meshing line
xrp1x1=xrp1sita1+xrp1pc1-erp1wc1;
xrp1x2=xrp1sita2+xrp1pc2-erp1wc2;
xrp1x3=xrp1sita3+xrp1pc3-erp1wc3;
xrp1x4=xrp1sita4+xrp1pc4-erp1wc4;
%relative displacement derivative of internal engagement along the meshing line
Dxrp1x1=Dxrp1sita1+Dxrp1pc1-Derp1wc1;
Dxrp1x2=Dxrp1sita2+Dxrp1pc2-Derp1wc2;
Dxrp1x3=Dxrp1sita3+Dxrp1pc3-Derp1wc3;
Dxrp1x4=Dxrp1sita4+Dxrp1pc4-Derp1wc4;
%inxternal engagement elastic force
Frp1x1=knp.*xrp1x1;
Frp1x2=knp.*xrp1x2;
Frp1x3=knp.*xrp1x3;
Frp1x4=knp.*xrp1x4;
%internal engagement damping force
Drp1x1=Cnp.*Dxrp1x1;
Drp1x2=Cnp.*Dxrp1x2;
Drp1x3=Cnp.*Dxrp1x3;
Drp1x4=Cnp.*Dxrp1x4;
%displacement of middle stage external engagement along meshing line
%relative displacement of equivalent torsional deformation along meshing line
xps2sita1=cos(betab1)*(rbp1*(x(:,29)+x(:,25))-rbs1*(x(:,41)-x(:,25)));
xps2sita2=cos(betab1)*(rbp1*(x(:,33)+x(:,25))-rbs1*(x(:,41)-x(:,25)));
xps2sita3=cos(betab1)*(rbp1*(x(:,37)+x(:,25))-rbs1*(x(:,41)-x(:,25)));
%relative displacement derivative of equivalent torsional deformation along meshing line
Dxps2sita1=cos(betab1)*(rbp1*(x(:,81)+x(:,77))-rbs1*(x(:,93)-x(:,77)));
Dxps2sita2=cos(betab1)*(rbp1*(x(:,85)+x(:,77))-rbs1*(x(:,93)-x(:,77)));
Dxps2sita3=cos(betab1)*(rbp1*(x(:,89)+x(:,77))-rbs1*(x(:,93)-x(:,77)));
% relative displacement of sun gear and planetary carrier equivalent radial deformation along meshing line
xps2sc1=cos(betab1)*(sin(afat1)*x(:,42)-cos(afat1)*x(:,43)-sin(afat)*x(:,26)+cos(afat)*x(:,27));
xps2sc2=cos(betab1)*(sin(afat1-pi/3*2)*x(:,42)-cos(afat1-pi/3*2)*x(:,43)-sin(afat-pi/3*2)*x(:,26)+cos(afat-pi/3*2)*x
```

```
(:,27));
xps2sc3=cos(betab1)*(sin(afat1-pi/3*4)*x(:,42)-cos(afat1-pi/3*4)*x(:,43)-sin(afat-pi/3*4)*x(:,26)+cos(afat-pi/3*4)*x
(:,27));
% xps2sc1=cos(betab1)*(sin(afat1+wc2*t).*x(:,42)-cos(afat1+wc2*t).*x(:,43)-sin(afat)*x(:,26)+cos(afat)*x(:,27));
%
xps2sc2=cos(betab1)*(sin(afat1-pi/3*2+wc2*t).*x(:,42)-cos(afat1-pi/3*2+wc2*t).*x(:,43)-sin(afat)*x(:,26)+cos(afat)*
x(:,27));
%
xps2sc3=cos(betab1)*(sin(afat1-pi/3*4+wc2*t).*x(:,42)-cos(afat1-pi/3*4+wc2*t).*x(:,43)-sin(afat)*x(:,26)+cos(afat)*
x(:,27));
% relative displacement derivative of sun gear and planetary carrier equivalent radial deformation along meshing line
Dxps2sc1=cos(betab1)*(sin(afat1)*x(:,94)-cos(afat1)*x(:,95)-sin(afat)*x(:,78)+cos(afat)*x(:,79));
Dxps2sc2=cos(betab1)*(sin(afat1-pi/3*2)*x(:,94)-cos(afat1-pi/3*2)*x(:,95)-sin(afat-pi/3*2)*x(:,78)+cos(afat-pi/3*2)*
x(:,79));
Dxps2sc3=cos(betab1)*(sin(afat1-pi/3*4)*x(:,94)-cos(afat1-pi/3*4)*x(:,95)-sin(afat-pi/3*4)*x(:,78)+cos(afat-pi/3*4)*
x(:,79));
%
Dxps2sc1=cos(betab1)*(sin(afat1+wc2*t).*x(:,94)+wc2*cos(afat1+wc2*t).*x(:,42)-cos(afat1+wc2*t).*x(:,95)+wc2*s
in(afat1+wc2*t).*x(:,43)-sin(afat)*x(:,78)+cos(afat)*x(:,79));
%
Dxps2sc2=cos(betab1)*(sin(afat1-pi/3*2+wc2*t).*x(:,94)+wc2*cos(afat1-pi/3*2+wc2*t).*x(:,42)-cos(afat1-pi/3*2+w
c2*t).*x(:,95)+wc2*sin(afat1-pi/3*2+wc2*t).*x(:,43)-sin(afat)*x(:,78)+cos(afat)*x(:,79));
%
Dxps2sc3=cos(betab1)*(sin(afat1-pi/3*4+wc2*t).*x(:,94)+wc2*cos(afat1-pi/3*4+wc2*t).*x(:,42)-cos(afat1-pi/3*4+w
c2*t).*x(:,95)+wc2*sin(afat1-pi/3*4+wc2*t).*x(:,43)-sin(afat)*x(:,78)+cos(afat)*x(:,79));
% relative displacement of planetary gear equivalent radial deformation along meshing line
xps2p1=cos(betab1)*(cos(afat1)*x(:,31)-sin(afat1)*x(:,30));
xps2p2=cos(betab1)*(cos(afat1)*x(:,35)-sin(afat1)*x(:,34));
xps2p3=cos(betab1)*(cos(afat1)*x(:,39)-sin(afat1)*x(:,38));
% relative displacement derivative of planetary gear equivalent radial deformation along meshing line
Dxps2p1=cos(betab1)*(cos(afat1)*x(:,83)-sin(afat1)*x(:,82));
Dxps2p2=cos(betab1)*(cos(afat1)*x(:,87)-sin(afat1)*x(:,86));
Dxps2p3=cos(betab1)*(cos(afat1)*x(:,91)-sin(afat1)*x(:,90));
%external engagement synthetic error
eps2wc1=ea3*sin(pi*(n1-nout)*zs1*t/30);
eps2wc2=ea3*sin(pi*(n1-nout)*zs1*t/30);
eps2wc3=ea3*sin(pi*(n1-nout)*zs1*t/30);
%external engagement synthetic error derivative
Deps2wc1=ea3*pi*(n1-nout)*zs1/30*cos(pi*(n1-nout)*zs1*t/30);
Deps2wc2=ea3*pi*(n1-nout)*zs1/30*cos(pi*(n1-nout)*zs1*t/30);
Deps2wc3=ea3*pi*(n1-nout)*zs1/30*cos(pi*(n1-nout)*zs1*t/30);
%relative displacement of external engagement along the meshing line
```

```
xps2x1=xps2sita1+xps2sc1+xps2p1-eps2wc1;
xps2x2=xps2sita2+xps2sc2+xps2p2-eps2wc2;
xps2x3=xps2sita3+xps2sc3+xps2p3-eps2wc3;
%relative displacement derivative of external engagement along the meshing line
Dxps2x1=Dxps2sita1+Dxps2sc1+Dxps2p1-Deps2wc1;
Dxps2x2=Dxps2sita2+Dxps2sc2+Dxps2p2-Deps2wc2;
Dxps2x3=Dxps2sita3+Dxps2sc3+Dxps2p3-Deps2wc3;
%external engagement elastic force
Fps2x1=ksp1.*xps2x1;
Fps2x2=ksp1.*xps2x2;
Fps2x3=ksp1.*xps2x3;
%external engagement damping force
Dps2x1=Csp1.*Dxps2x1;
Dps2x2=Csp1.*Dxps2x2;
Dps2x3=Csp1.*Dxps2x3;
%displacement of middle stage internal engagement along meshing line
%relative displacement of equivalent torsional deformation along meshing line
xrp2sita1=cos(betab1)*(rbb1*x(:,25)-rbp1*(x(:,29)+x(:,25)));
xrp2sita2=cos(betab1)*(rbb1*x(:,25)-rbp1*(x(:,33)+x(:,25)));
xrp2sita3=cos(betab1)*(rbb1*x(:,25)-rbp1*(x(:,37)+x(:,25)));
%relative displacement derivative of equivalent torsional deformation along meshing line
Dxrp2sita1=cos(betab1)*(rbb1*x(:,77)-rbp1*(x(:,81)+x(:,77)));
Dxrp2sita2=cos(betab1)*(rbb1*x(:,77)-rbp1*(x(:,85)+x(:,77)));
Dxrp2sita3=cos(betab1)*(rbb1*x(:,77)-rbp1*(x(:,89)+x(:,77)));
%relative displacement of planetary gear and planetary carrier equivalent radial deformation along meshing line
xrp2pc1=cos(betab1)*(sin(afat1)*x(:,26)+cos(afat1)*x(:,27)+sin(afat1)*x(:,30)+cos(afat1)*x(:,31));
xrp2pc2=cos(betab1)*(sin(afat1+pi/3*2)*x(:,26)+cos(afat1+pi/3*2)*x(:,27)+sin(afat1)*x(:,34)+cos(afat1)*x(:,35));
xrp2pc3=cos(betab1)*(sin(afat1+pi/3*4)*x(:,26)+cos(afat1+pi/3*4)*x(:,27)+sin(afat1)*x(:,38)+cos(afat1)*x(:,39));
%relative displacement derivative of planetary gear and planetary carrier equivalent radial deformation along meshing line
Dxrp2pc1=cos(betab1)*(sin(afat1)*x(:,78)+cos(afat1)*x(:,79)+sin(afat1)*x(:,82)+cos(afat1)*x(:,83));
Dxrp2pc2=cos(betab1)*(sin(afat1+pi/3*2)*x(:,78)+cos(afat1+pi/3*2)*x(:,79)+sin(afat1)*x(:,86)+cos(afat1)*x(:,87));
Dxrp2pc3=cos(betab1)*(sin(afat1+pi/3*4)*x(:,78)+cos(afat1+pi/3*4)*x(:,79)+sin(afat1)*x(:,90)+cos(afat1)*x(:,91));
%internal engagement synthetic error
erp2wc1=ea4*sin(pi*(n1-nout)*zs1*t/30);
erp2wc2=ea4*sin(pi*(n1-nout)*zs1*t/30);
erp2wc3=ea4*sin(pi*(n1-nout)*zs1*t/30);
%internal engagement synthetic error derivative
Derp2wc1=ea4*pi*(n1-nout)*zs1/30*cos(pi*(n1-nout)*zs1*t/30);
Derp2wc2=ea4*pi*(n1-nout)*zs1/30*cos(pi*(n1-nout)*zs1*t/30);
Derp2wc3=ea4*pi*(n1-nout)*zs1/30*cos(pi*(n1-nout)*zs1*t/30);
```

```
%relative displacement of internal engagement along the meshing line
xrp2x1=xrp2sita1+xrp2pc1-erp2wc1;
xrp2x2=xrp2sita2+xrp2pc2-erp2wc2;
xrp2x3=xrp2sita3+xrp2pc3-erp2wc3;
%relative displacement derivative of internal engagement along the meshing line
Dxrp2x1=Dxrp2sita1+Dxrp2pc1-Derp2wc1;
Dxrp2x2=Dxrp2sita2+Dxrp2pc2-Derp2wc2;
Dxrp2x3=Dxrp2sita3+Dxrp2pc3-Derp2wc3;
%internal engagement elastic force
Frp2x1=knp1.*xrp2x1;
Frp2x2=knp1.*xrp2x2;
Frp2x3=knp1.*xrp2x3;
%internal engagement damping force
Drp2x1=Cnp1.*Dxrp2x1;
Drp2x2=Cnp1.*Dxrp2x2;
Drp2x3=Cnp1.*Dxrp2x3;
%relative displacement of helical 7 and helical 8 along the directional meshing line
x781=cos(betab2)*((r1b.*x(:,45)-r2b.*x(:,49))+cos(afat2).*(x(:,47)-x(:,51))+sin(afat2).*(x(:,46)-x(:,50)));
Dx781=cos(betab2)*((r1b.*x(:,97)-r2b.*x(:,101))+cos(afat2).*(x(:,99)-x(:,103))+sin(afat2).*(x(:,98)-x(:,102)));
e78=ea5*sin(pi*n2*z2*t/30);
De78=ea5*pi*n2*z2/30*cos(pi*n2*z2*t/30);
x78=x781-e78;
Dx78=Dx781-De78;
F78=k78.*x78;
D78=C78.*Dx78;
%%%%%%%%%%%%%%%%%%%%%%%%%%%%%%%%%%%%%%%%%%%%%%%%%
Toutm=9.55*1000*p/n2;              %unit :Nm
Tc=0.3;       %torque change coefficient
Ta=Toutm*Tc;
deltaT1=Ta*sin(wc3*t);
Tout=Toutm+deltaT1;
Tinm1=Tinm/(1+zb/zs);
F1=Tinm1/4/rbs;
Tinm2=Tinm1/(1+zb1/zs1);
F2=Tinm2/rbs1/3;
Tinm3=Tinm2*z2/z1;
F3=Tinm3/r2b;
%%%%%%%%%%%%%%%%%%%%%%%%%%%%%%%%%%%%%%%%%%%%%%%%%
Ff1=Fps1x1/F1;
Ff2=Fps1x2/F1;
Ff3=Fps1x3/F1;
```

```
Ff4=Fps1x4/F1;
figure (1)
plot(t,Ff1);
title(['(damping dynamic load coefficient curve-input stage sun gear and planetary gear)']);
xlabel('time    t/s');
ylabel('using factor    KA');
box off;
hold on;
Ff5=Frp1x1/F1;
Ff6=Frp1x2/F1;
Ff7=Frp1x3/F1;
Ff8=Frp1x4/F1;
figure (2)
plot(t,Ff5);
title(['(damping dynamic load coefficient curve-input stage planetary gear and inner gear rim)']);
xlabel('time    t/s');
ylabel('using factor      KA');
box off;
      hold on;
Ff11=Fps2x1/F2;
Ff22=Fps2x2/F2;
Ff33=Fps2x3/F2;
figure (3)
plot(t,Ff11);
title(['(damping dynamic load coefficient curve-middle stage planetary gear and sun gear)']);
xlabel('time    t/s');
ylabel('using factor    KA');
box off;
      hold on;
Ff44=Frp2x1/F2;
Ff55=Frp2x2/F2;
Ff66=Frp2x3/F2;
 figure (4)
plot(t,Ff44);
title(['(damping dynamic load coefficient curve-middle stage planetary gear and inner gear rim)']);
xlabel('time    t/s');
ylabel('using factor    KA');
box off;
hold on;
 mm=F78/F3;
 figure (5)
```

A.2 Subprogram.m

```
          plot(t,mm);
        title(['(damping dynamic load coefficient curve-high speed stage)']);
xlabel('time    t/s');
ylabel('using factor    KA');
box off;
hold on;
function jjfc=mkcf(t,x)%jjfc express reduced order equation
midu=1.225;        %wind density      Kg/m3
R=52;            %radius of wind wheel      m
lamad=9;      %blade tip speed ratio
Cplamad=0.485;      % wind energy utilization coefficient
Ctlamad=Cplamad/lamad;      %torque coefficient
Vc=0.85;      % change coefficient
Vm=13;      % average wind speed
Va=Vm*Vc;    %wind velocity amplitude
Tinm=1/2*midu*pi*R^3*Ctlamad*Vm^2;

%input gear parameters:     b or n_internal gear        c_planet carrier        p_planet gear             s_sun gear
mn=12;                          %input stage module    mm
mn1=8;                          %middle stage module    mm
mn2=8;                          %output stage module    mm
bet=9.0724;                      %input stage helix angle
bet1=9.20947;                    %middle stage helix angle
bet2=4.35489;                    %output stage helix angle
beta=bet*pi/180;               % input stage helix angle    radian
beta1=bet1*pi/180;         % middle stage helix angle    radian
beta2=bet2*pi/180;           % output stage helix angle    radian
zs=44;                          %the number of input stage sun gear
zs1=38;                          % the number of middle stage sun gear
zp=53;                           % the number of output stage planetary gear
zp1=64;                          % the number of middle stage planetary gear
zb=151;                          %the number of input stage internal gear
zb1=165;                         % the number of middle stage internal gear
z1=86;                           %the number of out stage large gear
z2=29;                           %the number of output stage pinion
nin=13;                         %the input speed of input stage planetary carrier    r/min
wc1=2*pi*nin/60;
p=Tinm*nin/9549;                          %power    KW
deltaT=1/2*midu*pi*R^3*Ctlamad*Va^2*sin(wc1*t).*sin(wc1*t);      %alternating section of input torque
Tin=Tinm+deltaT;    %input torque
i1=1+zb/zs;         % transmission ratio of input stage
```

```
i2=1+zb1/zs1;     % transmission ratio of middle stage
i3=z1/z2;         % transmission ratio of out stage
nout=nin*i1;            %the speed of middle stage planetary carrier(the speed of input stage sun gear)    r/min
wc2=2*pi*nout/60;
n1=nout*i2;             % the speed of out stage large gear( the speed of middle stage sun gear)      r/min
n2=n1*i3;            %the speed of output pinion      r/min
wc3=2*pi*n2/60;
alfa=20;        %pressure angle of input stage
alfa1=20;       % pressure angle of middle stage
alfa2=20;       % pressure angle of output stage
afaw=alfa*pi/180;         %out meshing normal pressure angle of input stage    radian
afan=alfa*pi/180;         %internal meshing normal pressure angle of input stage    radian
afaw1=alfa1*pi/180;         %out meshing normal pressure angle of middle stage    radian
afan1=alfa1*pi/180;       % internal meshing normal pressure angle of middle stage    radian
afaw2=alfa2*pi/180;      % out meshing normal pressure angle of output stage    radian
gw=0.532;                    %tooth width of input stage    m
gw1=0.213;                     % tooth width of middle stage    m
gw2=0.346;                     % tooth width of output stage    m
bs=gw;                      %tooth width of input stage sun gear    m
bs1=gw1;                     % tooth width of middle stage sun gear    m
bp=gw;                       %tooth width of input stage planetary gear    m
bp1=gw1;                     % tooth width of middle stage planetary gear    m
bb=gw;                       %tooth width of input stage internal gear    m
bb1=gw1;                     % tooth width of middle stage internal gear    m
b1=gw2;                      % tooth width of out stage large gear    m
b2=gw2;                      % tooth width of out stage pinion    m
xb=-0.298194;               %normal modification coefficient of input stage internal gear    mm
xb1=-0.337459;              % normal modification coefficient of middle stage internal gear    mm
xp=-0.698194;               % normal modification coefficient of input stage planetary gear
xp1=-0.705062;              % normal modification coefficient of middle stage planetary gear
xs=1.09819;                 % normal modification coefficient of input stage sun gear
xs1=1.07267;                % normal modification coefficient of middle stage sun gear
x1=0;                       % normal modification coefficient of output stage large gear
x2=-0.605264;                 % normal modification coefficient of output stage pinion
%%%%%%%%%%%%%%%%%%%%%%%%%%%%%%%%%%%%%%%%%%%%%% middle parameter
afat=atan(tan(afaw)/cos(beta));                  % pressure angle at reference diameter of input stage    radian
betab=atan(tan(beta)*cos(afat));                   % helix angle at base diameter of input stage    radian
afat1=atan(tan(afaw1)/cos(beta1));              % pressure angle at reference diameter of middle stage    radian
betab1=atan(tan(beta1)*cos(afat1));             % helix angle at base diameter of middle stage    radian
afat2=atan(tan(afaw2)/cos(beta2));              % pressure angle at reference diameter of output stage    radian
betab2=atan(tan(beta2)*cos(afat2));             % helix angle at base diameter of output stage    radian
```

```
rs=mn*zs/cos(beta)/2000;                    %reference radius of input stage sun gear    m
rs1=mn1*zs1/cos(beta1)/2000;                % reference radius of middle stage sun gear    m
rbs=rs*cos(afat);                           %base radius of input stage sun gear    m
rbs1=rs1*cos(afat1);                        % base radius of middle stage sun gear    m
rp=mn*zp/cos(beta)/2000;                     % reference radius of input stage planetary gear    m
rp1=mn1*zp1/cos(beta1)/2000;                 % reference radius of middle stage planetary gear    m
rbp=rp*cos(afat);                             % base radius of input stage planetary gear    m
rbp1=rp1*cos(afat1);                          % base radius of middle stage planetary gear    m
rb=mn*zb/cos(beta)/2000;                      % reference radius of input stage inner gear rim    m
rb1=mn1*zb1/cos(beta1)/2000;                  % reference radius of middle stage inner gear rim    m
rbb=rb*cos(afat);                               % base radius of input stage inner gear rim    m
rbb1=rb1*cos(afat1);                            % base radius of middle stage inner gear rim    m
a1=mn*(zp+zs)/2000/cos(beta);      %centre distance of input stage external engagement before modification    m
a2=mn*(zb-zp)/2000/cos(beta);          % centre distance of input stage internal engagement before modification    m
a3=mn1*(zp1+zs1)/2000/cos(beta1); % centre distance of middle stage external engagement before modification    m
a4=mn1*(zb1-zp1)/2000/cos(beta1);    % centre distance of middle stage internal engagement before modification    m
a5=mn2*(z1+z2)/2000/cos(beta2);      % centre distance of output stage external engagement before modification    m
afatt1=21.4134*pi/180;         %transverse mesh angle of input stage external engagement    radian
afatt2=21.4134*pi/180;         % transverse mesh angle of input stage internal engagement    radian
afatt3=21.2891*pi/180;         % transverse mesh angle of middle stage external engagement    radian
afatt4=21.2891*pi/180;         % transverse mesh angle of middle stage internal engagement    radian
afatt5=18.2459*pi/180;         % transverse mesh angle of output stage external engagement    radian
aa=a1*cos(afat)/cos(afatt1);       %actual center distance of input stage    m
aa1=a3*cos(afat1)/cos(afatt3);    % actual center distance of middle stage    m
aa2=a5*cos(afat2)/cos(afatt5);    % actual center distance of output stage    m
rc=aa;                              %rotation radius of input stage planetary carrier    m
rc1=aa1;                            % rotation radius of middle stage planetary carrier    m
rbc=aa*cos(afat);                   %equivalent base radius of input stage planetary carrier    m
rbc1=aa1*cos(afat1);                % equivalent base radius of middle stage planetary carrier    m
r1=mn2*z1/cos(beta2)/2000;       % equivalent base radius of output stage planetary carrier    m
r2=mn2*z2/cos(beta2)/2000;       %reference radius of output stage pinion    m
r1b=r1*cos(afat2);                 % base radius of output stage large gear    m
r2b=r2*cos(afat2);                 % base radius of output stage pinion    m
rD=1.0475;
rD1=0.85;

han=1.0;     %addeneum coefficient
ysp=(aa-a1)*1000/mn;          %center distance modification coefficient of input stage external engagement
ysp1=(aa1-a3)*1000/mn1;     % center distance modification coefficient of middle stage external engagement
yrp=(aa-a2)*1000/mn;          % center distance modification coefficient of input stage internal engagement
yrp1=(aa1-a4)*1000/mn1;     % center distance modification coefficient of middle stage internal engagement
```

```
yn12=(aa2-a5)*1000/mn2;     % center distance modification coefficient of output stage external engagement
xsp=xp+xs;              % total modification coefficient
xsp1=xp1+xs1;
xrp=xb-xp;
xrp1=xb1-xp1;
xn12=x1+x2;
deltaysp=xsp-ysp;        %addendum modification coefficient
deltaysp1=xsp1-ysp1;
deltayrp=xrp-yrp;
deltayrp1=xrp1-yrp1;
deltay12=xn12-yn12;
hap=(han+xp-deltaysp)*mn/1000;          % addendum
hap1=(han+xp1-deltaysp1)*mn1/1000;
has=(han+xs-deltaysp)*mn/1000;
has1=(han+xs1-deltaysp1)*mn1/1000;
hab=(han-xb+deltayrp)*mn/1000;
hab1=(han-xb1+deltayrp1)*mn1/1000;
ha1=(han+x1-deltay12)*mn2/1000;
ha2=(han+x2-deltay12)*mn2/1000;
dap=2*rp+2*hap;        %tip diameter of input stage planetary gear    m
dap1=2*rp1+2*hap1;   % tip diameter of middle stage planetary gear    m
das=2*rs+2*has;        % tip diameter of input stage sun gear    m
das1=2*rs1+2*has1;   % tip diameter of middle stage sun gear    m
dab=2*rb-2*hab;        % tip diameter of input stage inner gear rim    m
dab1=2*rb1-2*hab1;   % tip diameter of middle stage inner gear rim    m
d1a=2*r1+2*ha1;        % tip diameter of output stage large gear    m
d2a=2*r2+2*ha2;        % tip diameter of output stage pinion gear    m

afaatp=acos(rbp/dap*2);                       % pressure angle at tip circle of input stage planetary gear
afaatp1=acos(rbp1/dap1*2);                    % pressure angle at tip circle of middle stage planetary gear
afaatb=acos(rbb/dab*2);                         % pressure angle at tip circle of input stage inner gear rim
afaatb1=acos(rbb1/dab1*2);                      % pressure angle at tip circle of middle stage inner gear rim
afaats=acos(rbs/das*2);                         % pressure angle at tip circle of input stage sun gear
afaats1=acos(rbs1/das1*2);                      % pressure angle at tip circle of middle stage sun gear
afaat1=acos(r1b/d1a*2);                           % pressure angle at tip circle of output stage large gear
afaat2=acos(r2b/d2a*2);                           % pressure angle at tip circle of output stage pinion

%%%%%%%%%%%%%%%%%%%%%%%%%%%%%%%%%%%%%%%%%%%%mass matrix
% 1:seeking the actual volume
vs=pi*rs*rs*bs;                   %the volume of input stage sun gear    m^3
vs1=pi*rs1*rs1*bs1;               % the volume of middle stage sun gear    m^3
```

```
vp=pi*rp*rp*bp;                    % the volume of input stage planetary gear    m^3
vp1=pi*rp1*rp1*bp1;                % the volume of middle stage planetary gear    m^3
vb=pi*(rD*rD-rb*rb)*bb;            % the volume of input stage inner gear rim    m^3
vb1=pi*(rD1*rD1-rb1*rb1)*bb1;      % the volume of middle stage inner gear rim    m^3
v1=pi*r1*r1*b1;                    % the volume of high speed stage large gear    m^3
v2=pi*r2*r2*b2;                    % the volume of high speed stage pinion    m^3
%2:seeking actual mass
no=7850;                      %density    unit: Kg/m^3
ms=vs*no;
ms1=vs1*no;
mp=vp*no;
mp1=vp1*no;
mb=vb*no;
mb1=vb1*no;
m1=v1*no;
m2=v2*no+180;
mc=4836+4*mp;
mc1=1915+3*mp1;
% 3: seeking rotating inertia
js=0.5*ms*rbs*rbs;                %rotating inertia at base circle of input stage sun gear    unit: Kg·m^2
js1=0.5*ms1*rbs1*rbs1;            % rotating inertia at base circle of middle stage sun gear    unit: Kg·m^2
jp=0.5*mp*rbp*rbp;                % rotating inertia at base circle of input stage planetary gear    unit: Kg·m^2
jp1=0.5*mp1*rbp1*rbp1;            % rotating inertia at base circle of middle stage planetary gear    unit: Kg·m^2
jc=0.5*mc*rbc^2;                  % rotating inertia of input stage planetary carrier    unit: Kg·m^2
jc1=0.5*mc1*rbc1^2;               % rotating inertia of middle stage planetary carrier    unit: Kg·m^2
jj1=0.5*m1*r1b^2;                   % rotating inertia of output stage large gear    unit: Kg·m^2
jj2=0.5*m2*r2b^2;                 % rotating inertia of output stage pinion    unit: Kg·m^2
% 4:seeking equivalent tooth number
zsn=zs/(cos(beta)^3);                     % equivalent tooth number of input stage sun gear
zsn1=zs1/(cos(beta1)^3);                  % equivalent tooth number of middle stage sun gear
zpn=zp/(cos(beta)^3);                      % equivalent tooth number of input stage planetary gear
zpn1=zp1/(cos(beta1)^3);                   % equivalent tooth number of middle stage planetary gear
zbn=zb/(cos(beta)^3);                      % equivalent tooth number of input stage inner gear rim
zbn1=zb1/(cos(beta1)^3);                   % equivalent tooth number of middle stage inner gear rim
zbn1=zb1/(cos(beta1)^3);                   % equivalent tooth number of output stage large gear
zn2=z2/(cos(beta2)^3);                     % equivalent tooth number of output stage pinion

%transverse contact ratio of external engagement
epxla1=(zp*(tan(afaatp)-tan(afatt1))+zs*(tan(afaats)-tan(afatt1)))/2/pi;          %input stage
epxla3=(zp1*(tan(afaatp1)-tan(afatt3))+zs1*(tan(afaats1)-tan(afatt3)))/2/pi;     %middle stage
epxla5=(z1*(tan(afaat1)-tan(afatt5))+z2*(tan(afaat2)-tan(afatt5)))/2/pi;          %output stage
```

```
% transverse contact ratio of internal engagement
epxla2=(zp*(tan(afaatp)-tan(afatt2))+zb*(tan(afatt2)-tan(afaatb)))/2/pi;          % input stage
epxla4=(zp1*(tan(afaatp1)-tan(afatt4))+zb1*(tan(afatt4)-tan(afaatb1)))/2/pi;     % middle stage
% flexibility of external engagement single tooth along the direction of tooth width on unit length
q1=0.04723+0.15551/zsn+0.25791/zpn-0.00635*xs-0.11654*xs/zsn-0.00193*xp-0.24188*xp/zpn+0.00529*xs*xs+0.00182*xp*xp;      %unit：mm*um/n
q3=0.04723+0.15551/zsn1+0.25791/zpn1-0.00635*xs1-0.11654*xs1/zsn1-0.00193*xp1-0.24188*xp1/zpn1+0.00529*xs1*xs1+0.00182*xp1*xp1;
q5=0.04723+0.15551/zn2+0.25791/zn1-0.00635*x2-0.11654*x2/zn2-0.00193*x1-0.24188*x1/zn1+0.00529*x2*x2+0.00182*x1*x1;
% flexibility of internal engagement single tooth along the direction of tooth width on unit length
q2=0.04723+0.15551/zpn+0.25791/zbn-0.00635*xp-0.11654*xp/zpn+0.00193*xb+0.24188*xb/zbn+0.00529*xp*xp+0.00182*xb*xb;          %unit：mm*um/n
q4=0.04723+0.15551/zpn1+0.25791/zbn1-0.00635*xp1-0.11654*xp1/zpn1+0.00193*xb1+0.24188*xb1/zbn1+0.00529*xp1*xp1+0.00182*xb1*xb1;
CB=(1+0.5*(1.2-1.4))*(1-0.02*((20-afan)*pi/180));
CM=0.8;
CR=1;
% meshing stiffness of external engagement single tooth along the direction of tooth width on unit length
kp1=CM*CR*CB*cos(beta)/q1;
kp3=CM*CR*CB*cos(beta1)/q3;
kp5=CM*CR*CB*cos(beta2)/q5;
% meshing stiffness of internal engagement single tooth along the direction of tooth width on unit length
kp2=CM*CR*CB*cos(beta)/q2;
kp4=CM*CR*CB*cos(beta1)/q4;
% meshing stiffness of external engagement single tooth along the direction of tooth width on whole length
tempKsp1=(0.75*epxla1+0.25)*kp1;
tempKsp3=(0.75*epxla3+0.25)*kp3;
tempKsp5=(0.75*epxla5+0.25)*kp5;
km1=tempKsp1*bp*1000000000;   %average stiffness, suitable for steel gear, meshing stiffness on whole gear tooth
km3=tempKsp3*bp1*1000000000;
km5=tempKsp5*b1*1000000000;
ksp=km1;
ksp1=km3;
k78=km5;
% meshing stiffness of internal engagement single tooth along the direction of tooth width on whole length
tempKsp2=(0.75*epxla2+0.25)*kp2;
tempKsp4=(0.75*epxla4+0.25)*kp4;
km2=tempKsp2*bp*1000000000;          %average stiffness, suitable for steel gear, meshing stiffness on whole gear
km4=tempKsp4*bp1*1000000000;
knp=km2;
```

```
knp1=km4;
% determine the support stiffness of each shaft on each gear    unit:N/m
kp=5*km2;                                   %support stiffness of planetary gear
kp1=5*km4;
ks=1.5*km1;                                 % support stiffness of sun gear
ks1=1.5*km3;
k7=1.5*km5;                 % support stiffness of large gear 7
k8=1.5*km5;                 % support stiffness of large gear 8
kcp=1.5*km2;                                % support stiffness of planetary carrier
kcp1=1.5*km4;
%ratational stiffness of planetary carrier
E=2.06e11;        %elastic modulus    Pa
% ko=0.02725*bc*(rc*2)^2*E/2;      %ratational stiffness of planetary carrier
ko=xxjstiffness(2.06e11,0.3,4,825,587,515,100,18.5,0.003,510,1.061,1,1.2,11.256,63.8,26.327,131.7,50,1.3,1.35);   %torsional rigidity of first stage planetary carrier
ko1=xxjstiffness(2.06e11,0.3,3,640,240,420,80,18.5,0.003,300,1.045,1,1.2,7.52,83.38,37.04,127.68,60,0.89,1.3);      % torsional rigidity of second stage planetary carrier
v=0.3;    %poisson’s ratio
G=E/2/(1+v);    %shear elastic modulus
D1=0.308;    % transverse diameter of gear section
L1=0.532;    %length of gear section
D2=0.42;    % transverse diameter of shaft section
L2=0.22;    % length of shaft section
kk1=G*pi*D1^4/32/L1;    %stiffness of gear section
kk2=G*pi*D2^4/32/L2;    % stiffness of shaft section
kcs=1/(1/kk1+1/kk2+1/ko1); %equivalent torsional stiffness of sun shaft
D3=0.24;          % transverse diameter of shaft section
L3=0.265;         % length of shaft section
D4=0.969;      % transverse diameter of gear section
L4=0.346;      % length of gear section
kk3=G*pi*D3^4/32/L3;    %stiffness of shaft section
kk4=G*pi*D4^4/32/L4;    % stiffness of gear section
kcs1=1/(1/kk3+1/kk4);    % equivalent torsional stiffness of middle stage sun shaft

%damping matrix
%damping of inner gear rim
Qg=0.1;
Cnp=2*Qg*sqrt(km2*mb*mp/(mp+mb));            %%meshing damping of inner gear rim and planetary gear
Cnp1=2*Qg*sqrt(km4*mb1*mp1/(mp1+mb1));
Csp=2*Qg*sqrt(km1*ms*mp/(mp+ms));            %% meshing damping of sun gear and planetary gear
Csp1=2*Qg*sqrt(km3*ms1*mp1/(mp1+ms1));
```

```
C78=2*Qg*sqrt(km5*m1*m2/(m1+m2));
%all of support damping is 0
Cs=0;%Csp;                    %support damping of sun gear
Cs1=0;
Cp=0;%=0.5*Cnp;               % support damping of planetary gear
Cp1=0;
Ccp=0;                        % support damping of planetary carrier
Ccp1=0;
C7=0;            % support damping of large gear 7
C8=0;            % support damping of pinion 8
Ccs=0;           % rotational damping of input stage sun shaft
Ccs1=0;          % rotational damping of middle stage sun shaft
Co=0;            % rotational damping of planetary carrier
%degree of freedom of input stage planetary carrier (torsion x、y、z): x(1), x(2), x(3), x(4)derivative: x(53), x(54), x(55), x(56)
%degree of freedom of input stage planetary gear 1 (torsion x、y、z): x(5), x(6), x(7), x(8) derivative: x(57), x(58), x(59), x(60)
%degree of freedom of input stage planetary gear 2 (torsion、x、y、z): x(9), x(10), x(11), x(12) derivative: x(61), x(62), x(63), x(64)
% degree of freedom of input stage planetary gear 3 (torsion、x、y、z): x(13), x(14), x(15), x(16) derivative: x(65), x(66), x(67), x(68)
% degree of freedom of input stage planetary gear 4 (torsion、x、y、z): x(17), x(18), x(19), x(20) derivative: x(69), x(70), x(71), x(72)
% degree of freedom of input stage sun gear(torsion、x、y、z):x(21),x(22),x(23),x(24) derivative:x(73),x(74),x(75),x(76)
% degree of freedom of middle stage sun gear( torsion、x、y、z): x(25), x(26), x(27), x(28) derivative: x(77), x(78), x(79), x(80)
% degree of freedom of middle stage planetary gear 1( torsion、x、y、z): x(29), x(30), x(31), x(32) derivative:x(81), x(82), x(83), x(84)
% degree of freedom of middle stage planetary gear 2( torsion、x、y、z): x(33), x(34), x(35), x(36) derivative: x(85), x(86), x(87), x(88)
% degree of freedom of middle stage planetary gear 3( torsion、x、y、z): x(37), x(38), x(39), x(40) derivative: x(89), x(90), x(91), x(92)
% degree of freedom of middle stage sun gear( torsion、x、y、z): x(41), x(42), x(43), x(44) derivative: x(93), x(94) , x(95), x(96)
% degree of freedom of output stage large gear( torsion、x、y、z): x(45), x(46), x(47), x(48) derivative: x(97), x(98), x(99), x(100)
% degree of freedom of output stage pinion( torsion、x、y、z): x(49), x(50), x(51), x(52) derivative: x(101), x(102), x(103), x(104)

% synthetic error
```

```
ea1=0;      % synthetic error of input stage external engagement
ea2=0;      % synthetic error of input stage internal engagement
ea3=0;      % synthetic error of middle stage external engagement
ea4=0;      % synthetic error of middle stage internal engagement
ea5=0;      % synthetic error of output stage external engagement
%displacement of input stage external engagement along meshing line
%relative displacement of equivalent torsional deformation along meshing line
xps1sita1=cos(betab)*(rbp*(x(5)+x(1))-rbs*(x(21)-x(1)));
xps1sita2=cos(betab)*(rbp*(x(9)+x(1))-rbs*(x(21)-x(1)));
xps1sita3=cos(betab)*(rbp*(x(13)+x(1))-rbs*(x(21)-x(1)));
xps1sita4=cos(betab)*(rbp*(x(17)+x(1))-rbs*(x(21)-x(1)));
% relative displacement derivative of equivalent torsional deformation along meshing line
Dxps1sita1=cos(betab)*(rbp*(x(57)+x(53))-rbs*(x(73)-x(53)));
Dxps1sita2=cos(betab)*(rbp*(x(61)+x(53))-rbs*(x(73)-x(53)));
Dxps1sita3=cos(betab)*(rbp*(x(65)+x(53))-rbs*(x(73)-x(53)));
Dxps1sita4=cos(betab)*(rbp*(x(69)+x(53))-rbs*(x(73)-x(53)));
% relative displacement of sun gear and planetary carrier equivalent radial deformation along meshing line
xps1sc1=cos(betab)*(sin(afat)*x(22)-cos(afat)*x(23)-sin(afat)*x(2)+cos(afat)*x(3));
xps1sc2=cos(betab)*(sin(afat-pi/2)*x(22)-cos(afat-pi/2)*x(23)-sin(afat-pi/2)*x(2)+cos(afat-pi/2)*x(3));
xps1sc3=cos(betab)*(sin(afat-pi)*x(22)-cos(afat-pi)*x(23)-sin(afat-pi)*x(2)+cos(afat-pi)*x(3));
xps1sc4=cos(betab)*(sin(afat-pi/2*3)*x(22)-cos(afat-pi/2*3)*x(23)-sin(afat-pi/2*3)*x(2)+cos(afat-pi/2*3)*x(3));
% xps1sc1=cos(betab)*(sin(afat+wc1*t).*x(22)-cos(afat+wc1*t).*x(23)-sin(afat)*x(2)+cos(afat)*x(3));
% xps1sc2=cos(betab)*(sin(afat-pi/2+wc1*t).*x(22)-cos(afat-pi/2+wc1*t).*x(23)-sin(afat)*x(2)+cos(afat)*x(3));
% xps1sc3=cos(betab)*(sin(afat-pi+wc1*t).*x(22)-cos(afat-pi+wc1*t).*x(23)-sin(afat)*x(2)+cos(afat)*x(3));
% xps1sc4=cos(betab)*(sin(afat-pi/2*3+wc1*t).*x(22)-cos(afat-pi/2*3+wc1*t).*x(23)-sin(afat)*x(2)+cos(afat)*x(3));
% relative displacement derivative of sun gear and planetary carrier equivalent radial deformation along meshing line
Dxps1sc1=cos(betab)*(sin(afat)*x(74)-cos(afat)*x(75)-sin(afat)*x(54)+cos(afat)*x(55));
Dxps1sc2=cos(betab)*(sin(afat-pi/2)*x(74)-cos(afat-pi/2)*x(75)-sin(afat-pi/2)*x(54)+cos(afat-pi/2)*x(55));
Dxps1sc3=cos(betab)*(sin(afat-pi)*x(74)-cos(afat-pi)*x(75)-sin(afat-pi)*x(54)+cos(afat-pi)*x(55));
Dxps1sc4=cos(betab)*(sin(afat-pi/2*3)*x(74)-cos(afat-pi/2*3)*x(75)-sin(afat-pi/2*3)*x(54)+cos(afat-pi/2*3)*x(55));
%
Dxps1sc1=cos(betab)*(sin(afat+wc1*t).*(x(74))+wc1*cos(afat+wc1*t).*(x(22))-cos(afat+wc1*t).*(x(75))+wc1*sin(a
fat+wc1*t).*(x(23))-sin(afat)*x(54)+cos(afat)*x(55));
%
Dxps1sc2=cos(betab)*(sin(afat-pi/2+wc1*t).*(x(74))+wc1*cos(afat-pi/2+wc1*t).*(x(22))-cos(afat-pi/2+wc1*t).*(x(7
5))+wc1*sin(afat-pi/2+wc1*t).*(x(23))-sin(afat)*x(54)+cos(afat)*x(55));
%
Dxps1sc3=cos(betab)*(sin(afat-pi+wc1*t).*(x(74))+wc1*cos(afat-pi+wc1*t).*(x(22))-cos(afat-pi+wc1*t).*(x(75))+w
c1*sin(afat-pi+wc1*t).*(x(23))-sin(afat)*x(54)+cos(afat)*x(55));
%
Dxps1sc4=cos(betab)*(sin(afat-pi/2*3+wc1*t).*(x(74))+wc1*cos(afat-pi/2*3+wc1*t).*(x(22))-cos(afat-pi/2*3+wc1*t
```

```
).*(x(75))+wc1*sin(afat-pi/2*3+wc1*t).*(x(23))-sin(afat)*x(54)+cos(afat)*x(55));
% relative displacement of planetary gear equivalent radial deformation along meshing line
xps1p1=cos(betab)*(cos(afat)*x(7)-sin(afat)*x(6));
xps1p2=cos(betab)*(cos(afat)*x(11)-sin(afat)*x(10));
xps1p3=cos(betab)*(cos(afat)*x(15)-sin(afat)*x(14));
xps1p4=cos(betab)*(cos(afat)*x(19)-sin(afat)*x(18));
% relative displacement derivative of planetary gear equivalent radial deformation along meshing line
Dxps1p1=cos(betab)*(cos(afat)*x(59)-sin(afat)*x(58));
Dxps1p2=cos(betab)*(cos(afat)*x(63)-sin(afat)*x(62));
Dxps1p3=cos(betab)*(cos(afat)*x(67)-sin(afat)*x(66));
Dxps1p4=cos(betab)*(cos(afat)*x(71)-sin(afat)*x(70));
%external engagement synthetic error
eps1wc1=ea1*sin(pi*(nout-nin)*zs*t/30);
eps1wc2=ea1*sin(pi*(nout-nin)*zs*t/30);
eps1wc3=ea1*sin(pi*(nout-nin)*zs*t/30);
eps1wc4=ea1*sin(pi*(nout-nin)*zs*t/30);
%external engagement synthetic error derivative
Deps1wc1=ea1*pi*(nout-nin)*zs/30*cos(pi*(nout-nin)*zs*t/30);
Deps1wc2=ea1*pi*(nout-nin)*zs/30*cos(pi*(nout-nin)*zs*t/30);
Deps1wc3=ea1*pi*(nout-nin)*zs/30*cos(pi*(nout-nin)*zs*t/30);
Deps1wc4=ea1*pi*(nout-nin)*zs/30*cos(pi*(nout-nin)*zs*t/30);
%relative displacement of external engagement along the meshing line
xps1x1=xps1sita1+xps1sc1+xps1p1-eps1wc1;
xps1x2=xps1sita2+xps1sc2+xps1p2-eps1wc2;
xps1x3=xps1sita3+xps1sc3+xps1p3-eps1wc3;
xps1x4=xps1sita4+xps1sc4+xps1p4-eps1wc4;
%relative displacement derivative of external engagement along the meshing line
Dxps1x1=Dxps1sita1+Dxps1sc1+Dxps1p1-Deps1wc1;
Dxps1x2=Dxps1sita2+Dxps1sc2+Dxps1p2-Deps1wc2;
Dxps1x3=Dxps1sita3+Dxps1sc3+Dxps1p3-Deps1wc3;
Dxps1x4=Dxps1sita4+Dxps1sc4+Dxps1p4-Deps1wc4;
%external engagement elastic force
Fps1x1=ksp.*xps1x1;
Fps1x2=ksp.*xps1x2;
Fps1x3=ksp.*xps1x3;
Fps1x4=ksp.*xps1x4;
%external engagement damping force
Dps1x1=Csp.*Dxps1x1;
Dps1x2=Csp.*Dxps1x2;
Dps1x3=Csp.*Dxps1x3;
Dps1x4=Csp.*Dxps1x4;
```

```
%displacement of input stage internal engagement along meshing line
%relative displacement of equivalent torsional deformation along meshing line
xrp1sita1=cos(betab)*(rbb*x(1)-rbp*(x(5)+x(1)));
xrp1sita2=cos(betab)*(rbb*x(1)-rbp*(x(9)+x(1)));
xrp1sita3=cos(betab)*(rbb*x(1)-rbp*(x(13)+x(1)));
xrp1sita4=cos(betab)*(rbb*x(1)-rbp*(x(17)+x(1)));
%relative displacement derivative of equivalent torsional deformation along meshing line
Dxrp1sita1=cos(betab)*(rbb*x(53)-rbp*(x(57)+x(53)));
Dxrp1sita2=cos(betab)*(rbb*x(53)-rbp*(x(61)+x(53)));
Dxrp1sita3=cos(betab)*(rbb*x(53)-rbp*(x(65)+x(53)));
Dxrp1sita4=cos(betab)*(rbb*x(53)-rbp*(x(69)+x(53)));
%relative displacement of planetary gear and planetary carrier equivalent radial deformation along meshing line
xrp1pc1=cos(betab)*(sin(afat)*x(2)+cos(afat)*x(3)+sin(afat)*x(6)+cos(afat)*x(7));
xrp1pc2=cos(betab)*(sin(afat+pi/2)*x(2)+cos(afat+pi/2)*x(3)+sin(afat)*x(10)+cos(afat)*x(11));
xrp1pc3=cos(betab)*(sin(afat+pi)*x(2)+cos(afat+pi)*x(3)+sin(afat)*x(14)+cos(afat)*x(15));
xrp1pc4=cos(betab)*(sin(afat+pi/2*3)*x(2)+cos(afat+pi/2*3)*x(3)+sin(afat)*x(18)+cos(afat)*x(19));
% xrp1pc1=cos(betab)*((sin(afat)*x(2)+cos(afat)*x(3))+sin(afat)*x(6)+cos(afat)*x(7));
% xrp1pc2=cos(betab)*((sin(afat)*x(2)+cos(afat)*x(3))+sin(afat)*x(10)+cos(afat)*x(11));
% xrp1pc3=cos(betab)*((sin(afat)*x(2)+cos(afat)*x(3))+sin(afat)*x(14)+cos(afat)*x(15));
% xrp1pc4=cos(betab)*((sin(afat)*x(2)+cos(afat)*x(3))+sin(afat)*x(18)+cos(afat)*x(19));
%relative displacement derivative of planetary gear and planetary carrier equivalent radial deformation along meshing
line
Dxrp1pc1=cos(betab)*(sin(afat)*x(54)+cos(afat)*x(55)+sin(afat)*x(58)+cos(afat)*x(59));
Dxrp1pc2=cos(betab)*(sin(afat+pi/2)*x(54)+cos(afat+pi/2)*x(55)+sin(afat)*x(62)+cos(afat)*x(63));
Dxrp1pc3=cos(betab)*(sin(afat+pi)*x(54)+cos(afat+pi)*x(55)+sin(afat)*x(66)+cos(afat)*x(67));
Dxrp1pc4=cos(betab)*(sin(afat+pi/2*3)*x(54)+cos(afat+pi/2*3)*x(55)+sin(afat)*x(70)+cos(afat)*x(71));
% internal engagement synthetic error
erp1wc1=ea2*sin(pi*(nout-nin)*zs*t/30);
erp1wc2=ea2*sin(pi*(nout-nin)*zs*t/30);
erp1wc3=ea2*sin(pi*(nout-nin)*zs*t/30);
erp1wc4=ea2*sin(pi*(nout-nin)*zs*t/30);
%internal engagement synthetic error derivative
Derp1wc1=ea2*pi*(nout-nin)*zs/30*cos(pi*(nout-nin)*zs*t/30);
Derp1wc2=ea2*pi*(nout-nin)*zs/30*cos(pi*(nout-nin)*zs*t/30);
Derp1wc3=ea2*pi*(nout-nin)*zs/30*cos(pi*(nout-nin)*zs*t/30);
Derp1wc4=ea2*pi*(nout-nin)*zs/30*cos(pi*(nout-nin)*zs*t/30);
%relative displacement of internal engagement along the meshing line
xrp1x1=xrp1sita1+xrp1pc1-erp1wc1;
xrp1x2=xrp1sita2+xrp1pc2-erp1wc2;
xrp1x3=xrp1sita3+xrp1pc3-erp1wc3;
xrp1x4=xrp1sita4+xrp1pc4-erp1wc4;
```

```
%relative displacement derivative of internal engagement along the meshing line
Dxrp1x1=Dxrp1sita1+Dxrp1pc1-Derp1wc1;
Dxrp1x2=Dxrp1sita2+Dxrp1pc2-Derp1wc2;
Dxrp1x3=Dxrp1sita3+Dxrp1pc3-Derp1wc3;
Dxrp1x4=Dxrp1sita4+Dxrp1pc4-Derp1wc4;
%inxternal engagement elastic force
Frp1x1=knp.*xrp1x1;
Frp1x2=knp.*xrp1x2;
Frp1x3=knp.*xrp1x3;
Frp1x4=knp.*xrp1x4;
%internal engagement damping force
Drp1x1=Cnp.*Dxrp1x1;
Drp1x2=Cnp.*Dxrp1x2;
Drp1x3=Cnp.*Dxrp1x3;
Drp1x4=Cnp.*Dxrp1x4;
%displacement of middle stage external engagement along meshing line
%relative displacement of equivalent torsional deformation along meshing line
xps2sita1=cos(betab1)*(rbp1*(x(29)+x(25))-rbs1*(x(41)-x(25)));
xps2sita2=cos(betab1)*(rbp1*(x(33)+x(25))-rbs1*(x(41)-x(25)));
xps2sita3=cos(betab1)*(rbp1*(x(37)+x(25))-rbs1*(x(41)-x(25)));
%relative displacement derivative of equivalent torsional deformation along meshing line
Dxps2sita1=cos(betab1)*(rbp1*(x(81)+x(77))-rbs1*(x(93)-x(77)));
Dxps2sita2=cos(betab1)*(rbp1*(x(85)+x(77))-rbs1*(x(93)-x(77)));
Dxps2sita3=cos(betab1)*(rbp1*(x(89)+x(77))-rbs1*(x(93)-x(77)));
% relative displacement of sun gear and planetary carrier equivalent radial deformation along meshing line
xps2sc1=cos(betab1)*(sin(afat1)*x(42)-cos(afat1)*x(43)-sin(afat1)*x(26)+cos(afat1)*x(27));
xps2sc2=cos(betab1)*(sin(afat1-pi/3*2)*x(42)-cos(afat1-pi/3*2)*x(43)-sin(afat1-pi/3*2)*x(26)+cos(afat1-pi/3*2)*x(2
7));
xps2sc3=cos(betab1)*(sin(afat1-pi/3*4)*x(42)-cos(afat1-pi/3*4)*x(43)-sin(afat1-pi/3*4)*x(26)+cos(afat1-pi/3*4)*x(2
7));
% xps2sc1=cos(betab1)*(sin(afat1+wc2*t).*x(42)-cos(afat1+wc2*t).*x(43)-sin(afat1)*x(26)+cos(afat1)*x(27));
%
xps2sc2=cos(betab1)*(sin(afat1-pi/3*2+wc2*t).*x(42)-cos(afat1-pi/3*2+wc2*t).*x(43)-sin(afat1)*x(26)+cos(afat1)*x
(27));
%
xps2sc3=cos(betab1)*(sin(afat1-pi/3*4+wc2*t).*x(42)-cos(afat1-pi/3*4+wc2*t).*x(43)-sin(afat1)*x(26)+cos(afat1)*x
(27));
% relative displacement derivative of sun gear and planetary carrier equivalent radial deformation along meshing line
Dxps2sc1=cos(betab1)*(sin(afat1)*x(94)-cos(afat1)*x(95)-sin(afat1)*x(78)+cos(afat1)*x(79));
Dxps2sc2=cos(betab1)*(sin(afat1-pi/3*2)*x(94)-cos(afat1-pi/3*2)*x(95)-sin(afat1-pi/3*2)*x(78)+cos(afat1-pi/3*2)*x
(79));
```

```
Dxps2sc3=cos(betab1)*(sin(afat1-pi/3*4)*x(94)-cos(afat1-pi/3*4)*x(95)-sin(afat1-pi/3*4)*x(78)+cos(afat1-pi/3*4)*x(79));
%
Dxps2sc1=cos(betab1)*(sin(afat1+wc2*t).*x(94)+wc2*cos(afat1+wc2*t).*x(42)-cos(afat1+wc2*t).*x(95)+wc2*sin(afat1+wc2*t).*x(43)-sin(afat1)*x(78)+cos(afat1)*x(79));
%
Dxps2sc2=cos(betab1)*(sin(afat1-pi/3*2+wc2*t).*x(94)+wc2*cos(afat1-pi/3*2+wc2*t).*x(42)-cos(afat1-pi/3*2+wc2*t).*x(95)+wc2*sin(afat1-pi/3*2+wc2*t).*x(43)-sin(afat1)*x(78)+cos(afat1)*x(79));
%
Dxps2sc3=cos(betab1)*(sin(afat1-pi/3*4+wc2*t).*x(94)+wc2*cos(afat1-pi/3*4+wc2*t).*x(42)-cos(afat1-pi/3*4+wc2*t).*x(95)+wc2*sin(afat1-pi/3*4+wc2*t).*x(43)-sin(afat1)*x(78)+cos(afat1)*x(79));
% relative displacement of planetary gear equivalent radial deformation along meshing line
xps2p1=cos(betab1)*(cos(afat1)*x(31)-sin(afat1)*x(30));
xps2p2=cos(betab1)*(cos(afat1)*x(35)-sin(afat1)*x(34));
xps2p3=cos(betab1)*(cos(afat1)*x(39)-sin(afat1)*x(38));
% relative displacement derivative of planetary gear equivalent radial deformation along meshing line
Dxps2p1=cos(betab1)*(cos(afat1)*x(83)-sin(afat1)*x(82));
Dxps2p2=cos(betab1)*(cos(afat1)*x(87)-sin(afat1)*x(86));
Dxps2p3=cos(betab1)*(cos(afat1)*x(91)-sin(afat1)*x(90));
%external engagement synthetic error
eps2wc1=ea3*sin(pi*(n1-nout)*zs1*t/30);
eps2wc2=ea3*sin(pi*(n1-nout)*zs1*t/30);
eps2wc3=ea3*sin(pi*(n1-nout)*zs1*t/30);
%external engagement synthetic error derivative
Deps2wc1=ea3*pi*(n1-nout)*zs1/30*cos(pi*(n1-nout)*zs1*t/30);
Deps2wc2=ea3*pi*(n1-nout)*zs1/30*cos(pi*(n1-nout)*zs1*t/30);
Deps2wc3=ea3*pi*(n1-nout)*zs1/30*cos(pi*(n1-nout)*zs1*t/30);
%relative displacement of external engagement along the meshing line
xps2x1=xps2sita1+xps2sc1+xps2p1-eps2wc1;
xps2x2=xps2sita2+xps2sc2+xps2p2-eps2wc2;
xps2x3=xps2sita3+xps2sc3+xps2p3-eps2wc3;
%relative displacement derivative of external engagement along the meshing line
Dxps2x1=Dxps2sita1+Dxps2sc1+Dxps2p1-Deps2wc1;
Dxps2x2=Dxps2sita2+Dxps2sc2+Dxps2p2-Deps2wc2;
Dxps2x3=Dxps2sita3+Dxps2sc3+Dxps2p3-Deps2wc3;
%external engagement elastic force
Fps2x1=ksp1.*xps2x1;
Fps2x2=ksp1.*xps2x2;
Fps2x3=ksp1.*xps2x3;
%external engagement damping force
Dps2x1=Csp1.*Dxps2x1;
```

```
Dps2x2=Csp1.*Dxps2x2;
Dps2x3=Csp1.*Dxps2x3;
%displacement of middle stage internal engagement along meshing line
%relative displacement of equivalent torsional deformation along meshing line
xrp2sita1=cos(betab1)*(rbb1*x(25)-rbp1*(x(29)+x(25)));
xrp2sita2=cos(betab1)*(rbb1*x(25)-rbp1*(x(33)+x(25)));
xrp2sita3=cos(betab1)*(rbb1*x(25)-rbp1*(x(37)+x(25)));
%relative displacement derivative of equivalent torsional deformation along meshing line
Dxrp2sita1=cos(betab1)*(rbb1*x(77)-rbp1*(x(81)+x(77)));
Dxrp2sita2=cos(betab1)*(rbb1*x(77)-rbp1*(x(85)+x(77)));
Dxrp2sita3=cos(betab1)*(rbb1*x(77)-rbp1*(x(89)+x(77)));
%relative displacement of planetary gear and planetary carrier equivalent radial deformation along meshing line
xrp2pc1=cos(betab1)*(sin(afat1)*x(26)+cos(afat1)*x(27)+sin(afat1)*x(30)+cos(afat1)*x(31));
xrp2pc2=cos(betab1)*(sin(afat1+pi/3*2)*x(26)+cos(afat1+pi/3*2)*x(27)+sin(afat1)*x(34)+cos(afat1)*x(35));
xrp2pc3=cos(betab1)*(sin(afat1+pi/3*4)*x(26)+cos(afat1+pi/3*4)*x(27)+sin(afat1)*x(38)+cos(afat1)*x(39));
% xrp2pc1=cos(betab1)*((sin(afat1)*x(26)+cos(afat1)*x(27))+sin(afat1)*x(30)+cos(afat1)*x(31));
% xrp2pc2=cos(betab1)*((sin(afat1)*x(26)+cos(afat1)*x(27))+sin(afat1)*x(34)+cos(afat1)*x(35));
% xrp2pc3=cos(betab1)*((sin(afat1)*x(26)+cos(afat1)*x(27))+sin(afat1)*x(38)+cos(afat1)*x(39));
%relative displacement derivative of planetary gear and planetary carrier equivalent radial deformation along meshing
line
Dxrp2pc1=cos(betab1)*(sin(afat1)*x(78)+cos(afat1)*x(79)+sin(afat1)*x(82)+cos(afat1)*x(83));
Dxrp2pc2=cos(betab1)*(sin(afat1+pi/3*2)*x(78)+cos(afat1+pi/3*2)*x(79)+sin(afat1)*x(86)+cos(afat1)*x(87));
Dxrp2pc3=cos(betab1)*(sin(afat1+pi/3*4)*x(78)+cos(afat1+pi/3*4)*x(79)+sin(afat1)*x(90)+cos(afat1)*x(91));
% Dxrp2pc1=cos(betab1)*((sin(afat1)*x(78)+cos(afat1)*x(79))+sin(afat1)*x(82)+cos(afat1)*x(83));
% Dxrp2pc2=cos(betab1)*((sin(afat1)*x(78)+cos(afat1)*x(79))+sin(afat1)*x(86)+cos(afat1)*x(87));
% Dxrp2pc3=cos(betab1)*((sin(afat1)*x(78)+cos(afat1)*x(79))+sin(afat1)*x(90)+cos(afat1)*x(91));
%internal engagement synthetic error
erp2wc1=ea4*sin(pi*(n1-nout)*zs1*t/30);
erp2wc2=ea4*sin(pi*(n1-nout)*zs1*t/30);
erp2wc3=ea4*sin(pi*(n1-nout)*zs1*t/30);
%internal engagement synthetic error derivative
Derp2wc1=ea4*pi*(n1-nout)*zs1/30*cos(pi*(n1-nout)*zs1*t/30);
Derp2wc2=ea4*pi*(n1-nout)*zs1/30*cos(pi*(n1-nout)*zs1*t/30);
Derp2wc3=ea4*pi*(n1-nout)*zs1/30*cos(pi*(n1-nout)*zs1*t/30);
%relative displacement of internal engagement along the meshing line
xrp2x1=xrp2sita1+xrp2pc1-erp2wc1;
xrp2x2=xrp2sita2+xrp2pc2-erp2wc2;
xrp2x3=xrp2sita3+xrp2pc3-erp2wc3;
%relative displacement derivative of internal engagement along the meshing line
Dxrp2x1=Dxrp2sita1+Dxrp2pc1-Derp2wc1;
Dxrp2x2=Dxrp2sita2+Dxrp2pc2-Derp2wc2;
```

```
Dxrp2x3=Dxrp2sita3+Dxrp2pc3-Derp2wc3;
%internal engagement elastic force
Frp2x1=knp1.*xrp2x1;
Frp2x2=knp1.*xrp2x2;
Frp2x3=knp1.*xrp2x3;
%internal engagement damping force
Drp2x1=Cnp1.*Dxrp2x1;
Drp2x2=Cnp1.*Dxrp2x2;
Drp2x3=Cnp1.*Dxrp2x3;
%relative displacement of helical 7 and helical 8 along the directional meshing line
x781=cos(betab2)*((r1b*x(45)-r2b*x(49))+cos(afat2)*(x(47)-x(51))+sin(afat2)*(x(46)-x(50)));
Dx781=cos(betab2)*((r1b*x(97)-r2b*x(101))+cos(afat2)*(x(99)-x(103))+sin(afat2)*(x(98)-x(102)));
e78=ea5*sin(pi*n2*z2*t/30);
De78=ea5*pi*n2*z2/30*cos(pi*n2*z2*t/30);
x78=x781-e78;
Dx78=Dx781-De78;
F78=k78.*x78;
D78=C78.*Dx78;
%external engagement
Toutm=9.55*1000*p/n2;          %unit :Nm
Tc=0.3;      %torque change coefficient
Ta=Toutm*Tc;
deltaT1=Ta*sin(wc3*t);
Tout=Toutm+deltaT1;
%%%%%%%%%%%%%%%%%%%%%%%%%%%%%%%%%%%%%%%%%%%%%%%%%%%%%%%%
%description function before descending order：         Mx''+cx'+kx=F
%differential equation of input stage planetary carrier
j1=(Tin-cos(betab)*rbc*(Dps1x1+Dps1x2+Dps1x3+Dps1x4+Drp1x1+Drp1x2+Drp1x3+Drp1x4+Fps1x1+Fps1x2+Fp
s1x3+Fps1x4+Frp1x1+Frp1x2+Frp1x3+Frp1x4)-Co*(x(53))-ko*(x(1)))/jc;       %rotational direction
j2=(cos(betab)*(Dps1x1*sin(afat)+Dps1x2*sin(afat-pi/2)+Dps1x3*sin(afat-pi)+Dps1x4*sin(afat-pi*3/2)-Drp1x1*sin(
afat)-Drp1x2*sin(afat+pi/2)-Drp1x3*sin(afat+pi)-Drp1x4*sin(afat+pi*3/2)+Fps1x1*sin(afat)+Fps1x2*sin(afat-pi/2)+
Fps1x3*sin(afat-pi)+Fps1x4*sin(afat-pi*3/2)-Frp1x1*sin(afat)-Frp1x2*sin(afat+pi/2)-Frp1x3*sin(afat+pi)-Frp1x4*si
n(afat+pi*3/2))-Ccp*x(54)-kcp*x(2))/mc;        %x direction
j3=(-cos(betab)*(Dps1x1*cos(afat)+Dps1x2*cos(afat-pi/2)+Dps1x3*cos(afat-pi)+Dps1x4*cos(afat-pi*3/2)+Drp1x1*c
os(afat)+Drp1x2*cos(afat+pi/2)+Drp1x3*cos(afat+pi)+Drp1x4*cos(afat+pi*3/2)+Fps1x1*cos(afat)+Fps1x2*cos(afat-
pi/2)+Fps1x3*cos(afat-pi)+Fps1x4*cos(afat-pi*3/2)+Frp1x1*cos(afat)+Frp1x2*cos(afat+pi/2)+Frp1x3*cos(afat+pi)+
Frp1x4*cos(afat+pi*3/2))-Ccp*x(55)-kcp*x(3))/mc;       %y direction
j4=(sin(betab)*(-Dps1x1-Dps1x2-Dps1x3-Dps1x4+Drp1x1+Drp1x2+Drp1x3+Drp1x4-Fps1x1-Fps1x2-Fps1x3-Fps1x
4+Frp1x1+Frp1x2+Frp1x3+Frp1x4)-Ccp*x(56)-kcp*x(4))/mc;            %z direction
%differential equation of input stage sun gear
j5=(cos(betab)*rbs*(Dps1x1+Dps1x2+Dps1x3+Dps1x4+Fps1x1+Fps1x2+Fps1x3+Fps1x4)-Ccs*(x(73)-x(77))-kcs*(x
```

```
(21)-x(25)))/js;        %rotational direction
j6=(cos(betab)*(-Dps1x1*sin(afat)-Dps1x2*sin(afat-pi/2)-Dps1x3*sin(afat-pi)-Dps1x4*sin(afat-pi*3/2)-Fps1x1*sin(a
fat)-Fps1x2*sin(afat-pi/2)-Fps1x3*sin(afat-pi)-Fps1x4*sin(afat-pi*3/2))-Cs*x(74)-ks*x(22))/ms;   %x direction
j7=(cos(betab)*(Dps1x1*cos(afat)+Dps1x2*cos(afat-pi/2)+Dps1x3*cos(afat-pi)+Dps1x4*cos(afat-pi*3/2)+Fps1x1*c
os(afat)+Fps1x2*cos(afat-pi/2)+Fps1x3*cos(afat-pi)+Fps1x4*cos(afat-pi*3/2))-Cs*x(75)-ks*x(23))/ms; %y direction
j8=(sin(betab)*(Dps1x1+Dps1x2+Dps1x3+Dps1x4+Fps1x1+Fps1x2+Fps1x3+Fps1x4)-Cs*x(76)-ks*x(24))/ms;
%
j5=(cos(betab)*rbs*(Dps1x1+Dps1x2+Dps1x3+Dps1x4+Fps1x1+Fps1x2+Fps1x3+Fps1x4)-Ccs*(x(73)-x(77))-kcs*(x
(21)-x(25)))/js;                    %rotational direction
%
j6=(cos(betab)*(-Dps1x1.*sin(afat+wc1*t)-Dps1x2.*sin(afat-pi/2+wc1*t)-Dps1x3.*sin(afat-pi+wc1*t)-Dps1x4.*sin(a
fat-pi*3/2+wc1*t)-Fps1x1.*sin(afat+wc1*t)-Fps1x2.*sin(afat-pi/2+wc1*t)-Fps1x3.*sin(afat-pi+wc1*t)-Fps1x4.*sin(a
fat-pi*3/2+wc1*t))-Cs*x(74)-ks*x(22))/ms;          %x direction
%
j7=(cos(betab)*(Dps1x1.*cos(afat+wc1*t)+Dps1x2.*cos(afat-pi/2+wc1*t)+Dps1x3.*cos(afat-pi+wc1*t)+Dps1x4.*co
s(afat-pi*3/2+wc1*t)+Fps1x1.*cos(afat+wc1*t)+Fps1x2.*cos(afat-pi/2+wc1*t)+Fps1x3.*cos(afat-pi+wc1*t)+Fps1x4.
*cos(afat-pi*3/2+wc1*t))-Cs*x(75)-ks*x(23))/ms;          %y direction
%
j8=(sin(betab)*(Dps1x1+Dps1x2+Dps1x3+Dps1x4+Fps1x1+Fps1x2+Fps1x3+Fps1x4)-Cs*x(76)-ks*x(24))/ms;
                                                  %z direction
%differential equation of input stage planetary gear
j9=(cos(betab)*rbp*(-Dps1x1+Drp1x1-Fps1x1+Frp1x1))/jp;          %rotational direction
j10=(cos(betab)*rbp*(-Dps1x2+Drp1x2-Fps1x2+Frp1x2))/jp;
j11=(cos(betab)*rbp*(-Dps1x3+Drp1x3-Fps1x3+Frp1x3))/jp;
j12=(cos(betab)*rbp*(-Dps1x4+Drp1x4-Fps1x4+Frp1x4))/jp;
j13=(cos(betab)*(Dps1x1*sin(afat)-Drp1x1*sin(afat)+Fps1x1*sin(afat)-Frp1x1*sin(afat))-Cp*x(58)-kp*(x(6)))/mp;
       %x direction
j14=(cos(betab)*(Dps1x2*sin(afat)-Drp1x2*sin(afat)+Fps1x2*sin(afat)-Frp1x2*sin(afat))-Cp*x(62)-kp*(x(10)))/mp;
j15=(cos(betab)*(Dps1x3*sin(afat)-Drp1x3*sin(afat)+Fps1x3*sin(afat)-Frp1x3*sin(afat))-Cp*x(66)-kp*(x(14)))/mp;
j16=(cos(betab)*(Dps1x4*sin(afat)-Drp1x4*sin(afat)+Fps1x4*sin(afat)-Frp1x4*sin(afat))-Cp*x(70)-kp*(x(18)))/mp;
j17=(-cos(betab)*(Dps1x1*cos(afat)+Drp1x1*cos(afat)+Fps1x1*cos(afat)+Frp1x1*cos(afat))-Cp*x(59)-kp*(x(7)))/m
p;          %y direction
j18=(-cos(betab)*(Dps1x2*cos(afat)+Drp1x2*cos(afat)+Fps1x2*cos(afat)+Frp1x2*cos(afat))-Cp*x(63)-kp*(x(11)))/
mp;
j19=(-cos(betab)*(Dps1x3*cos(afat)+Drp1x3*cos(afat)+Fps1x3*cos(afat)+Frp1x3*cos(afat))-Cp*x(67)-kp*(x(15)))/
mp;
j20=(-cos(betab)*(Dps1x4*cos(afat)+Drp1x4*cos(afat)+Fps1x4*cos(afat)+Frp1x4*cos(afat))-Cp*x(71)-kp*(x(19)))/
mp;
j21=(-sin(betab)*(Dps1x1-Drp1x1+Fps1x1-Frp1x1)-Cp*x(60)-kp*(x(8)))/mp;          %z direction
j22=(-sin(betab)*(Dps1x2-Drp1x2+Fps1x2-Frp1x2)-Cp*x(64)-kp*(x(12)))/mp;
j23=(-sin(betab)*(Dps1x3-Drp1x3+Fps1x3-Frp1x3)-Cp*x(68)-kp*(x(16)))/mp;
j24=(-sin(betab)*(Dps1x4-Drp1x4+Fps1x4-Frp1x4)-Cp*x(72)-kp*(x(20)))/mp;
```

```
%differential equation of middle stage planetary carrier
j25=(cos(betab1)*rbc1*(-Dps2x1-Dps2x2-Dps2x3-Drp2x1-Drp2x2-Drp2x3-Fps2x1-Fps2x2-Fps2x3-Frp2x1-Frp2x2-F
rp2x3)-Ccs*(x(77)-x(73))-kcs*(x(25)-x(21)))/jc1;          %rotational direction
j26=(cos(betab1)*(Dps2x1*sin(afat1)+Dps2x2*sin(afat1-pi*2/3)+Dps2x3*sin(afat1-pi*4/3)-Drp2x1*sin(afat1)-Drp2x
2*sin(afat1+pi*2/3)-Drp2x3*sin(afat1+pi*4/3)+Fps2x1*sin(afat1)+Fps2x2*sin(afat1-pi*2/3)+Fps2x3*sin(afat1-pi*4/
3)-Frp2x1*sin(afat1)-Frp2x2*sin(afat1+pi*2/3)-Frp2x3*sin(afat1+pi*4/3))-Ccp1*x(78)-kcp1*x(26))/mc1;
                    %x direction
j27=(-cos(betab1)*(Dps2x1*cos(afat1)+Dps2x2*cos(afat1-pi*2/3)+Dps2x3*cos(afat1-pi*4/3)+Drp2x1*cos(afat1)+Dr
p2x2*cos(afat1+pi*2/3)+Drp2x3*cos(afat1+pi*4/3)+Fps2x1*cos(afat1)+Fps2x2*cos(afat1-pi*2/3)+Fps2x3*cos(afat1
-pi*4/3)+Frp2x1*cos(afat1)+Frp2x2*cos(afat1+pi*2/3)+Frp2x3*cos(afat1+pi*4/3))-Ccp1*x(79)-kcp1*x(27))/mc1;
                     %y direction
j28=(-sin(betab1)*(Dps2x1+Dps2x2+Dps2x3-Drp2x1-Drp2x2-Drp2x3+Fps2x1+Fps2x2+Fps2x3-Frp2x1-Frp2x2-Frp
2x3)-Ccp1*x(80)-kcp1*x(28))/mc1;              %z direction
%differential equation of middle stage sun gear
j29=(cos(betab1)*rbs1*(Dps2x1+Dps2x2+Dps2x3+Fps2x1+Fps2x2+Fps2x3)-Ccs1*(x(93)-x(97))-kcs1*(x(41)-x(45))
)/js1;                  %rotational direction
j30=(cos(betab1)*(-Dps2x1*sin(afat1)-Dps2x2*sin(afat1-pi*2/3)-Dps2x3*sin(afat1-pi*4/3)-Fps2x1*sin(afat1)-Fps2x
2*sin(afat1-pi*2/3)-Fps2x3*sin(afat1-pi*4/3))-Cs1*x(94)-ks1*x(42))/ms1;           %x direction
j31=(cos(betab1)*(Dps2x1*cos(afat1)+Dps2x2*cos(afat1-pi*2/3)+Dps2x3*cos(afat1-pi*4/3)+Fps2x1*cos(afat1)+Fps
2x2*cos(afat1-pi*2/3)+Fps2x3*cos(afat1-pi*4/3))-Cs1*x(95)-ks1*x(43))/ms1;             %y direction
j32=(sin(betab1)*(Dps2x1+Dps2x2+Dps2x3+Fps2x1+Fps2x2+Fps2x3)-Cs1*x(96)-ks1*x(44))/ms1;
    %z direction
%
j29=(cos(betab1)*rbs1*(Dps2x1+Dps2x2+Dps2x3+Fps2x1+Fps2x2+Fps2x3)-Ccs1*(x(93)-x(97))-kcs1*(x(41)-x(45))
)/js1;                  %rotational direction
%
j30=(cos(betab1)*(-Dps2x1.*sin(afat1+wc2*t)-Dps2x2.*sin(afat1-pi*2/3+wc2*t)-Dps2x3.*sin(afat1-pi*4/3+wc2*t)-F
ps2x1.*sin(afat1+wc2*t)-Fps2x2.*sin(afat1-pi*2/3+wc2*t)-Fps2x3.*sin(afat1-pi*4/3+wc2*t))-Cs1*x(94)-ks1*x(42))/
ms1;         %x direction
%
j31=(cos(betab1)*(Dps2x1.*cos(afat1+wc2*t)+Dps2x2.*cos(afat1-pi*2/3+wc2*t)+Dps2x3.*cos(afat1-pi*4/3+wc2*t)
+Fps2x1.*cos(afat1+wc2*t)+Fps2x2.*cos(afat1-pi*2/3+wc2*t)+Fps2x3.*cos(afat1-pi*4/3+wc2*t))-Cs1*x(95)-ks1*x(
43))/ms1;         %y direction
% j32=(sin(betab1)*(Dps2x1+Dps2x2+Dps2x3+Fps2x1+Fps2x2+Fps2x3)-Cs1*x(96)-ks1*x(44))/ms1;
%differential equation of middle stage planetary gear
j33=(cos(betab1)*rbp1*(-Dps2x1+Drp2x1-Fps2x1+Frp2x1))/jp1;               %rotational direction
j34=(cos(betab1)*rbp1*(-Dps2x2+Drp2x2-Fps2x2+Frp2x2))/jp1;
j35=(cos(betab1)*rbp1*(-Dps2x3+Drp2x3-Fps2x3+Frp2x3))/jp1;
j36=(cos(betab1)*(Dps2x1*sin(afat1)-Drp2x1*sin(afat1)+Fps2x1*sin(afat1)-Frp2x1*sin(afat1))-Cp1*x(82)-kp1*x(30
))/mp1;              %x direction
j37=(cos(betab1)*(Dps2x2*sin(afat1)-Drp2x2*sin(afat1)+Fps2x2*sin(afat1)-Frp2x2*sin(afat1))-Cp1*x(86)-kp1*x(34
```

```
))/mp1;
j38=(cos(betab1)*(Dps2x3*sin(afat1)-Drp2x3*sin(afat1)+Fps2x3*sin(afat1)-Frp2x3*sin(afat1))-Cp1*x(90)-kp1*x(38
))/mp1;
j39=(-cos(betab1)*(Dps2x1*cos(afat1)+Drp2x1*cos(afat1)+Fps2x1*cos(afat1)+Frp2x1*cos(afat1))-Cp1*x(83)-kp1*x
(31))/mp1;              %y direction
j40=(-cos(betab1)*(Dps2x2*cos(afat1)+Drp2x2*cos(afat1)+Fps2x2*cos(afat1)+Frp2x2*cos(afat1))-Cp1*x(87)-kp1*x
(35))/mp1;
j41=(-cos(betab1)*(Dps2x3*cos(afat1)+Drp2x3*cos(afat1)+Fps2x3*cos(afat1)+Frp2x3*cos(afat1))-Cp1*x(91)-kp1*x
(39))/mp1;
j42=(-sin(betab1)*(Dps2x1-Drp2x1+Fps2x1-Frp2x1)-Cp1*x(84)-kp1*x(32))/mp1;          %z direction
j43=(-sin(betab1)*(Dps2x2-Drp2x2+Fps2x2-Frp2x2)-Cp1*x(88)-kp1*x(36))/mp1;
j44=(-sin(betab1)*(Dps2x3-Drp2x3+Fps2x3-Frp2x3)-Cp1*x(92)-kp1*x(40))/mp1;
%differential equation of output stage large gear
j45=(cos(betab2)*r1b*(-D78-F78)-Ccs1*(x(97)-x(93))-kcs1*(x(45)-x(41)))/jj1;     %rotational direction
j46=(cos(betab2)*sin(afat2)*(-D78-F78)-C7*x(98)-k7*x(46))/m1;                   %x direction
j47=(cos(betab2)*cos(afat2)*(-D78-F78)-C7*x(99)-k7*x(47))/m1;                   %y direction
j48=(sin(betab2)*(-D78-F78)-C7*x(100)-k7*x(48))/m1;                             %z direction
%differential equation of output stage pinion
j49=(cos(betab2)*r2b*(D78+F78)-Tout)/jj2;                                       %rotational direction
j50=(cos(betab2)*sin(afat2)*(D78+F78)-C8*x(102)-k8*x(50))/m2;                   %x direction
j51=(cos(betab2)*cos(afat2)*(D78+F78)-C8*x(103)-k8*x(51))/m2;                   %y direction
j52=(sin(betab2)*(D78+F78)-C8*x(104)-k8*x(52))/m2;                              %z direction

jjfc=[x(53);         %dx(1)~dx(4)     degree of freedom of input stage planetary carrier
      x(54);
      x(55);
      x(56);
      x(57);         %dx(5)~dx(8)    degree of freedom of input stage planetary gear 1
      x(58);
      x(59);
      x(60);
      x(61);         %dx(9)~dx(12)    degree of freedom of input stage planetary gear 2
      x(62);
      x(63);
      x(64);
      x(65);         %dx(13)~dx(16)    degree of freedom of input stage planetary gear 3
      x(66);
      x(67);
      x(68);
      x(69);       %dx(17)~dx(20)    degree of freedom of input stage planetary gear 4
      x(70);
```

```
x(71);
x(72);
x(73);      %dx(21)~dx(24)   degree of freedom of input stage sun gear
x(74);
x(75);
x(76);
x(77);      %dx(25)~dx(28)   degree of freedom of middle stage planetary carrier
x(78);
x(79);
x(80);
x(81);      %dx(29)~dx(32)   degree of freedom of middle stage planetary gear 1
x(82);
x(83);
x(84);
x(85);      %dx(33)~dx(36)   degree of freedom of middle stage planetary gear 2
x(86);
x(87);
x(88);
x(89);      %dx(37)~dx(40)   degree of freedom of middle stage planetary gear 3
x(90);
x(91);
x(92);
x(93);           %dx(41)~dx(44)   degree of freedom of middle stage sun gear
x(94);
x(95);
x(96);
x(97);           %dx(45)~dx(48)   degree of freedom of output stage large gear
x(98);
x(99);
x(100);
x(101);          %dx(49)~dx(52)     degree of freedom of output stage pinion
x(102);
x(103);
x(104);
j1;           %dx(53)   i.e. ddx(1)    dd is second derivative
j2;           %dx(54)   i.e. ddx(2)
j3;           %dx(55)   i.e. ddx(3)
j4;           %dx(56)   i.e. ddx(4)
j9;           %dx(57)   i.e. ddx(5)
j13;          %dx(58)   i.e. ddx(6)
j17;          %dx(59)   i.e. ddx(7)
```

```
j21;        %dx(60)   i.e. ddx(8)
j10;        %dx(61)   i.e. ddx(9)
j14;        %dx(62)   i.e. ddx(10)
j18;        %dx(63)   i.e. ddx(11)
j22;        %dx(64)   i.e. ddx(12)
j11;        %dx(65)   i.e. ddx(13)
j15;        %dx(66)   i.e. ddx(14)
j19;        %dx(67)   i.e. ddx(15)
j23;        %dx(68)   i.e. ddx(16)
j12;        %dx(69)   i.e. ddx(17)
j16;        %dx(70)   i.e. ddx(18)
j20;        %dx(71)   i.e. ddx(19)
j24;        %dx(72)   i.e. ddx(20)
j5;         %dx(73)   i.e. ddx(21)
j6;         %dx(74)   i.e. ddx(22)
j7;         %dx(75)   i.e. ddx(23)
j8;         %dx(76)   i.e. ddx(24)
j25;        %dx(77)   i.e. ddx(25)
j26;        %dx(78)   i.e. ddx(26)
j27;        %dx(79)   i.e. ddx(27)
j28;        %dx(80)   i.e. ddx(28)
j33;        %dx(81)   i.e. ddx(29)
j36;        %dx(82)   i.e. ddx(30)
j39;        %dx(83)   i.e. ddx(31)
j42;        %dx(84)   i.e. ddx(32)
j34;        %dx(85)   i.e. ddx(33)
j37;        %dx(86)   i.e. ddx(34)
j40;        %dx(87)   i.e. ddx(35)
j43;        %dx(88)   i.e. ddx(36)
j35;        %dx(89)   i.e. ddx(37)
j38;        %dx(90)   i.e. ddx(38)
j41;        %dx(91)   i.e. ddx(39)
j44;        %dx(92)   i.e. ddx(40)
j29;        %dx(93)   i.e. ddx(41)
j30;        %dx(94)   i.e. ddx(42)
j31;        %dx(95)   i.e. ddx(43)
j32;        %dx(96)   i.e. ddx(44)
j45;        %dx(97)   i.e. ddx(45)
j46;        %dx(98)   i.e. ddx(46)
j47;        %dx(99)   i.e. ddx(47)
j48;        %dx(100)  i.e. ddx(48)
```

A.3 plantary_carrier_Stiffness.m

```
j49;        %dx(101)  i.e. ddx(49)
j50;        %dx(102)  i.e. ddx(50)
j51;        %dx(103)  i.e. ddx(51)
j52];       %dx(104)  i.e. ddx(52)
function ko=xxjstiffness(E,mu,n,rh,rf,hc,c,Fa,Fm,sn,kL,betaL,kc,afa1,afa2,afa3,afa4,rs,cc1,cc2)
hL=rh-rf;%altitude of trapezoid cross section；
a=(rf*afa1+rs*afa2)*pi/180;% length of short base of connecting plate trapezoid cross section;
b=(rh*afa3+rs*afa4)*pi/180;% length of long base of connecting plate trapezoid cross section；
rL=rh-hL*(a+2*b)/3/(a+b);%radius of the circle with the connecting plate cross section centroid    mm
Lc=2*pi*rL/n;%arc length of two connecting plate cross section centroid on the planetary carrier cross section    mm
betac=1.74*n*hc*Fa*Fm/rL;% plate shape coefficient
Ac=hc*c;%area of plate cross section    mm2
AL=(a+b)*hL/2;%area of connecting plate cross section
jc=hc*c^3/12;%inertia moment of plate axial section on y axis
jL=hL*(a+b)*(a^2+b^2)/48;% inertia moment of connecting plate cross section on y axis
lc=Lc-2*(a+(hL-hL*(a+2*b)/3/(a+b))*(b-a)/2/hL);%paper fig.3.3
Lcy=cc1*lc;%effective length of plate，1.3 is obtained from figure；
sL=sn+c;%center line distance of two plate thickness, mm
Sny=cc2*sn;% effective length of connecting plate，1.35 is obtained from figure；
ac=(Lcy^3/24/jc+kc*(1+mu)*Lcy/Ac)*betac*Lc;%plate effect coefficient；
aL=(Sny^3/3/jL+2*kL*(1+mu)*Sny/AL)*betaL*sL;% connecting plate effect coefficient
delt=((sL/Lc)^3*ac+aL)/E/sL; %flexibility of the planetary carrier
ko=1/delt*pi/180/rL;%torsion stiffness of planetary carrier
```

A.4 Excitation.m

```
function w=jili(nin,zs,zb)
nout=nin*(1+zb/zs);             %the speed of middle stage planetary carrier(the speed of input stage sun gear )    r/min
wh=pi*(nout-nin)*zs/30;    %meshing frequency
w=wh;
```

Appendix B
Codes of Time-frequency Analysis of Vibration Signals

B.1 time domain waveform.m

```
2.1 time domain waveform.m
xt=load('xt.dat');
x=reshape(xt,25,2000);x=x';
yt=load('yt.dat');
y=reshape(yt,25,2000);y=y';
figure (1)
plot(y(:,1),y(:,16),'k')
ylabel('Disp of y/\mum','fontsize',14,'fontweight','bold')
xlabel('Time(Sec)','fontsize',14,'fontweight','bold')
```

B.2 fft.m

```
xt=load('xt.dat');
x=reshape(xt,25,2000);x=x';
yt=load('yt.dat');
y=reshape(yt,25,2000);y=y';
N=2000;
dt=(x(2000,1)-x(1,1))/2000;
fs=1/dt;
t=0:(1/fs):((N-1)/fs);
f=fs/(N)*(0:N/2-1);
xs=detrend(x(:,16));
Y1=fft(xs,N);
Pxx1=sqrt(Y1.*conj(Y1))/(N/2);
ys=detrend(x(:,17));
Y2=fft(ys,N);
Pxx2=sqrt(Y2.*conj(Y2))/(N/2);
 [Axx1,I]=max(Pxx1);Axx1=Axx1    %amplitude spectrum: amplitude of the maximum amplitude spectrum
f1=f(I)                         % amplitude spectrum: frequency of the maximum amplitude spectrum
figure (6)
plot(f,Pxx1(1:N/2),'k')
xlabel('Frequency(Hz)','fontsize',14,'fontweight','bold')
ylabel('Amplitude(\mum)','fontsize',14,'fontweight','bold')
```

Q. Han et al., *Dynamics and Vibration Analyses of Gearbox in Wind Turbine*,
DOI 10.1007/978-981-10-2747-5

B.3 main_3D_FFT.m

```
%   ====================== first step: read data==========================
fp=fopen('xt1.dat','r');
x=fscanf(fp,'%f',1024);
fclose(fp);
%   ======================second step: data processing=======================
N=1024;
fs=3000;
nfft=N/8;
nov=nfft/2;
  [b1,ff,tt]=specgram(x,nfft,fs,[],nov);%time frequency power spectrum
b=detrend(b1);
tt;
abs(b');
ff;
tt=tt*1000*length(x)/(2*(length(x))/nfft+1);
%   ======================third step: display graphic=======================
figure;
waterfall(ff,tt,abs(b'));
title('three-dimensional spectral array ');
ylabel('time/ms');
xlabel('frequency/Hz');
zlabel('power spectral density');
```

Appendix C
Codes of Hilbert-Huang Transform Analysis of Vibration Signals

emd.m

```
%emd.m
% the function is used to complete the EMD decomposition
function [c,rn,nIMF]=emd(y,Ns,fs)
s1=y;    %data
  Ns=length(y);
  fs=6.4*1000*2.56;
s2=s1;
for i=1:Ns
  s2(Ns-i+1)=s1(i);
end
s=[s2 s1 s2];    % left and right extension of original signal
t=0:(1/fs):((3*Ns-1)/fs);
X0=s;
X=X0;
tic
[Xa Xb]=EvelopeData(X);
toc
figure (3)
plot(Xa(:,1),Xa(:,2),'or')
hold on
plot(s)
%EMDdecomposition process
%IMF calculation
```

Q. Han et al., *Dynamics and Vibration Analyses of Gearbox in Wind Turbine*,
DOI 10.1007/978-981-10-2747-5

```
c=[];
 h1=X;
 IMFflag=1;
 for i_IMF=1:30
   for k=1:420
        [Xa Xb]=EvelopeData(h1);
          [Ma,Na]=size(Xa);[Mb,Nb]=size(Xb);
        if min(Ma,Mb)<2
               Ma
               Mb
                 IMFflag=0;break
        end
        Ya=spline(Xa(:,1)/fs,Xa(:,2),t);
        Yb=spline(Xb(:,1)/fs,Xb(:,2),t);
        m1=(Ya+Yb)/2;
        h1k=h1-m1;
        SD=sum((h1-h1k).^2/h1.^2);
        if SD<0.25
                 h1=h1k;
                 r1=X-h1;
               break
      end
      h1=h1k;
 end
%
if IMFflag==0
      break;
end
c1=h1;
r1=X-c1;
c=[c c1'];
X=r1;
h1=X;
end
c;
rn=r1;                          % remnant
t=0:(1/fs):((Ns-1)/fs);
c=c(Ns+1:2*Ns,:);
rn=rn(Ns+1:2*Ns);
rn=rn';
[Ns3,nIMF]=size(c);
nIMF
```

C.1 hhspectrum.m

```
%hhspectrum.m
%the function is used to calculate Hilbert-Huang spectrum
% [A,f,tt] = HHSPECTRUM(x)
% inputs:
%      - x      : matrix with one signal per row
% outputs:
%      - A      : instantaneous amplitudes
%      - f      : instantaneous frequencies
%      - tt    : truncated time instants
% program
function [A,f,tt] = hhspectrum(x)
   t=1:size(x,2);                                  %    t: time instants
   l=1;                                             %    l: estimation parameter for instfreq (integer >=1 (1:default))
if min(size(x)) == 1
       if size(x,2) == 1
              x = x';
              t = 1:size(x,2);
       end
       Nmodes = 1;
else
       Nmodes = size(x,1);
end
lt=length(t);
tt=t((l+1):(lt-l));
for i=1:Nmodes
   an(i,:)=hilbert(x(i,:)')';
   f(i,:)=instfreq(an(i,:)',tt,l)';
   A=abs(an(:,l+1:end-l));
end
```

C.2 toimage.m

```
%tomimage.m
%the function is used to transform one dimensional spectrum into two dimensional spectrum
% inputs :      - A        : amplitudes of modes (1 mode per row of A)
%               - f        : instantaneous frequencies
%               - t        : time instants
% outputs :     - im       : 2D image of the spectrum
%               - tt       : time instants in the image
%               - ff       : centers of the frequency bins
%program
function [im,tt,ff] = toimage(A,f)
DEFSPL =800;% frequency normalization
    t = 1:size(A,2);                %t: time instants
    sply = DEFSPL;                  %sply : number of rows of the output im (frequency resolution).
    splx = length(t);               %splx : number of columns of the output im (time resolution).
                                    %If different from (tlength), works only for uniform sampling.
if isvector(A)
  A = A(:)';
  f = f(:)';
end
f = min(f,0.5);
f = max(f,0);
indf = round(2*f*(sply-1)+1);
indt = repmat(round(linspace(1,length(t),splx)),size(A,1),1);
im = accumarray([indf(:),indt(:)],A(:),[sply,splx]);
indt = indt(1,:);
tt = t(indt);
ff = (0:sply-1)*0.5/sply+1/(4*sply);
end
```

C.3 disp_hhs.m

```
%disp_hhs.m
%the program is used to display Hilbert-Huang spectrum
% inputs:    - im: image matrix (e.g., output of "toimage")
%            - t (optional): time instants (e.g., output of "toimage")
%            - inf (optional): -dynamic range in dB (wrt max)
%              default: inf = -20
%            - fs: sampling frequency
% use:    disp_hhs(im) ; disp_hhs(im,t) ; disp_hhs(im,inf)
%         disp_hhs(im,t,inf) ; disp_hhs(im,inf,fs) ; disp_hhs(im,[],fs)
%         disp_hhs(im,t,[],fs) ; disp_hhs(im,t,inf,fs)

%program
function disp_hhs(varargin)

error(nargchk(1,3,nargin));
fs = 0;
inf = -20;
im = varargin{1};
t = 1:size(im,2);
switch nargin
    case 1
        %raf
    case 2
        if isscalar(varargin{2})
            inf = varargin{2};
        else
            t = varargin{2};
        end
    case 3
        if isvector(varargin{2})
            t = varargin{2};
            inf = varargin{3};
        else
            inf = varargin{2};
            fs = varargin{3};
        end
    case 4
        t = varargin{2};
        inf = varargin{3};
        fs = varargin{4};
end

if isempty(inf)
```

```
    inf = -20;
end

if inf > 0
    inf = -inf;
elseif inf == 0
    error('inf must be nonzero')
end

M=max(max(im));

warning off
im = 10*log10(im/M);
warning on

figure(6)
if fs == 0
    imagesc(t,[0,0.5],im,[inf,0]);
    ylabel('normalized frequency')
else
    imagesc(t*0.00039,[0,0.5*fs],im,[inf,0]);
    ylabel('Frequency /Hz','fontsize',8)

end
set(gca,'YDir','normal')
xlabel('Time /sec','fontsize',8)
```